Predicting Retinal Haemorrhage following Retinal Vein Occlusion

by

Atrayee Bhattacharya

A thesis submitted to the College of Science and Engineering at the University of Glasgow for the degree of Doctor of Philosophy

School of Mathematics and Statistics
College of Science and Engineering
University of Glasgow

December 2025

Abstract

The retina is the layer of sensory tissue that lines the interior surface of the human eye. The retinal cells are nourished by a network of blood vessels, which are fed by a single artery/vein pair that enters and exits through the optic nerve. Retinal vein occlusion is a blockage in one of the veins of the retinal circulation, which can subsequently lead to retinal haemorrhage. Such blockages often occur at points of arterio-venous crossing, where the retinal vein and artery share a common sheath, and gradual swelling of the artery (due to arteriosclerosis) results in compression of the adjacent vein, narrowing the blood vessels, damaging their wall and eventually leading to a venous thrombus which rapidly occludes the vein. Retinal vein occlusion is the second most common retinal vascular disease and a common cause of vision loss in older patients. For the first time, we aim to understand how occlusion in one part of the retinal circulation can lead to haemorrhage in other parts of the network using a combination of cutting-edge image analysis and a mathematical model based on continuum mechanics. The clinical images suggest that the bursting of vessels occurs several generations upstream of the site of arterio-venous crossing. To investigate this clinical observation, we develop a one-dimensional network model composed of three generations of vessels informed by clinical images; we consider a locally applied (external) perturbation to drive an occlusion of the vein. We find that wave propagation only plays a significant role on timescales much faster than the typical timescales of thrombus growth, and so expansion of upstream vessels is more clearly aligned to the accumulation of blood upstream of the constriction due to the reduced outflow. Using this viscous model, we show that such flows can be captured with a model based only on Stokes flow and observe that as an external pressure is applied to the parent vein, there is a substantial overshoot in blood pressure in the generation of vessels immediately upstream of the occlusion. However, this overshoot diminishes as we increase the perturbation time and eventually becomes negligible. Furthermore, we show that the pressure increases monotonically in generations which are further upstream of the occlusion without exhibiting any overshoot.

In summary, this thesis develops a general framework for building realistic arterial and venous networks from patient images to study the retinal micro-circulation, which can be easily extended to bigger networks. Moreover, at the end, we use our three-generation arterio-venous model to study the real patient data extracted directly from images. Hence, our model does not predict a clear mechanism which might lead to a localised increase in blood pressure, which could drive

vessel rupture and help explain retinal haemorrhage in the vessel upstream of the constriction. Further work is therefore necessary to refine the model to robustly predict the onset of retinal haemorrhage.

This research has been presented at several national and international conferences, including the British Applied Mathematics Colloquium (BAMC), the UK Fluids Conference, and the Soft-Mech International Tissue Workshop. Manuscripts are currently in preparation for submission to relevant journals.

Acknowledgements

First and foremost, I would like to thank my three supervisors, Professor Peter Stewart, Dr Hao Gao and Professor Dirk Husmeier. I would like to thank them for their support and guidance over these past four years. I am forever grateful to Peter, who dedicated countless hours to my development as a mathematician, researcher and scholar. This thesis would not have been possible without his assistance. I could not have asked for a better supervisor than them. I would like to thank the College of Science and Engineering, University of Glasgow, EPSRRC and SofTMech Glasgow for funding this project over the course of 3.5 years. Additionally, I am also indebted to Dr Jay Mackenzie for the contribution to develop reconstructed vessel tree in Chapter 3. I would like to thank all members of the 'Maths In Eye' research group for enriching me with lots of technical knowledge over the years. The Maths & Stats IT and admin teams of the School of Mathematics, University of Glasgow, were extremely helpful, and they supported me throughout this journey.

Last but not least, I would like to acknowledge the contribution of my support system, my parents, Mira and Provash, my brother Shakya and my loved ones for always standing behind me through thick and thin. They have my unreserved and enduring thanks. Finally, I express my gratitude to all the people back home in India and in Glasgow who have ever crossed my path, enriched me knowingly and unknowingly.

Contents

List of Tables

List of Figures

Chapter 1

Introduction

The retina is the layer of highly specialised sensory neuronal cells lining the back surface of the human eye [128, 170]. The retina plays a critical role in vision by identifying light stimuli from the external environment and transforming them into electrical signals [170]. These signals are transmitted through the optic nerve to the visual cortex of the brain, where they are interpreted to form the visual experience [170]. This transformation of light into neural impulses is made possible by the complex structure of the constituent cells known as photoreceptors. For the proper functioning of these cells, the retina relies on a dense and specialised vascular system composed of two circulations: the retinal circulation and the choroidal circulation. The former is the focus of this study and supplies the nutrients for the innermost part of the retina.

The retinal vasculature represents a unique microcirculation in the body that can be observed *in vivo* [90, 128]. Moreover, the retinal vasculature possesses a distinctive structure and function, shaped by the retina's high metabolic demands and the presence of blood-retinal barriers [90]. Despite these unique features, it shares structural and functional similarities with other vascular systems, particularly the cerebral vasculature, in terms of blood flow regulation and barrier properties [90]. The retinal vascular network comprises arteries, veins, arterioles, venules, and capillaries, all of which play a crucial role in delivering oxygen, metabolites, and vital nutrients essential for maintaining retinal health and function. The retina is vulnerable to a variety of internal and external disturbances that can trigger pathological processes and result in retinal conditions such as retinal haemorrhage. This thesis concerns a particular pathway to retinal haemorrhage as a result of retinal vein occlusion.

The following section provides a brief overview of the retina and retinal vasculature (see section 1.1). Section 1.2 highlights key pathological changes associated with retinal haemorrhage. A detailed discussion on mathematical models for vascular networks, including the retinal circulation, is given in section 1.3. The following sections discuss different modalities of retinal imaging (see section 1.4), the basics of fundus imaging (see section 1.5), and a brief overview of pre-processing techniques is given in section 1.6. The next two subsections list all the components used for feature extraction from the fundus image (see section 1.7) and different retinal

vessel segmentation approaches (see section 1.8). Following this, section 1.9 outlines the novelty and the contribution of this thesis. In the last subsection 1.10, we discuss the research question, hypothesis and the objectives of this thesis.

1.1 The retina and retinal vasculature

Figure 1.1(a) presents the cross-sectional view of the human eye showing different parts of the eye and the relative position of the retina. The sagittal view of the human eye reveals three distinct structural layers (see figure 1.1a). The outer layer comprises the sclera and cornea. The middle layer, known as the uveal tract, is divided into three parts: the anterior iris, the intermediate ciliary body, and the posterior choroid. The inner layer, also known as the sensory layer, is the retina [170]. Three distinct chambers are located within three distinct layers discussed above (see figure 1.1a) [51]; the anterior chamber, located between the cornea and the iris, is filled with aqueous humour (see figure 1.1a) [51]; the posterior chamber lies between the iris and lens, enclosed by the ciliary body, and it also contains aqueous humor, which is the fluid that nourishes these structures and maintains intraocular pressure (see figure 1.1a) [51]; the vitreous chamber, situated between the lens and the retina, is filled with a transparent, colourless, gel-like substance known as the vitreous or vitreous body (see figure 1.1a) [51].

In this work, we focus mainly on the structure of the retina and retinal circulation. We start by discussing the anatomical structure of the retina in detail (see subsection 1.1.1). Then, the next two subsections outline the blood supply to and drainage from the retina (see subsection 1.1.2), and various techniques that have been developed to assess the hemodynamics of both human and animal eyes (see subsection 1.1.3).

1.1.1 Structure of the retina

The retina is a thin, semi-transparent, and highly organised structure composed of multiple layers of neurons. It lines the inner surface of the posterior two-thirds of the eye wall and plays a central role in visual processing [170]. The retina is an extension of the central nervous system and is connected to the brain by the optic nerve [51]. The retina has two primary layers: retinal pigment epithelium (RPE), and an inner neuro-sensory retina or neural retina [170, 10]; figure 1.1(b) shows a schematic diagram of the human retina. The RPE is derived from the outer layer of neuroectoderm, and the neural retina is derived from the inner layer of neuroectoderm [10, 170].

The RPE is a layer of cells adjacent to the Bruch's membrane (see green dashed line in figure 1.1b), separating the retina from the choroid [170]. There exists a potential space between the RPE and the neural retina, referred to as the sub-retinal space. The RPE regulates the movement of fluids, nutrients, metabolites, and waste to and from the highly vascularized choroid to the

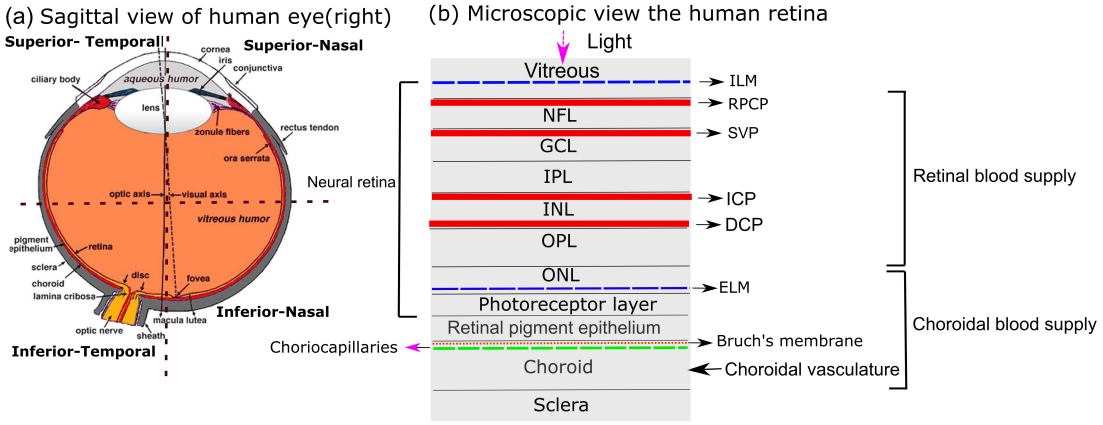

Figure 1.1: Organisation of retina showing:(a) Microscopic view of the vertical section through human peripheral retina and four quadrants of the right eye. Image source: Webvision[170], and (b) micrograph of a vertical section through the central human retina.

deep layers of the retina [128]. Both the vascular endothelium (lining of the blood vessels) and the RPE contain well-developed cell-cell junctions crucial for maintaining tissue integrity [128]. Moreover, the RPE contributes to forming the specialized blood-retinal barrier (BRB), which is essential for protecting the microenvironment required for the proper function of the retina and its microvasculature [128].

The other layer of the retina is the neural retina. The neural retina can further divided into nine distinct layers, including: the layers of outer and inner segments of photoreceptors (rods and cones), external limiting membrane (ELM), the outer nuclear layer (ONL), the outer plexiform layer (OPL), the inner nuclear layer (INL), the inner plexiform layer (IPL), the ganglion cell layer (GCL), the nerve fiber layer (NFL), and the inner limiting membrane (ILM) (see figure 1.1b) [128, 170]. The neural retina is firmly attached at two key points: anteriorly at the ora serrata (see figure 1.1a) and posteriorly at the optic disc (optic nerve head) [170].

Within all layers of the retina discussed above, there are six cell types, each with a specialised role in converting incoming light into electrical signals. The six different cell types in the retina include: photoreceptors (rods and cones), retinal ganglion cells, bipolar cells, horizontal cells, amacrine cells, and Müller glia cells [128, 168, 170]. Structurally, all retinal layers are supported and interconnected by specialized radial glial cells known as Müller cells, which span the entire thickness of the retina [128]. They are the principal glial cell in the retina, helping to maintain the retinal environment and metabolic regulation [157]. The output neurons of the retina, the retinal ganglion cells, are located in the GCL and are responsible for generating action potentials [128, 170]. The axons of ganglion cells form the NFL, where they converge and exit the eye through the lamina cribrosa at the optic disc, collectively forming the optic nerve that transmits visual information to the brain [128, 170]. This area lacks photoreceptors and is often referred to as the blind spot [128].

The densities of the retinal layers of cells are not the same across all parts of the retina. Based on these, the retina is functionally and anatomically divided into two main regions: the central

retina and the peripheral retina [10, 90]. There exists an imaginary circular line called the equator that divides the eye into anterior (peripheral retina) and posterior (central retina) hemispheres, located midway between the anterior and posterior poles (see figure 1.1a) [10]. The central retina comprises the macula lutea, with the fovea centralis (or simply fovea) situated at its centre, specialised for high-acuity vision (see figure 1.1a) [170]. The fovea lies at the posterior pole of the eye (see figure 1.1a) [128]. At the core of the fovea is the foveola, where the retinal layers are significantly thinner than other parts of the retina, enabling the light to reach the underlying photoreceptors [86, 170]. The peripheral retina encircles the central retina and stretches from the outer margin of the macula to the ora serrata [168]. It can be further divided into different zones according to their distance from the fovea. The structure of the retinal layers varies between the central and peripheral regions. While the central retina is rich in cones, the peripheral retina is predominantly composed of rods [98, 128, 170]. A significant difference is observed in the relative thicknesses of the inner plexiform layer (IPL), ganglion cell layer (GCL), and nerve fiber layer (NFL) when comparing the central and peripheral retina. This difference is due to the large quantity and dense packing of ganglion cells necessary for the working pathways of cone in the central retina, in contrast to the rod-dominated peripheral retina [98, 170].

Based on spatial orientation, the retina is anatomically divided into four quadrants: superior nasal, superior temporal, inferior nasal, and inferior temporal (see figure 1.1a). The central retina is located in the superior temporal and inferior temporal quadrants of the retina, while the peripheral retina fully spans over above four quadrants. The quadrant system is essential for accurately localizing and describing retinal landmarks, vascular structures, or pathological changes, and is commonly used in clinical examinations and imaging interpretations. In our mathematical model, we consider the parameter values from the superior temporal quadrant.

To get the proper nutrients and blood flow, the different parts of the retina, retinal cells, and retinal layers primarily depend on two blood supplies: the choroidal circulation and the retinal circulation. In the following subsection, we discuss the two circulations that support the retina.

1.1.2 Blood flow in the retina

The human eye receives its blood supply primarily from the ophthalmic artery (OA), which branches into the different arteries to supply blood nutrients to the retina, choroid, and other parts of the human eye [10, 48]. The choroidal circulation is responsible for the majority of ocular blood flow, accounting for approximately $65-85\%$ of the total flow [10, 81, 170]. In contrast, the remaining blood supply is delivered through the retinal circulation [170].

The choroidal circulation is a component of the choroidal vascular system (or uveal system) that contains the iris, the ciliary body, and the choroid [48]. The choriocapillaris, the innermost capillary layer of the choroid, plays a crucial role in supplying oxygen and nutrients to the outer one-third of the retina, including bipolar cells, the RPE, and the photoreceptor layer of the retina, which are among the most metabolically active cells in the human body (see figure 1.1b) [128,

130, 170]. It also nourishes the avascular fovea, which lacks direct retinal blood vessels [90, 128, 170]. The choriocapillaris lies directly beneath the RPE (see figure 1.1b) [90, 128, 170]. The choriocapillaris receives its blood supply from Sattler's layer, which contains medium-sized vessels branching from the larger vessels of Haller's layer, the outermost layer of the choroid [90, 128, 130]. This vascular system is supplied by the short posterior ciliary arteries, branches of the ophthalmic artery, and venous drainage occurs through the vortex veins [128, 130, 90].

The retinal circulation contains the central retinal artery (CRA) and central retinal vein (CRV), retinal arterioles and venules, and capillary plexi, and they together form the retinal vascular bed. The retina receives blood and all necessary nutrient supply from the central retinal artery, a branch of the ophthalmic artery, and the CRV drains the blood from the retina [90, 128, 130]. The CRA nourishes the inner retinal layers, including the NFL, GCL, IPL, and INL (see figure 1.1b), and also the most anterior portion of the optic nerve head [48, 128, 130].

The CRA emerges at the centre of the optic disc (the blind spot, see figure 1.1a), where it divides into two branches, namely superior and inferior branches, which further divide into temporal and nasal vessels [90]. Each of these branches nourishes a quadrant of the retina and further divides into smaller branches. The CRV drains the blood from the retina into the superior ophthalmic vein [128]. The CRV exits the eye, passing through the optic nerve, and runs parallel to the CRA [128]. The CRV is the merging of four major venules (i.e., superotemporal, superonasal, inferotemporal, and inferonasal) that drain different regions of the retina [128]. These branches roughly follow the same pattern as the branches of the CRA.

The major retinal arteries and veins travel through the superficial NFL and branch to precapillaries (see figure 1.1b) [90, 157]. Pre-capillaries branch out to form the retinal capillary plexi, which are anatomically organised into three distinct layers: the superficial, intermediate, and deep plexi [90, 128]. The superficial vascular plexus (SVP) is supplied by the central retinal artery and is composed of larger arteries, arterioles, capillaries, venules, and veins. SVP is primarily in the GCL. There are two deeper capillary networks above and below the INL, referred to as the intermediate capillary plexus (ICP) and deep capillary plexus (DCP), respectively, which are supplied by small blood vessels that form connections between two plexi, known as vertical anastomoses from the SVP (see figure 1.1b) [90, 128, 162]. The deep capillary plexus is typically denser and more intricate than the superficial one [90, 128]. There is another capillary network called the radial peripapillary capillary plexus (RPCP) [128]. The radial peripapillary capillaries run in parallel with the ganglion cell axons in the NFL [128]. The RPCP is crucial for supplying the densely packed NFL bundles in this region [128]. Retinal capillaries are arranged in parallel layers, with the highest density near the optic disc and decreasing toward the periphery [128].

The capillary network acts as the crucial link between the arterial and venous systems, facilitating the exchange of oxygen, nutrients, and waste products between the blood and retinal tissues. It is important to note that in Chapter 6, we incorporate the capillary plexi to construct a complete arterio-venous network comprising three vascular generations. Building on this under-

standing of the retinal vasculature, we can now explore how blood flow in the retinal vasculature is measured both in animals and humans.

1.1.3 Measurement of retinal blood flow

There are several methods for retinal blood flow measurement, but no gold standard is available. Studies have been conducted both on human and animal models, including genetically modified animals in laboratory [157]. Measuring ocular blood flow is challenging because the posterior pole of the eye is supplied by two distinct vascular systems: the retina and the choroid. These two systems differ markedly in their physiological functions and pathological characteristics.

The primary techniques presently employed to assess ocular blood flow in humans are, namely: Colour Doppler Imaging (CDI), Angiographic Techniques, Blue Field Entoptic Technique, Laser Speckle Technique, and Laser Doppler Velocimetry [48, 47]. Details of the principles behind these techniques are given in [157]. However, all the above-mentioned techniques are limited in that they provide information only on blood velocity, not on actual blood flow per unit of time [47]. As a result, interpreting the findings becomes challenging, since it is difficult to determine whether an observed increase in blood velocity reflects a true rise in blood flow or is instead due to constriction within the measured vascular bed [47].

To determine blood flow accurately, the exact determination of vessel diameter is important [47, 157]. The retinal vessel analyser (RVA) is a system for real-time measurement of vessel diameter, which contains a fundus camera attached to a computer, allowing the computation of the retinal arterial and venous diameters [157].

More advanced techniques to measure retinal blood flow combine the blood flow measurement technique with the retinal vessel diameter measurement techniques. The Canon Laser Doppler blood flowmeter (CLDF) is one of the methods that combines the Laser Doppler Velocimetry with a retinal vessel diameter assessment system [157].

Optical coherence tomography (OCT) is used to take images of retinal structure, and this method generates cross-sectional or three-dimensional images by measuring the echo time delay and magnitude of reflected light [47, 157]. Doppler OCT is an advanced non-invasive imaging technique that integrates OCT with Doppler velocimetry [93]. DOCT aims to provide quantitative volumetric information about blood flow, together with the vascular and structural anatomy of retinal layers [93].

Garhofer et.al. carried out a study to measure retinal blood flow in 64 healthy volunteers [76]. In this work, the vessel diameters are measured using the dynamic vessel analyser (DVA), and then retinal blood velocities are computed using Laser-Doppler Velocimetry (LDV) [76]. Garhofer et. al. measured the total retinal blood flow as $44.0 \pm 13.3 \mu L/\text{min}$ [76]. Among the retinal quadrants, blood flow is highest in the temporal inferior quadrant, followed by the temporal superior, nasal inferior, and nasal superior quadrants [76]. Measurements indicate that retinal blood flow is $42.1 \pm 13.0 \mu L/\text{min}$ in the venules and $43.3 \pm 12.1 \mu L/\text{min}$ in the arterioles [76].

1.2 Retinal vein occlusion (RVO) and retinal haemorrhage (RH)

Retinal vein occlusion (RVO) is a blockage in the retinal venous network, either in the main veins or in one of the smaller veins. Retinal vein occlusion (RVO) is the second most common retinal vascular occlusive disorder, following diabetic retinopathy [69]. It typically presents as a sudden, painless loss of vision in a patient's eye. The severity of vision loss varies depending on the degree of retinal involvement and the status of macular perfusion [22, 69].

According to the site of occlusion, there are mainly two types of RVO, namely branch retinal vein occlusion or BRVO, and central retinal vein occlusion or CRVO [22, 70]. BRVO involves the blockage of a branch of the retinal vein. This may affect a major vein draining one retinal quadrant, a macular branch vein serving part of the macula, or a peripheral branch vein supplying a section of the retinal periphery [70]. CRVO is the occlusion of the CRV, and it takes place at the level of or posterior to the lamina cribrosa [69, 70]. The specific site of the CRVO can influence the optic nerve head swelling [69, 70]. A CRVO without optic nerve head swelling may occur at the level of the lamina cribrosa, whereas occlusions located further posteriorly are more likely to be associated with such swelling [70]. Among the two main types of RVO, BRVO is more common than CRVO [22]. It is important to note that in this work, our primary focus is on BRVO.

BRVO most commonly occurs at arterio-venous (A-V) crossings [70]; however, not all vessels with A-V crossings exhibit BRVO. At the A-V crossing, the artery and vein share a common vascular wall along with a thickened adventitial and glial sheath, regardless of which vessel, the artery or the vein, is positioned internally [22, 70]. A typical clinical image of the retinal circulation in the aftermath of the BRVO is shown in figure 1.2(b), obtained from our clinical collaborator. It shows the retinal blood vessel network (red lines) along with an arterio-venous crossing, which is labelled in figure 1.2(b). The clinical expert identified BRVO from an arterio-venous crossing (see the annotation in figure 1.2b).

The condition that promotes BRVO is believed to result from a combination of three systemic changes collectively known as Virchow's triad [22, 69]:

- hemodynamic changes (venous stasis or slowing of blood flow in vessels),
- degenerative changes of the vessel wall, and
- blood hypercoagulability.

However, the role of hypercoagulability in the formation of RVO is not yet fully understood [22, 70].

The second component of Virchow's triad, i.e., the vessel wall damage, plays a key role in the development of BRVO [22, 70]. Figure 1.3(a-d) describes the steps involved in BRVO occurring at the A-V crossing. Figure 1.3(a) shows a typical cross-sectional view of A-V crossing and the relative positions of artery and vein bounded by a common sheath. Atherosclerosis is a

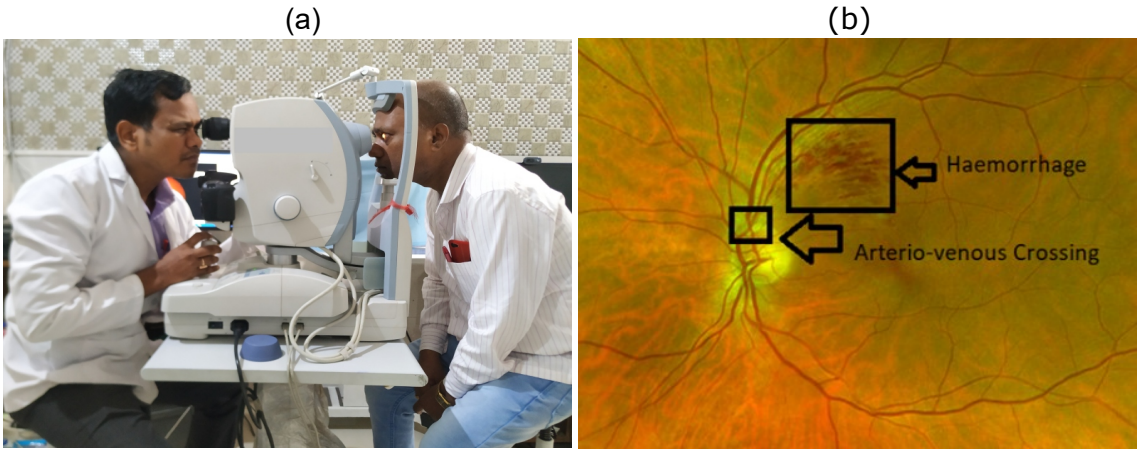

Figure 1.2: (a) Fundus photo of a patient is being taken by an expert in a fundus camera. Image source: StatPearls Publishing [169] and (b) clinical image of branch retinal vein occlusion (BRVO) showing the site of occlusion at an arterio-venous crossing and an associated retinal haemorrhage clearly visible

.

pathological condition characterised by the accumulation of plaques within the arterial wall (see figure 1.3b). These plaques, composed of cholesterol, fat, and other blood-borne substances, deposit on the artery walls, leading to thickening and loss of elasticity of the wall. This arterial stiffening is believed to play a significant role in the development of BRVO [22, 70, 154]. At the points of A-V crossing, the swelling of the arterial wall due to atherosclerosis results in the compression of the adjacent thin-walled vein (see figure 1.3b) [22, 69]. This causes damage to the endothelial membrane of the vein, which then fails to control the blood pressure and to maintain the anticoagulant surface of the vascular bed [22, 36, 69]. The damaged endothelium expresses pro-coagulant behaviour and loses its ability to repel blood cells. Consequently, platelets and red blood cells begin to adhere to the injured venous wall (see figure 1.3c). As a result, blood flow through the vein becomes slow, which is known as stasis [22]. The resulting stasis and cellular adhesion promote the development of an intravenous thrombus, a blood clot formed within the vein [22, 36]. This thrombus progresses to occlude the vein over time (see figure 1.3d) [22]. A venous occlusion can interrupt or even completely shut off the venous outflow. The sudden obstruction of venous outflow prevents the retinal venous network from draining blood properly, leading to a rapid increase in intravascular pressure within the retinal circulation proximal to the site of the venous thrombus [22].

As pressure increases in the retinal capillaries and small venules upstream of the site of RVO, retinal capillaries are fragile and thin-walled; they can not withstand the increased pressure and rupture. As a result, blood leaks out onto the surface of the retina, and this eventually leads to retinal haemorrhage (bleeding in the retina). Figure 1.2(b) shows the additional patches of blood (haemorrhage) resulting from the rupture of capillaries and smaller (possibly more fragile) veins.

Retinal haemorrhages (RH) are classified into various types depending on their anatomical location, each presenting with distinct characteristics [158]. Based on the anatomical locations

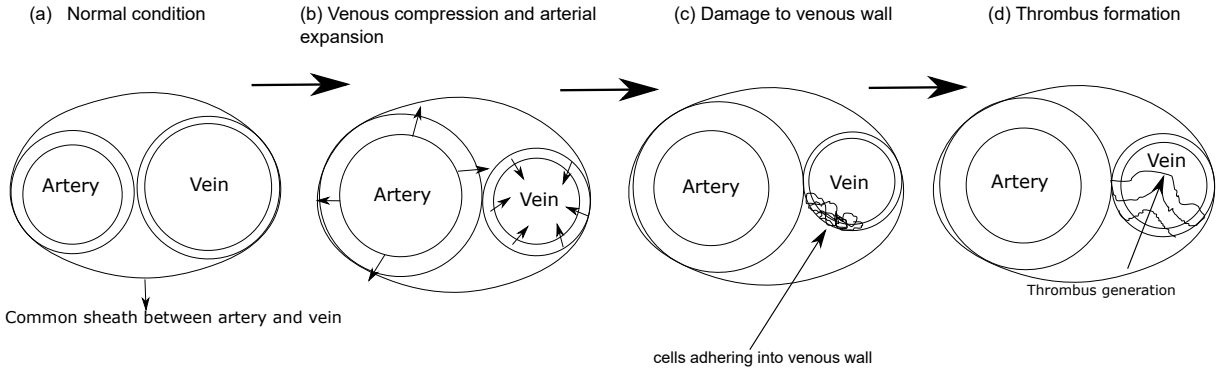

Figure 1.3: Progression of venous occlusion at arterio-venous (A-V) crossing showing:(a) normal condition, (b) arterial wall thickening because of atherosclerosis, (c) damage to the venous wall due to arterial wall thickening and (d) thrombus production and retinal vein occlusion at A-V crossing.

RH can be localised in the anterior chamber (known as hyphema), vitreous cavity (known as vitreous haemorrhage), beneath the posterior hyaloid membrane, a thin layer located between the posterior vitreous cortex and the ILM (known as subhyaloid haemorrhage), or beneath the ILM but anterior to the NFL (known as sub-ILM haemorrhage) [158]. Within the NFL, RH often appear as superficial, linear, or flame-shaped haemorrhages [158]. In the GCL, IPL, and INL, RH typically appear as a dot and blot [158]. Haemorrhages in Henle's layer of the choroid inside the OPL present a petaloid pattern, while those beneath the neurosensory retina or the RPE are termed as sub-retinal and sub-RPE haemorrhages, respectively [158]. Bleeding may occur within the choroid or in the suprachoroidal space, which lies between the choroid and sclera and in this case, the haemorrhage is known as suprachoroidal haemorrhage [158]. Haemorrhage can happen at the optic disc, known as optic disc haemorrhage [158]. Additionally, retinal haemorrhages are also observed in infants and typically resolve within a few days [87]. However, when caused by violent shaking, such as in cases of shaken baby syndrome, a form of physical non-accidental injury to infants, characterised by acute retinal haemorrhages, may lead to permanent visual impairment [35, 87]. Figure 1.2(b) is a typical example of a flame-shaped retinal haemorrhage. However, note that haemorrhage occurs several generations of blood vessels proximal to the A-V crossing site.

1.3 Different mathematical models for microcirculation

Mathematical models enable a deeper understanding of a wide range of complex systems, and the human circulatory system is no exception. The human circulatory system comprises the four-chamber heart (including the four heart valves), the systemic vessels that supply blood to and collect blood from the peripheral organs, and the pulmonary vessels that deliver blood through the lungs for the exchange of oxygen and carbon dioxide. The systemic and pulmonary vessels each can be divided into a bifurcating network of aorta/pulmonary artery, main and small arteries,

arterioles, veins, venules, vena cava/pulmonary vein, and capillaries [72]. As blood flows from the aorta into the arteries, arterioles, and eventually the capillaries, the vessels branch in a tree-like pattern. With each successive generation of branching, the diameter of individual vessels decreases [72]. The aorta and the larger arteries are elastic, working as reservoirs that help buffer the pulsatile flow generated by the heart [72]. Similarly, the vena cava and larger veins are elastic, and some veins, which have venous valves to control the directionality of blood flow, are also subjected to the compressive action of the surrounding muscles, providing a pumping action that returns blood to the right side of the heart [72]. Due to the changing vessel properties and bifurcations, there are pulse wave reflections in the arterial system. Generally, the mean intra-luminal pressure and the pressure pulsatility decrease along the blood flow direction from arteries to veins, although in the aorta and larger arteries, the pulsatile nature can increase due to pulse wave reflections [72]. Like all fluid dynamical systems, blood flow in the cardiovascular system must obey the laws of mass conservation, momentum conservation, and energy conservation.

Over the past half-century, considerable effort has been devoted to modelling the human circulatory system [33]. In this context, mathematical models can be manipulated to test the hypotheses, predict future outcomes and uncertainties, and conduct non-invasive experiments that would be otherwise unfeasible [39, 122]. Haemodynamic modelling was introduced in the 20^{th} century by McDonald [53], Womersley [3, 4], and Pedley [9]. Over the time, in micro-circulatory modelling studies, the focus is shifted to more domain-specific modelling, such as the systemic circulation [23, 68, 89, 94], the pulmonary circulation [50, 96], the retinal micro-circulation [61] or the coronary circulation [52] while representing regions outside this domain using a lumped parameter approach. Domains of particular interest are modelled using in $0D$, $1D$ and $3D$ models providing boundary conditions. $3D$ models for the entire cardiovascular system are not feasible due to high computational expense [144].

Initial attempts have been made to model the human arterial tree using the lumped parameter models. The first Windkessel model (2-element) was a lumped parameter model of the whole arterial tree, which was introduced by Frank et. al. [1]. This lumped parameter model considered the entire arterial tree as a parallel combination of the arterial compliance and the peripheral resistance [1]. The 3-element Windkessel added aortic characteristic impedance to the 2-element Windkessel model [108]. Other simple mathematical models of the cardiovascular system have been developed using hydrodynamic equations [21], while some mathematical models employ electrical analogues to represent the vascular system [5, 21]. However, the lumped-parameter model provides limited insight into regional circulatory system issues. Moreover, these early models overlook the intricate details of pressure and wave propagation through the arterial network. The regular expansion and contraction of arteries (the pulse) follows cardiac contraction, propagating in the form of pulse waves [54]. The pulse wave propagation is a unique characteristic of the arterial blood circulation. These produce continuous changes in blood pressure and flow, which can be analysed as pressure and flow wavefronts running away from (forward) and

towards the heart (backward), respectively, with backward wavefronts originating from reflected forward wavefronts at sites of vascular impedance mismatch [54]. Pulse waves travel along the elastic arteries at a speed known as the pulse wave velocity. Pulse wave propagation in arteries is crucial for transporting blood from the heart to tissues and organs throughout the body. The pulsatile flow in rigid tubes was first studied by Witzig et. al. [2]. Then, Womersley et. al. provided the solution for the velocity profile in a rigid tube [3]. It was further extended to address pulsatile flow in elastic-walled tubes, incorporating wall viscoelasticity [4]. McDonald's work was mainly concerned with pulsatile blood flow and associated pulsatile pressure changes. Womersley et. al. applied mathematical and computational techniques to the analysis of arterial blood flow, and described a dimensionless parameter, the Womersley parameter, $\alpha = R\sqrt{\frac{\omega}{\nu}}$, where R is the tube radius, ω is the angular frequency, and ν is the kinematic viscosity [3]. This Womersley parameter characterises the nature of unsteady flows. When the Womersley parameter value is low, viscous forces dominate; when the Womersley parameter is large, the unsteady inertial forces dominate the total flow [26]. In general, smaller vessels are considered as Womersley-type vessels (i.e., Womersley number is low) while the primary branches are modelled based on one-dimensional Navier-Stokes equations [45]. Pedley et. al. and Lighthill et. al. studied the propagation of small-amplitude pressure waves in the fluid through a bifurcating network of elastic-walled tubes [8, 12]. Later, Pedley et. al. conducted pioneering research on the fluid-structure interactions in elastic-walled tubes and the pressure drop within the lung [9]. The inviscid flow in each constituent vessel of a small arterial network is described through a characteristic impedance, and the division of mass across the network junction is characterised by a reflection coefficient [6]. This type of approach has been applied for larger networks to mimic the human cardiovascular system with physiological parameter values [11, 54]. Commonly, cardiovascular flows can be considered as quasi-$1D$ flow because the wavelengths of pressure pulses are much longer than the diameter of blood vessels [7]. Olufsen et. al. developed an arterial $1D$ flow model by using the impedance of a structured tree as the outlet boundary condition and showed a better pressure/flow phase relationship compared to models with a constant peripheral impedance [23, 29, 31]. Vaughan et. al. extended the work of Olufsen et. al. to develop a new model for the pulmonary circulation, including arterial and venous flows and pressures, and connecting the arterial and venous sides using boundary conditions [68, 80]. This boundary condition allowed him to capture venous pulse wave dynamics [68, 80]. Later, Qureshi et. al. developed and expanded Vaughan's $1D$ flow model to improve its ability to predict pulmonary arterial and venous blood flow and pressure dynamics [85]. The improvement was done by refining the venous morphometry, physiological parameters, and boundary conditions, and by extending the model to predict pressure drop across vascular beds [85]. Mynard et. al. and Nithiarasu et. al. designed a $1D$ flow model for the coronary and systemic circulations that includes the compression of the coronary vasculature by the left ventricle [52]. The external pressure applied to the coronary vasculature was modelled using the constitutive relation for vessel lumen area, fol-

lowing the same approach later used in this thesis for modelling external pressure for mimicking retinal vein occlusion, as well as by Müller et al. [94] and Mackenzie et. al. [143] in the context of pulmonary and coronary circulation modelling. Formaggia et. al., Quarteroni et. al., and Veneziani et. al. offered a thorough overview of the current state of the art in the modelling of the cardiovascular system [65]. All of the models discussed above are $1D$ flow models for which the authors have made reasonable assumptions and approximations to linearise the Navier–Stokes equations.

Blood flow in arterial networks is influenced by wave propagation and wave reflection. To study the role of wave reflections in shaping pressure and flow waveforms in systemic arteries, wave separation analysis (WSA) and wave intensity analysis (WIA) have been used extensively [59, 108]. WSA uses measured aortic pressure and flow waves directly to distinguish forward waves from the backward (reflected) waves, where the pressure and flow waveforms at any arterial site are a superposition of a forward and backward wave [7, 59, 163]. Forward waves in the arterial systems are largely caused by the heart, and backward waves are considered to be the result of reflections [59]. The pulse pressures (both forward pressure ΔP_F and backward pressure ΔP_B) are calculated from the amplitudes of $P_F(t)$ and $P_B(t)$ [163]. The ratio of ΔP_B to ΔP_F is called the reflection magnitude (RM), and the ratio of ΔP_B to the sum of ΔP_F and ΔP_B is defined as the reflection index (RI) [163]. RM and RI are used to quantify the reflected wave in the aorta. WIA is also based on measured pressure and flow, but unlike WSA, to separate forward and backward waves it uses time derivatives of pressure (dP) and flow (dU), where dP and dU are the differences in the measured $P(t)$ and $U(t)$ during the interval dt [108]. The water hammer equation gives the relationship between dP and dU across a wavefront, and it follows from the method of characteristics [59, 108]. The water hammer equations can be written as

$$dP_F = \rho c dU_F \quad \text{for forward wavefronts [59]}$$
$$dP_B = \rho c dU_B \quad \text{for backward wavefronts [59].}$$

where ρ is the density of blood, which is assumed to be constant. c the wave speed at any particular position is a constant. dP can be positive (compression) or negative (decompression), and dU can be positive (acceleration) or negative (deceleration) [59]. The wave intensity dI is defined as the product of the measured dP and dU where $dI(t) = (dP(t)/dt) \times (dU(t)/dt)$ [59, 163]. dI is positive for forward waves and negative for backward waves[59]. A key limitation of these approaches is their inability to explain diastolic behaviour, i.e., the exponential fall-off of pressure and zero velocity during diastole (pressure decay with near-zero flow).

This problem gave rise to the reservoir-wave hypothesis [59]. According to the reservoir-wave hypothesis, the arterial pressure consists of two components, namely a reservoir pressure generated because of the expansion of the elastic arteries during systole, followed by their contraction during diastole (the Windkessel effect, describing the gradual fall in pressure) and a wave pressure, which is responsible for the propagation of arterial waves [59, 108]. It is also impor-

tant to understand how these waves propagate through the network when there are impedance mismatches (e.g., bifurcations, diameter changes) in the network. Whenever a wave encounters a discontinuity of conditions, such as a change in vessel diameter, a bifurcation, or a variation in the local wave speed, it gives rise to reflected and transmitted waves which must satisfy the boundary conditions at sites of impedance mismatch [59, 88]. Waves generated by the heart propagate toward the periphery and are reflected at impedance mismatches in smaller vessels [59]. As these reflected waves travel back, they undergo repeated reflections at bifurcations, generating successive forward and backward waves [59]. This process of reflection and transmission of waves plays a crucial role in understanding blood flow in the vascular network [59].

There are studies available specifically focused on the retinal microcirculation. The model presented in this thesis captures arterial and venous flow and pressure in retinal microcirculation. To mimic RVO, retinal veins are occluded by applying external pressure to the vein. It is designed to be implemented using only data that can be directly measured or inferred from physiological observations, making it applicable to modeling any arterial or venous system, provided sufficient data are available. There are many predecessors to this model. Below, we highlight some of the most notable.

Takahashi et. al. described the retinal micro circulation using a simple mathematical model by considering the vessel as rigid tubes [61]. He proposed a simple computational model to analyse blood flow dynamics within an idealised representation of the retinal microvascular network [61]. The microcirculatory model is based on a system characterised by symmetric dichotomous branching [61]. In this idealised network, each parent vessel gives rise to two daughter vessels, and then each of these daughter vessels gives rise to two further offspring, and so on [61]. Four capillaries are considered to originate from each precapillary [61]. The theoretical model developed in quantifies the hemodynamic parameters, including blood pressure in the idealised network, shear rate, shear stress, blood flow, and flow velocity as a function of vessel diameter [61]. Table 1.1 presents the morphological and geometrical parameters of the idealised retinal arteries and veins, as adopted from [61]. Our model for the arterio-venous network given in Chapter 6 is greatly inspired by Takhashi's microcirculatory model, but there are key notable differences which we discuss in the following section. We adopted the values from Takahashi's work given in the table 1.1 for the simulation in the rest of the thesis. As discussed in subsection 1.1, the central retinal artery and central retinal vein (CRA, CRV) enter the eye through the optic nerve. These are denoted as generation 1. Upon entering the retina, the CRA and CRV divide into two primary branches: the superior and inferior. These are denoted as generation 2. The superior and inferior branches further divide into the superior temporal, superior nasal, inferior temporal and inferior nasal branches. These branches are denoted as generation 3. We follow a similar naming convention in the rest of the thesis, and we consider the artery and vein of generations 3 and 5 in the superior temporal quadrant of the retinal circulation to show different numerical results in later chapters. The input data for vessel diameters r_0^* (for vein $147\mu m$ and

for artery $108\mu m$) listed in the table 1.1 for generation 3 were measured from the superior temporal quadrant in normal eyes of 13 healthy young human male volunteers ranging from 19 to 23 years [61]. The length L^* of the blood vessel segments between the midpoint of bifurcations was derived using the branch length-radius relationship $L^*(r) = 7.4(r_0^*)^{1.15}$ [61]. The appearent viscosity μ^* of blood for different vessel size is given by

$$\mu^*(r_0^*) = \frac{\mu_\infty^*}{(1+\delta/r_0^*)^2},$$

where μ_∞^* is the asymptotic viscosity of blood flowing through the large tubes [61]. μ_∞^* is give by an empirical formula $\mu_\infty^* = 1.09e^{0.024\times \mathrm{Hct}}$ where Hct is the hematocrit of the systemic blood [61]. The constant δ is 4.29 [61]. The blood viscosity in venular vessels was approximately 8% higher than in arteriolar vessels, primarily due to the relatively low shear rate [61]. Total retinal blood flow was measured in 64 healthy human volunteers, and the value was reported as $44.0 \pm 13.3 \mu L/min$ [76]. Based on total retinal blood flow, we considered that each of these retinal quadrants gets almost an equal amount of blood flow, which is approximately $1.88\times 10^{-4} ml/s$. The Poisson's ratio ν was determined using the digital image correlation (DIC) technique to measure the induced strains of 9 healthy human coronary arteries at two different longitudinal strain rates: $5mm/min$ and $20mm/min$ [114]. The findings showed that the mean Poisson's ratio for healthy adults was 0.49098 at a strain rate of $5mm/min$ and 0.49156 at a strain rate of $20mm/min$ [114]. Poisson's ratio of the venous wall is assumed to be the same as that for the arterial wall [91].In principle, the Young's modulus of the tissue can be obtained (approximately) from experimental measurements of the pulse wave velocity (PWV) within human retinal blood vessels [136]. However, PWV measurements in retinal arteries provide a wide range of values, including $4\times 10^{-4} ms^{-1}$, $0.01 - 0.03 ms^{-1}$, and $0.6 ms^{-1}$ [136]. However, it is very unlikely that such variability is seen between patients [136]. Due to these inconsistencies in measurement, we take $E^* = 0.3 MPa$ in the artery and $E^* = 0.6 MPa$ in the vein, as a baseline value of Young's modulus, which have previously been used in different studies to model the retinal circulation [136, 91] and are of comparable magnitude to Young's modulus of similarly sized blood vessels elsewhere in the body [136]. The value for the vessel wall thickness h^* listed in table 1.1 was used in others studies [136, 91]. The value was initially obtained from the cross-sectional study which was conducted over 23 patients of age 57.5 ± 9.4 years with acute transitory ischemic attack or lacunar cerebral infarct, who were compared with two age-matched control groups of 83 patients of age 53.7 ± 5.5 years with essential hypertension and 16 normotensive patients of age 52.2 ± 8.3 years [55]. The detailed discussion on 'tube law' parameters, namely vessel stiffness k^* is given in the subsection 4.2.1 of Chapter 4.

Stewart et. al. considered a theoretical model to study the venous pulsation in the central retinal vein, focusing on self-excited oscillations in a collapsible channel [131]. He modelled the flow through a long flexible-walled channel, which is formed from four compliant and rigid

Table 1.1: Reference parameter values of the artery and the vein of generations 3 and 5 in the retinal network at the superior temporal quadrant.

generation 3	**parameter**	**symbol**	**unit**	**arterial value**	**venous value**	**source**
	lumen radius	r_0^*	μm	94	73.5	[61]
	length	L^*	μm	726.9	1036.2	[61]
	apparent viscosity	μ^*	$Pa-s$	0.0037	0.0042	[61]
	blood flow	Q^*	mls^{-1}	1.88×10^{-4}	1.88×10^{-4}	[61]
	wall thickness	h^*	μm	32.1570	8.6670	[136]
	wall stiffness	k^*	Pa	2106	32.40	[136]
	Young's modulus	E^*	Pa	243000	486000	[136]
	Poisson ratio	ν	-	0.49	0.49	[91, 114]
	density of blood	ρ^*	kgm^{-3}	10^3	10^3	[12]
generation 5	**parameter**	**symbol**	**unit**	**arterial value**	**venous value**	**source**
	lumen radius	r_0^*	μm	33.2	45.2	[61]
	length	L^*	μm	415.5	592.3	[61]
	apparent viscosity	μ^*	$Pa-s$	0.0034	0.0039	[61]
	blood flow	Q^*	mls^{-1}	4.71×10^{-5}	4.71×10^{-5}	[61]
	wall thickness	h^*	μm	26.0472	7.0203	[136]
	wall stiffness	k^*	Pa	1706	26.244	[136]
	Young's modulus	E^*	Pa	196800	393700	[136]
	Poisson ratio	ν	-	0.49	0.49	[91]
	density of blood	ρ^*	kgm^{-3}	10^3	10^3	[12]

compartments arranged alternately in series [131]. This study explored the parameter space and found that if the flow rate along the vein is reduced, the onset of oscillations can be delayed until the intraocular pressure (IOP) becomes significantly larger [131]. Additionally, this delay in oscillation is accompanied by a notable increase in the frequency of the oscillations [131].

Spelman et. al. developed theoretical frameworks to study the response of the eye to an acute rise in cerebrospinal fluid (CSF) pressure in the brain (or the intracranial pressure (ICP)), which leads to retinal haemorrhage, accompanied by a rise of intraocular venous pressure [136, 165]. The proposed theoretical model studied the propagation of large amplitude elastic jumps (shock waves) in retinal blood vessels, and also through a junction from a parent vessel into two (identical) daughter vessels, which arise because of an acute change in ICP [136, 165]. However, this study focuses on retinal haemorrhage because of accidental head injury, where the timescale of perturbation is significantly shorter than in our case here. The timescale of perturbation is considered as $t_p^* \approx 0.1-10ms$ in [136], which is comparable to the estimated timescale of contact for free-fall, whereas in this study, we consider that t_p^* is in the range of seconds.

1.4 Different modalities of retinal imaging

The retina is the only human tissue where blood vessels can be visualised non-invasively in vivo, making the study of the retinal hemodynamics and blood flow regulation particularly valuable for

studying the physiological and pathological conditions of the retina [73, 74, 125, 127]. Fundus examination allows for direct observation of the retinal blood vessels and any related abnormalities [110].

Fundus imaging originated in the early 20th century and has undergone significant advancements since then [99]. The earliest attempt to capture an image of the retina was made by French physician Jean Mery, who demonstrated that the retinal vessels in a cat could be seen externally [64]. Subsequently, the fundamental concepts of the ophthalmoscope were introduced in 1823 by Czech scientist Jan Evangelista Purkyně (often spelled Purkinje), and later reinvented in 1845 by Charles Babbage [64]. The first images of the retina were published by the Dutch ophthalmologist van Trigt in 1853 [64]. The first useful photographic images of the retina, showing blood vessels, were obtained in 1891 by the German ophthalmologist Gerloff [64]. In 1910, Gullstrand developed the fundus camera, a concept still used to image the retina today, and he later received the Nobel Prize for this invention [64].

There are a handful of imaging modalities available that can acquire both 2D and 3D images using both invasive and non-invasive imaging techniques, which include fluorescein angiography (FA), optical coherence tomography (OCT), and digital fundus photography [110]. These techniques are employed not only for diagnosing and classifying diseases but also for monitoring their progression over time [110]. Fundus imaging is increasingly being recognized as a valuable tool for assessing retinal health and for diagnosing and managing various pathological conditions, such as retinal haemorrhage and diabetic retinopathy [73, 74], age-related macular degeneration [127], and glaucoma [125]. Moreover, fundus imaging is also useful in studying several systemic diseases that are directly linked to the changes in the geometrical features of retinal vasculature [75, 92]. Though in this work we have used digital fundus photography to extract retinal vessel geometry, we begin by introducing two other techniques and their limitations.

Fluorescein angiography (FA), a 2-D imaging technique, has served as the gold standard for *invivo* imaging of the retinal vasculature and its primary advantage lies in its ability to provide dynamic information about vascular flow and vessel permeability, features not captured by most other imaging modalities [103]. However, FA is an invasive procedure requiring the injection of an intravenous dye [103]. It must be conducted with caution, particularly in patients with advanced DR and coexisting systemic vascular conditions [103].

Unlike FA, OCT is a 3-D, high-resolution imaging technique, capturing cross-sectional views of internal retinal layers by detecting optical reflections and the echo time delay of light [64, 103]. OCT was first introduced in 1991 as a diagnostic tool in ophthalmology and has become a cornerstone of retinal imaging [103]. However, digital fundus imaging is a commonly used retinal imaging technique to extract retinal vessel geometry. It provides high-resolution images with minimal radiation exposure, and its non-invasive nature makes it a safer option for children, pregnant women, and those needing frequent examinations [64]. It is affordable, easy to use, and facilitates convenient storage and sharing, offering reduced overall risk and enhanced diagnostic

accuracy [64].

Digital fundus imaging is a non-invasive imaging technique where the reflected light from the retina creates a two-dimensional (2D) representation of the three-dimensional (3D) semi-transparent retinal tissues projected onto the imaging plane [64]. Fundus cameras are used to take digital fundus images. Fundus cameras can be of two types: standard fundus cameras and wide-field laser-based cameras [99]. Most clinicians use standard fundus cameras. In this procedure, the first step is to dilate the pupil of the human eye. However, some modern cameras do not need that. After that, a beam of light is directed toward the patient's retina through the pupil to illuminate the retina [116]. Then the reflected rays off the retina are condensed to a real retinal image using a handheld indirect ophthalmoscopy lens [116]. Then, clinicians can see the real inverted fundus image of retinal vasculature from the handheld lens [116]. Nowadays, smartphone fundus photography is also gaining popularity, which uses a simple technique to obtain ocular fundus pictures using a smartphone camera and a conventional handheld indirect ophthalmoscopy lens [116]. The overall working principle for smartphone fundus photography is similar to the conventional one we discussed earlier [116]. Figure 1.2(a) displays a typical standard fundus camera used to capture a digital fundus photograph of a patient, and figure 1.2(b) shows a typical fundus image.

In this work, we have used colour fundus images, which are a special type of digital fundus image (see figure 1.2b). It is important to note that the digital fundus images analysed in this work are based on a single-time observation, serving as a snapshot (static) within the biological cycle rather than a continuous longitudinal observation. Due to the static nature of digital fundus images, they have technical and physiological limitations in capturing rapid, subtle variations in vessel geometry caused by pulsatility linked to the cardiac cycle. For a more detailed discussion of how pulsatility may influence the measurement of geometrical attributes of retinal vessels, refer to Chapter 3. The retinal vasculature, consisting of a branching network of arteries, veins, arterioles, and venules, with several generations of vessels, arterio-venous (A-V) crossing, and retinal haemorrhage, can be observed in figure 1.2(b). For a detailed discussion on colour fundus image, please see subsection 1.5. However, there are other types of digital fundus photography available, including red-free imaging (RFFP), stereo fundus photography, hyperspectral imaging, scanning laser ophthalmoscopy (SLO), adaptive optics SLO, fluorescein angiography, and indocyanine angiography [64, 110]. A detailed discussion of these photography techniques is out of the scope of this chapter.

1.5 Introduction to digital fundus imaging

Our objective is to segment retinal blood vessels up to the eighth generation from the background and subsequently extract geometrical properties such as blood vessel length and radius.

We begin by introducing the fundamental concepts of digital imaging in subsection 1.5.1;

then summarise the RGB colour image and its properties in subsection 1.5.2, and then introduce the concept of a single-colour channel image and its mathematical representation in subsection 1.5.3.

1.5.1 Basics of digital images

Fundus images are a type of digital image made up of a finite number of pixels. The centre of each pixel is positioned at a specific location in the $\mathbb{R}^2$ plane, defined by the coordinates (x, y). A digital image has two main properties, namely size (i.e, width $\times$ height) and colour space. The colour space F provides information about the colours of each pixel of the image in a standard way; RGB (red, green and blue) is an example of such a colour space, composed of three channels for the three constituent colours.

In mathematical notation, a (continuous) image is a mapping $I : \Omega \mapsto F$ from an image domain $\Omega \subset \mathbb{R}^2$ to the colour space F. If we choose the set of pixel locations $\Omega = \{(x_i, y_j) : i = 0, ..., n-1, j = 0, ..., m-1\}$ as an array of discrete points in $\mathbb{R}^2$, then I is called a discrete image, also known as a digital image in practice. For the remainder of this thesis, we will refer to a digital image simply as an image unless stated otherwise.

For a given pixel located at (x_i, y_j) in I, the pixel of the image I generally contains information from multiple colour channels present in F. These colour spaces are discussed in more detail in the following section.

For a grayscale image, the colour space F consists of only one channel, and each pixel (x_i, y_j) holds information from this single channel, with pixel intensity values ranging from 0 to 255. Generally, a pixel value of 0 indicates black and 255 indicates white. Hence, smaller pixel values (close to zero) represent darker shades, and the larger values (close to 255) represent lighter shades. However, a colour image uses more than one channel, each with its own intensity. For a detailed discussion on colour space F and its geometrical representation, see the discussion below in the subsection 1.5.2.

1.5.2 RGB fundus image and its analysis

In colour fundus images obtained from our clinical collaborators, each pixel contains information about three colour channels, namely red (R), green (G), and blue (B). The RGB colour space of the image, representing the full range of colours achievable through combinations of red, green, and blue intensities, can be visualised as a cube in three-dimensional space, with the origin at the corner $(0, 0, 0)$. Figure 1.4 provides the schematic diagram of the colour cube model, where we consider three axes: R, G, and B. We know all pixel values range from 0 to 255, but for convenience, we normalise all colour values to assume the cube as a unit cube so that all values of red (R), green (G), and blue (B) are in the range $[0, 1]$. Each point on the surface or inside of the RGB cube can be interpreted as a three-dimensional vector extending from the origin to that point

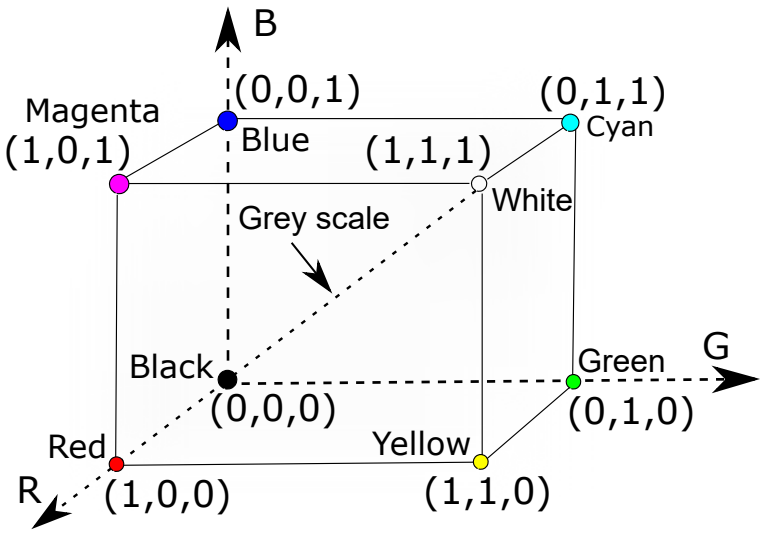

Figure 1.4: A schematic representation of the colour model showing the spatial locations of different colours red, green, black, blue, magenta, yellow, grey, and cyan in the unit cube.

in the plane. Each component of the vector represents the colour intensity of the red, green, and blue colours, respectively, and overall colour information of the given pixel (x_i, y_j) is determined by the superposition of the pixel intensities of the given amount of red, the given amount of blue, and the given amount of green. All grey colours are placed on the main diagonal of this cube (see figure 1.4) extending from black ($R = 0, G = 0, B = 0$) to white ($R = 1, G = 1, B = 1$). Red ($R = 1, G = 0, B = 0$), green ($R = 0, G = 1, B = 0$), and blue ($R = 0, G = 0, B = 1$) colours are at three corners of the cube, and magenta ($R = 1, G = 0, B = 1$), cyan ($R = 0, G = 1, B = 1$) and yellow ($R = 1, G = 1, B = 0$) colours are at other three corners.

The first step to separate the retinal blood vessels from the background is to select the appropriate colour channel from the three available colour channels (i.e., red, green and blue). In the case of vessel segmentation, it is common and convenient to use only a single-colour channel image [46, 74]. Therefore, in Chapter 2 below, we select only a single colour channel image from the RGB image, as it simplifies the algorithm, reduces computational load, and offers the best contrast between blood vessels and the background.

1.5.3 Single-colour channel image

A single-colour channel image is typically represented as a finite matrix structure I, commonly of size $n \times m$, where n and m denote the height and width of the image in pixels, respectively. In this case, we denote the pixel at $(x_i, y_j) \in \Omega$ as the $(i, j)^{th}$ pixel and $I(x_i, y_j) = I_{ij}$ is the corresponding pixel value for that colour channel. The pixel value is also called the pixel intensity at the point (x_i, y_j). By convention, the direction of the i coordinate runs from top to bottom, and the j

coordinate goes from left to right. The matrix I is given by the following compact form:

$$I(x_i, y_j) = I_{ij} = \begin{bmatrix} I_{0,0} & I_{0,1} & \cdots & I_{0,m-1} \\ I_{1,0} & I_{1,1} & \cdots & I_{1,m-1} \\ \vdots & \vdots & \vdots & \vdots \\ I_{n-1,0} & I_{n-1,1} & \cdots & I_{n-1,m-1} \end{bmatrix}. \tag{1.1}$$

These pixel values are used for vessel/non-vessel pixel classification in Chapter 2. The methodology for extracting a single colour image from an RGB image is described in the section 2.2 in Chapter 2. From this point forward, only a single-color channel image will be used for further processing.

Pre-processing is a crucial first step in preparing the image before feeding it into the vessel segmentation algorithm. In section 1.6, we discuss the general approach to performing pre-processing on a single-colour channel image.

1.6 Overview of pre-processing techniques

Image pre-processing refers to transforming raw fundus images into formats suitable for vessel segmentation and interpretation. It allows us to eliminate unwanted distortion and enhance blood vessels essential for segmentation work. There are several techniques available for the fundus image pre-processing.

One of the first steps in pre-processing images is to resize and crop all the images to a uniform size and aspect ratio. This can help reduce computational cost while also avoiding distortion and inconsistency in the input image. The processes of resizing, formatting, and cropping are discussed in greater detail in section 2.3.1 of Chapter 2.

1.6.1 Background removal

Background removal is another commonly used pre-processing technique that isolates the region of interest (ROI), such as blood vessels and haemorrhage, from the image background. This is particularly beneficial when retinal images include a black area outside the ROI, as focusing solely on the ROI can enhance both the efficiency and accuracy of the segmentation process. However, the images provided by our collaborator, as illustrated in figure 1.2(b), contain only the ROI without any surrounding black regions. Consequently, this pre-processing step is not required in our case.

1.6.2 Histogram equalization and adaptive histogram equalization

The histogram of a single colour channel image is a graphical representation of the distribution of pixel intensity values in that image. It shows how frequently each pixel's intensity value appears.

Histogram equalization (HE) is an important image pre-processing technique where the high pixel intensity values in the histogram are spread out to enhance the image [159]. The workflow for creating a histogram equalization is as follows. Firstly, we calculate the frequency of each pixel intensity value i.e., count how many times each pixel intensity level (ranging from 0 to 255) appears in the image. Suppose the original image I contains W number of pixels in total, and the pixel intensity range lies in the interval $[X_0, X_{L-1}]$, where $X_0 = 0, X_{L-1} = 255$ [141]. Next, we plot these frequencies against the corresponding pixel intensity values to generate the histogram, which visually represents the distribution of pixel intensities. After that, we normalise the histogram by dividing each frequency by the total number of pixels W in the image I, resulting in a probability distribution $H(X_k) = n_k/W$, $0 \leq k \leq L-1$, where n_k is the total number of pixels in the image that have the intensity level X_k. $H(X_k)$ indicates the likelihood of occurrence of each intensity value X_k. Then, we compute the 'Cumulative Distribution Function (CDF)' by summing these probabilities $H(X_k)$ cumulatively from the lowest to the highest pixel intensity values, and the CDF is given by $CDF(X_k) = \Sigma_{i=0}^{k} H(X_i)$. Note that the CDF is always a non-decreasing function that ranges from 0 to 1. In the last step, traditional HE maps the original pixel intensity to a new pixel intensity using the intensity remapping function (or CDF) given by $f(X) = X_0 + (X_{L-1} - X_0)CDF(X)$ such that overall pixel intensity of the histogram spread evenly across $[X_0, X_{L-1}]$ [141].

Histogram equalisation is commonly used to increase the overall contrast in digital images. Although the HE method is simple and effective for globally enhancing image contrast, but often results in an unrealistic appearance of the image by over-enhancing small pixel intensity values [159]. Additionally, it amplifies image noise, causes bright pixels to become overexposed, and makes dark pixels appear underexposed [137, 142, 159]. However, adaptive histogram equalization (AHE), a local histogram equalization technique, is used when traditional global histogram equalization cannot produce useful outcomes, as local details are necessary for retinal image segmentation.

Adaptive Histogram Equalization (AHE) is a contrast enhancement technique that extends the traditional histogram equalization approach. In AHE, the input image is divided into multiple non-overlapping sub-regions of pixels, called 'tiles'. For each tile, a histogram of pixel intensity values is computed, typically using 256 bins. Histogram equalization is then performed independently on each tile, following the standard procedure of histogram equalization as discussed above. From the resulting histogram of all tiles of the image, a Cumulative Distribution Function (CDF) is derived. Each pixel intensity for all pixels obtained from the histogram obtained in last step is then remapped using the CDF. This process results in locally enhanced tiles that better reveal image details. To ensure smooth transitions across tile boundaries and avoid artifi-

cial tile boundaries, bilinear interpolation is applied between adjacent tiles during the intensity remapping step.

AHE increases noise in low pixel intensity areas and homogeneous areas where pixel intensity values do not change significantly [19].

CLAHE is an improved variant of AHE designed to address the limitations of both Histogram Equalization (HE) and Adaptive Histogram Equalization (AHE), as explained in detail in the subsection 2.3.2 of Chapter 2.

1.7 Overview of the feature extraction from fundus images

Feature extraction is the initial step of the retinal vessel segmentation for detecting retinal blood vessels in fundus images, aiming to distinguish them from the background. Feature extraction involves identifying and isolating the most important information (features) from the image, such as edges, shapes, or pixel intensity values. When the input image is too large to be processed for image segmentation, then we usually transform the input image into a reduced representation by obtaining the set of features [92]. By applying the feature extraction technique, we reduce the amount of information to be processed for vessel segmentation into a manageable, lower-dimensional space while preserving the essential aspects needed for further analysis.

Feature extraction is a pixel-based technique where we use a feature vector that comprises a set of features to measure for each pixel of the input image in order to classify pixels as vessel or non-vessel pixels and all other necessary features of interest.

In this study, we focus on four distinct features, namely:

1. Gradient orientation analysis (GOA)
2. Morphological transformation
3. Gabor filter response
4. Principal curvature

It is important to note that our final feature vector used in Chapter 2 includes these four features. Each of these four features is discussed in greater detail in the subsections below (subsection 2.4.2- subsection 2.4.5) in Chapter 2.

The next step is to use the feature vectors discussed above to segment blood vessels. There are different approaches available for retinal vessel segmentation (see subsection 1.8). In the first part of this work, we use an unsupervised machine learning approach to segment blood vessels in retinal images based on the constructed feature vector (see subsection 2.4 of Chapter 2). Building on this, we develop a more robust vessel segmentation method using a deep learning-based approach (see subsection 2.8 of Chapter 2).

1.8 A different vessel segmentation approach

Vessel segmentation is a necessary first step for accurately determining vessel length, radius, and diagnosing vascular-related diseases. Several retinal vessel segmentation methods are available in the literature. The state-of-the-art vessel segmentation methods can generally be categorised into two main groups based on their underlying principles: rule-based methods and machine learning-based methods [132].

The rule-based method is a segmentation method that uses predefined rules and human knowledge to partition an image into meaningful regions or objects. The predefined rules may be intensity-based (e.g., thresholding approach) or texture-based (e.g., Gabor filter). The rule-based vessel segmentation methods can be further subdivided into the following: Hessian matrix-based [27, 28], matching filtering-based [46], mathematical morphology-based [84], minimal path-based [25], and graph-based methods [132]. It is important to emphasise that in this study, the Hessian-matrix-based approach (see subsection 2.4.5 of Chapter 2) and the mathematical morphology-based approach (see subsection 2.4.3 of Chapter 2) are each incorporated as components of our final feature vector [132]. The matching filter-based approach (e.g., line strength feature [46]) is a type of rule-based segmentation approach where a line of fixed length is considered at each pixel location (known as a target pixel) of the image at multiple orientations [46]. For each orientation, the average and maximum pixel intensity values of the pixels in the selected window along each of these lines are measured [46]. Finally, the line strength of the target pixel is obtained by subtracting the average and maximum pixel intensities [46]. In practice, using the line strength feature, we can separate the retinal blood vessel pixels from the background pixels [46]. Minimal path-based or commonly known as minimal spanning tree (MST) techniques, are commonly used in interactive frameworks [25]. In the minimal path-based technique, the segmentation problem is formulated as the problem of finding the shortest paths between pixels in an image. In the graph-based technique, the image is considered as a graph where pixels correspond to nodes, and edges connect neighboring nodes (or pixels). We use a similar concept in the Chapter 3 to track blood vessels of different generations. However, in recent times, machine-learning-based segmentation approaches are gaining attention due to their high accuracy and efficiency in segmenting complex retinal vasculature.

The machine learning-based algorithms can be broadly divided into three major groups, namely: the conventional or classical machine learning-based method, the decision-tree-based method, and the deep neural network-based method [132]. Each of these methods can be broadly classified into two types based on their underlying working principles: unsupervised and supervised [75, 132]. Unsupervised machine learning techniques have been widely used to discover the latent pattern of the underlying images without prior observations of the images. In these approaches, the training data or hand-labelled ground-truth data do not contribute directly to the design of the algorithm. Supervised learning techniques consist of two main phases: the training phase and the testing phase. In the training phase, the process begins with an input image

alongside its corresponding target segmentation output. A set of features extracted from the input image, each linked to a specific label, is fed into the algorithm. The algorithm learns retinal vessel extraction rules from a training dataset composed of manually processed and segmented reference images. In these ground truth images, vascular structures are precisely annotated by ophthalmologists. The algorithm analyses these annotated examples in a multidimensional feature space to extract various relevant properties. Following the training phase, the system proceeds to the testing phase, where it classifies new input images that lack labelled data. A key advantage of a supervised classification algorithm is its ability to detect and correct classification errors. The classification decisions are guided by ground truth data derived from predefined features. However, this approach requires the availability of accurately labeled ground truth data, which can be a limitation in practical applications where such data may be scarce. In this work, we have used both unsupervised and supervised machine learning approaches for retinal vessel segmentation. The detailed discussion on the conventional unsupervised approach is given in the subsection 2.4 of Chapter 2. Following this, a detailed discussion on deep learning-based approaches for retinal vessel segmentation is given in subsection 2.8 of Chapter 2.

The idea of the decision-tree based ensemble approach is to combine the strong features to enhance the ability to distinguish between vessel and non-vessel pixels [74, 106, 109, 132]. One of the most commonly used decision-based methods for retinal vessel segmentation is the ensemble of decision trees, particularly random forest-based approaches [49]. Fraz et al. applied an ensemble system of bagged and boosted decision trees for segmentation [74]. Shahrian et al. proposed a classifier based on ensembles of n decision trees to segment vessels in colour retinal images [106]. Aslani et al. employed a random forest-based vessel segmentation method, utilising 17 features due to its advantages in speed, simplicity, and effective information fusion [109]. A detailed discussion of decision tree-based approaches is outside the scope of the thesis.

Deep learning (DL) is a subset of machine learning that focuses heavily on methods based on artificial neural networks (see subsection 2.8.1 in Chapter 2 for a detailed discussion). Deep learning techniques can be applied in both supervised and unsupervised learning settings and have recently gained greater attention from the research community due to their performance in segmenting medical images [140, 161]. One of the advantages of deep learning-based methods is that deep learning algorithms can automatically learn complex, hierarchical features from raw pixel data through their layered structures (see Chapter 2 for a detailed discussion), reducing the need for human intervention for manual feature engineering and improving the generalisation and accuracy of automatic segmentation methods. Over the years, several deep learning networks have been utilised in the field of retinal image segmentation. Among all the different types of deep learning networks, the CNNs have drawn greater attention in numerous applications, especially in medical image analysis [154, 160]. Following the success of CNN, several variants of CNN have been formulated over the years for retinal image segmentation. U-Net, a special type of CNN network architecture, known for its unique structure and high segmentation accuracy, is

discussed in greater detail in subsection 2.9 in Chapter 2.

1.9 Contributions of this thesis

The present study is motivated by the aim to quantify the onset of retinal haemorrhage (i.e. bleeding of the retinal blood vessels at the back of the eye) following the retinal vein occlusion (RVO). Due to different pathological conditions like RVO, the blood flow direction in the retinal microcirculation can be altered. The clinical hypothesis attributes retinal haemorrhage following RVO to the fact that retinal haemorrhage arises as a result of an increase in blood pressure upstream to the point of constriction, as blood can not leave the vessel because of RVO. According to the hypothesis, this increased blood pressure spreads through the retinal circulation and drives expansion of the vessel walls, and possible rupture, of more fragile vessels in the distal parts of the network [22].

In the clinical image (see figure 1.2b), we observe the spatial separation between the site of haemorrhage and the site of occlusion. It is also important to note that the localisation of haemorrhage is observed upstream to the point of occlusion. As discussed in subsection 1.2, branch retinal vein occlusion (BRVO) most commonly occurs at the arterio-venous crossing, known as the site of occlusion. The condition that promotes BRVO is commonly known as Virchow's triad (see the discussion given in subsection 1.2). According to the triad, at the arterio-venous crossing, due to arterial thickening, the corresponding vein gets compressed following the venous wall damage. Platelets and red blood cells start to adhere to the injured venous wall. As a result, we observe intravenous thrombus formation, which over time becomes large enough to occlude the vein. The possible mechanism of progression of venous occlusion at A-V crossing is given in figure 1.3.

There are modelling frameworks developed to study retinal haemorrhage [136, 165]. However, those models focus on quantifying retinal haemorrhage following a traumatic brain injury. In traumatic brain injury, retinal haemorrhage is thought to result from the propagation of pressure waves through the vascular network [165]. An abrupt increase in pressure at the inlet to the parent vessel produces a shock wave that propagates through the parent vessel and interacts with the junction of the network [165]. Furthermore, this shock wave splits into propagating shock waves that travel along the two daughter vessels and reflect a rarefaction wave towards the inlet [165]. The main contribution of this thesis is to fill this gap and to develop a mathematical model for $1D$ blood flow and blood pressure to investigate the onset of retinal haemorrhage following retinal vein occlusion in the retinal microcirculation. To investigate the mechanism of RVO, in this work, we will combine fundus image analysis and mathematical modelling (based on continuum mechanics). The proposed network consists of a two-sided arterial-venous tree, along with capillary beds in between. The intention is to use the fundus image to construct the network geometry. We will then mimic the condition of RVO or the mechanical obstruction on

the large vein due to the thrombosis by considering a localised external pressure that will be applied to the venous side of the tree. By applying occlusion in one vessel, we will predict how that changes the shape, blood pressure, and flow dynamics in the network. We aim to develop a novel modelling framework to study retinal microcirculation in both health and disease that will incorporate fluid-structure interaction, which is necessary to model the capacitance effect of the retinal veins. Generally, veins can be considered as blood reservoirs, and their ability to hold this much blood is due to their high capacitance, that is, their capacity to expand to store a high volume of blood, even at a low pressure. The large lumens and relatively thin walls of veins make them far more distensible than arteries; thus, they are said to be capacitance vessels.

1.10 Organisation of this thesis

This thesis is organised into six Chapters. This, the first Chapter 1, provides an overview of the retinal, retinal haemorrhage, basics of medical and fundus imaging and discusses some of the history of cardiovascular, pulmonary, coronary and retinal microcirculation modelling. In Chapter 2, we discuss different techniques used in fundus images obtained from a clinical collaborator to extract the vessel tree outline. In the following Chapter 3, we adopted a graph-based technique to track the retinal vessel of each generation to infer useful information such as the vessel outline and the length and radius of the constituent blood vessels, several generations of vessels, so that we can use them to parameterise the mathematical model developed in later chapters. Then, in Chapter 4, for simplicity, we initially model the retinal network as a long single vessel and discuss different numerical schemes used to solve the single vessel model. The insights gained from the single-vessel model and the network structure extracted in Chapter 2 and Chapter 3 are used to construct a bifurcation model for both arteries and veins, consisting of two generations of blood vessels discussed in Chapter 5. Then, in Chapter 6, we join the two bifurcation models for arteries and veins by considering capillary beds in between to make a three-generation arterio-venous network. It is important to note that the segmentation method developed in Chapter 2 and graph-based tracking algorithm developed in 3 have been used directly in Chapter 6 to extract the vessel length and radius from the clinical image. The extracted values have been used to parameterise the mathematical model developed for the arterio-venous network in Chapter 6.

Chapter 2

Retinal vessel segmentation

2.1 Introduction

The intricate structure of the retinal vasculature presents significant challenges for retinal image segmentation. These difficulties are further amplified by arterio-venous (A-V) crossings and the presence of pathological features such as haemorrhages (see figure 1.2b in Chapter 1). Additional elements commonly observed in retinal images include the retinal boundary, the optic disc, and various other pathological signs, such as bright and dark lesions and exudates. In this chapter, the primary goal is to segment a retinal fundus image to isolate up to 8-9 generations of retinal blood vessels from the background.

The organisation of the chapter is as follows. In section 2.2, basic concepts for extracting single-channel images (i.e., green channel images) are introduced. Pre-processing steps of vessel segmentation are discussed in section 2.3, and section 2.4 provides an unsupervised method for image segmentation using an ensemble classifier. Section 2.5 and 2.6 explain the K-means and weighted K-means clustering approaches, which have been employed to obtain the final segmented image. In the following subsection 2.7, we outline the limitations of the classical machine learning based unsupervised approach. Subsection 2.8 provides an overview of deep learning based approach. Subsection 2.9 introduces the U-Net-based retinal vessel segmentation approach, and then in the following subsection 2.10, we evaluate the performance of the two segmentation approaches, namely the classical unsupervised approach and the U-Net-based approach, against a ground truth image. Finally, in subsection 2.11, we conclude the chapter by summarising its objectives and intended purposes.

2.2 Extraction of the green channel from the RGB image

As discussed earlier in subsection 1.5.2 in Chapter 1, the first step for processing fundus images is to select an appropriate single-colour channel image I from the original RGB image [74],[75]. Figure 2.1 shows a typical colour fundus image showing haemorrhage, blood vessel, the optic

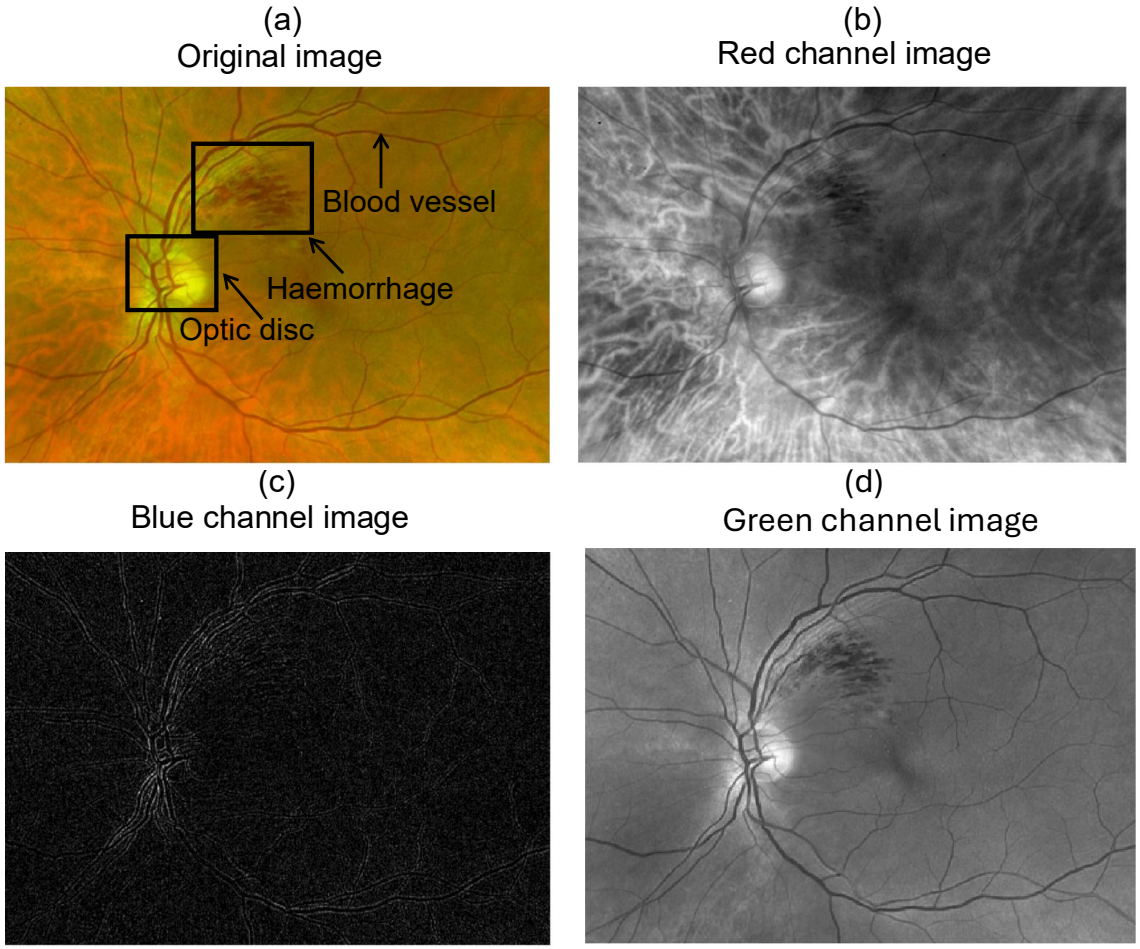

Figure 2.1: (a) The original fundus image showing blood vessel, haemorrhage area and optic disc and three channels: (b) R,(c) B and (d) G, respectively.

disc (figure 2.1a) along with the corresponding red (see figure 2.1b), blue (see figure 2.1c), and green (see figure 2.1d) colour channel images. These three colour channels (i.e., red, blue, and green) from the original fundus image are extracted using the '*imsplit*' built-in function from the image processing toolbox in MATLAB 2023a. By visually inspecting the results it is evident that the green channel image (figure 2.1d) provides the highest contrast between haemorrhages, blood vessels, the optic disc, and the background and contains all necessary information compared to the red (figure 2.1b) and blue (figure 2.1c) channels of the original image (figure 2.1a).

To process the image figure 2.1(a) further, we start with the green channel image. The standard procedure for extracting vessels from fundus images involves three main steps: image preprocessing (if required, see section 2.3), and vessel segmentation (see section 2.4). The general approaches for each of these two main steps are discussed in detail in two subsections 1.6 and 1.8 of Chapter 1, respectively. In this chapter, we mainly focus on how the methods are applied to our images.

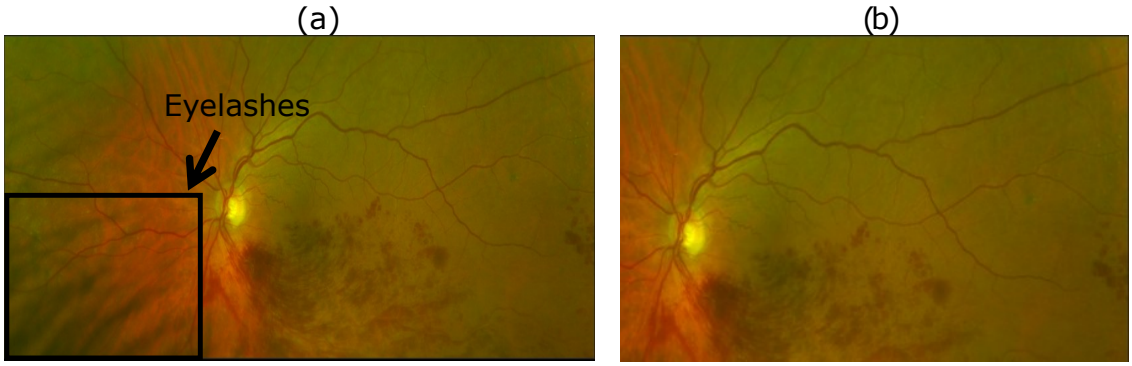

Figure 2.2: Cropping of eyelashes from images obtained from collaborator showing:(a) original image and (b) cropped image obtained from (a).

2.3 Pre-processing of the green channel image

Pre-processing is an important step to ensure that our image dataset obtained from the collaborator is consistent and displays only relevant features. There are different steps involved in pre-processing, which we discuss in detail in the subsection 1.6 of Chapter 1. In subsection 2.3.1, we outline the cropping and resizing procedure applied to all our images, and the subsection 2.3.2 describes the enhancement technique used to improve the visibility of retinal blood vessels. These steps are essential to simplify the workload for the subsequent vessel segmentation process.

2.3.1 Cropping, formatting and resizing

Cropping, formatting, and resizing are three important pre-processing tasks because original images obtained from our collaborator often vary in size, with some having cropped sections at the top or bottom of the image, requiring standardisation. Some fundus images obtained from our clinical collaborator contain eyelashes, necessitating cropping. Figure 2.2 shows such an example where cropping is necessary. Figure 2.2(a) shows the original image obtained from the clinical collaborator, where eyelashes appear in one corner of the fundus image (see the black box in figure 2.2a). Figure 2.2(b) is the final image obtained after cropping the region containing eyelashes in the figure 2.2(a).

All images are converted to '.png' format with a resolution of 400×500 pixels (i.e., $n = 400$, $m = 500$). This resolution is chosen because it effectively preserves all important features, which include both large and small retinal blood vessels up to 8–9 generations, as well as retinal haemorrhages. To avoid image distortion after cropping, we maintain the original aspect ratio (the relationship between width and height of the image before cropping) and avoid stretching the image pixels.

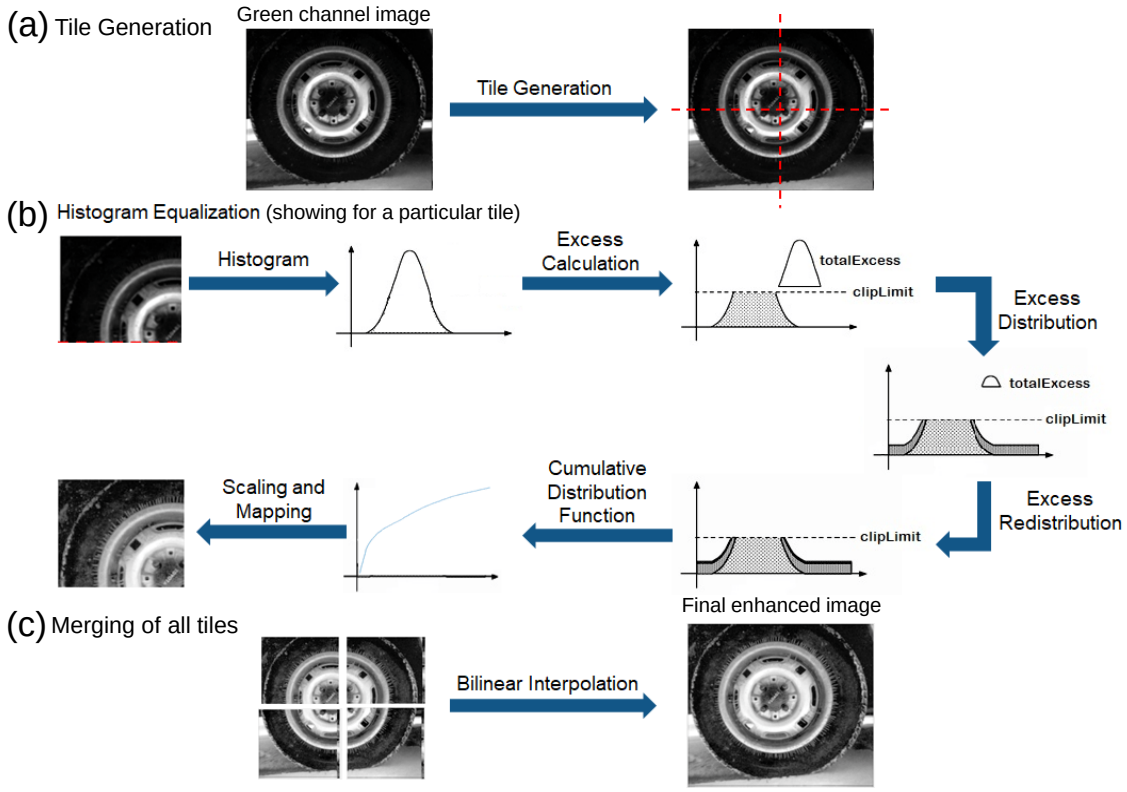

Figure 2.3: A typical workflow of the CLAHE algorithm applied to a sample image showing: (a) tile generation, (b) histogram equalisation, and (c) merging of all tiles [153].

2.3.2 Contrast limited adaptive histogram equalization (CLAHE)

We apply contrast-limited adaptive histogram equalisation (CLAHE) as a pre-processing step on the green channel image (see figure 2.1(d) above) to enhance the distinction between the blood vessel and the background.

Traditional histogram equalisation works well when the pixel values are similar throughout the image. For a detailed discussion of HE and AHE techniques, please refer to the section 1.6.2 in Chapter 1. In our images, pixel values vary widely as they contain pathological regions like haemorrhage. Adaptive histogram equalization (AHE), a refinement of traditional histogram equalization, enhances image assessment quality and contrast. However, the enhancement by the AHE method causes breakups of small structures like retinal blood vessels, causing a discontinuity in the overall structure of the retinal vasculature.

CLAHE is a refinement of the adaptive histogram equalisation (AHE) technique [100]. It is effective in enhancing our low-contrast medical images while reducing the issue of over-enhancement associated with AHE [100]. It is also beneficial for enhancing the particular characteristics (for blood vessels) of the image while preserving the inherent structural information present in the original image. To apply CLAHE to the image, we use the built-in function 'adapthisteq' from the image toolbox in MATLAB 2023a.

Figure 2.3 explains the typical workflow of the CLAHE technique for a sample image. Firstly, CLAHE divides the green channel image into multiple non-overlapping sub-regions of pixels

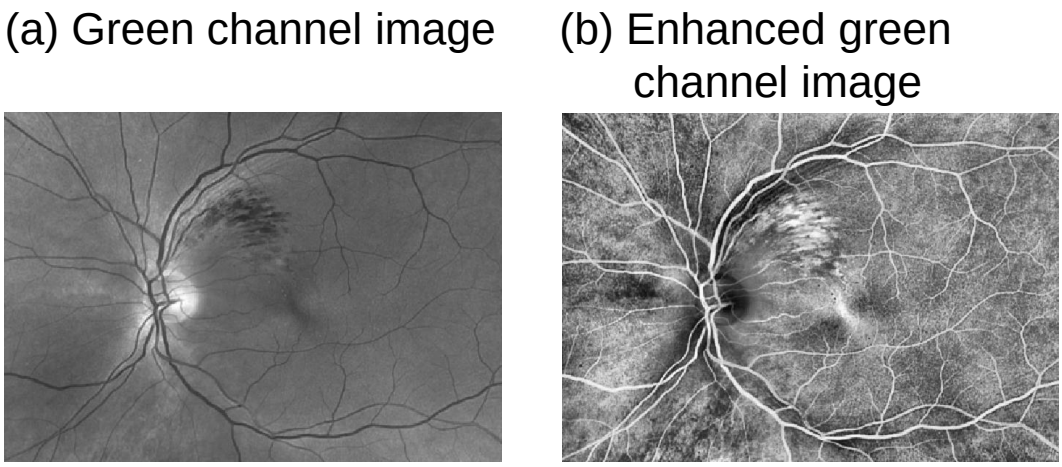

Figure 2.4: CLAHE applied on the green channel image showing: (a) green channel image and (b) enhanced green channel image. The image resolution is 400×500 pixels.

called a 'tile' (see figure 2.3a). We select an arrangement of 8 rows and 8 columns of tiles, resulting in each tile having dimensions of approximately 50×62 pixels. The original image size is 400×500 pixels. The numbers 50×62 pixels come directly from dividing the original image height 400 pixels by 8 ($= 40$ pixels) and the original image height 500 pixels by 8 (≈ 62.5 pixels). In this case, we round the value to the nearest integer.

To understand how CLAHE operates on each tile, we first focus on a single tile and then generalise the idea to all tiles across the image. Figure 2.3(b) shows how the CLAHE is applied to each tile. For the chosen tile, we compute a histogram of pixel intensity values as a set of bins (which is 256 here, the number of elements in the colour map). After computing the histogram of the tile, a threshold (which is applicable for all tiles across the image) is defined for the maximum height of any bin in the histogram, i.e., allowable frequency of image pixels —this is referred to as the 'clip limit'. In our case, we chose the default clip limit value of 0.01. Histogram bin height higher than the clip limit 0.01 is accumulated and evenly distributed across all bins (i.e., 256 bins in each tile) in the histogram. The clip limit prevents the over-amplification of noise and excessive contrast in nearly uniform intensity regions. Then we follow the same procedure as explained for adaptive histogram equalisation in subsection 1.6.2 in chapter 1 to create a new image tile with enhanced contrast.

We repeat the steps given in figure 2.3(b) for all tiles. Figure 2.3(c) shows how the resulting remapped tiles are stitched together using bilinear interpolation to generate an enhanced green channel image with improved contrast to eliminate artificially induced tile boundaries.

Figure 2.4 shows the green channel image (figure 2.4a) before and after applying the CLAHE (figure 2.4b). Looking at figure 2.4(b), it is evident that the blood vessels are significantly enhanced after applying CLAHE. We use the enhanced green channel image (figure 2.4b) for the vessel segmentation work in this thesis. In the following subsection 2.4, we first discuss the unsupervised vessel segmentation approach in detail.

2.4 Unsupervised machine learning-based approach for retinal vessel segmentation

Among the various available unsupervised techniques, clustering algorithms are the most popular and have a long-standing history for retinal vessel segmentation [66]. In the initial part of this work, we integrate ensemble methods with K-Means clustering for retinal vessel segmentation. We apply K-means clustering to ensemble all features into a feature vector. K-means clustering is a classical unsupervised machine learning technique that partitions data into groups based on similarities (e.g., pixel intensity values) in the image. Other traditional methods include the K-nearest neighbor (KNN) classifier [38], Fuzzy C-means clustering [44], Gaussian mixture model (GMM)-based classifiers [43], and approaches based on Support Vector Machines (SVM) [121]. A detailed discussion of each of these methods falls outside the scope of this work.

The first step of unsupervised segmentation is finding an efficient feature vector. In the following subsection 2.4.1, we provide a detailed discussion of the feature vector employed in this work.

2.4.1 Feature extraction

A feature vector is a collection of features that we extract from the input image. In our case, we wish to identify information about each pixel so that classifiers can differentiate retinal blood vessels from the background [74]. Our target is to choose a small and robust set of features that can efficiently differentiate vessel and non-vessel pixels, and also extract existing patterns in our images. This section presents only the set of feature vectors used for segmentation purposes. Although we experimented with other alternative features, their poor performance on images led us to exclude them from the final feature set.

All the features used in this chapter are computed from the enhanced green channel image (see figure 2.4b) of the original image (see figure 2.1a), unless specified otherwise. Our final feature vector contains four features, namely:

1. multi-scale orientation analysis of the gradient vector field (see subsection 2.4.2),
2. morphological transformation (see subsection 2.4.3),
3. multi-scale Gabor filter response (see subsection 2.4.4),
4. the principal curvature (see subsection 2.4.5).

It is important to note that we do not apply any post-processing techniques to the segmented images obtained from each feature because we have observed that post-processing has no significant impact on these images. However, the exception is feature 4, i.e., the maximum principal curvature, where we post-process the image using iterative self-organising data analysis (ISO)

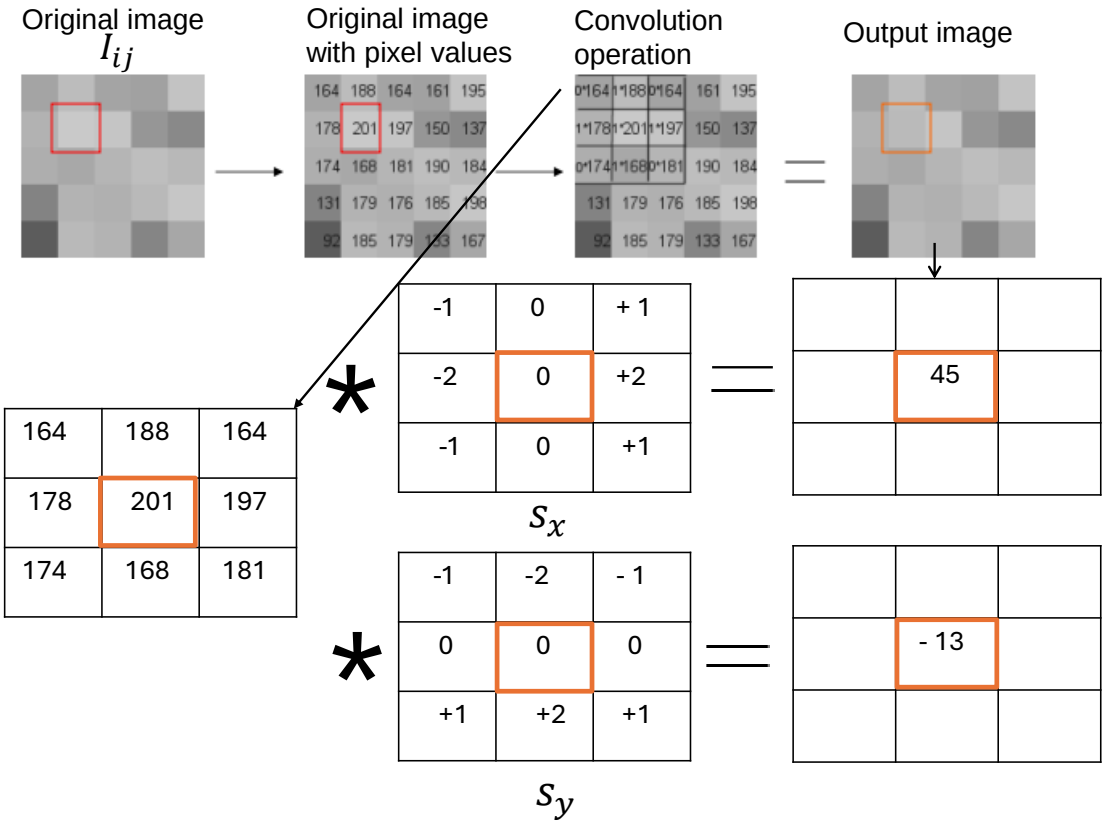

Figure 2.5: A typical illustration of convolution operation showing how 3×3 kernel operates on the original digital image I.

thresholding to remove disconnected white regions from the segmented image. The detailed discussion on the ISO thresholding approach is given in subsection 2.4.5.

2.4.2 Multi-scale orientation analysis of gradient vector field (GOA)

The orientation analysis of the pixel intensity gradient vector field (or GOA) is our first feature. In the GOA method, the idea is to check each pixel in the given input discrete image I and then identify where the pixel intensity changes significantly (i.e., above a set threshold value ϵ, see below) from one pixel to the next. This enables us to isolate fine anatomical structures like retinal blood vessels. To do that more accurately and systematically, the multi-scale GOA method looks for a gradient measuring the change in pixel intensity in multiple directions using the directional derivative on multiple spatial scales to capture the vessel across different length scales.

At each location (x_i, y_j) in the image I, the gradient vectors in the principal directions are calculated based on the enhanced green channel image, figure 2.4(b). To obtain the gradient vectors in $x-$ and $y-$ directions, we consider a convolution operation between the input (the enhanced green channel image I) and first derivative kernels in x and y directions, denoted as

s_x and s_y, respectively. Mathematically, the operation can be written as

$$\begin{aligned} G_x(x_i, y_j) &= \big[I * s_x\big](x_i, y_j) \\ &= \Sigma_l \Sigma_k s_x(l,k) I(x_i - l, y_j - k), \quad l,k \in \{-1,0,1\}, \\ G_y(x_i, y_j) &= \big[I * s_y\big](x_i, y_j) \\ &= \Sigma_l \Sigma_k s_y(l,k) I(x_i - l, y_j - k), \quad l,k \in \{-1,0,1\}. \end{aligned} \tag{2.1}$$

The operation '*' is called the discrete convolution operation. It is a commonly used fundamental operation in image segmentation due to its ability to effectively extract and analyse spatial features from an image. We choose a 'Sobel kernel' of size 3×3, which is significantly smaller than the input image. A smaller kernel concentrates on a localised region of the image, enabling the detection of fine-grained features such as edges and blood vessels, whereas larger kernels may lead to over-smoothing, resulting in the loss of fine details. Here, the kernel can be thought of as a spatial filter, and the convolution operation can be viewed as a spatial operation. The convolution operation described above does not allow the centre of each kernel to overlap the outermost element of the input image. As a result, this operation reduces the height and width of the output feature map compared to the input matrix. To maintain the dimension throughout, zero padding is used (see figure 2.17 in subsection 2.8).

Figure 2.5 provides the visual representation of the process of the convolution operation between the image and the kernels s_x and s_y, respectively. In case of the discrete convolution operation, the chosen kernel convolves on the input image, and convolution computes a weighted average of the pixel intensity values of the input image I using the kernel s_x or s_y as given in figure 2.5. To compute the corresponding pixel value of the output image at each spatial position (x_i, y_j), the kernel is applied to the image point by point, and then the resultant values are added together using (2.1).

The next step involves determining the direction in which the pixel intensity changes are maximal. To achieve this, we compute the unit gradient vectors in the x and y directions, denoted as u_x and u_y, respectively, by normalising the gradient components G_x and G_y. The unit gradient vectors at point (x_i, y_j) are defined as

$$\begin{aligned} u_x(x_i, y_j) &= G_x(x_i, y_j) / \sqrt{G_x^2 + G_y^2}, \\ u_y(x_i, y_j) &= G_y(x_i, y_j) / \sqrt{G_x^2 + G_y^2}. \end{aligned} \tag{2.2}$$

The direction of maximum pixel intensity change is θ of the gradient vector relative to the $x-$ axis and is given by

$$\theta = \arctan\left(\frac{I_y}{I_x}\right).$$

Unit vectors are considered to be zero if the magnitude of the gradient is too small ($< \epsilon$). To

find an appropriate threshold value ϵ, we first calculate the mean value of the magnitude of the gradient. We then use a trial-and-error method to check what works best for our images. We choose ϵ to be 10% of the mean gradient magnitude.

Once the direction of maximum pixel intensity change has been determined for each pixel in the image, the next step is to analyze how this direction evolves spatially as we move from one pixel to the next across the image. To do that we compute the first-order derivatives of the unit gradient vector u_x and u_y along the principal directions x and y. These derivatives are commonly referred to as the Laplacian or directional derivatives. The first-order derivatives of the unit gradient vectors are obtained by convolving the kernels over the unit gradient vectors in both directions, and are given by

$$\begin{aligned}
d_{xx}(x_i, y_j) &= \Big[u_x * s_x\Big](x_i, y_j) \\
&= \sum_l \sum_k s_x(l,k) u_x(x_i - l, y_j - k), \quad l,k \in \{-1,0,1\}, \\
d_{xy}(x_i, y_j) &= \Big[u_x * s_y\Big](x_i, y_j) \\
&= \sum_l \sum_k s_y(l,k) u_x(x_i - l, y_j - k), \quad l,k \in \{-1,0,1\}, \\
d_{yy}(x_i, y_j) &= \Big[u_y * s_y\Big](x_i, y_j) \\
&= \sum_l \Sigma_k s_y(l,k) u_y(x_i - l, y_j - k), \quad l,k \in \{-1,0,1\}, \\
d_{yx}(x_i, y_j) &= \Big[u_y * s_x\Big](x_i, y_j) \\
&= \sum_l \Sigma_k s_x(l,k) u_y(x_i - l, y_j - k), \quad l,k \in \{-1,0,1\}.
\end{aligned} \tag{2.3}$$

Laplacians are sensitive to changes in the gradient, such as high curvature or abrupt changes in pixel intensity across blood vessels.

Next, we calculate the magnitude of the Laplacians obtained from equation (2.3) to quantify the total discontinuities in the gradient orientation for each spatial location (x_i, y_j). The discontinuity magnitude in the gradient orientation D is given by

$$D_{ij} = D(x_i, y_j) = \sqrt{d_{xx}^2(x_i, y_j) + d_{xy}^2(x_i, y_j) + d_{yx}^2(x_i, y_j) + d_{yy}^2(x_i, y_j)}. \tag{2.4}$$

The scalar value D_{ij} obtained for a given pixel (x_i, y_j) from the equation (2.4) represents how strongly the gradient orientation (i.e., edge direction) is changing around the point (x_i, y_j). A low value of D_{ij} indicates that the orientation of edges is fairly smooth and continuous (e.g., along the blood vessels), and a high value of D means the orientation of edges is rapidly changing. A typical example of D is given in figure 2.6(a), where we see that it contains a GOA map of

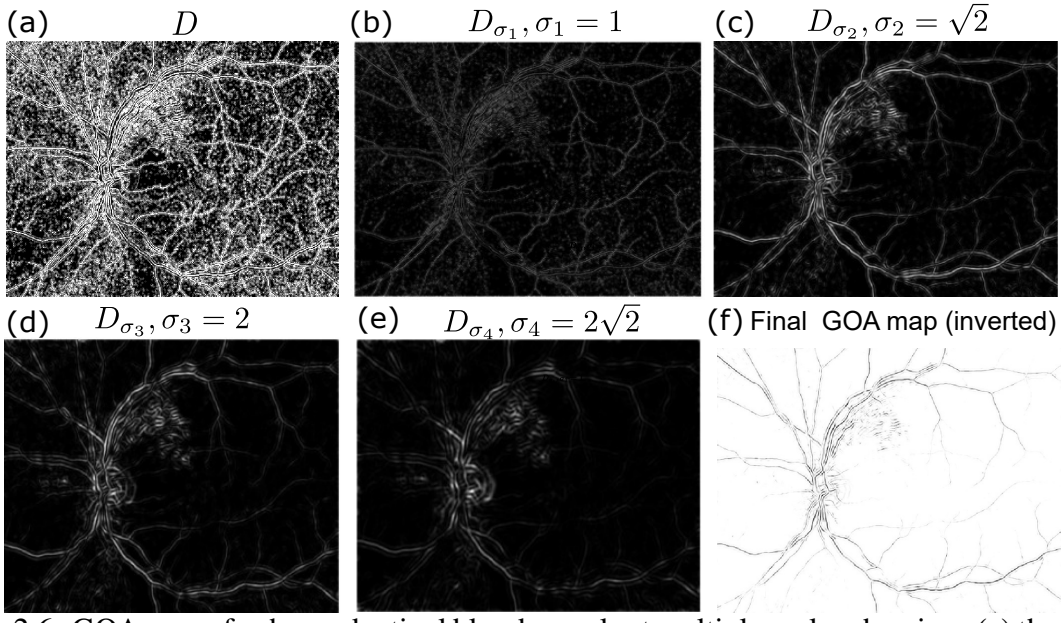

Figure 2.6: GOA map of enhanced retinal blood vessels at multiple scales showing: (a) the image of D obtained using equation (2.4), (c) $\sigma = 1$, (d) $\sigma = 2\sqrt{2}$, (e) $\sigma = 2$ and (f) $\sigma = 2\sqrt{2}$.

curvilinear-shaped retinal blood vessels that are enhanced but with much noise.

Since the length and width of the retinal blood vessels vary as they traverse radially from the optic disk, it is essential to incorporate a measurement technique that can capture these vessel dimensions. Multi-scale techniques have been introduced to measure different geometric features of retinal blood vessels at different spatial scales. To introduce a multi-scale feature, we first introduce a Gaussian kernel of the form

$$g(x_i, y_j; \sigma) = \frac{1}{2\pi\sigma^2} \mathrm{e}^{-\left(\frac{x_i^2 + y_j^2}{2\sigma^2}\right)}, \tag{2.5}$$

where σ is the standard deviation of the Gaussian function and (x_i, y_j) is the position of a particular pixel in the image. Here, σ determines the extent of the smoothing effect and controls the size and spread of the Gaussian kernel. We convolve the GOA map D with the Gaussian kernel g for different choices of length scale σ, denoted by

$$\begin{aligned} D_\sigma(x_i, y_j) &= \big[D * g\big](x_i, y_j, \sigma) \\ &= \sum_{l=1}^{n} \sum_{k=1}^{m} g(l, k, \sigma) D(x_i - l, y_j - k). \end{aligned} \tag{2.6}$$

The size of the D is $n \times m$ pixels, which is the same size as I. To capture both fine and coarse-scale features, we use a range of four different σ values namely $\sigma_1 = 1$,$\sigma_2 = \sqrt{2}$,$\sigma_3 = 2$,$\sigma_4 = 2\sqrt{2}$, and obtain four distinct D_σ values at each pixel location, each corresponding to one of the chosen σ values. In particular, we denote the discontinuity magnitude of gradient orientation at each of the four scales by D_{σ_1}, D_{σ_2}, D_{σ_3} and D_{σ_4} as shown in figure 2.6(b),(c),(d) and (e), respectively.

Depending on the value of σ, we see that blood vessels or parts of blood vessels in different directions are enhanced. To preserve small-scale features like fine vessels and capillaries, smaller values of σ are used (see figure 2.6b,c), while for large-scale features like large blood vessels and the overall structure of the retinal vasculature, larger values of σ are used (see figure 2.6d,e).

The GOA map is obtained by adding up all the individual maps obtained at these four scales (see figure 2.6b,c,d, and e) and is given by

$$D_{GOA}(x_i, y_j) = \sqrt{D^2_{\sigma_1}(x_i, y_j) + D^2_{\sigma_2}(x, y) + D^2_{\sigma_3}(x_i, y_j) + D^2_{\sigma_4}(x_i, y_j)}. \tag{2.7}$$

Then we first rescale all the pixels of the image D_{GOA} in the range of $0-255$ and then invert the final segmented image obtained from GOA (mathematically $D_{GOA,\text{inverted}}(x_i, y_j) = 255 - D_{GOA}(x_i, y_j)$ at each pixel position (x_i, y_j)) so that the vessels appear brighter than the background. Figure 2.6(f) shows the final inverted GOA map. It is evident from figure 2.6(f) that the curvilinear-shaped blood vessels are enhanced while noises and non-vessel structures are suppressed. To quantify the enhancement, we assess the performance of our unsupervised vessel segmentation approach by comparing the segmented image obtained after integrating all four features with the ground truth image, as presented at the end of this chapter, in subsection 2.10.

The GOA method relies on the orientation of the gradient vector field rather than the magnitude of the gradient vector, making it particularly beneficial for our image segmentation. This is because our images are often noisy and suffer from non-uniform illumination. Since GOA relies on the orientation of the gradient rather than its magnitude, GOA remains effective even when illumination varies across the image. This method is also less affected by noise, as it emphasises directional changes in the image rather than absolute pixel values.

2.4.2.1 Algorithm: Orientation Analysis of a Gradient vector

The proposed algorithm 1 for the orientation analysis of the gradient field vector is implemented in MATLAB (MathWorks, Natick, MA) using the built-in functions ‘imgradient’ and ‘imgaussfilt’ from the image processing toolbox.

2.4.3 Morphological transformation

Morphological transformation is the second component of our feature vector.

Morphological transformation is a widely used feature extraction technique in retinal image processing, primarily employed to reveal the underlying structure of the retinal vasculature. The foundation of morphological image processing lies in two basic operations: erosion and dilation. All other morphological operations, like opening, closing, top hat, and black hat transformation, are derived from combinations of these two essential processes. In the following subsection 2.4.3.1, we begin by examining the mathematical formulations of erosion and dilation, followed

Algorithm 1 Orientation Analysis of a Gradient vector

Require: Enhanced green channel image $I(x, y)$, Sobel operators s_x and s_y, standard deviation σ

Ensure: The inverted GOA map of the enhanced blood vessel

1: Obtain the gradient vectors using equation (2.1).
2: Calculate $G = \sqrt{G_x^2 + G_y^2}$.
3: Calculate $\epsilon = mean(G(:)) * 0.1$
4: Derive the unit gradient vectors using equation (2.2).
5: The unit gradient vectors are zero if $\sqrt{G_x^2 + G_y^2} < \epsilon$.
6: Find the first order derivatives of $u_x(x, y), u_y(x, y)$ in both directions using equation (2.3).
7: Sum up all the derivatives obtained in step 6 using equation (2.4).
8: Employ $D(x, y)$ at for different scales $\sigma = \{1, \sqrt{2}, 2, 2\sqrt{2}\}$.
9: Add all four individual maps obtained at step 8 using equation (2.7).
10: Invert the image obtained at step 9.

by an exploration of the operations derived from these fundamental techniques. Then, in subsection 2.4.3.2, we focus on the specific morphological transformation operations applied to our images.

2.4.3.1 Basics of morphological operations

Morphological operations were first applied to binary images [13]. A binary image is a digital image that consists of pixels that can have one of exactly two colours, usually black and white, so the matrix I can have only two pixel intensity values, either 0 (for black) or 1 (for white). Next, we extend the idea of morphological transformation from binary images to single colour channel images [17].

In general, a morphological operation needs two inputs: one is the original single colour channel image, and the second is called the structuring element, an array of pixels. The structuring element is typically smaller in size compared to the original image. Depending on the structure and size of the structuring element, we can use it to extract different patterns from the images.

Morphological transformation for binary image: Suppose I is the binary input image and B is the structuring element, where the size of B is smaller than the size of I. There are two types of pixels in the binary image I, namely foreground and background pixels. The pixel intensity value of the foreground pixel is 1, and the pixel intensity value of the background pixel is 0. B contains a combination of both foreground and background pixels. The centre pixel of B is known as the 'anchor point'. Dilation and erosion are two operations derived from two basic set operations, namely, reflection and translation. We first revisit the definitions of reflection and translation of sets.

Suppose b is the element of the set B then the reflection of the set B about its origin is denoted

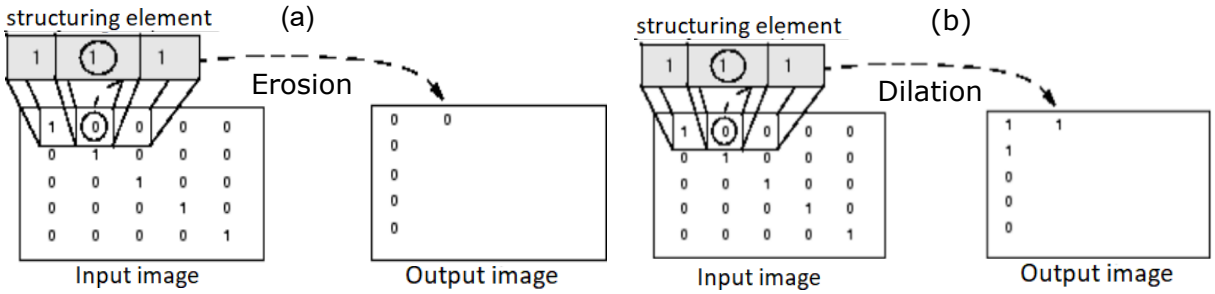

Figure 2.7: Schematic representation of morphological transformation on a binary image showing: (a) erosion [146] and (b) dilation [146].

by $\hat{B}$ and is defined as

$$\hat{B} = \{r | r = -b, b \in B\}. \tag{2.8}$$

Likewise, the translation of B by an element (i.e.,pixel) β is denoted by $(B)_\beta$ and is defined as

$$(B)_\beta = \{w | w = b + \beta, b \in B\}. \tag{2.9}$$

Figure 2.7(a) illustrates the erosion operation applied to a binary image. The structuring element determines the neighbourhood surrounding the pixel of interest (the pixel marked by the circle). This circled pixel is the anchor point of the structuring element. The erosion function assigns to each output pixel the minimum pixel intensity value found among all the pixels in its neighbourhood (i.e, the neighbourhood of the circle) defined by the structuring element. In a binary image, a pixel intensity value is set to 0 if any of the neighbouring pixels have the intensity value 0 (see figure 2.7a). The erosion of I by a structuring element B, denoted as $I \ominus B$, is defined as the set of all pixels β such that B, when translated by β, is completely contained within I. Mathematically, this can be expressed as

$$I \ominus B = \{\beta | (B)_\beta \subseteq I\}. \tag{2.10}$$

Figure 2.7(b) illustrates the dilation of a binary image. The structuring element defines the neighbourhood of the pixel of interest (i.e, pixel in circle centred at in figure 2.7b). The dilation function assigns to each output pixel the maximum pixel intensity value among all the pixels in its neighbourhood as defined by the structuring element. In a binary image, a pixel intensity value is set to 1 if any of the neighbouring pixels have the intensity value 1 in case of the dilation operation (see figure 2.7b). The dilation operation on the image I is a combination of reflection and translation operations and is defined as

$$I \oplus B = \{\beta | [(\hat{B}_\beta) \cap I] \subseteq I\}, \tag{2.11}$$

where $\hat{B}$ is the reflection of the structuring element B about the origin (see equation (2.8)) and then we translate $\hat{B}$ by β (see equation (2.9)).

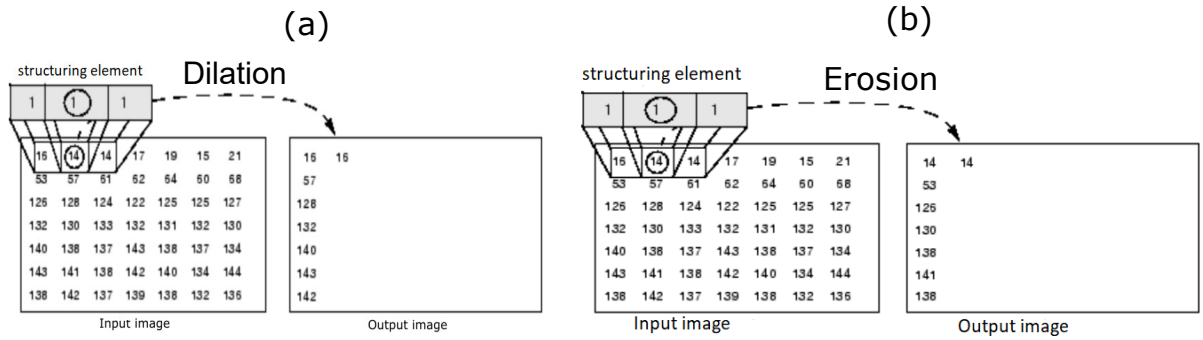

Figure 2.8: Schematic representation of morphological transformation on a single colour channel image showing: (a) dilation [146] and (b) erosion [146].

Now we extend the idea of the dilation and erosion for the single colour channel image.

Morphological transformation for the single colour channel image: The dilation operation for a single colour channel image is similar to that of a binary image. Figure 2.8(a) explains the dilation operation on a single colour channel image by a linear structuring element $\boldsymbol{B}$. According to the dilation operation rule, as described in the case of the binary image (see figure 2.7b), the dilation operation is performed in the neighbourhood of the anchor point of $\boldsymbol{B}$. The structuring element $\boldsymbol{B}$ slides over the image $\boldsymbol{I}$ until it covers all the pixels in $\boldsymbol{I}$. Then, we compute the local maximum for the pixel intensity value from the overlapping region of $\boldsymbol{I}$ and $\boldsymbol{B}$. Then, in the output matrix, the pixel intensity value at the pixel location corresponding to the anchor point of the structuring element is replaced with the local maximum value (see figure 2.8a). The dilation operation for the single colour channel image is defined as

$$(I \oplus B)(x_i, y_j) = \max_{(s,t)\in B} \{I(x_i - s, y_j - t)\}. \tag{2.12}$$

In retinal fundus images, dilation restores the general shape of the vessel structure while dilating the bright structure, like retinal blood vessels. It also fills small dark holes inside the vessels or connects broken parts of the vessels.

In the erosion operation, unlike the dilation operation explained above, we compute the local minima of the pixel intensity values from the overlapping region of $\boldsymbol{I}$ and $\boldsymbol{B}$. Figure 2.8(b) explains the erosion operation on the single colour channel image by a structuring element $\boldsymbol{B}$. The erosion operation for the single colour channel image is defined as

$$(I \ominus B)(x_i, y_j) = \min_{(s,t)\in B} \{I(x_i + s, y_j + t)\}. \tag{2.13}$$

Erosion effectively eliminates small bright artefacts such as camera light reflections, exudates, and image noise. Additionally, it smooths vessel boundaries by trimming their edges and helps separate closely connected vessels or pathological regions by breaking narrow connections, thereby improving the accuracy of detection.

There are other important morphological operations available for the image segmentation

task. These operations are essentially the combination of erosion and dilation operations. These operations include opening, closing, top-hat, and black-hat transformations.

The opening of an image I involves performing a erosion, followed by dilation [32, 56]. The opening of set I by a structuring element B, denoted by $I \circ B$ and is defined as

$$(I \circ B)(x_i, y_j) = \Big[(I \ominus B) \oplus B\Big](x_i, y_j). \tag{2.14}$$

The opening operation smooths out the background that does not fit the structuring element [32, 56]. Since dilation follows erosion, it preserves overall structures while removing overlapping narrow regions, which is crucial for obtaining clear segmented blood vessels [32, 56].

The closing of an image I involves a dilation followed by erosion [32, 56]. The closing of set I by structuring element B, denoted by $I \bullet B$ and is defined as

$$(I \bullet B)(x_i, y_j) = \Big[(I \oplus B) \ominus B\Big](x_i, y_j). \tag{2.15}$$

The closing operation is used to smooth the edges of blood vessels, eliminate small holes within them, thereby enhancing the continuity and clarity of retinal vessel structure [32, 56].

The black-hat operation is a type of morphological transformation that computes the difference between the closing of the input image and the original input image [32, 56]. Mathematically, the black-hat transformation I_{bh} can be written as

$$I_{bh}(x_i, y_j) = \Big[(I \bullet B) - I\Big](x_i, y_j). \tag{2.16}$$

The black-hat transformation is effective for detecting dark features (e.g., vessels) that are smaller than the structuring element and are located on a bright background [32, 56]. However, retinal fundus images have bright vessels on a dark background, so we do not include the Black-hat transformation in our feature vector.

The top-hat operation is a morphological transformation that calculates the difference between the original input image and its opening [32, 56]. This operation is especially effective for extracting small, bright features, such as blood vessels, that appear against a darker background. It is particularly beneficial to our images, where the vessels are bright, and the background is dark, and we apply the sum of top hat transformation to the image as our second feature vector to extract blood vessels.

The next step is to use the sum of top-hat morphological transformations to extract small bright structures like branches of retinal blood vessels of different widths from the complex background of the image containing pathological regions like haemorrhage. First, we explain how the top-hat transformation is applied to the image, followed by an introduction to the concept of the sum of top-hat transformations.

Before applying the morphological transformation to our image, we invert the enhanced green channel image by using the following expression

$$I^{(i)}(x_i, y_j) = 255 - I(x_i, y_j),$$

for all the spatial locations (x_i, y_j). $I^{(i)}$ is the inverted green channel image. Inverting the enhanced green channel is an important pre-processing step that helps us enhance the blood vessels and fine structures to appear brighter than the background. Before explaining the process of applying morphological transformation to images, we briefly explain the basics of morphological transformation.

2.4.3.2 Top-hat transformation and sum of top-hat transformation

The two important input elements for the top-hat transformation are the inverted discrete enhanced green channel image $I^{(i)}$ and the structuring element S_e at a given pixel (x_i, y_j).

The purpose of the structuring element S_e is to eradicate the vessel or some part of the vessel, which can only be achieved when the structuring element is oriented orthogonal to the vessel. Mathematically, this means the dot product between the direction vector of the blood vessel at a given pixel (x_i, y_j) and the direction vector of the rotated structuring element at a given pixel (x_i, y_j) is zero. A more detailed discussion of the underlying mathematics is provided later in this section.

To account for the orientation of the structuring element, we introduce a parameter θ' in the structuring element S_e, representing the angular rotation measured relative to the $x-$ axis. From this point onward, we refer to the structuring element as $S_e^{\theta'}$. Moreover, the shape of the structuring element $S_e^{\theta'}$ influences the shape of the extracted features, and retinal blood vessels can be thought of as a piecewise linear structure— we choose a linear structuring element for the morphological transformation to effectively enhance the vessels. Additionally, the structuring element must not be entirely contained within the vessel to ensure removal of only parts of the vessel (such as narrow branches or small non-vessel structures), which is useful for enhancing vessel edges and protecting overall retinal vasculature structure during the morphological operation. Taking this into consideration, the structuring element $S_e^{\theta'}$ is chosen to be smaller in size than the size of the blood vessels contained in the inverted green channel image. However, the size of the $S_e^{\theta'}$ needs to be large enough so that we can extract the blood vessels having large diameters. Depending on the size of the retinal blood vessels in Fundus images in this study, we find that the number of pixels in retinal blood vessels is not more than 21 pixels, so we consider a structural element of 21 pixels long and 1 pixel wide. We start with the $\theta' = \pi/2$ to see how well the structuring element extracts blood vessels when the $S_e^{\theta'}$ is perpendicular to the $x-$ axis of the image. Then, in the next step, we consider multiple θ' values between 0 and π to extract blood vessels in different directions.

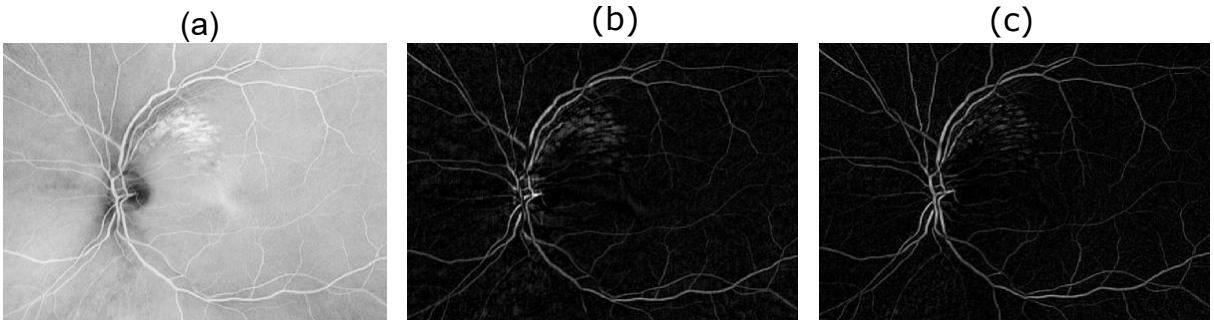

Figure 2.9: Morphological transformation:(a) inverted enhanced green channel image, (b) top-hat transformed image, and (c) sum of top-hat transformed image.

The first step is to perform the opening operation on the enhanced green channel image using the structuring element $S_e^{\theta'}$. The opening operation is the combination of two basic morphological operations, namely erosion and dilation. The opening operation is applied using the built-in function 'imopen' from MATLAB. The opening operation is denoted by '$\circ$'.

The next step is to subtract the opened image $I^{(i)} \circ S_e^{\theta'}$ from the inverted green channel image $I^{(i)}$. This is known as the top-hat transform, and it can be defined as

$$I_{th}^{\theta'}(x_i, y_j) = \left[I^{(i)} - (I^{(i)} \circ S_e^{\theta'})\right](x_i, y_j). \tag{2.17}$$

As previously discussed, retinal vessels vary in both width and orientation. To effectively extract vessels oriented in different directions, we compute the sum of top-hat transformations performed along multiple orientations. This cumulative top-hat transformation using a set of linear structuring elements is expressed as:

$$I_{S_{th}}(x_i, y_j) = \sum_{\theta'} I_{th}^{\theta'}(x_i, y_j), \quad \theta' \in \{0, \frac{\pi}{8}, \frac{\pi}{4}, \frac{3\pi}{8} ..., \pi\}, \tag{2.18}$$

where $I_{S_{th}}$ is the sum of all top-hat transformation. Equation (2.18) is obtained essentially by summing all top-hat transformations obtained in multiple directions. The structuring element $S_e^{\theta'}$ is rotated at an angle between 0 and π in steps of $\frac{\pi}{8}$. It is important to note that it is a trial-and-error method, so we consider other angles. We observe that including additional values of θ' improves the results, but the improvement is not substantial compared to the increase in computational time. To quantify the improvement, we assess the performance of our unsupervised vessel segmentation approach by comparing the segmented image obtained after integrating all four features with the ground truth image, as presented at the end of this chapter, in subsection 2.10. Therefore, we trade off between accuracy and computational efficiency.

Figure 2.9 provides the resultant image obtained after applying the sum of the top hat transform. Figure 2.9(a) provides the inverted enhanced green channel image, and figure 2.9(b) is the top-hat transformed image after applying the top-hat transformation as given in equation (2.17). Figure 2.9(c) shows the resultant image obtained using the sum of all top-hat transformations

using equation (2.18). It is clear that in the final image (see figure 2.9c), the retinal blood vessels are enhanced regardless of their directions, including small vessels.

2.4.3.3 Algorithm: Morphological transformation

A sample algorithm 2 for morphological transformation is given below and implemented in MATLAB (MathWorks, Natick, MA) using the Image Processing Toolbox.

Algorithm 2 Sum of top-hat transformation

Require: $I^{(i)}$ and length, angle (θ') and type of S_e
Ensure: Resultant image $I_{S_{th}}$
1: Create a linear structuring element S_e of 21 pixel long and with angle $\pi/2$.
2: Perform opening operation using S_e on $I^{(i)}$
3: Find I_{th} using equation $I_{th} = I^{(i)} - (I^{(i)} \circ S_e)$
4: $\theta' \leftarrow 0 : \frac{\pi}{8} : \pi$
5: **for** $\theta' \leftarrow 0$ to π
6: Given S_e vary the angle θ' and obtain the structuring element $S_e^{\theta'}$
7: Given $S_e^{\theta'}$, find $I_{th}^{\theta'}$ using equation (2.17) and step 3.
8: Add all $I_{th}^{\theta'}$ to obtain the final image $I_{S_{th}}$ using equation (2.18)
9: **end for**

2.4.4 Multiscale Gabor filter

The Gabor filter response is the third component in the feature vector.

Gabor filters are highly effective tools that have been extensively used as feature extractors for vessel segmentation purposes in image processing [58, 74, 115]. In this work, we use a Gabor $2D$ filter, which has been shown to mimic human visual processing by forming a filter combining a sinusoidal wave with a Gaussian function [24]. The sinusoidal wave controls frequency and orientation sensitivity of the filter, and the Gaussian function controls localization of the filter in space. Overall, Gabor filters, with their ability to selectively detect oriented features and fine-tune to particular frequencies and scales, serve as effective edge detectors [74]. Both the spatial and frequency domains can be adjusted to specific frequencies, scales, and directions. As a result, they facilitate noise suppression, feature extraction, and vessel enhancement concurrently in a single operation [58, 74].

The Gabor filter is capable of extracting blood vessels of different widths in multiple directions, and we use it to enhance different types of edges present in the image while suppressing noise. To detect edges of retinal blood vessels of varying widths at multiple scales, we construct the Gabor filter bank by combining the maximum Gabor filter responses. We first discuss the mathematical construction of $1D$ Gabor filter and then generalise the idea of $1D$ Gabor filter to $2D$.

The response of the $1D$ Gabor filter kernel is a wave of wavenumber k_0 multiplied by a Gaussian function and is given by

$$g(x) = \frac{1}{\sqrt{2\pi}} e^{-\frac{x^2}{2\sigma^2}} e^{ik_0 x}, \tag{2.19}$$

where $\frac{1}{\sqrt{2\pi}} e^{-\frac{x^2}{2\sigma^2}}$ is a Gaussian-shaped function, known as the envelope, and $e^{ik_0 x}$ is a complex sinusoid response, known as the carrier. Here, σ is the standard deviation of the Gaussian function. Also, $k_0 = (2\pi/\lambda)$ where λ is the wavelength of the sinusoidal term inside the Gaussian envelope. Suppose we have a $1D$ image and the idea is to convolve the 1D image with the $1D$ Gaussian kernel g given in (2.19) to enhance the edges present in the image while suppressing the noise. The convolution operation is already discussed in subsection 2.4.2. In reality, the fundus images we are using in this work are of $2D$, so we have to use a $2D$ Gaussian kernel for convolution.

The $1D$ Gabor filter response can be extended to $2D$ rotating to a new coordinate system (x', y') form as

$$g(x, y; \lambda, \alpha, \psi, \sigma, \gamma) = e^{-\frac{1}{2}\left(\frac{x'^2 + \gamma y'^2}{2\sigma^2}\right)} e^{i\left(2\pi \frac{x'}{\lambda} + \psi\right)}, \tag{2.20}$$

where (x', y') are the rotated coordinates

$$x' = x\ \cos\alpha + y\ \sin\alpha, \quad y' = -x\ \sin\alpha + y\ \cos\alpha. \tag{2.21}$$

In the multiscale Gabor filtering approach, we rotate the $2D$ filter, which is mathematically equivalent to rotating the coordinate system to obtain a new coordinate system at each orientation, to capture different edges at multiple orientations and scales. The rotated coordinate system is connected to the original coordinate system by the expression given in (2.21). This is particularly important in fundus images, as retinal blood vessels appear with varying widths and in different directions. In the literature (e.g., [74]), it is suggested that λ values for retinal vessel segmentation usually lie between $1/2$ and 2. We choose $\lambda = 2$ as it is found to work best for our images to capture the comparatively thicker blood vessels. Note that ψ is the phase offset, and we consider $\psi = 0$ as this gives a symmetric Gabor filter, and the symmetric kernel responds strongly to lines and structures like blood vessels that match its orientation. Also, γ is the spatial aspect ratio of the envelope. When $\gamma < 1$, the Gaussian envelope is elongated along the x' direction compared to the y' direction. We consider the aspect ratio $\gamma = 1/2$, which means the Gaussian envelope is twice as spread out along the x' direction compared to the y' direction. This gives a Gaussian envelope elongated along the direction of its preferred orientation (i.e., x') and improves sensitivity to the elongated structures. Usually, the retinal blood vessels are elongated, so it is sufficient to enhance the vessel structures in the chosen orientation. Here, α is the orientation and σ is the

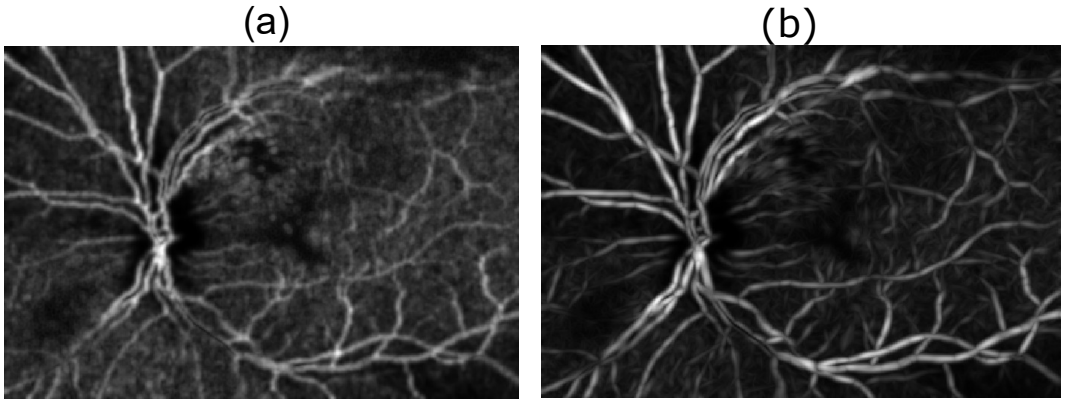

Figure 2.10: Gabor filter response:(a) average Gabor filter response, and (b) the maximum Gabor filter response.

Gaussian envelope scale and ranges of α, σ are given below.

The filter defined in (2.20) has a real and an imaginary component. The real part of the Gabor filter can be written as

$$g_{real}(x, y; \lambda, \alpha, \psi, \sigma, \gamma) = e^{-\frac{1}{2}\left(\frac{x'^2+\gamma y'^2}{2\sigma^2}\right)} \cos\left(2\pi\frac{x'}{\lambda} + \psi\right) \tag{2.22}$$

and the imaginary part is given by

$$g_{im}(x, y; \lambda, \alpha, \psi, \sigma, \gamma) = e^{-\frac{1}{2}\left(\frac{x'^2+\gamma y'^2}{2\sigma^2}\right)} \sin\left(2\pi\frac{x'}{\lambda} + \psi\right). \tag{2.23}$$

Now we convolve the green channel image I using the Gabor filter defined above to obtain an image with enhanced blood vessels. In this work, only the real part of the Gabor filter (2.22) is used for convolution to enhance elongated structures (blood vessels). This is because the real component of the Gabor filter contains a cosine function, which is an even function, so the filter becomes mirror-symmetric about its centerline. As a result, the filter responds strongly to structures (e.g., blood vessels) that have similar pixel intensity on both sides of the filter axis. Moreover, the input enhanced green channel image is real-valued, so for simplicity and computational efficiency, the real part of the Gabor filter alone is sufficient.

To extract multi-scale and multi-orientation features from the fundus image, a Gabor filter bank is constructed, which is made of filters composed of four different spatial scales (i.e, σ values) and 19 different orientations (i.e, different α values). We find that 19 different values of α are sufficient to enhance the large blood vessels of interest, which are used later for the parameterisation of the mathematical model. To quantify the performance, we compare the image obtained from an unsupervised vessel segmentation approach after integrating all four features with the ground truth image, as presented at the end of this chapter, in subsection 2.10. To extract blood vessels at multiple scales and orientations, we perform a convolution between the enhanced green channel image I and the real part of the Gabor filter, which is designed for various scales and

directions and $G_{\sigma,\alpha}$ is the filtering response at a given pixel location (x_i, y_j) which is obtained by applying a $2D$ convolution operation. For a given σ, and α, the convolution operation is defined as:

$$\begin{aligned} G_{\sigma,\alpha}(x_i, y_j) &= \big[I * g_{real}(\lambda, \alpha, \psi, \sigma, \gamma)\big](x_i, y_j) \\ &= \sum_{l=1}^{n} \sum_{k=1}^{m} g_{real}(l, k, \lambda, \alpha, \psi, \sigma, \gamma) I(x_i - l, y_j - k). \end{aligned} \tag{2.24}$$

where '*' is the convolution operation. For the detailed discussion on the convolution operation, see subsection 2.4.2. We use the built-in function 'gabor' from MATLAB to compute the Gabor filter.

The next step is to find the maximum and average magnitude of the Gabor filter response given in equation (2.24). Here, $Gmax$ is the maximum Gabor filter response at a given pixel (x_i, y_j) and is defined as

$$Gmax(x_i, y_j) = \max_{\sigma \in S, \alpha \in T} (G_{\sigma,\alpha})(x_i, y_j), \;\; S = \{2,3,4,5\}, \;\; T = \{0, \frac{\pi}{18}, \frac{\pi}{9}, ..., \pi\}, \tag{2.25}$$

and $Gavg$ is the average Gabor filter response at a given pixel (x_i, y_j) and is defined as

$$Gavg(x_i, y_j) = mean_{\sigma \in S, \alpha \in T} (G_{\sigma,\alpha})(x_i, y_j), \;\; S = \{2,3,4,5\}, \;\; T = \{0, \frac{\pi}{18}, \frac{\pi}{9}, ..., \pi\}; \tag{2.26}$$

$Gmax$ and $Gavg$ are the two matrices of the same size as the input enhanced green channel image. Here we experiment with different values for α, observing that the above values for α are sufficient to enhance blood vessels in different directions. For σ values, we observe that the large retinal vessels in all our clinical images (5-6 images in total) obtained from the collaborator are $4-5$ pixels wide. Based on our observation of all the clinical images studied so far, the specified range for vessel widths appears to be appropriate in our case. We use 'imgaborfilt' from the MATLAB image toolbox to obtain the magnitude of the filter response.

Figure 2.10 shows the inverted green channel image and responses of the maximum (figure 2.10b) and average Gabor filter (figure 2.10c), which are calculated at different scales for different orientations. After applying the Gabor filter on the enhanced green channel image given in figure 2.10(a), we observe the suppression of background noise while enhancing the blood vessels. We choose the maximum Gabor filter response given in figure 2.10(b) as our feature vector because the maximum Gabor filter response enhances contrast, making vessel structures more distinguishable from the background. Moreover, the maximum Gabor filter response captures the highest Gabor filter response across all directions and scales at a given pixel (x_i, y_j), so this is ideal for detecting elongated structures like blood vessels, which strongly respond to Gabor filters at a specific orientation and scale.

2.4.4.1 Algorithm: Maximum of Gabor filter response

The proposed algorithm 3 for Gabor filter response is implemented in MATLAB (MathWorks, Natick, MA) using the Image Processing Toolbox.

Algorithm 3 Algorithm: Gabor filter response

Input: $I(x, y)$, wavelength (λ) and orientation α
Output: Maximum Gabor filter response
$\lambda \leftarrow 0.5 : 0.5 : 2, \psi \leftarrow 0$
$\sigma \leftarrow 2, 3, 4, 5$
$\alpha \leftarrow 0 : 15° : 180°$
Create a Gabor filter with λ and θ
Apply the Gabor filter bank on the input image I to find the magnitude response matrix $gabormag$ for the Gabor filter bank
for $i \leftarrow 0$ to number of rows of $gabormag$
    for $j \leftarrow 0$ to number of columns of $gabormag$
        Find the maximum response of the Gabor filter bank $gabormag(i, j)$
    end for
end for

2.4.5 Maximum principal curvature

Maximum principal curvature is the fourth component in the feature vector.

The principal curvature is a feature that has been shown to improve edge contrast in digital images, yielding clearer segmentation results. The principal curvatures of a surface K at a point p in the surface S are the maximum and minimum values of the curvatures of curves through p. The maximum principal curvature is used to detect edges on a dark background. The directions corresponding to these principal curvatures are known as the principal directions. The principal curvatures and directions are a convenient way of indicating how the surface curves in the vicinity of a point on the surface. The changes in the surface indicate the sharp changes in pixel intensity values in the image.

The principal curvatures can be computed in various ways. The easiest way to calculate curvature is to compute the Hessian matrix based on the second-order derivative of the Gaussian kernel convoluted on the image. The principal curvatures are then proportional to the eigenvalues of the Hessian matrix. For structure analysis, such as vessel detection, the eigenvalues help identify regions of high or low curvature by analysing how the pixel intensity changes around a given pixel in the image I.

We employ the principal curvature at multiple scales to improve the contrast of lines and edges of different widths in retinal blood vessel segmentation.

2.4.5.1 Principal curvature

To find the curvature of the enhanced green channel image I, we first find the height map K of I. Recall that the pixel intensity value at given pixel (x_i, y_j) is $I(x_i, y_j)$. The height map K is given by

$$K(x_i, y_j) = (x_i, y_j, I(x_i, y_j)). \tag{2.27}$$

The image I forms a $2D$ surface embedded in $3D$. Finding the curvature of the surface K is equivalent to finding the eigenvalues of the Hessian matrix of I. Structures like blood vessels, which are of high curvature, are known as ridges. The local shape characteristics of the surface K at a given pixel (x_i, y_j) where $i \in \{0, 2, ..., n-1\}, j \in \{0, 2, ..., m-1\}$ is given by the Hessian matrix $\mathbb{H}$ and is defined as

$$\mathbb{H}(x_i, y_j) = \begin{bmatrix} I_{xx} & I_{xy} \\ I_{yx} & I_{yy} \end{bmatrix}, \tag{2.28}$$

where $I_{xx}, I_{xy}, I_{yx}, I_{yy}$ are second order derivatives of I along the $x-$ and $y-$ directions. It is important to note that $\mathbb{H}$ is defined at a pixel (x_i, y_j) only when all the second-order partial derivatives of I exist at that pixel.

In order to compute the second-order derivatives of the discrete image I, we convolve I with the Gaussian kernel $g(x_i, y_j, \sigma)$ given in the equation (2.5) (see subsection 2.4.2) and compute the second-order derivatives of I for a given pixel (x_i, y_j) in the $x-$ and $y-$ directions are defined as

$$I_{xx}(x_i, y_j; \sigma) = \frac{\partial^2}{\partial x^2}\Big[g(\sigma) * I\Big](x_i, y_j). \tag{2.29}$$

Here,'$*$' denotes a $2D$ convolution operation (for details about the convolution operation see subsection 2.4.2). Due to the linearity and shift-invariance of convolution and differentiation, the equation (2.29) is equivalent to:

$$I_{xx}(x_i, y_j; \sigma) = \Big[\frac{\partial^2 g(\sigma)}{\partial x^2} * I\Big](x_i, y_j) = \Big[g_{xx}(\sigma) * I\Big](x_i, y_j). \tag{2.30}$$

Similarly, all other second-order derivatives of I in $x-$ and $y-$ directions can be written as

$$\begin{aligned} I_{xy}(x_i, y_j; \sigma) &= \Big[g_{xy}(\sigma) * I\Big](x_i, y_j), \\ I_{yx}(x_i, y_j; \sigma) &= \Big[g_{yx}(\sigma) * I\Big](x_i, y_j), \\ I_{yy}(x_i, y_j; \sigma) &= \Big[g_{yy}(\sigma) * I\Big](x_i, y_j). \end{aligned} \tag{2.31}$$

The size of the Gaussian kernel g is the same as that of the image I, where σ is the spatial scale parameter of the Gaussian kernel. The symmetric Gaussian kernel is used to ensure that

derivative estimates remain consistent regardless of the vessel orientation. We have to choose σ values carefully so that we can enhance blood vessels and reduce the noise. Using the trial-and-error method, we observe that $\sigma = 1.45 - 1.5$ is sufficient to enhance multiple generations of blood vessels and also minimises the noise present in the image.

The eigenvalues obtained from the Hessian matrix $\mathbb{H}$ given in equation (2.28) are known as the principal curvatures at a given pixel (x_i, y_j). The evaluation of the principal curvatures is performed at every pixel location (x_i, y_j) of the image I (see figure 2.11a). Let us consider that $\lambda_{ij}^{(1)}$ and $\lambda_{ij}^{(2)}$ are the two eigenvalues of the Hessian matrix $\mathbb{H}$ given in equation (2.28) obtained at a pixel (x_i, y_j). Then, the maximum and the minimum values of the eigenvalues are given by

$$\begin{aligned} \lambda_{ij}^{+} &= max\{\lambda_{ij}^{(1)}, \lambda_{ij}^{(2)}\}, \\ \lambda_{ij}^{-} &= min\{\lambda_{ij}^{(1)}, \lambda_{ij}^{(2)}\}. \end{aligned} \tag{2.32}$$

In the next step, we construct two eigenvalue matrices at every point (x_i, y_j) in image I where one contains the maximum eigenvalues λ_{ij}^{+} and the other contains the minimum eigenvalues λ_{ij}^{-}. Let Λ^{+}, Λ^{-} denote the matrices representing the maximum and minimum principal curvatures, respectively, and are defined as follows:

$$\begin{aligned} \Lambda^{+} &= (\lambda_{ij}^{+})_{n \times m}, \\ \Lambda^{-} &= (\lambda_{ij}^{-})_{n \times m}. \end{aligned} \tag{2.33}$$

Both the matrices Λ^{+} and Λ^{-} have the same dimensions as the input image I. Now we have the image obtained from the matrix of the maximum principal curvature (Λ^{+}), but with much noise.

2.4.5.2 Post-processing using thresholding

The maximum principal curvature captures the maximum changes of pixel intensity values at each pixel location on the surface defined above. Unlike other features we have seen, these kinds of curvature-derived features are often sensitive to minor fluctuations in pixel values. ISO thresholding is a method to regularise or stabilise fluctuations in pixel values before further processing [155]. This is used in image processing to determine an optimal threshold for separating an image into foreground and background. This thresholding approach helps isolate regions where maximum principal curvature exceeds a certain value, which often corresponds to significant anatomical features like blood vessels [155].

The first step is to start with an initial threshold value T_0. A common choice is the middle of the grey-level range $T_0 = 128$. Now we divide the image pixels into two groups: foreground, pixels with intensity $\geq T_0$, and background: pixels with intensity $\leq T_0$. The next step is to compute mean intensities where (m_f): mean of foreground pixel values and (m_b): mean of background pixel values. Then, we compute the new threshold value T_1 as the average of these two means,

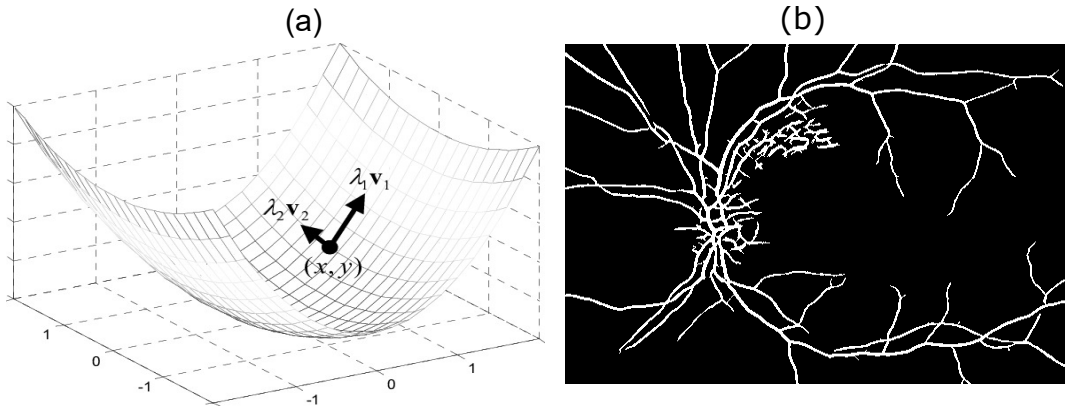

Figure 2.11: Principal curvature: (a) schematic diagram of principal curvature and principal direction, and (b) principal curvature applied on the inverted green channel image.

where

$$T_1 = \frac{m_f + m_b}{2}.$$

Now we update the threshold value T_0 by setting $T_0 = T_1$ and repeat these steps until the threshold stabilises (i.e., it no longer changes).

The final segmented image figure 2.11(b) is obtained using ISO Data thresholding. We see that principal curvature enhances all vessels irrespective of the vessel width.

2.4.5.3 Algorithm: Maximum principal curvature

The proposed principal curvature algorithm 4 is implemented in MATLAB (MathWorks, Natick, MA) using the Image Processing Toolbox.

2.5 K-means clustering for pixel classification

As discussed earlier in subsection 2.4, we first apply an unsupervised machine learning (clustering) approach to obtain the final segmented image from each of the four features discussed above. Clustering is a widely used vessel segmentation approach. In the clustering approach, we group all pixels of the image based on certain pre-defined similarity criteria. Each of these groups is called a cluster. There are different clustering approaches available. However, the K-means algorithm is computationally simple compared to other clustering algorithms [66, 134], so we start with the K-means clustering in the proposed work, and it provides satisfactory results. For a detailed discussion on other conventional machine learning approaches, please see subsection 1.8 of chapter 1 and subsection 2.4.

In K-means clustering, all the pixels are classified based on their distance from the cluster means, the arithmetic average of all the data points in that cluster. It takes the input parameter, K, as a number of clusters and partitions a data set into K clusters so that the resulting objects of one cluster are dissimilar based on their distance from the cluster means to other clusters and

Algorithm 4 Principal Curvature

Require: $I(x, y)$, standard deviation σ
Ensure: Output: $I_s(x, y; \sigma)$

Apply erosion operation on I using diamond shaped structuring element of size 20 pixels
$\sigma \leftarrow 1.45$ and apply a Gaussian filter on the image obtained in step 1
Find maximum principal curvature of the image obtained in step 3 using PRINCUR function
Apply histogram equalisation on the resultant image
Compute global image threshold using the iterative isodata method on the image obtained in step 5
Obtain the binary image of the resultant image
Use connected component analysis to filter out all small vessels
$g_x \leftarrow$ first order derivative of I along x direction
$g_y \leftarrow$ first order derivative of I along y direction
$g_{xx} \leftarrow$ first order derivative of g_x along x direction
$g_{xy} \leftarrow$ first order derivative of g_x along y direction
$g_{yy} \leftarrow$ first order derivative of g_y along y direction
$m \leftarrow$ number of rows in I
$n \leftarrow$ number of columns in I
▷ % Defining functions%
function λ_1 =PRINCUR(I)
    Find g_{xx}, g_{xy}, g_{yy}
▷ % Finding maximum (λ_1) and minimum (λ_2) eigen values of hessian matrix%
    for $i \leftarrow m$
        for $i \leftarrow n$
            $[\lambda_1(i,j), \lambda_2(i,j)]$=$LAMDAFIND(g_{xy}(i,j), g_{xx}(i,j), g_{yy}(i,j))$
        end for
    end for
    Find λ_1 using equation (2.32)
end function
function $[\lambda_1, \lambda_2]$=$LAMDAFIND(g_{xx}, g_{xy}, g_{yy})$
    Find Hessian matrix $\mathbb{H}$ using equation (2.28)
    Obtain eigenvalues
%Obtain maximum and minimum lambda values% **if** $\lambda_+ > \lambda_-$ **then**
        $\lambda_1 = \lambda_+$
    $\lambda_2 = \lambda_-$
    $\lambda_+ < \lambda_-$
    $\lambda_1 = \lambda_-$
    $\lambda_2 = \lambda_+$ **else**
        $\lambda_1 = \lambda_+$
    $\lambda_2 = \lambda_-$

end function
function $[threshold, MAT, MBT] = isodata(I)$
    Compute mean intensity of image from histogram, set $T = mean(I)$
    Compute Mean above T(MAT), Mean below T (MBT) and cumulative sum using T
    $new_T(i) = round(MAT + MBT)/2$
    Do step 3 to n: repeat step 2 if $T(i) \neq T(i-1)$
    Normalize the threshold to the range $[i, 1]$
end function

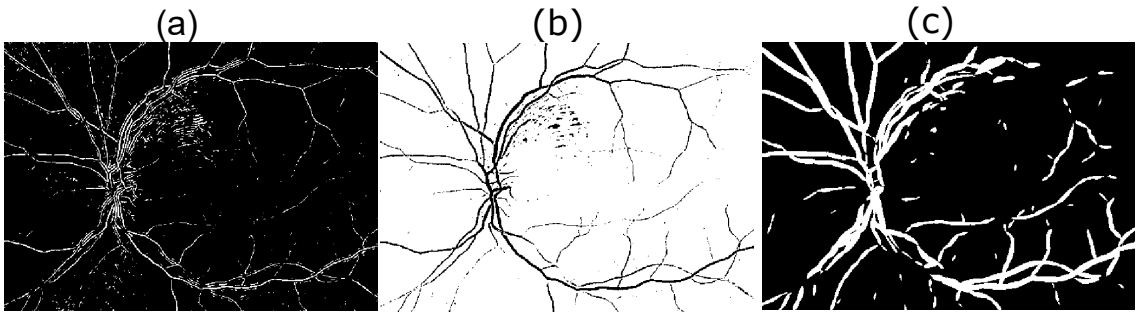

Figure 2.12: $K-$means clustering applied on the three feature vectors showing images obtained from: (a) GOA (I_1'), (b) sum of top hat transformation (I_2'), and (c) multiscale Gabor filter response (I_3'), respectively.

similar to objects of the same cluster. The similarity of the data point depends on the distance of the data point from the cluster mean. All the points whose distance from the cluster mean is below a threshold value then all of them belong to the same cluster. For applying a feature-wise clustering algorithm, the number of clusters is provided by the user. However, the performance of segmentation is highly sensitive to the cluster centers and their numbers, which are sometimes challenging for users to determine directly in advance. For simplicity, we set the number of clusters to $K = 2$, namely C_v(vessel), the cluster containing vessel pixels, and C_{nv}(non-vessels), the cluster containing non-vessel pixels. It is important to note that the resultant image obtained after applying $K-$means clustering becomes a binary image, i.e., the image contains only two types of pixels (i.e., vessel and non-vessel pixels). In the following subsection 2.5.1, we discuss the mathematical concept behind the $K-$means clustering approach. Subsection 2.5.2 outlines the post-processing techniques applied to the image obtained from the $K-$means clustering approach.

2.5.1 K-means clustering

We consider a data set consisting of $n \times m$ pixel intensity values $x_1, x_2, ..., x_{n\times m} \in \mathbb{R}$. We partition the data points into $K = 2$ clusters C_1, C_2 based on the objective (or cost function)

$$Cost(\mathbf{x}, C_1, C_2) = \min_{C_1,C_2} \sum_{l=1}^{2} \frac{1}{|C_l|} \sum_{i,j\in C_l} ||x_i - x_j||^2. \tag{2.34}$$

This cost function (2.34) is a weighted average of the cluster variances, with weights proportional to cluster size in terms of the number of points $|C_l|$ in the cluster C_l. Let,

$$\mu_l = \frac{1}{|C_l|} \sum_{i\in C_l}^{n\times m} x_i$$

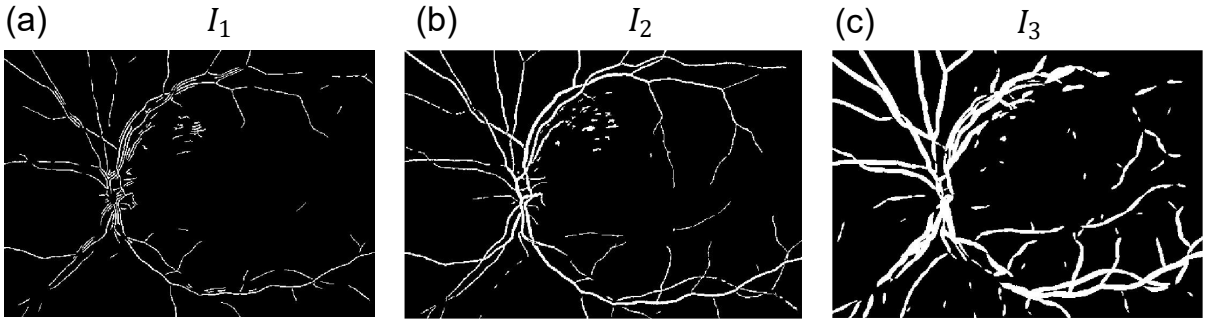

Figure 2.13: Final images obtained after applying $K-$means and post-processing showing: (a) I_1 for gradient orientation analysis, (b) I_2 for morphological transformation, and (c) I_3 for the multiscale Gabor filter.

be the centroids of the cluster C_l. Now the cost function (2.34) can be rewritten in terms of μ_l as

$$Cost(\mathbf{x}, C_1, C_2) = \min_{\substack{C_1,C_2 \\ \mu_1,\mu_2}} \sum_{j=1}^{2} \sum_{i \in C_j} ||x_i - \mu_j||^2 \tag{2.35}$$

We choose a set of binary indicator variables $r_{i,j} \in \{0,1\}$ where $i = 1,..,n \times m, j = 1,2$ indicating that the data point x_i is assigned to any one of the 2 clusters or not. If the pixel intensity x_i is assigned to j cluster then $r_{i,j} = 1$ and $r_{i,j} = 0$ for $j \neq i$. We define an objective function J known as the distortion measure, and the goal of K-means clustering is to minimise J over all $|K|$ clusters. This distortion measure J is given by

$$J = \sum_{j=1}^{2} \sum_{i \in C_j} r_{i,j} ||x_i - \mu_j||^2, \tag{2.36}$$

representing the sum of the squares of the distances of each data point to its assigned vector $\boldsymbol{\mu}_K$. We aim to find the values for $\{r_{n,K}\}$ and $\{\boldsymbol{\mu}_K\}$ so that we can minimize J. We do this using an iterative procedure where each iteration has two successive steps corresponding to successive optimisations with respect to $\{r_{n,K}\}$ and $\{\boldsymbol{\mu}_K\}$. In the first step, we keep $\boldsymbol{\mu}_K$ fixed, and we minimise J with respect to $r_{n,K}$. In the second step, we minimise J with respect to the $\boldsymbol{\mu}_K$, keeping $r_{n,K}$ fixed. This two-stage optimisation process is repeated until convergence or until some maximum number of iterations is exceeded.

After creating the feature vector as given in subsection 2.4.1, we apply the $K-$means clustering algorithm separately to each extracted feature (i.e. gradient orientation analysis in subsection 2.4.2, morphological transformation in subsection 2.4.3, multiscale Gabor filter in subsection 2.4.4 and maximum principal curvature in subsection 2.4.5), resulting in two clusters assignments for each pixels present in each feature. Let, I_1' be the image obtained after applying $K-$means on the orientation analysis of the gradient vector (see subsection 2.4.2), I_2' be the image obtained after applying $K-$means on the morphological transformation (see subsection 2.4.3) and I_3' be the image obtained after applying $K-$means on the multiscale Gabor filter

response (see subsection 2.4.4).

Figure 2.12 shows the images I_1'(see figure 2.12a), I_2' (see figure 2.12b) and I_3' (see figure 2.12c). We observe that vessels of different generations are enhanced, but with much noise (see figure 2.12). The noises appear in the form of isolated white pixels that do not belong to any vessels. At this stage, it is crucial to remove this noise as it will hamper the performance of the vessel tracking algorithm developed in Chapter 3. To eliminate the noise present in the image, the next step involves a post-processing technique. In the following subsection 2.5.2, we discuss the post-processing used to obtain the final images from each feature discussed above. It is important to note that we have not applied the Connected Component Labelling (CCL) post-processing technique to the image obtained from maximum principal curvature, as we have already implemented another post-processing approach (ISO thresholding in subsection 2.4.5.2).

2.5.2 Post-processing

The Connected Component Labelling (CCL) algorithm is a fundamental post-processing technique in image processing used to detect and label connected regions (also called components) in binary images. It is important to note that the resultant image obtained after $K-$ means clustering is a binary image. To detect and eliminate all irrelevant small white regions (noise) in the resulting image that do not represent vessel pixels, we apply the Connected Component Labeling (CCL) algorithm.

The basic idea behind the CCL algorithm is to group pixels that belong to the same connected component and are indexed with a unique label, where a connected component is a set of pixels that are connected via some predefined criterion. The most common criterion used for defining connected components is 4-connectivity or 8-connectivity. In 4-connectivity, two pixels are considered connected if they share a common edge, while in 8-connectivity, two pixels are considered connected if they share a common edge or corner. We implement the CCL algorithm using the built-in function 'bwconncomp' from MATLAB, and the 8-connectivity is considered. A detailed discussion of the CCL algorithm is out of the scope of this work.

Figure 2.13(a,b,c) shows the final images obtained after applying the $K-$means and CCL algorithm on the images obtained from three features, namely gradient orientation analysis (see figure 2.13a), sum of top hat transformation (see figure 2.13b) and maximum Gabor filter (see figure 2.13c) which show that the CCL algorithm successfully removes the unnecessary white spots.

I_1 is the final image obtained after applying $K-$means and CCL technique on the orientation analysis of the gradient vector (see section 2.4.2), I_2 is the final image obtained after applying $K-$means and CCL technique on the morphological transformation (see section 2.4.3), I_3 is the final image obtained after applying $K-$means and CCL technique on the multiscale Gabor filter response (see section 2.4.4) and I_4 is the final image obtained from the maximum principal curvature after applying thresholding approach (see subsection 2.4.5).

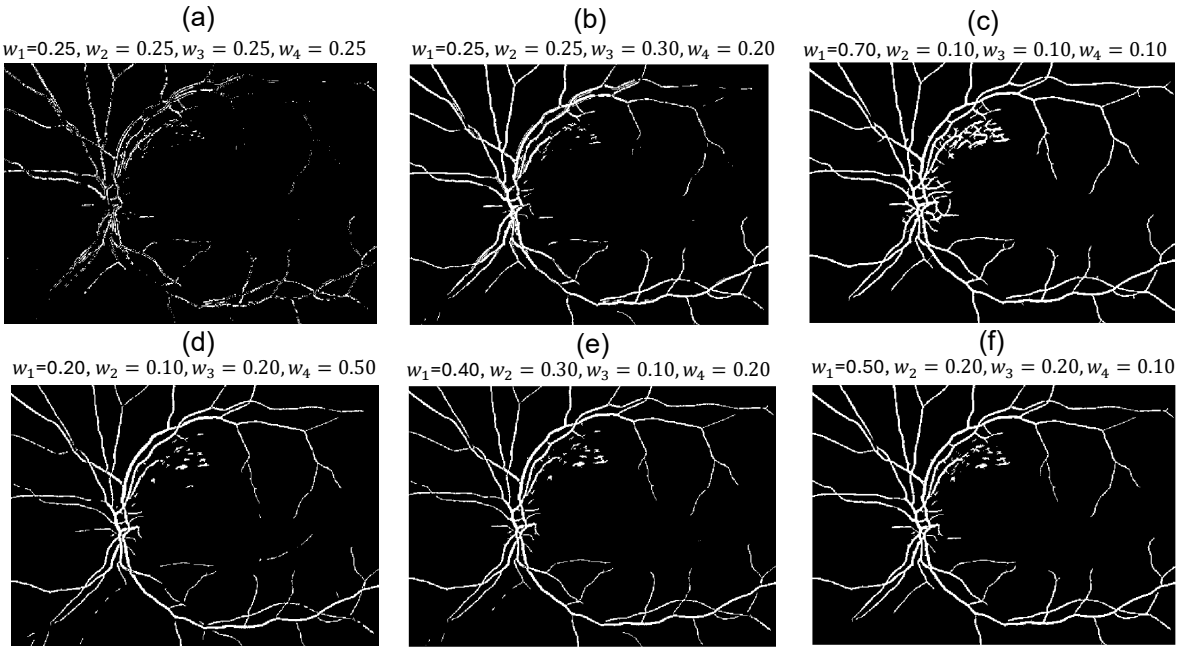

Figure 2.14: Weighted K-Means clustering applied on the inverted green channel image with variable weights: (a) w_1-means clustering applied, and (b) CCL algorithm applied on the image.

To combine the four classified images obtained from the four features after applying the K-means and post-processing algorithms, we compute a weighted sum, and the detailed discussion on this is given in the following subsection.

2.6 Weighted K-means clustering for feature fusion

We select a set of weights w_1, w_2, w_3, w_4 corresponding to each feature in such a way that their total sum $w = w_1 + w_2 + w_3 + w_4$ equals 1. Each weight corresponds to a specific feature: w_1 for image I_1, w_2 for I_2, w_3 for I_3, and w_4 for I_4. The expression to obtain the final segmented image is given by

$$\begin{aligned} I_{\text{final}} &= w_1 I_1 + w_2 I_2 + w_3 I_3 + w_4 I_4, \\ w_1 + w_2 + w_3 + w_4 &= 1. \end{aligned} \tag{2.37}$$

We consider different combinations of weight values. Figure 2.14 shows the final image I_{final} obtained with different weights. In figure 2.14(a), for all weights equal, we observe that blood vessels are not clear at all. In figure 2.14(b,d,e,f), large blood vessels are broken in a few spatial locations in the image. As our ultimate goal is to track large blood vessels using a graph-based approach (see Chapter 3), it is beneficial to have a segmented image where vessels are not broken in between. However, it is evident that among all these in figure 2.14(c), the blood vessels are enhanced in all directions while the structures of large blood vessels are mostly preserved. Considering all these, we decide to keep figure 2.14(c) as our final segmented result obtained from the unsupervised vessel segmentation approach.

2.7 Limitations of the classical machine learning approach

Classical machine learning techniques, as discussed above in sections 2.4 and 2.6, require human intervention to manually select the proper features for creating a feature vector. Additionally, these feature selection methods often rely on trial and error, require expert knowledge, and are not well-suited for large-scale fundus retinal vessel segmentation. Moreover, these feature extraction methods are more subjective and may not perform consistently across different images, indicating a lack of robustness. As we have seen, the classical vessel segmentation algorithm discussed above performs well on images of a similar type (see figure 1.2b). However, its effectiveness declines in images in poorly illuminated fundus images, which may result from camera quality, inadequate dilation of the pupil in the eye, or variation in the location and severity of the retinal haemorrhages. In that situation, the current set of features yields unsatisfactory results. To improve segmentation accuracy, it is necessary to identify and incorporate a new set of features. Additionally, the weights assigned to these features within the K-means clustering framework need to be carefully adjusted to enhance performance.

In contrast to these more conventional approaches, deep learning-based vessel segmentation approaches are more robust and require less human intervention for feature selection. To overcome the limitations of the unsupervised segmentation approach and to reduce the requirement of human intervention for designing the feature vector, we build a deep learning-based vessel segmentation algorithm. Deep learning methods excel by automatically learning complex, hierarchical features from images, making them more robust and well-suited for tasks that demand high precision and accuracy. In the next subsection 2.8, we outline the workflow of deep learning-based approaches and highlight several advantages of using deep learning-based techniques. In the following subsection 2.9, we provide a detailed discussion of the U-Net-based retinal vessel segmentation approach.

2.8 Deep learning based approach for retinal vessel segmentation

Deep learning (DL) is a subset of supervised-based machine learning approach that focuses on methods based on neural networks (see subsection 2.8.1). Deep learning methods have recently gained greater attention from the research community due to their performance in segmenting medical images [140, 161]. As mentioned earlier, one of the advantages of deep learning-based methods is that deep learning algorithms can automatically learn complex, hierarchical features from raw pixel data through their layered structures (see subsection 2.8.1), reducing the need for human intervention for manual feature engineering and improving the generalization and accuracy of automatic segmentation methods.

Over the years, several deep learning networks have been utilized in the field of retinal image

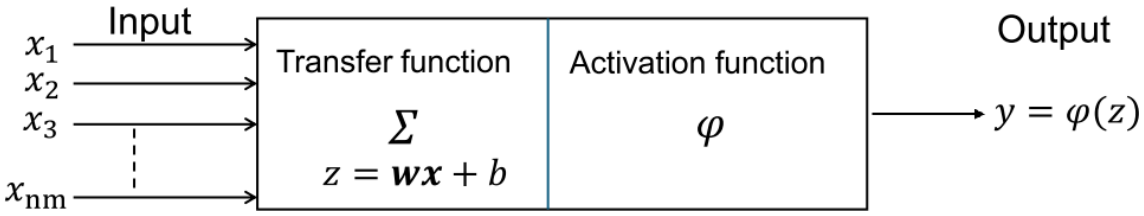

Figure 2.15: Workflow of a single artificial neuron

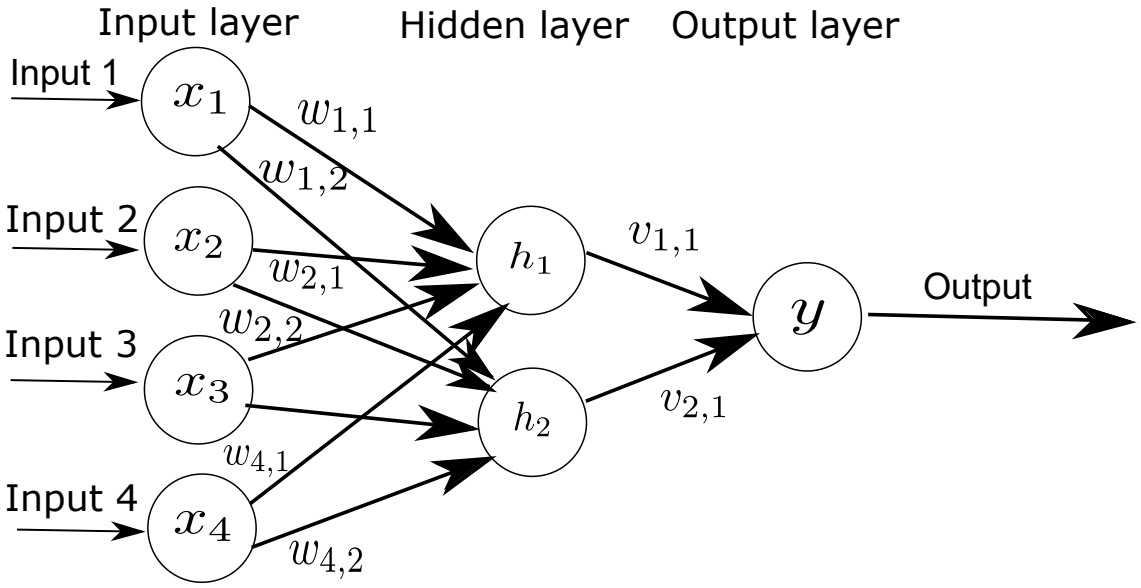

Figure 2.16: Structure of a simple neural network containing only one hidden layer

segmentation. Among all the different types of deep learning networks, the CNNs have drawn greater attention in numerous applications, especially in medical image analysis [154, 160]. To understand the convolutional neural networks, it is important to discuss the basics of neural networks (NNs). In the next subsection 2.8.1, we begin by outlining the fundamental concepts of NN and its workflow. Then, in subsection 2.8.2, we discuss the basic idea of a convolution neural network. Following the success of CNN, there are several variants of CNN have been developed over the years for retinal image segmentation. U-Net, a special type of CNN network architecture, known for its unique structure and high segmentation accuracy, is discussed in subsection 2.9.

2.8.1 Basics of neural network (NN)

Artificial Neural Networks (NNs) are biologically inspired nonlinear computational models designed to mimic the information processing of the human brain using simple computational units called artificial neurons, which are organised into structures known as layers. NN can potentially perform complex calculations, similar to the human brain [63]. NNs can be classified into different types, such as feed-forward neural networks, cascade neural networks, recursive neural networks, recurrent neural networks (RNN), bi-directional NNs, and stochastic NNs [71]. In this work, we specifically concentrate on the concept of the feed-forward NNs.

To understand the workflow of feedforward NNs, it is crucial to recall the basic structure of

the biological neuron. A biological neuron has a cell body, a branching input structure (or the dendrite), and a branching output structure (or the axon) [71]. The axon connects the dendrite via synapses [71]. Electrochemical signals are transferred from the dendritic input, through the cell body, and then reach the axon to other neurons [71]. NN can be thought of as a collection of all single neurons that are interconnected in an acyclic order (i.e., there are no feedback cycles or loops and the information flows strictly forward from input to output nodes without cycles) [71]. A basic artificial neural network consists of three layers of nodes (or artificial neurons): an input layer (also referred to as the first layer or the 0^{th} layer), an intermediate layer (also known as the hidden layer), and an output layer. Similar to a biological neuron, in this framework, the input is passed to the input layer, which distributes it to the hidden layers [71], and the final result is obtained from the output layer. Typically, the input takes the form of a multidimensional vector. The output of one neuron becomes the input of another neuron [71]. This process is known as learning, where the hidden layers make decisions based on the outputs of the previous layer and assess how a random internal change influences or improves the final result [71]. Each of the hidden layers plays a crucial role in extracting and refining features that contribute to the final segmentation result. Each layer connects to the next layer with weights. These weights can be fine-tuned by training the network on data with known outputs (known as training data). The array of collection of all such weights is called the kernel. The detailed discussion on each layer is given in subsection 2.8.2. Figure 2.15 shows a typical example of a simple fully connected neural network with no hidden layer, and figure 2.16 shows an artificial fully connected neural network containing only one hidden layer.

We start with a simple fully connected neural network containing an input layer and an output layer (see figure 2.15). Suppose, the input to the input layer of NN is a grayscale image I of size $n \times m$ (see figure 2.15).I_{ij} $(i = 0, 1, ..., n-1, j = 0, 1, ..., m-1)$ represent the pixel intensity values of the image I in a given pixel location (x_i, y_j). Now, we write all the I_{ij} in a column vector called $\mathbf{x} \in \mathbb{R}^{nm \times 1}$ is given by

$$\mathbf{x} = \begin{pmatrix} I_{0,0} \\ \vdots \\ I_{0,m-1} \\ \vdots \\ I_{1,m-1} \\ \vdots \\ I_{n-1,m-1} \end{pmatrix} = \begin{pmatrix} x_1 \\ x_2 \\ \vdots \\ x_{nm}. \end{pmatrix}$$

The process of converting a $2D$ matrix into a $1D$ vector is called flattening of the image. The input $\mathbf{x}$ is processed in the neuron through weights denoted by $w_i, i = 1, 2..., nm$, producing an output z which is then transformed into the final output y through a function ϕ such that $y = \phi(z)$.

The quantity z can be computed as follows

$$\begin{aligned} z(\mathbf{x}) &= (w_1, w_2, \cdots, w_{nm}) \begin{pmatrix} x_1 \\ x_2 \\ \vdots \\ x_{nm} \end{pmatrix} + b \\ &= \sum_{i=1}^{nm} w_i x_i + b \\ &= \mathbf{w} \cdot \mathbf{x} + b \end{aligned} \tag{2.38}$$

where $\mathbf{w} \in \mathbb{R}^{1 \times nm}$. Here $b \in \mathbb{R}$ is the bias term. Biases arise in the neural networks from various sources, including the image datasets and the training process. The bias term plays a crucial role in enhancing the flexibility of the neural network model by improving its ability to capture non-linear complex relationships in the image data, and boosting model performance and robustness in the image segmentation task. A detailed discussion on biases is outside the scope of this work.

The process of converting nm-inputs into a scalar result $z(\mathbf{x})$ is known as the transfer function [147]. Here, we consider the weighted sum operator as the transfer function. It is essential to note that numerous alternative transfer functions are available, depending on specific needs [147].

The final output y is obtained by applying both the transfer function (linear) z and the activation function (non-linear) $\phi(z)$ on the inputs $x_i, i = 1, 2, ..., n$,

$$\begin{aligned} y &= \phi(\Sigma_{i=1}^{nm} w_i x_i) \\ &= \phi(\mathbf{w} \cdot \mathbf{x} + b). \end{aligned} \tag{2.39}$$

The idea is to generalise the output $z(\mathbf{x})$ for a neural network that contains multiple neurons. The first step is to rewrite (2.39) in a functional form, and then we use this function to generate an output for a neural network containing several neurons. (2.39) can be written in a functional form as

$$y = f_1(x_1, x_2, ..., x_{nm}) = \phi(\mathbf{w^1} \cdot \mathbf{x} + b^1), \tag{2.40}$$

where $\mathbf{w^1}$ is the weight and b^1 is the bias for the single neuron [147]. The function ϕ is known as the activation function. ReLU, sigmoid, or tanh are a few examples of activation functions, which are introduced in more detail in the following subsection 2.8.2. The activation function is responsible for introducing the nonlinearity in the neural network model. The activation function should satisfy certain fundamental properties, such as being differentiable and monotonic, meaning it should maintain the direction of the gradient vector [147].

Now, we extend the idea for the NN with more than one layer. The network with more than one middle layer is called a multilayer perceptron (MLP). When the NN contains fewer hidden layers (typically one), it is referred to as a shallow neural network (see figure 2.16). Having

multiple hidden layers stacked upon each other is commonly called a deep learning network [71]. The generalisation of equation (2.40) for multi-layers is straightforward. As explained before, inputs to a neuron are processed, typically as a weighted linear combination, and the resulting output is passed on as input to neurons in the next layer. This flow of information from one layer to the next is referred to as feed-forward propagation. Mathematically, a multilayer perceptron is a function $F : \mathbb{R}^{nm} \rightarrow \mathbb{R}^{nm}$ and it can be written as

$$F(\mathbf{x}) = \phi(f_L(f_{L-1}(...f_1(\mathbf{x})))), \tag{2.41}$$

where $f_j(\mathbf{x})$ are an affine function of the form $f_j(\mathbf{x}) = \mathbf{w}^j\mathbf{x} + b^j$ [147]. Re-writing this in equation (2.41), we obtain

$$\mathbf{y} = F(\mathbf{x}) = \phi(\mathbf{w}^L...(\mathbf{w}^2(\mathbf{w}^1\mathbf{x} + b^1) + b^2)... + b^L), \mathbf{x} \in \mathbb{R}^{nm\times 1}, \tag{2.42}$$

which applies a nonlinear function ϕ to a composition of n affine functions of the form $\mathbf{w}^j\mathbf{x} + b^j, j = 1, \cdots, L$ [147]. The column vector $\mathbf{y}$ contains scalar values, generally known as class scores. The final layer typically contains as many outputs as there are target classes of the problem. By target classes, we mean a group of pixels that represent a particular structure of the image, namely, in our case, the vessel class, non-vessel class, background class, etc. An output vector from the final fully connected layer is given by $\mathbf{y} = \left[y_1, y_2, ..., y_L\right]$, where each $y_i, i = 0, 1, 2, ..., L$ is the logit corresponding to the L^{th} class.

The output layer most commonly does not have an activation function. Usually, for the vessel segmentation task, the output layer contains a softmax function. The softmax function normalises the class scores to the target class probabilities, where each value ranges between 0 and 1 and all values sum to 1. This final output performs the final classification task. A softmax function is applied to $\mathbf{y}$ to convert these values into probabilities, indicating the likelihood of each pixel belonging to a given class. Mathematically, the softmax function can be written as

$$y_i = \frac{e^{y_i}}{\sum_{j=1}^{L} e^{y_j}}. \tag{2.43}$$

2.8.1.1 Training a convolutional neural network

Since we employ a pre-trained neural network model in this work, we have not implemented any training steps. We restrict ourselves to a brief overview of the training process instead of an in-depth discussion.

Training a NN involves teaching it to learn key features from input ground truth images using corresponding ground truth labels. Suppose we have a training set of k ground truth images at our disposal $(\mathbf{x}_i, \gamma_i)_{i=1}^{k}$, where $\mathbf{x}_i$ is the flattened input image and γ_i is the corresponding ground truth class labels, for instance, class of vessel pixels and class of non-vessel pixels, etc. In other

words, γ_i can be thought of as a response we expect from the MLP F (see equation (2.42)) with $\mathbf{x}$ as input.

The first step before training is to identify an appropriate loss function C, a non-negative real-valued function to quantify the model's performance on new, unseen data. The loss function or cost function quantifies how well the model predictions match the actual labels γ of the input data. The choice of a loss function depends on the specific problem and dataset. For instance, for image classification tasks, the binary cross-entropy loss function is often used. Other options include mean squared error, hinge loss, or focal loss, depending on the nature of the problem. The ultimate goals of the NN are to adjust its parameters to minimise the loss function, enabling it to identify similar features in new, unseen images.

Now we define a risk function R which is the average over the training set and is given by

$$R = \frac{1}{k}\sum_{i=1}^{k} C(F(\mathbf{x}_i), \gamma_i). \tag{2.44}$$

The goal of learning is to find parameters $\mathbf{w}, \mathbf{b}$ such that R is minimal.

Training of NN consists of two phases, namely, the forward phase and the backward phase. During the forward phase, the input image is passed through the network layer by layer (see figure 2.19). Each layer performs the computations, and the result is a scalar loss R. Once the forward phase is completed, the backward phase or backpropagation algorithm begins (see figure 2.19). As mentioned earlier, we want to minimise R by computing the derivative of R with respect to the model parameters, i.e., weights $\mathbf{w}$ and biases $\mathbf{b}$. However, numerically evaluating such derivatives is computationally expensive. Using the backpropagation algorithm, we can determine the derivatives in an efficient way.

The idea is to find the derivatives

$$\frac{\partial R}{\partial w^l_{kj}}, \frac{\partial R}{\partial b^l_j},$$

where w^l_{kj} is the weight (i.e., an entry in the matrix $\mathbf{w}$) connecting the j^{th} entry of the l^{th} layer of neurons to the k^{th} neuron in $(l-1)^{th}$ layer and b^i_j is the corresponding bias. It is important to note that to train the NN model efficiently, we require a sufficiently large image dataset, as neurons are fully connected between different layers, which increases the total number of weights and biases in the system [138]. As a result, a standard fully connected neural network introduces a vast number of parameters to train during the training process.

In the backpropagation algorithm, we want to know how much changing the model's output $\mathbf{z}$ would change the risk function R. The derivative of the risk function R with respect to $\mathbf{z}$ indicates how much we need to change parameters in $\mathbf{z}$ to minimise R. It acts as the error term that gets propagated backwards through the network to update parameters. We denote it by ϵ^l_j,

the error of the j^{th} node in the l^{th} layer, and is given by

$$\begin{aligned}\epsilon_j^l &= \frac{\partial R}{\partial z_j^l} \\ &= \sum_k \frac{\partial R}{\partial z_k^{l+1}} \frac{\partial z_k^{l+1}}{\partial z_j^l}\end{aligned} \tag{2.45}$$

We compute ϵ_j^l iteratively using ϵ_j^{l+1}, so we proceed by computing the error from the last layer L using the chain rule

$$\epsilon_j^L = \sum_k \frac{\partial R}{\partial y_k^L} \frac{\partial y_k^L}{\partial z_j^L} \tag{2.46}$$

and, when $k \neq L$ and $\mathbf{y} = \phi(\mathbf{z})$,

$$\epsilon_j^L = \frac{\partial R}{\partial y_j^L} \frac{\partial y_j^L}{\partial z_j^L} = \frac{\partial R}{\partial y_j^L} \phi'(z_j^L) \tag{2.47}$$

Now, for all other layers, we compute a rule to derive ϵ_j^l from ϵ_j^{l+1}. Now looking into the (2.46), we can rewrite the first term on the right-hand side of the equation as

$$\frac{\partial z_k^{l+1}}{\partial z_j^l} = w_{kj}^{l+1} \phi'(z_j^l). \tag{2.48}$$

The final expression for the ϵ_j^l becomes

$$\epsilon_j^l = \sum_k \epsilon_j^{l+1} w_{kj}^{l+1} \phi'(z_j^l) \tag{2.49}$$

This is called the backpropagation rule. In summary, to compute the derivative of R with respect to the weights and biases, it is sufficient to obtain the error ϵ^l. This can be done using (2.47) for the final layer L and using (2.49) for all other layers.

Now building upon the basic principles of the feed-forward neural network, we discuss a special type of feed-forward neural network commonly known as the convolutional neural network [140].

2.8.2 Introduction to convolutional neural network (CNN)

In the context of medical image segmentation, the convolutional neural network (CNN), influenced by the structure of the human visual cortex, is used widely to interpret data with a grid pattern, such as images [138, 156]. CNN's straightforward yet effective architecture, combined with its strong performance and accuracy in feature extraction, makes it the preferred choice for image segmentation tasks, while also reducing the number of parameters required to train deep

learning models [132, 140, 164].

In subsection 2.8.2.1, we first introduce the basic terminology used in CNN. Subsection 2.8.2.2 discusses the general structure of the CNN. Then subsection 2.8.2.3 highlights the different types of CNN available for medical image segmentation.

2.8.2.1 Terminology used in CNN

The following terminologies are consistently used throughout this section and in the following Chapter 2, where we discuss CNN and related models.

Learnable parameter: The 'learnable parameter' stands for a variable that is automatically learned during the training process.

Hyperparameter: The 'hyperparameter' is a variable that needs to be fixed before the training process begins.

Kernel: A 'kernel' refers to the collection of learnable parameters (called weights here) applied for convolution operations. We often use 'weight' and 'parameter' interchangeably in general. However, we use 'weight' to refer to 'parameter' outside of convolutional layers (see subsection 2.8.2.2), for example, the parameters in fully connected layers (see subsection 2.8.2.2).

Stride: Stride is a parameter that dictates the movement of the kernel, or filter, across the input image. When performing a convolution operation or a pooling operation (see subsection 2.8.2.2), the stride determines how many units the filter or the kernel shifts at each step. This shift of the kernel can be horizontal, vertical, or both, depending on the configuration of the stride.

Zero padding: Zero padding is a technique where rows and columns of zeros are added on each side of the input image to fit the center of a kernel on the outermost element of the input image and keep the dimension of the input image the same throughout the convolution operation. Without zero padding, each successive feature map would get smaller after the convolution operation, and eventually, we would lose spatial information on each subsequent operation.

Overfitting: Overfitting occurs when the error margin between the model's output and the training dataset is below a set threshold value (depends on the specific task), making it unable to generalise well to new, unseen images outside the training dataset [124].

2.8.2.2 Building blocks of CNN architecture

A CNN has three main building blocks, namely, convolutional layers, pooling layers, and fully-connected layers. The first two layers are used for feature extraction, and the fully connected layer is used to make predictions based on extracted features from previous layers. It is important to note that there are various CNN architectures available that have been proposed over the years for solving different image segmentation tasks. The general computational blocks are the same in all of these architectures. However, depending on the task, the number of intermediate layers may vary. For instance, LeNet-5 [18] and AlexNet [78] share very similar general building blocks;

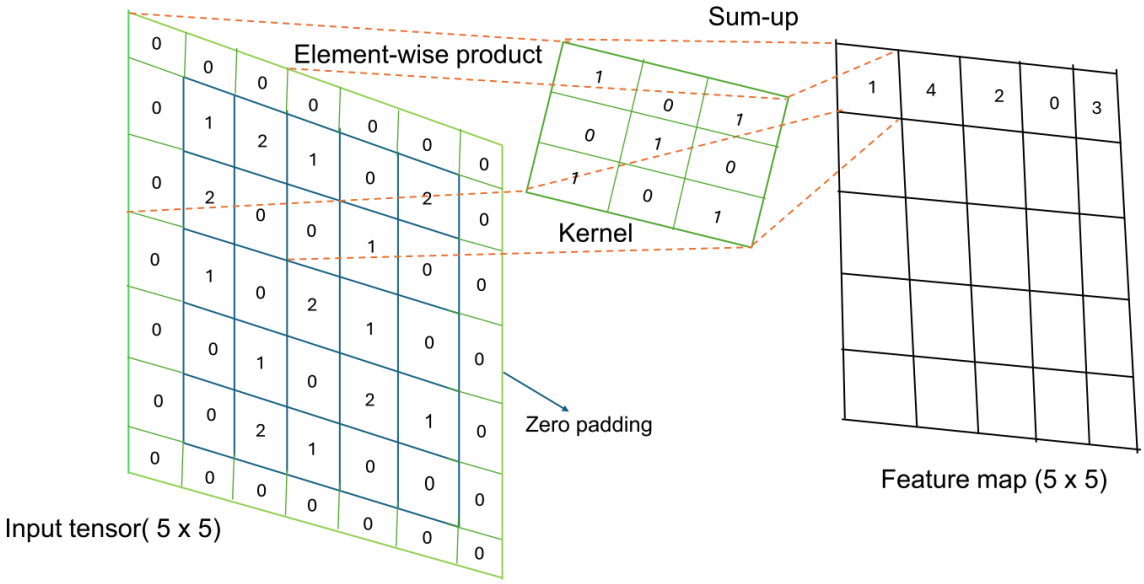

Figure 2.17: A convolution operation with zero padding to retain in-plane dimensions. Note that an input dimension of 5×5 is kept in the output feature map. In this example, a kernel size of 3×3 and a stride of 1 are set.

however, AlexNet incorporates a greater number of hidden layers compared to LeNet-5. Now, we will explain each building block of the CNNs. Unlike the classical vessel segmentation approach, CNNs do not require separating the three colour channels from the RGB image; instead, the original RGB image can be used directly as input image I (see figure 1.2b). Figure 2.17 shows a typical structure of a CNN and its training process [126].

Convolutional layers: The convolutional layers serve as the primary building blocks of the CNN and are the first few layers in the CNN through which the image data is processed (see figure 2.17). The convolution layer consists of a combination of linear and nonlinear operations, i.e., a convolution operation and an activation function (e.g., ReLU function, see discussion below on activation function). In a convolutional layer, CNN employs a convolution in at least one of its layers to extract different features from the input image.

Figure 2.17 shows the schematic representation of the convolution operation on an input tensor (single colour channel) of size 5×5 by a kernel K of size 2×2 and produces a feature of size 5×5. The output image obtained from the convolution operation is called a 'feature map' (see figure 2.17). The detailed discussion on the convolution operation is given in subsection 2.4.2 of Chapter 2. The input image for the convolution operation discussed in subsection 2.4.2 is a single colour channel image. However, in this case for CNN , the input image is an RGB colour image of dimension $n \times m \times 3$, where n is the number of rows, m is the number of columns, and 3 represents the number of colour channels in I. Similarly, the kernel K is of dimension $f \times f \times 3$, where f is the spatial dimension of the filter. The given pixel (x_i, y_j) of the kernel K contains a vector of three weights for each channel. The convolution operations are carried out in the same way as for the single colour channel images (see figure 2.17 and subsection 2.4.2 of Chapter 2). When a filter K is applied to an RGB image, it convolves across all three channels.

The convolution operation is performed across all three channels using three different kernels and computes a weighted sum of the pixel values in each channel. Mathematically, for a filter K and an input image I:

$$S_{i,j,3} = S(x_i, y_j, 3) = [I * K](x_i, y_j) = \sum_{a=0}^{n-1} \sum_{b=0}^{m-1} \sum_{c=1}^{c=3} K(a,b,c) I(x_i - a, y_j - b, c), \tag{2.50}$$

where '*' is the discrete convolution operation, c denotes the color channel, and (x_i, y_j) represents the spatial location in the output feature map. After the convolution operation, each filter produces a single feature map S. This convolution procedure is repeated by using different kernels to construct an arbitrary number of feature maps, which represent different features of the image. Each of these kernels is responsible for extracting a particular feature from the input tensor. To extract that particular feature, the same kernel is used in all spatial locations of the image. This is called weight sharing. The advantage of weight sharing is that it reduces the model's complexity by reducing the number of parameters, making the model training process easier.

Additionally, kernels establish local connectivity with a small portion of the input image, referred to as the receptive field (RF) (see figure 2.19). The RF represents the size of the input region that contributes to the generation of a particular feature. The size of RF is defined by the size of the kernel. This is particularly useful for identifying regional changes in the image, for example, edges, and also reduces the number of parameters compared to traditional NN discussed in subsection 2.8.1. Moreover, the two key hyperparameters, the size and number of kernels, describe the convolution operations.

Non-linear activation function: After the convolution operation, the output S is passed through a nonlinear activation function (see figure 2.17). The concept of activation function is motivated by the biological neuron. Non-linearities are essential for neural network design to detect the nonlinear features (i.e., pathological regions like haemorrhage, curvatures, vessel crossings, vessel boundaries) and to improve the training speed of the CNN. The Rectified Linear Unit (ReLU) is one of the most widely used activation functions and has been found to train CNNs effectively [67]. Mathematically, ReLU is defined as

$$\phi_{i,j,3} = \phi(x_i, y_j, 3) = max(S_{i,j,3}, 0) \tag{2.51}$$

where $S_{i,j,3}$ given in equation (2.51) is the input to the ReLU, and $\phi_{i,j,3}$ is the output. The ReLU activation function is applied independently to each element of the feature map. The ReLU function keeps the positive part of the input and sets the negative part to zero. There are other types of activation functions available, namely leaky ReLU (or LReLU), Exponential Linear Unit (or ELU), and the Sigmoid function.

Pooling layers: The pooling layer is generally placed after the convolution layer, and a CNN

structure can contain more than one pooling layer (see figure 2.19). Similar to the convolutional layer, the pooling layer also applies filters to the input image, but filters are not weights; instead, an aggregation function. The aggregation function can be a maximum, summation, mean, or average function. The most popular pooling operation is the maximum pooling function.

The pooling layer takes the feature map ϕ from the last layer as its input, and the purpose of the pooling layer is to reduce the spatial dimensions (width and height of the feature map) of the input feature maps while retaining the most important information. This process is known as down-sampling of the feature map. Eventually, it reduces the number of learnable parameters and the computational burden during the training process. Moreover, the pooling layer introduces translation invariance to small shifts and distortions in the feature map. However, the depth dimension of feature maps remains unchanged in this layer.

The pooling operation involves sliding a $2D$ filter (of size $f \times f$) over each channel of the feature map ϕ and combining the features lying within the region covered by the filter. Figure 2.18 illustrates the maximum pooling operation on an image of size 4×4 by a 2×2 filter with a stride size 2. It extracts patches from the input feature maps, outputs the maximum pixel intensity value in each patch, and discards all the other values (see figure 2.18). Mathematically, max pooling can be written as

$$s_{i,j,3} = \max_{n,m} \phi(x_i * v_x + n, y_j * v_y + m, 3), \tag{2.52}$$

where s is the output of the max pooling function, v_x and v_y are the stride values of the $2D$ max pooling filter in the horizontal and vertical directions, respectively, and the pooling window is defined by the filter size $f \times f$ and centered at the output index (x_i, y_j). It is important to note that there is no learnable parameter in any of the pooling layers, whereas filter size, stride, and padding are hyperparameters in pooling operations.

For input feature map $\phi_{i,j,3}$ having dimensions $n \times m \times 3$, the dimensions of output $s_{i,j,3}$ obtained after a pooling layer is given by $((n-f+1)/s') \times ((m-f+1)/s') \times 3$ where s' is the size of the stride which is usually 1 or 2 and these dimensions are always integers. The stride size of 1 is common when it is important to maintain a high resolution of features, which is particularly important in the initial layers of the CNN. In figure 2.18, the stride size is 2.

Fully connected layers (FC): Once the features have been extracted by the convolutional layers and down-sampled by the pooling layers, they are passed to one or more fully connected layers. Each neuron in the fully connected layer receives its inputs from all the neurons in the previous layer and produces an output by applying a set of weights and biases, followed by an activation function. The final output obtained after applying the activation function is a probability that classifies pixels to obtain the final segmented image.

The workflow in fully connected layers is similar to the one discussed for a fully connected neural network in subsection 2.8.1. As explained in subsection 2.8.1, features s obtained from the last layer are converted to a $1D$ vector $\mathbf{x}$. By connecting every neuron to every other neuron

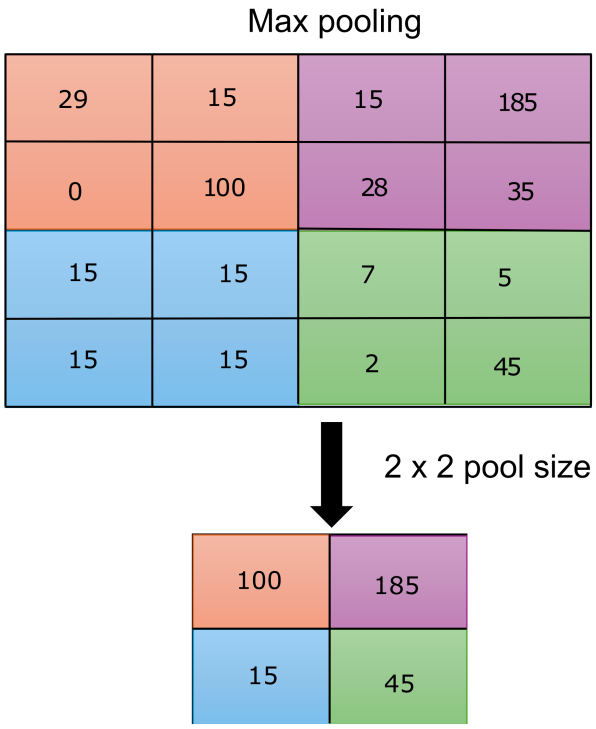

Figure 2.18: Illustration of Max Pooling with a 2×2 pixel filter size from 4×4 pixel input. At max pooling, each filter takes the maximum value, then is arranged into a new output with a size of 2×2 pixels.

in the fully connected layer, the fully connected layer serves as a powerful tool for learning relationships and dependencies in image pixels, converting the learned features into a format suitable for classification tasks.

Though the large number of parameters in CNN models allows the network to learn complex representations, this also increases the risk of overfitting of data. To effectively overcome the overfitting problem, regularization techniques are employed. The fully connected (FC) layer of CNN plays a key role in model regularization. Most commonly used regularization techniques are dropout [77], L1 regularisation, and L2 regularisation [124] are often applied after the final FC layers. The detailed discussion on regularisation is given in the subsection 2.9 of Chapter 2.

2.8.2.3 Different types of CNN

There are different DL networks available for the image segmentation task. In this work, we restrict ourselves to the CNN models that are specially designed to study medical images. DL is used in various fields of medicine, including the classification and identification of various diseases. In 2012, AlexNet, the first modern deep CNN, developed by Krizhevsky et al., won the ImageNet competition, marking a pivotal moment for the rapid advancement of neural networks [78]. AlexNet showed that deep convolutional neural networks (CNNs) can reach remarkable accuracy in image classification tasks [78]. Following the success of AlexNet in the 2012 ImageNet competition, other architectures such as VGGNet [97], GoogleNet [107], and ResNet

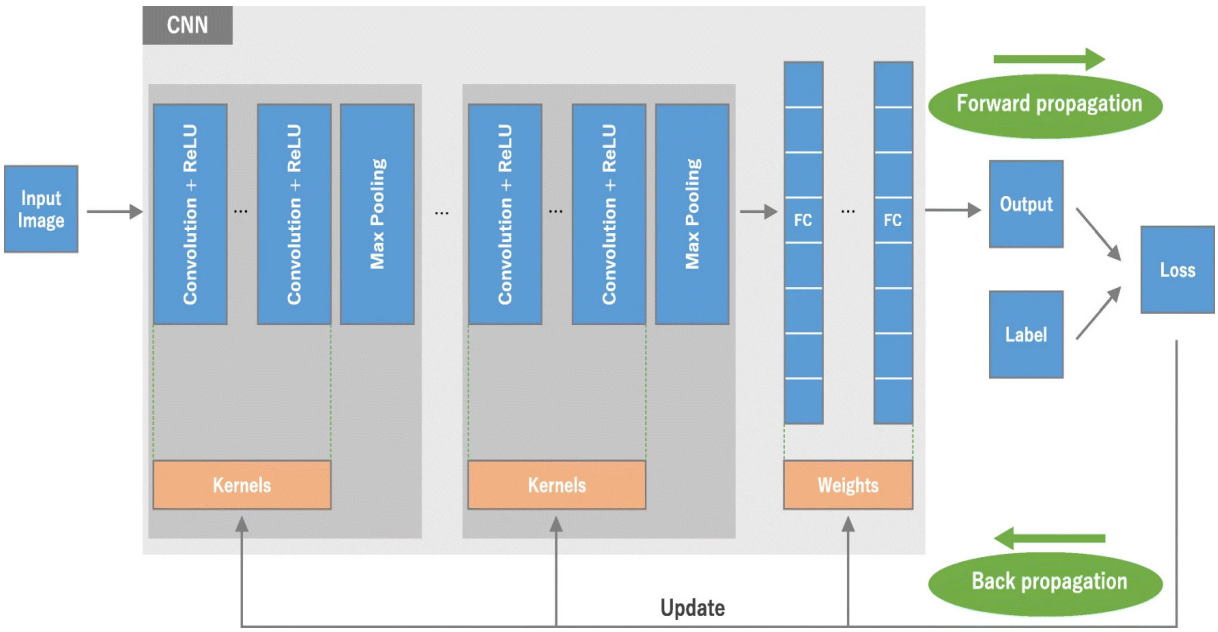

Figure 2.19: Typical structure convolutional neural network (CNN) architecture and the training process [126]

[113] gained significant attention, further enhancing the advancement of DL algorithms. In VGGNet, Simonyan and Zisserman et. al. explained that increasing network depth,i.e., number of channels using small 3×3 convolution kernels, can improve image segmentation performance significantly [97]. Following the success of VGGNet and GoogleNet, He et al. introduced the ResNet architecture, which addressed the vanishing gradient problem in deep networks through the use of skip connections [113]. The vanishing gradient problem occurs during the backpropagation process in the training of deep neural networks (see the subsection 2.8.1.1) when the gradients (partial derivatives of the loss with respect to the weights) become extremely small (close to zero) as they are propagated backwards in the network. As a result, weights in the early layers learn very slowly or may even stop updating altogether. To overcome this problem, skip connections are used, which we discuss in detail in subsection 2.9. This concept transformed CNN design by enabling the efficient training of models with depths of up to 1000 layers [113]. Following this trend, in 2015, Long et al. introduced the Fully Convolutional Network (FCN), which replaced fully connected layers with deconvolution (or transposed convolution) layers [101]. The deconvolution layer performs the reverse operation of the regular convolution operation. Instead of reducing the spatial dimensions of the final feature map (as in traditional convolutions), a deconvolution layer increases the spatial dimensions (height and width). This architecture enabled the upsampling of the final convolutional feature maps, allowing for dense, pixel-wise predictions [101]. In 2015, inspired by FCN, Ronneberger et al. introduced U-Net, a U-shaped architecture built upon the fully convolutional network, featuring skip connections that bridge corresponding layers in the encoder and decoder [105]. Due to its high segmentation accuracy and strong performance, U-Net has inspired numerous variants over time, representing a major advancement in the task of retinal vessel segmentation. [105]. In this work, the lack of

hand-labelled ground truth images, where vascular structures are manually annotated by experts, poses a challenge initially for applying supervised methods to retinal vessel segmentation. As a result, we begin by employing unsupervised learning approaches to better analyze and process the fundus images. In this approach, we first identify various features of interests from the input image which contains useful information about each pixel of the input image and then apply an unsupervised weighted K-means clustering (see subsection 2.6) approach to each of these four features to decide if a given pixel is part of a vessel (or not). For a detailed discussion of unsupervised techniques used for retinal images, please refer to the subsection 2.4.

2.9 U-Net-based retinal vessel segmentation approach

To train a fully connected neural network, it requires a large number of images. However, in medical image segmentation, thousands of training images are beyond reach. It is important to note that there are open-source repositories (for e.g DRIVE, STARE, ARIA, REVIEW, CHASEDB1, FIVES) for retinal vessel segmentation, available for studying retinal vasculature [148]. To the best of our knowledge, most open-source repositories are primarily derived from patients with diabetic retinopathy (DRIVE, ARIA, REVIEW, FIVES), age-related macular degeneration (ARIA, FIVES), or glaucoma (FIVES). However, in this thesis, the primary focus is on retinal haemorrhage following RVO to understand the spatial scale separation between the site of occlusion and the site of haemorrhage (upstream to the point of occlusion). Therefore, open source repositories are not sufficient to test our research hypothesis. As a result, we rely on real patient images obtained from a clinical collaborator with visible retinal haemorrhage following RVO.

U-Net is a CNN architecture that is particularly useful when a large training dataset is not readily available, as in our case. In addition to the typical strengths of deep learning models described in subsection 2.7 U-Net architecture leverages an encoder-decoder structure (for detailed discussion see subsection 2.9.1) along with skip connections (for detailed discussion see subsection 2.9.1) to capture both broad contextual information and precise spatial details required to map complex retinal vascular networks, leading to high accuracy for pixel-level classification (e.g., separating vessels from background) and provides a high degree of ground truth similarity [135]. As a result, U-Net is better suited for our retinal image segmentation task due to its high accuracy, which provides better measurement for geometrical attributes extracted in Chapter 3.

The number of images required to train a U-Net model varies significantly based on the complexity of the segmentation task. To train a U-Net model for the retinal vessel segmentation task, a minimum of 32 images (see [152]) to 150 images (see [117]) are required. At present, we lack access to a sufficient number of images, and the available ones are inconsistent in terms of patient age, gender, ethnicity, clinical conditions, medications and the type of fundus camera used to capture them. Moreover, we do not have access to ground truth images annotated by clinicians, which is necessary to train a U-Net model effectively. In future, we aim to establish a formal

database of retinal images that takes all these factors into account, accompanied by ground truth images. Due to the limited availability of consistent training image data, a pre-trained U-Net model is utilised.

The pre-trained U-Net model is developed by Arkaniva Sarkar [152], with necessary modifications made to suit our segmentation task. This model is trained and tested on images from HRF, DRIVE and STARE datasets [152]. Pre-training on retinal images makes it adept at recognising the specific features required for our study. The training dataset is split into 70 : 30 ratio for training and validation [152]. The training process is already explained briefly in subsection 2.8.1.1. In the training process, IoU (Intersection over Union) loss is used as the loss function [152]. IoU, also known as the Jaccard index, is the most commonly used metric for comparing the similarity between two arbitrary shapes [133]. For two finite sample sets A and B, their IoU is defined as the intersection $(A \cap B)$ divided by the union $(A \cup B)$ of A and B [133]. The IoU loss is defined as $L_{IoU} = 1 - IoU$ [133]. As IoU satisfies $0 \leq IoU \leq 1$, then the L_{IoU} is also bounded between 0 and 1 [133]. The testing dataset contains 10 images from the DRIVE and STARE datasets and 12 images from the HRF dataset [152]. HRF contains 15 images of healthy patients, 15 images of patients with diabetic retinopathy and 15 images of glaucomatous patients [82]. The DRIVE ((Digital Retinal Images for Vessel Extraction) database were obtained from a diabetic retinopathy screening program in the Netherlands [38]. DRIVE consists of a total of 40 colour fundus photographs [38]. The screening population consisted of 453 subjects between 31 to 86 years of age [38]. Of the 40 photographs, 33 show no signs of diabetic retinopathy, and 7 contain pathology, namely exudates, haemorrhages, and retinal pigment epithelium changes [38]. The STARE (Structured Analysis of the Retina) dataset contains 20 colour fundus images [34]. Of the 20 images, ten images show signs of different diseases that distort or obscure the blood vessel appearance [34].

In the following subsection 2.9.1, we briefly outline the building blocks of the U-Net model. Subsection 2.9.2 focuses on the unique characteristics of the attention U-Net model. Finally, subsection 2.9.3 presents segmentation maps of various types of fundus images provided by the clinical collaborators using the U-Net model.

2.9.1 Basic structure of U-Net

Figure 2.20 shows the U-Net architecture proposed by [105]. The structure of the U-Net looks like the English letter 'U', from where the name comes. The U-Net architecture can be divided into two components: a contracting path, also known as the encoder path (left side of figure 2.20), and an expanding path, also referred to as the decoder path (right side of figure 2.20). We explain here the working process of the U-Net step by step as given in figure 2.20, considering an example image of size 572×572. This is exactly what we follow to process all our images.

Contracting Path: The contracting path has a similar architecture to the CNN (see subsection 2.8.2.2 of Chapter 1). It contains a total of 5 blocks [105]. We start by explaining each block

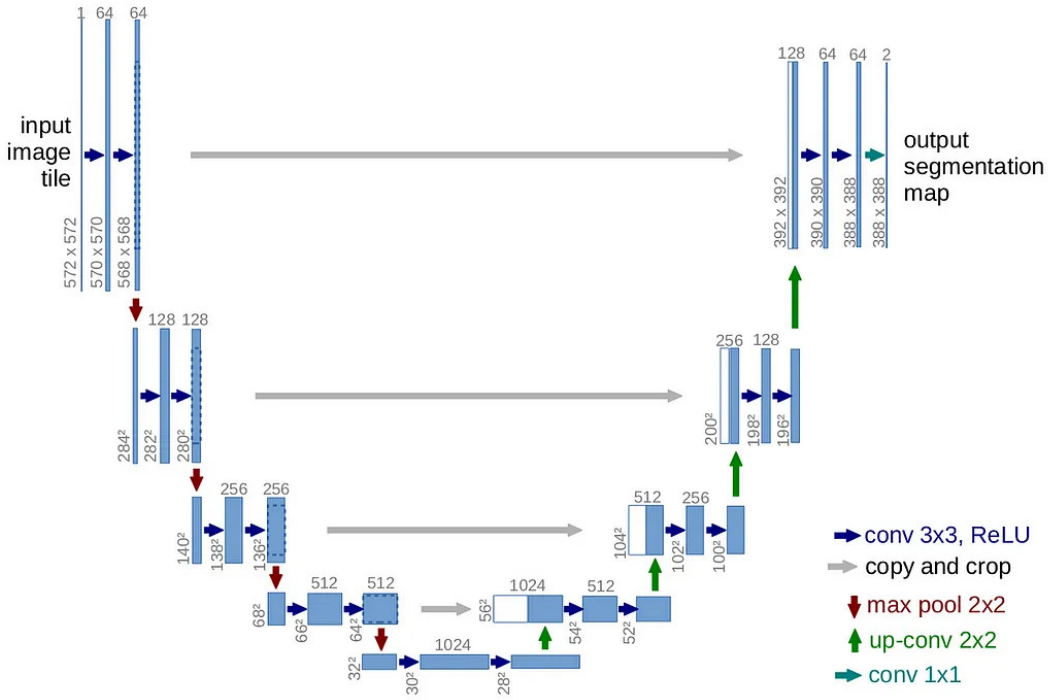

Figure 2.20: Structure of U-Net where the long grey arrows represent the skip connections between contracting and expanding path, the blue boxes represent the feature map at each layer of the network, and the small white boxes represent the cropped feature maps from the contracting path. This structure of U-Net was first proposed by [105].

and its purpose. In Block 1, suppose we start with a green channel image as the input image of dimensions 572×572 (see figure 2.20). In the next phase, the input image is passed to the convolution layers. Each convolution layer performs a convolution operation (unpadded convolution, i.e., no layer of pixels of intensity 0 added outside the image) on the input image using a filter of size 3×3 [105]. At this stage, the input image is convolved with 64 different filters to extract 64 different features of the input image [105]. These features include edges, pixel intensity information, etc. In the original U-Net architecture developed by Ronneberger et al., the contracting path has 64 filters at this stage [105]. However, some other U-Net variants modify the number of filters. These 64 feature maps (or matrices) are stacked together along the depth dimension of the output feature map, and each of them is called a channel of the output feature map. In this case, the total number of channels now becomes 64. Each convolution operation is followed by a non-linear rectified linear unit activation function (ReLU). The ReLU is one of the most widely used activation functions, which takes the feature map as its input and keeps the positive part of the input and sets the negative part to zero. The detailed discussion on the ReLU activation function is given in subsection 2.8.2.2 (see (2.51) of Chapter 1). A 2×2 max pooling operation with a stride of size 2 is then applied on the feature maps (for detailed discussion on max pooling operation see Subsection 2.8.2.2 of Chapter 1). This reduces (or downsamples) the size of the feature maps to 284×284 (see figure 2.20). Down-sampling reduces the spatial resolution (height and width) of feature maps.

In blocks 2,3, and 4, we repeat the same sequence of operations as in block 1. With each subsequent block, the number of filters is doubled, which increases the number of feature maps and the number of channels. In the final block of the contracting path, the number of feature channels reaches 1024 ($64\times2\times2\times2\times2$) after being doubled at each block. Once all complex features and patterns have been extracted from the input image, the final feature maps obtained from the contracting path are passed to the expanding path.

Expanding Path: The novelty of the U-Net lies in the extracting path, where at each step the feature map is up-sampled using the up-convolution operation [105]. In Block 5, continuing from the contracting path, a second 3×3 convolution (unpadded) is applied, followed by applying the ReLU activation function. Then in Block 4, a 2×2 convolution (up-convolution) layer is applied on the feature map for up-sampling the spatial dimensions of the feature maps. In the next stage, the feature map from the corresponding layer in the contracting path is cropped and concatenated onto the up-sampled feature map in the expanding path using a skip connection, doubling the channel numbers of the resultant feature map to 1024. The cropping on the feature map is performed to match the loss of border pixels of the feature map in every convolution operation (the working principle of the convolution operation is given in subsection 2.8.2.2 of Chapter 2). This is followed by two successive 3×3 convolution operations followed by a ReLU activation, reducing the channel numbers to 512. After that, again a 2×2 convolution (up-convolution) operation is applied on the feature map to up-sample the spatial dimension of the feature map. In the next two blocks, i.e., block 3 and block 2, we repeat the same process as discussed above. In the final Block 1, an additional 1×1 convolution operation followed by a Sigmoid activation function is applied on the feature map obtained from Block 2. The Sigmoid function is a mathematical function which is commonly used in a segmentation task like this, where the aim is to classify each pixel as a vessel pixel or a non-vessel pixel (see the discussion Sigmoid function in subsection 2.8.2.2 of Chapter 2). Mathematically, the Sigmoid function can be written as

$$\sigma_u = \frac{1}{1+e^{-u}} \tag{2.53}$$

where u is the input pixel value and e is Euler's number ($e \approx 2.718$). The output of the Sigmoid function lies between 0 and 1, which indicates the likelihood of belonging of u to a target class (e.g., vessel class or non-vessel class). This produces a probability measure for each pixel of the feature map for performing the final vessel/non-vessel pixel classification (i.e., binary classification), similar to the process explained in the case of CNN (see subsection 2.8.2.2 of Chapter 2). Moreover, this reduces the spatial dimensions of the feature map by reducing the number of channels of the feature map. In our case, the required number of channels for the final feature map is 2, i.e., one for vessel pixels and the other for non-vessel pixels. At the end of the process, we obtain the final segmented image as the final output of the U-Net model. We have seen before that in the U-Net architecture, unpadded convolution is used, resulting in an output image size that is smaller than the input image size. The missing pixels in the border of the final feature

map are extrapolated from the input image. This overlap strategy for pixels is important for large images; otherwise, the resolution of the final output images would be limited.

There are many variants of the U-Net available based on the task. In the following subsection 2.9.2, we focus on one of those variants called Attention U-Net.

2.9.2 Introduction to attention U-Net

Despite having many advantages of the U-Net, this architecture relies on multi-stage cascaded CNNs. In this cascaded framework, multiple processing blocks are arranged sequentially to extract a region of interest (ROI) by repeatedly refining the prediction. Feature maps are passed through all these processing blocks for both low and high-level feature extractions. As a result, computational resources and model parameters (for example, biases, weights of the kernels used in convolution) are used excessively and redundantly; for instance, similar low-level features are extracted repeatedly within the network cascade. However, attention gate (AG) focuses on target-specific structures without further increasing computational overhead and does not introduce a large number of learnable model parameters. In this work, we focus on specific objects like blood vessels while ignoring unnecessary areas, e.g., haemorrhage, optic disc (see figure 2.1a). Incorporating an AG unit in the traditional U-Net structure, known as the attention U-net, achieves this type of object-specific segmentation.

An AG is a unit that filters features that are not relevant to the current segmentation task, e.g., the haemorrhage area present in our images (see figure 2.1a). The overall structure of the attention U-net model is very similar to the general U-net model discussed in the last subsection 2.9.1. However, in the attention U-net model, the AG unit is attached to the skip connections of the decoding path, through which the corresponding features from the contracting path must pass. Adding the AG after each layer significantly improves segmentation performance. First, we explain the use of the attention gate unit for a simple segmentation task and its workflow. Then we extend the idea of attention gate for the segmentation task having multiple classes, for example, blood vessels vs background, bifurcation of branches, etc.

Suppose we start with a U-Net model having multiple layers cascaded into it. Suppose the feature maps produced by the encoder block of the U-Net (i.e., the left-hand side of the U-Net shown in figure 2.20) for the layer L are $X^L \in \mathbb{R}^{F_L \times n \times m \times c}$, where F_L corresponds to the number of feature maps in layer L and X^L is a matrix of size $n \times m$ containing c channels. Suppose each pixel value of each channel for a given spatial location (i, j) of X^L is contained in a pixel vector $X^L_{ij,c} \in \mathbb{R}^{F_L}$ where $i = 1, 2, .., n, j = 1, 2, .., m$ denotes the spatial location of the corresponding pixel. $X^L_{ij,c}$ is then the input to the attention gate. The attention gate usually contains a coefficient called the attention coefficient, denoted by $\alpha_{ij} \in [0, 1]$, which identifies the key spatial locations in the feature map X^L specific to the task and filters out unnecessary regions to preserve only the responses relevant to the specific task. The output of AG is the element-wise multiplication

of $X^L_{ij,c}$ and attention coefficients α_{ij}. Mathematically, the output of AG can be written as

$$\hat{X}^L_{ij,c} = X^L_{ij,c}\alpha_{ij}. \tag{2.54}$$

A single scalar attention value is computed for each pixel vector $X^L_{ij,c}$ for all channels. If a region of the feature map has α_{ij} close to 1, then the region is of higher importance compared to the region having α_{ij} value near 0, which gets relatively lower importance. In the case of a multiple-class segmentation task, we generally use multidimensional attention coefficients. Each AG coefficient has a specific task to enhance salient features passed through the skip connection during the segmentation process. We now explain the workflow of getting a multi-dimensional additive attention coefficient.

Suppose the feature map of the decoder block for the layer L is $D^L \in \mathbb{R}^{F_g \times n_1 \times m_1 \times c_1}$ and the gating vector is $g_{ij} = D^L$. D^L is a matrix of size $n_1 \times m_1$ containing c_1 channels and F_g corresponds to the number of gating vectors in layer L of the decoder. Usually, the feature map extracted at a coarse scale of the decoder is chosen as a gating vector g_{ij}, as in this stage, feature maps are still low-resolution and contain global context. g_{ij} is used to determine focus regions by trimming lower-level noisy, unnecessary feature responses for each pixel at location (i, j) of the feature map. To obtain an additive attention coefficient, both $X^L_{ij,c}$ and g_{ij} are passed through two different convolution layers $W_X \in F_L \times F_{int}$ and $W_g \in F_g \times F_{int}$ to perform channel-wise convolution and each of these two convolution layers employs a kernel of size $1 \times 1 \times 1$. Then, the two outputs are concatenated and passed through the ReLU activation function. F_{int} is the intermediate space where the concatenated features $X^L_{ij,c}$ and g_{ij} are linearly mapped. Now the output of the ReLU is again passed through another $1 \times 1 \times 1$ convolution followed by a Sigmoid activation function to get an output map containing only one channel (but the spatial dimensions are preserved), where each spatial location of the feature map has a score between 0 and 1 indicating how much importance to be given to a particular region of the image. Mathematically, the additive attention coefficient can be written as

$$f^L_m = \Psi(\phi(W_X X^L_{ij} + W_g g_{ij} + b_g)) + b_\psi, \tag{2.55}$$

where $W_X \in \mathbb{R}^{F_L \times F_{int}}$, $W_g \in \mathbb{R}^{F_g \times F_{int}}$ and $\Psi \in \mathbb{R}^{F_{int} \times 1}$ are two linear transformations and $b_g \in \mathbb{R}^{F_{int}}$ and $b_\psi \in \mathbb{R}$ are two bias terms. Finally, the input $X^L_{ij,c}$ is multiplied by the attention coefficient f^L_m, producing the final output of the attention block

$$\alpha_{ij} = \sigma_1(f^L_m(X^L_{ij}, g_{ij}; \gamma_m)), \tag{2.56}$$

where $\sigma_1(X_{ij,c}) = (1 + \exp(-X_{ij,c}))^{-1}$ is the sigmoid activation function (see discussion in 2.9.1). Note that, γ_m contains W_X,W_g,ψ, bias terms b_g and b_ψ.

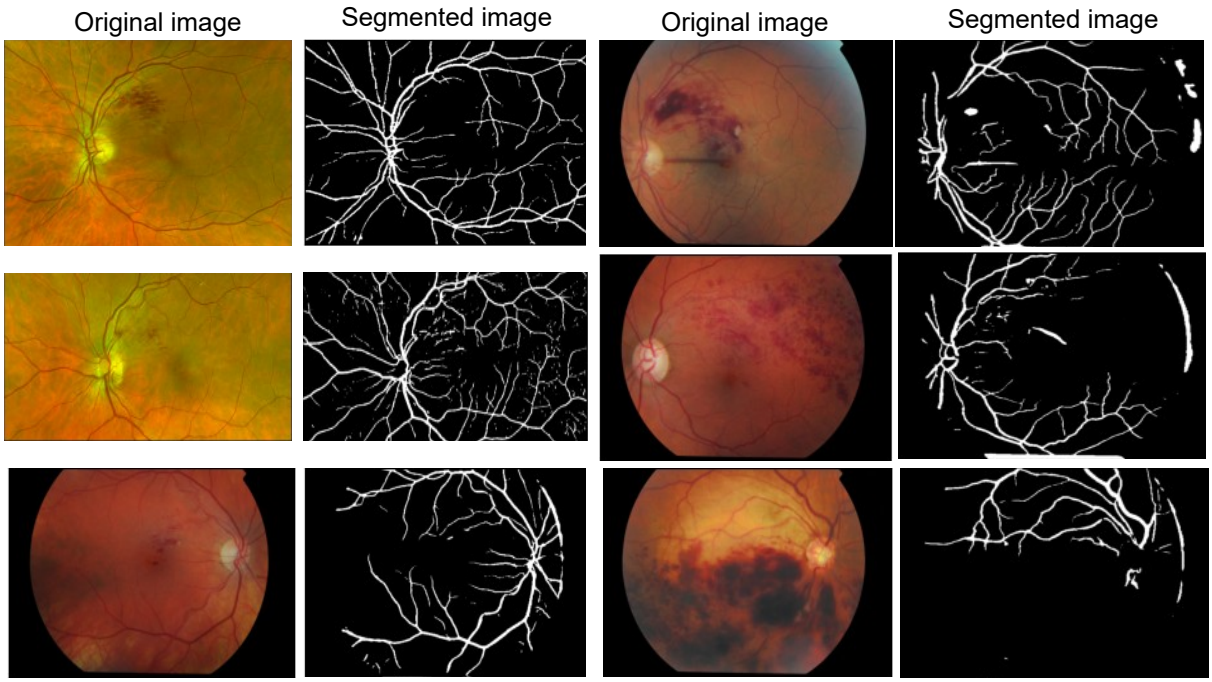

Figure 2.21: Segmented image obtained using attention U-Net model

2.9.3 Segmentation results obtained using attention U-net model

Figure 2.21 shows the original images obtained from the clinical collaborator and the corresponding segmented images using the proposed attention U-Net model. Several example images are considered in figure 2.21, where the U-Net model has performed well despite significant variations in the type and location of pathological regions. This strong performance is because features are not hand-crafted and are rather learned hierarchically from raw images through different convolution filters. However, in a classical machine learning based approach, we use different handcrafted features and threshold values, which are mainly based on the pixel intensity values (for e.g., figure 2.14). However, those features and threshold values might not always be appropriate for all types of fundus images containing different pathological regions, and manual adjustment is often necessary.

As discussed earlier in subsection 2.3.1, we have shown that if the image contains anything other than the region of interest (e.g., eyelashes), cropping the unnecessary element from images is important before applying a classical machine learning based segmentation approach. However, in the U-net-based approach, any prior cropping or resizing of images is not needed before segmentation (see figure 2.21).

2.10 An evaluation of performance measures for the vessel segmentation algorithm

In subsection 2.6, we obtain the final segmented image using the weighted feature fusion using the K-means algorithm. Then, from subsection 2.9.3, we use the U-Net-based deep learning approach to segment the fundus images. Figure 2.22 shows the segmented image obtained from the two different approaches to the same argued image. The performance assessment of a given segmentation result can be done by either doing a qualitative or a quantitative analysis. The qualitative analysis is performed visually, which is more susceptible to human error and also time-consuming [129]. In the quantitative analysis approach, the final segmented image is compared to a ground truth reference image via a computed numerical measure. The reference ground truth image is a manually segmented image where the segmentation is performed manually by us (figure 2.22b). The dice similarity coefficient is commonly used to evaluate the performance of image segmentation by comparing the segmented image with the ground truth image [139]. There are other performance measures for vessel segmentation available, such as average Hausdorff distance [139], Jaccard index [139], etc. However, in this chapter, we only consider the dice coefficient. The dice coefficient compares the segmented image and its corresponding ground truth image pixel by pixel. This is called the overlap-based measures, where the coefficient is measured based on the overlap of the corresponding pixel values between two images. For pixel-to-pixel comparison, it is always easier to use binary images. For dice score measurement, since both the segmented images are already binary images so we convert the ground truth image (figure 2.22b) into a binary image where pixel values are either 0 or 1. The formula for the dice similarity coefficient is given by

$$DICE(X,Y) = 2 \times \frac{|X \cap Y|}{|X| + |Y|} \tag{2.57}$$

where X is the set of pixels obtained from the segmented image and Y is the set of pixels obtained from the ground truth image. There is no well-defined or fixed range specified for the DICE score in retinal vessel segmentation. Generally, the higher the value of the dice coefficient, the better the agreement between the segmented image and the ground truth image and therefore better segmentation performance. Evaluation is primarily done on DRIVE, STARE, and CHASEDB1 datasets. The DICE score for the DRIVE dataset is 0.8692, for the STAR dataset is 0.8847 and for the CHASEDB1 is 0.8799 [166]. It is important to note that the dice score reflects only the overlap accuracy between the segmented image and the ground truth image, not all aspects of accuracy.

The author manually segmented the image shown in figure 2.22(b) to obtain a ground truth image. For the segmented image obtained from the classical unsupervised approach given in figure 2.22(c), we have the dice score of ≈ 0.750. Similarly, the dice score for the segmented

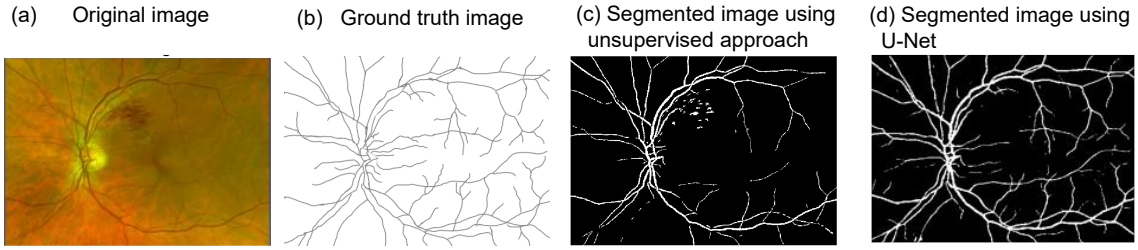

Figure 2.22: Comparison between two segmentation approaches showing: (a) original image, (b) ground truth image, (c) segmented image obtained using classical machine learning based unsupervised approach (K-means clustering) and (d) segmented image obtained from U-Net.

image obtained from the U-Net-based approach given in figure 2.22(d) is 0.905. Based on the dice score value, we conclude that the segmented image obtained from the U-Net-based approach has better agreement with the ground truth image compared to the segmented image obtained from the classical unsupervised approach. It is also important to note that compared to the DICE scores reported in the literature (for e.g. [166]) for vessel segmentation in fundus images, the pre-trained U-Net model performs quite well on our dataset. It is important to note that we would need to do this on more images to be sure the agreement is better. Considering the dice score, we proceed with the segmented image obtained from the U-Net model (figure 2.22d) for further analysis.

2.11 Conclusion

In this chapter, we started with a colour fundus image of retinal haemorhhage provided by the clinical collaborator. We wanted to extract the vessel tree from the colour fundus image. However, initially, we did not have sufficient images available, and to gain a good understanding of these types of images, we started with a traditional machine learning approach. We essentially followed the following pipeline: the extraction of the green colour channel image, pre-processing if needed and finally extraction of feature vectors to study the nature of each pixel of the image. This pipeline is designed for vessel segmentation from colour fundus images using a feature-based approach. It leverages the green channel for enhanced vessel contrast, followed by preprocessing to normalise image quality and extraction of pixel-level feature vectors to characterise vascular structures. This unsupervised ensemble method is intended for datasets with no annotations available and aims to provide interpretable features for analysis. We successfully formed a feature vector containing four features, namely gradient orientation analysis, multiscale morphological transformation, multiscale Gabor filter and principal curvature. The idea behind this multiscale feature vector was to enhance all blood vessels irrespective of their orientations, widths and thickness. We then combined all four images obtained after applying these four features to obtain the final segmented image. To do that, we used the K-means feature fusion approach. First, we applied the K-means clustering algorithm to each of those four images obtained from four features to obtain a binary image, containing only two types of pixels, namely vessel pixels

(with pixel value 1) and non-vessel pixels (with pixel value 0). We then combined these four final images by applying weighted K-means clustering to form the final segmented image. In this approach, we assigned a weight to each of the four images based on their performance. We also set the sum of the four weights to 1 and varied the individual weights accordingly to obtain different segmented images. The novelty of this pipeline lies in a two-stage unsupervised feature fusion framework for vessel segmentation. The compact yet effective feature vector integrates complementary descriptors of vascular structures. While each feature has been studied individually, their combined use provides a unified representation capturing directional, structural, and geometric characteristics of vessels across multiple scales. This strategy preserves the discriminative strengths of individual features while enabling adaptive fusion, resulting in improved segmentation of vessels across varying scales and imaging conditions. However, we noticed that the traditional approach sometimes is not very robust, and the segmentation performance was significantly deteriorated in some images. Also, in the unsupervised approach, other types of images (see the original images given in figure 2.21) containing a black background needed to be treated separately to remove the black background before processing them for segmentation.

Considering all these factors, we decided to try a deep learning-based algorithm to see whether the segmentation results improve. Due to time constraints and limited availability of data, we started with a pre-trained attention U-Net model and made necessary adjustments to segment our images. At the end, by comparing the dice score of the two segmented images obtained from two different approaches, we observed that the attention U-Net algorithm outperformed the unsupervised algorithm for our example image. However, we are aware that we have only compared one sample and the fact that the dice score is not the only measurement for comparing the segmentation result. There is a possibility that the unsupervised model might score better on a different performance measure. Also, the segmentation performance of the U-Net model could be enhanced by fine-tuning its parameters and retraining it on our own retinal image dataset.

For now, in the absence of a more expensive set of retinal fundus images, we consider retinal vessel trees extracted from images processed by the alternative U-Net method. Extraction of the vessel tree is described in Chapter 3, and we then use this information in the later modelling chapters.

Chapter 3

Retinal Vessel Tracking, Vessel Length and Radius Measurement

3.1 Introduction

Our ultimate goal is to construct a mathematical model for an arterio-venous network, whose structure is informed by the retinal vessel network obtained from fundus images provided by our clinical collaborator. In particular, we wish to parameterise the mathematical model using vessel length and radius information extracted from these images. From Chapter 2, we have already obtained a final segmented image using two different methods. In this Chapter, we now focus on how to extract the length and radius of the retinal blood vessels from the segmented image (see figure 3.1a). For this, we need to track the centreline of the blood vessels across different generations of the vascular tree.

We begin our discussion with how to isolate the centreline of the vessel in the segmented image (see subsection 3.2). In section 3.3, we discuss the vessel tracking algorithm in detail to form a connected network. Then, in the following two sections 3.4 and 3.5, the statistical methods for measuring the length and radius of vessels of different generations are given. In section 3.6, we briefly outline the possible sources of uncertainties in the measurement related to the length and radius of the blood vessels. Finally, in subsection 3.7, we conclude the chapter by highlighting the outcomes from this chapter.

3.2 Skeletonisation of the segmented image

Figure 3.1(b) is an example of a final segmented image obtained from the methods outlined in Chapter 2. We denote this digital image I_{ij} as I. The first step is to detect the centerline of the vessel from this segmented image I. This process is commonly known as skeletonisation. This skeletonisation process is typically applied to the binary image, where each pixel value of image I is either 0 or 1 (see detailed discussion on Chapter 1) [57]. It is important to note that

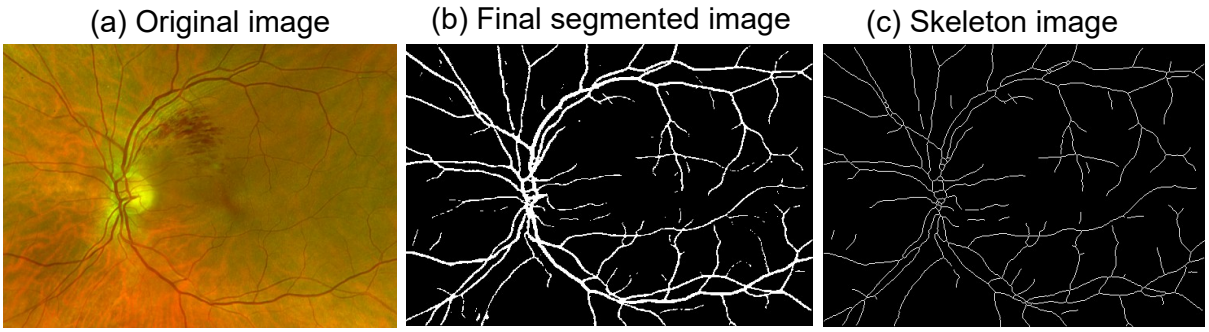

Figure 3.1: Skeletonisation of segmented image I showing: (a) original image, (b) final segmented image, and (c) skeleton image of (a).

a white pixel (i.e., pixel value is 1) dictates a vessel pixel while a black pixel (i.e., pixel value is 0) dictates a background pixel. There are various skeletonisation methods available in digital image processing [57]. The morphological skeletonisation process is one of them, which is our primary focus. For simplicity, we refer to morphological skeletonisation as skeletonisation in the rest of this chapter.

The process of skeletonisation reduces the width of the retinal vessels to a 1−pixel wide structure, while preserving the overall essential structure of the vessel and vessel topology. The centreline of the vessel is important for different quantitative measurements of geometrical attributes like length and radius of the vessel.

Morphological skeletonisation is an operation that can be obtained by combining two basic morphological operations as described in subsection 2.4.3.1 of Chapter 1, known as erosion and opening operations. Mathematically, the skeletonisation operation is defined as [16]

$$S(I) = \bigcup_{k=0}^{K} S_k(I), \tag{3.1}$$

where

$$S_k(I) = (I \ominus kB) - ((I \ominus kB) \circ B);$$

as before '$\ominus$' denotes the erosion operation while '$\circ$' denotes the opening operation. S_k is commonly known as the morphological granulometric function, which extracts structures of size k. Here, B is the structuring element, and kB denotes the structuring element obtained by scaling the original structuring element B by k. Mathematically, kB is defined as

$$kB = kb : b \in B.$$

We consider a linear structuring element for the skeletonisation process. The detailed discussion on the structuring element is given in subsection 2.4.3 of Chapter 2. K is the largest scale factor k such that eroding the image I by the scaled structuring element kB results in a non-empty set, i.e., $I \ominus kB \neq \phi$. In the first step, we apply the erosion operation on I by the structuring element

kB to trim edges and to separate closely connected vessels and finally obtain an image of the same size as I. To smooth out the boundaries of the edges of the eroded image, we apply an opening operation on the eroded image, i.e.,$(I \ominus kB) \circ B$. Now we subtract the opening eroded image from the eroded image to keep all the vessel structures which are of size around kB. It is important to note that I is already a binary image, and so we can readily apply the skeletonisation operation on I. To perform the skeletonisation operation, we use the built-in function 'bwskel' from the MATLAB 2023a image toolbox.

Figure 3.1 shows the final segmented image (figure 3.1b) and the skeletonised image S of the final segmented image (figure 3.1c). Figure 3.1(c) shows the centerline of the vessels appearing in figure 3.1(b) while preserving the overall structure of the retinal vessel network. For further analysis, we consider figure 3.1(c).

3.3 Construction of vascular tree

The algorithm to develop a vascular tree used in this work was originally developed by Dr J. Mackenzie (PhD 2021, University of Glasgow) for building a computational domain to perform the haemodynamic simulations in the myocardium by using a graph-based approach to represent the corresponding vasculature [167]. Building on the core concept of Mackenzie's algorithm, we adapted it as necessary.

We begin by introducing the basic terminology of graph theory in subsection 3.3.1, which will be used frequently in this chapter. The detailed discussion on the algorithm developed for retinal vascular tree construction is given in subsection 3.3.2.

3.3.1 Basic terminology of graph theory

Let us consider, $G = \{V, E\}$ is a graph with n nodes $v_1, v_2, ..., v_n \in V$ and m edges $e_1, e_2, ..., e_m \in E \subseteq V \times V$, where $e_i = (v_i, v_j) \subseteq E$ contains the connection from node v_i to node v_j. A graph G is said to be undirected if there exists an edge between node v_i to v_j that does not have a direction. The edges in an undirected graph represent a two-way relationship, in which each edge can be traversed in both directions and is counted as one edge. In the undirected graph, the total number of edges m is $\frac{1}{2}n(n-1)$.

Let the neighbourhood N_i of a node v_i be the set of nodes v_j such that $e_j = (v_j, v_i) \subseteq E$. The degree d_i of a node v_i is the number of its incident edges e_j, and is given by $d_i = N_i$.

3.3.2 Graph-based algorithm

We now explain the algorithm step by step. In the following subsection 3.3.2.1, we start with choosing vertices from the skeleton image S.

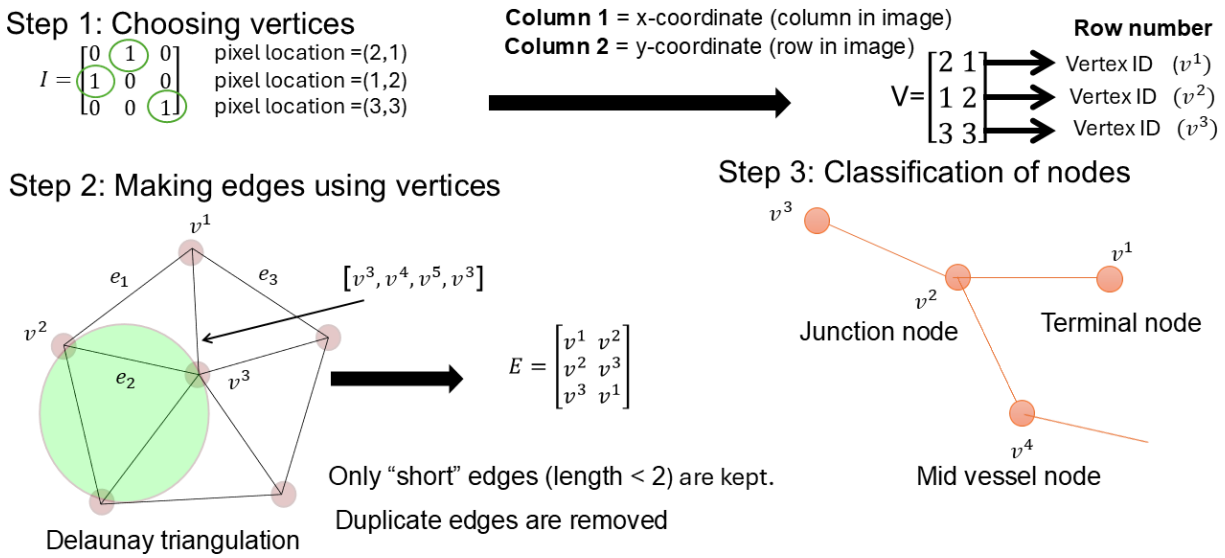

Figure 3.2: Schematic diagram of Delaunay triangulation with the circumcircles of the triangle.

3.3.2.1 Step 1: Choosing vertices

The next step is to identify all the pixel locations (x_i, y_j) of S where pixel value S_{ij} is 1 (see Step 1 in figure 3.2), which correspond to white pixels (i.e., vessel pixels). We refer to all the white pixels as the vertices or nodes of the graph S. For this example image in figure 3.2, the vascular tree is represented by a set of $N = 6218$ nodes, each of which has a known location in R^2. It is important to note that these nodes lie along the centre lines of the retinal vessel following the process of skeletonisation. Then, we save all the vertices (i.e., the white pixel locations) in a matrix V (see Step 2 in figure 3.2) where the row number works as a unique identifier of the corresponding pixel location (i.e., vertex location) to identify each vertex of S. These unique numbers corresponding to each vertex are called the vertex IDs. We denote the vertex ID with the corresponding number in the superscript of that vertex. Thus, V contains the location of each vertex of S and the corresponding vertex IDs. From now on, we denote each vertex by its vertex ID, and alternatively, term the vertex ID as a vertex for simplicity.

The next step is to join two adjacent vertices from the set V by a straight line to make an edge. The easiest way to create a set of edges from a set of vertices is to form a Delaunay triangulation. In the following subsection 3.3.2.2, we explore the Delaunay triangulation in greater detail.

3.3.2.2 Step 2: Making edges using vertices

A triangulation is a technique for partitioning the nodes of the set V into simplices (e.g., triangles in 2D), such that no two simplices overlap and every element of V is a vertex of at least one triangle. An example of triangulation is provided in step 2 of figure 3.2, where the black triangles are the simplices in 2D. Every triangle has a unique circumcircle that passes through all three vertices of that triangle.

A Delaunay triangulation is a special type of triangulation that obeys the Delaunay condi-

tion. According to the Delaunay condition, the circumcircle of any triangle of the triangulation contains no vertex $v^i \in V$ in its interior. An example of such a circle is shown in green in figure 3.2(b).

Delaunay triangulation outputs a list of triangles, each triangle contains 3 vertices from V. It is important to remember, in graph theory, in order to close the structure of the simplices, the starting vertex and the ending vertex have to be the same. Keeping that in mind, the next step is to choose the three vertex IDs, namely $v^i \rightarrow v^j \rightarrow v^k \rightarrow v^i$ at one step from the set V, which forms three edges e_i, e_j, e_k respectively by joining the following vertices $v^i \rightarrow v^j$,$v^j \rightarrow v^k$ and $v^k \rightarrow v^i$ to make one triangle in the Delaunay triangulation (see step 2 of figure 3.2). We repeat the process until the algorithm visits all the vertices of V. Finally, the starting node and the ending node of each edge are saved in a new matrix E. For this image given in figure 3.1(c), there are 6205 unique edges. We use the built-in 'delaunay' function in MATLAB to build the Delaunay triangulation.

Delaunay triangulation not only connects immediate neighbours but also vertices that are far apart. However, to get a realistic vessel tracking, we only want to join the direct neighbouring vertices, i.e, adjacent or diagonal vertices of a given vertex. To do that, we have to restrict the length l_i of the edge e_i (which joins two adjacent vertices v^i and v^j) of the triangle obtained from the Delaunay triangulation. The length l_i is calculated using the Euclidean distance between two vertices (i.e., $x-$ and $y-$ coordinates of white pixel). If two vertices v^i and v^j are adjacent horizontally or vertically, then $l_i = 1$. If the two vertices are diagonal neighbours, then $l_i = \sqrt{2}$. we impose a condition on the length of l_i of each edge of the triangle. However, in both cases, the length l_i of the edge e_i is always less than 2. Based on this, we impose a condition on the maximum value of the length l_i and choose $l_i < 2$, i.e.,$l_i \geq 2$ means the pixels are not considered to be adjacent. As a result, by implementing this condition, we effectively filter out long triangulation edges, keeping local connections only (i.e., pixels that are immediate neighbours in the skeleton) and removing spurious edges.

At the end of this step, we obtain the actual edge rather than a full triangular mesh, where we can track the path connecting one vertex to another. This approach is useful for us to find the length of the retinal vessel of any given generation. The vascular data form a graph $G = \{V, E\}$, and it can be thought of as an undirected graph.

Once we have vertex IDs for all edges, in the next step, we characterize a given vertex id v^i based on the degree d_i of that vertex, given in the following subsection 3.3.2.3 (For discussion on d_i, see subsection 3.3.1).

3.3.2.3 Step 3: Characterisation of vertices

As the edges in E are unique, it is straightforward to categorise a node given the number of times it appears in E. If the node appears exactly once in E, it is called a terminal node; if it appears exactly twice, it is a mid-vessel node or body node. If the node appears more than twice, then

it is a junction node. Body nodes lie between two junction nodes or between a junction and a terminal node. The order of a junction corresponds to the number of daughter branches. In the case of a bifurcation (a one-to-two branching), the junction node appears three times in E. This is called the characterisation of the vertices of the graph. We save all the terminal nodes in a list T, mid-vessel nodes in the list M, and junction nodes in the list J.

Before proceeding to step 4 given in 3.3.2.4, we look for connected components. Connected components are groups of nodes that can be reached by traversing edges starting from an initial node. The search for these connected nodes is carried out using the Dijkstra algorithm. The Dijkstra algorithm is a widely used graph algorithm that finds the shortest paths between nodes in a weighted graph. A weighted graph is a graph where numerical values, called weights, are assigned to its edges. These weights are the distance here. According to the Dijkstra algorithm, the first step is to calculate the initial distances from the source node (say v^1) to all other nodes in the graph [42]. From node v^1, the algorithm examines all directly connected neighbours [42]. Next, the algorithm selects the unvisited node with the smallest known distance [42]. Again, the algorithm selects the next unvisited node and repeats this process until all the nodes are visited [42]. These distances represent the shortest path tree originating from node v^1, showing the minimum distance to reach every other node in the graph [42].

All nodes that cannot be reached from the initial node are considered disconnected and therefore discarded; there are 26 such nodes. After disconnected nodes are removed, their edges corresponding to these nodes can also be discarded, but we find that there are no edges related to the disconnected nodes. There are now 6192 nodes in N for this image given in figure 3.1(c).

To reduce the complexity of the graph G and to make the algorithm computationally efficient, we join adjacent edges into larger edges or segments, which effectively represent longer connections between vertices. In the following subsection 3.3.2.4, we discuss how to make segments from edges.

3.3.2.4 Step 4: Making segments

The adjacent mid-vessel nodes between two junctions or between a junction and a terminus are joined to obtain edges, and edges are further connected to build a segment. Segments can be thought of as a set of edges E_1 with the set of nodes V_1 consisting of the junction and terminal nodes. Together, E_1 and V_1 form a simple connected graph G_1, containing 563 segments for this example image given in figure 3.1(c). G_1 is significantly smaller than the original graph G which contains 6205 edges, so it is more convenient to work with G_1.

To build a segment, the first step is to choose an inlet node from T and run Dijkstra's algorithm to find paths starting from the inlet terminal node and traversing through all terminal nodes given in T [145]. For a given inlet node v^1, the algorithm finds the next body node v^2 from the collection M and continues to find the next node from the newest node v^2 until reaching a junction node given in J. This results in a path from the inlet terminal node to a given terminal node. However,

if the path reaches a junction node in between, it splits to create new paths between a junction and another junction node or a junction to a terminus node. This path is made of a set of connected nodes, including terminal nodes, mid-vessel nodes, and junction nodes, referred to as a segment. The set of paths spans to cover the entire vascular tree, so do the segments.

3.3.2.5 Removing spurious segments

Once all nodes are visited, we have obtained all the required segments, and we call the collection (or set) of all segments S_1. S_1 contains spurious edges, which are likely to be artefacts coming from the image segmentation and skeletonisation process, and they need to be removed. Before removing, we first sort the segments into their respective generations. Sorting is useful because it helps us easily locate vessels from different generations, which is important for us to extract the length and radius of a particular generation. Also, this hierarchy information about vessel generations provides insight into the expected anatomical hierarchy, which in turn helps identify and remove spuriously short segments.

Segments in S_1 can be hierarchically ordered according to the generation to which they belong. The 0^{th} generation contains the segment with the inlet node. Given the i^{th} sorted generations, the $(i+1)^{th}$ generation contains segments that start with the final nodes of the i^{th} generation. In this way, all the segments can be sorted into different generations.

By construction, we have seen that a segment should always contain at least two nodes, but those containing exactly two nodes are quite short segments (it is basically an edge). Now we want to remove the short segments. When the short segments are mistakenly inserted as artefacts within the reconstructed tree structure (i.e., vessel tree), they indicate two bifurcations taking place in immediate succession, which is often misleading, indicating pseudo-trifurcations. These need to be corrected by first identifying daughters connected to this spurious short segment and then reassigning the proximal node of each daughter branch to the proximal node of the short segment. Doing these, all these short segments are discarded, effectively connecting the daughters directly to their parents. As a result, the daughter segments are effectively moved up one generation, and the spuriously short segment can be removed without loss of information. There are 563 such short segments that are detected and removed in the sample image.

3.3.2.6 Choosing the pathway

Considering the mathematical model we want to construct, we include retinal vessels of generations $3, 4$ and 5 for both arteries and veins. The pathway we want to construct is the collection of three generations of arteries and three generations of veins that transport blood to and form the retina. It is important to note that this pathway is also a subtree of the original, as it can only contain segments and nodes that were present in the original tree. Also, all the segments of our chosen pathway must be accessible from the root, i.e. the graph must be simply connected.

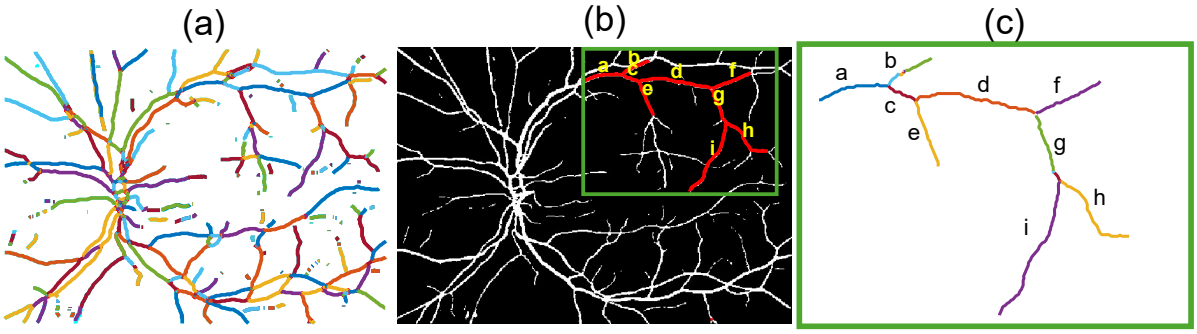

Figure 3.3: Vessel tracking using the algorithm showing:(a) reconstructed vessel trees using the graph-based algorithm, (b) the three generations of vessels marked in the original segmented image and (c) extracted vessels used for vessel length measurements.

Now, because we want to model both arterial and venous networks separately and later combine them using capillaries, we need to extract the length for both arteries and veins. There are different graph-based and U-net-based methods available to identify arteries and veins from fundus images [117],[149]. However, given the time constraints, we have not applied any computational algorithm to distinguish between arteries and veins. After discussing with the clinical collaborator and exploring relevant literatures, it is evident that in fundus images, veins are often identified as thicker, darker vessels compared to the thinner, brighter, and straighter arteries [119]. We therefore characterise the network of thicker vessels as the veins and the network of thinner vessels as the arteries.

Figure 3.3(a) plots the reconstructed vessel tree obtained using the graph-theory-based algorithm discussed above, and different colour schemes represent vessels obtained at different generations. Reconstruction of all the large blood vessels is done quickly while keeping the necessary connected vessels. We occasionally observe isolated vertices, some representing true vessel nodes and others arising from noise. Though it is possible to remove this noise, considering the computational complexity and our interest in modelling the blood flow in large vessels, we refrain from further modifying the tree. In figure 3.3(b), we overlay the reconstructed vessel tree on the original segmented image, and it is evident that they match quite well. In figure 3.3(b), we choose three generations of vessels, of which we want to find the length and radius later in this chapter. The red lines in figure 3.3(b) show the venous network, consisting of three generations. We name each branch of each generation alphabetically in ascending order.

We have all the required information for each segment, and in the following subsection 3.4, we discuss the method used to determine the length of the vessel.

3.4 Finding the length of the vessel

The first step is to select the vessels of interest, for which we want to find the length. Suppose we want to find the length of the vessel network containing vessels a, b, c, d, e, f as labelled in

figure 3.3(b). We describe the process of finding the length for a particular vessel, say a (see figure 3.3b), and necessarily repeat the same process for all others.

Firstly, to calculate the length of each vessel, we need the required pixel locations (i.e., x and y coordinates) for all vertices (i.e., white pixels) contained in the vessel segments a. The vertex IDs for each segment are already saved in the list S_1. Also, the x and y coordinates (i.e., pixel location) corresponding to each vertex ID can be accessed from V. Suppose, $\mathbf{v}_x$ contains all the x coordinates and $\mathbf{v}_y$ has all y coordinates for the given vessel a (see figure 3.3b). We have all the information that we need to find the length of the vessel. From subsection 3.4.1-3.4.4, we explain the process for finding the length of the vessel step by step.

3.4.1 Step 1: Fitting a smoothing spline

We have data $\mathbf{v}_x$ and $\mathbf{v}_y$, but we do not know the curve or the functional form that describes the relationship between $\mathbf{v}_x$ and $\mathbf{v}_y$. The process of finding this curve is known as curve fitting. There are different methods available for curve fitting. In this work, we use a special type of curve-fitting approach called spline interpolation or spline fitting.

Splines, a complex smooth curve, are used to represent the smooth shape. Splines are created using a small set of control points or knots, along with a function that generates the curve through these control points. A curve that actually passes through each control point is known as an interpolating curve. The spline interpolation is a process to draw a piecewise polynomial curve that passes exactly through all data points given. It is a way to draw a smooth curve through n points $(x_1, y_1), \ldots, (x_n, y_n)$. Thus, we seek a smooth function $f(x)$ so that $f(x_i) = y_i$ for all $i = 1, 2, \ldots, n$. In particular, we seek n smoothing polynomials $p_0, \ldots, p_{n-1}$ so that $f(x) = p_i(x)$ for all x in the interval $\left[x_i, x_{i+1}\right]$.

The next step is to find a spline curve that passes through $\mathbf{v}_x$ and $\mathbf{v}_y$.

3.4.2 Step 2: Prepare for interpolation

Suppose the length of the vector $\mathbf{v}_x$ is n. The idea is to compute the vessel length by summing the Euclidean distances between consecutive white pixels. However, the retinal vessels are not perfectly straight lines, but in a few spatial locations, they bend. With the coarse sampling we have, the approximation of length is rough and can underestimate the true length. However, using interpolation techniques, we can create more data points along the length of the vessel to calculate a smoother and more accurate length. As the interpolated points follow the curve more closely, they reduce the error in length estimation.

To do that, we create a finer sequence $1 : 0.2 : n$ of $x-$ coordinates which subdivides the segment along the length, so we have five times as many intermediate points.

The next step is to interpolate the original $x-$ coordinates from $\mathbf{v}_x$ onto the new finer sequence obtained above.

Vessel name	Vessel generation	Length(in pixels)	Diameter(pixels)
a	5	56	3
b	6	39	3
c	6	25	2
d	7	96	2
e	7	44	1
f	8	54	1
g	8	41	1
h	9	79	1
i	9	109	1

Table 3.1: Vessel length and radius (rounded to the nearest pixel) calculated directly from fundus images

3.4.3 Step 3: Interpolate $x-$ coordinates and corresponding $y-$ values

We use the built-in function 'interp1' from Matlab to interpolate the original $x-$ coordinates linearly onto the finer sequence obtained from step 3.4.2. We obtain a new vector $\mathbf{v}_x^{temp}$ that contains all $x-$ values spaced more densely along the vessel a. In a similar manner, we interpolate the $y-$ values using the smoothing spline approach and obtain a new vector $\mathbf{v}_y^{temp}$ containing all $y-$ values. We have all the $x-$ and $y-$ values along the vessel a, and we want to calculate the length of the vessel using these points as discussed in the following subsection 3.4.4.

3.4.4 Step 4: Compute the distance between consecutive points

Once we have all the $x-$ and $y-$ values, then we can compute the change in $x-$ and $y-$ values between consecutive points (x_i, y_i) and (x_{i-1}, y_{i-1}) using the built-in function 'diff' from Matlab. We denote the changes in $x-$ values where $x-$ values contained in $\mathbf{v}_x^{temp}$, by d_x and the changes in the $y-$ values ($y-$ values contained in $\mathbf{v}_y^{temp}$) are denoted by d_y.

Finally, we compute the Euclidean distance d_{xy} between each interpolated consecutive pair of points from d_x and d_y. Mathematically, we write this as

$$d_{xy} = \sqrt{d_x^2 + d_y^2}. \tag{3.2}$$

We repeat all the steps 3.4.1-3.4.4 for all other vessels to obtain the required length of each vessel of the network.

Figure 3.3(c) shows the paths shown extracted from figure 3.3(b). The length of the vessels is given in the table 3.1. We compare the lengths given in table 3.1 to the values given for idealised retinal circulation in [61]. The original generations of vessel a and vessel b in the retinal vasculature visible in figure 3.3(b) are 8 and 9. As discussed in subsection 1.3 of Chapter 1, the parameter values for the retinal circulation provided in [61] correspond to the superior-temporal quadrant, which originates from generation 3 of the retinal vasculature. We want to

compare the value of the lengths obtained from images with the values given [61]. To avoid any ambiguity in the derivation of the unit for the length obtained from images, we consider the ratio of lengths rather than the direct values of the length of a particular generation. From figure 3.3, taking the ratio between vessel a and vessel b, we get 0.69, and similarly, considering the corresponding vessels of generation 5 and 6 from the literature [61], we obtain 0.78.

There are potential reasons for discrepancies between our value and Takhahasi's value [61]. First of all, they consider an idealised model of dichotomous branching where parents bifurcate into two identical daughters. In contrast, we are using real patient images where the daughters are of different lengths. Moreover, no details are available on how the values are measured and what type of images/experiments they have used to measure these quantities. Using different methods can be a potential source of discrepancies.

3.5 Finding the radius of the vessel

We compute the vessel diameter from the reconstructed retinal vasculature given in figure 3.1(c). The approach consists of two steps: candidate point selection from the skeleton image and diameter estimation. Figure 3.4 explains the process of candidate points selection on the skeleton, and also the boundary point detection on the segmented vessel. Figure 3.5 shows how we apply our radius detection algorithm on the segmented vessel image.

3.5.1 Candidate point selection from the skeleton image

Suppose we want to find the diameter of the vessel d (figure 3.5a), we select three different types of vertices from $\mathbf{v}_x^{temp}$ and $\mathbf{v}_y^{temp}$. As the two vectors contain finer grid points along the length of the vessel so it is effective to choose the centre location more precisely than choosing from $\mathbf{V}_x$ and $\mathbf{V}_y$. Firstly, we choose the middle point from $\mathbf{v}_x^{temp}$ and $\mathbf{v}_y^{temp}$. This vertex represents the centre location (x_c, y_c) of vessel d (figure 3.5b). To make sure the centre is not a bifurcation point (i.e., where one parent vessel bifurcates into two daughter vessels), two additional measurement points are chosen at 10% of the vessel length away from either end of the segment. These are called left and right reference points of vessel d and are denoted by (x_r, y_r) and (x_l, y_l), which are the closest points to 10% from the vessel end (figure 3.5c,d). The diameter of the vessel is not always the same along the length of the vessel, and to make sure the vessel diameter measurements are not influenced by bifurcations or by extreme vertices of a segment, we choose these three different locations of vertices to obtain the diameter.

In the following subsection 3.5.2, we discuss how we find the radius using these three types of vertices.

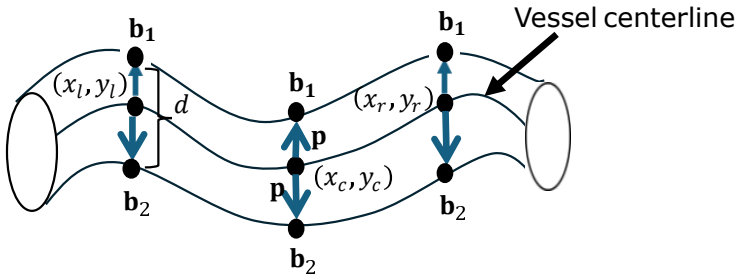

Figure 3.4: Diameter estimation by detecting boundary points

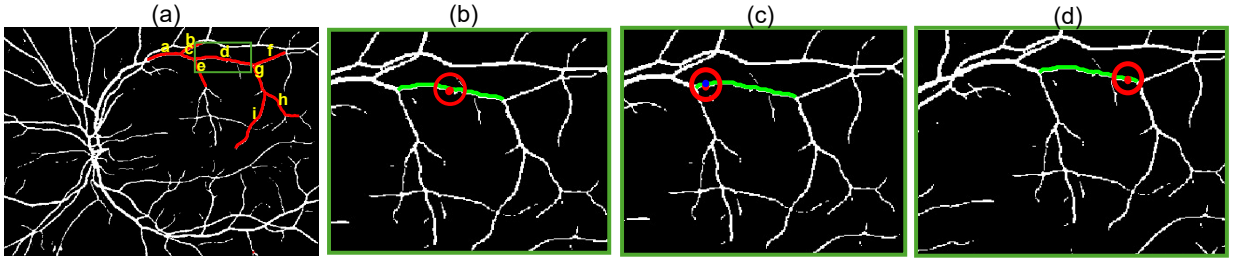

Figure 3.5: Diameter estimation by detecting boundary points showing: (a) identification of the vessel, detection of (b) the midpoint (x_c, y_c), (c) the left point (x_l, y_l) and (d) the right point (x_r, y_r) along the length of the vessel.

3.5.2 Diameter estimation

We denote the $x-$ coordinate and $y-$ coordinated of the i^{th} vertex as (x_i, y_i) where $i = c, l, r$. Also, as before, we discuss the process of finding the diameter for the vessel segment d (see figure 3.3c). For all other vessels, we necessarily repeat the same process as discussed here.

We apply the following steps at each selected point (x_i, y_i) where $i = c, l, r$ discussed in subsection 3.5.1:

Compute vessel tangent: For a given (x_i, y_i), the local tangent t is calculated using the two immediate neighbors (x_{i+1}, y_{i+1}) and (x_{i-1}, y_{i-1}) :

$$\mathbf{t} = \frac{(x_{i+1} - x_{i-1}, y_{i+1} - y_{i-1})}{||x_{i+1} - x_{i-1}, y_{i+1} - y_{i-1}||}. \tag{3.3}$$

The unit vector perpendicular to the tangent t given in (3.3) is: $\mathbf{p} = (-t_y, t_x)$ (see figure 3.4).

3.5.2.1 Boundary detection:

Now we want to detect the boundary vertices of the vessel segment d in both directions (vertical) of (x_i, y_i) (see figure 3.4). Starting from (x_i, y_i), we step along both the positive and negative directions of $\mathbf{p}$. At each step, the pixel intensity values of all pixels in d are checked (see figure 3.4). Traversal continues until the intensity falls below 1 (i.e., leaving the vessel region). It is important to note that in this case we can have only two pixel intensities, either 0 for background or 1 for vessel. The last foreground pixels (i.e., pixel value is 1) encountered on either side of (x_i, y_j) are called the vessel boundary points and denoted by $\mathbf{b}_1, \mathbf{b}_2$.

3.5.2.2 Diameter calculation:

The vessel diameter at (x_i, y_i) is computed as the Euclidean distance between $\mathbf{b}_1$ and $\mathbf{b}_2$:

$$d = ||\mathbf{b}_1 - \mathbf{b}_2||. \tag{3.4}$$

We record three local diameter measurements for the vessel segment a: d_c at the midpoint (x_c, y_c), d_l at the left offset (x_l, y_l), and d_r at the right offset (x_r, y_r). The mean diameter per vessel d is then computed as the arithmetic mean $\frac{1}{3}(d_l + d_c + d_r)$ (see figure 3.4). This provides a robust estimate of vessel diameter, minimising the effect of local irregularities.

3.6 Uncertainties in the measurements of length and radius of the vessel

There are various uncertainties in the method used for the extraction of the skeleton image, lengths and radii of the vessels. The choice of hyperparameters used in vessel segmentation can also be a potential source of uncertainty. In particular, there are possible uncertainties related to the vessel length measurements, which come from the spline fitting approach for reconstructing vessel centerlines from segmented images. Also, the particular choices of splines and their orders used could be a potential source of uncertainty. Moreover, when a smoothing spline is used, the choice of the smoothing parameter can generate uncertainties in the outcome.

Diameter estimation from skeleton image and boundary points is inherently sensitive to pixel-level segmentation errors. A small segmentation inaccuracy of one pixel at the vessel boundary can affect the estimated diameter. Because vessel widths in our images are only a few pixels, a one-pixel deviation represents a substantial fraction of the total width and based on that, the computed diameter can be overestimated or underestimated. To mitigate this, we calculate the width of the vessel at three different locations and then take their average as the final diameter. This approach reduces the impact of local irregularities and random segmentation fluctuations along the vessel boundary. Another potential source of uncertainty in measuring radius arises from pulsatility, as mentioned in subsection 1.4 in Chapter 1. During each cardiac cycle, the vessel diameter does not remain constant as the vessel wall expands during systole and contracts during diastole. The image we use in this study is a single snapshot that captures the vessel at a single time point. This means the measured radius may be slightly overestimated or underestimated, depending on when the image was acquired. However, measurements of diameters for large retinal venules are generally less variable [37]. It is important to note that uncertainty quantification analysis is not included in this thesis as it requires a dedicated framework, which will be addressed in future work.

3.7 Conclusion

Initially, we started with the segmented image obtained from Chapter 2. However, we intended to extract the length and radius of arteries and veins from the given images so that we can use those extracted values of the geometrical attributes to parameterise a three-generation arterio-venous network developed in Chapter 6. Before extracting the length and radius from the segmented image, it was important to track several generations of the blood vessels. In order to track these blood vessels, the first step was to reconstruct the segmented image. In a skeletonised form based on a graph-based reconstruction algorithm was initially developed by Dr Jay Mackenzie from the University of Glasgow [167]. After reconstructing the vessel tree, we were able to use the pixel information to calculate the vessel lengths and diameters for five generations of vessels, which will be used to parameterise the arterio-venous network in Chapter 6.

Chapter 4

Flow along a single blood vessel

4.1 Introduction

In Chapter 1, we discuss how the venous wall can become damaged at the site of A-V crossing because of arteriosclerosis. This can spontaneously lead to a venous thrombosis (a blood clot in a vein), which further constricts the vein's lumen on a much faster timescale. Over time, it can lead to retinal haemorrhage. For a detailed discussion on this, see the subsection 1.2 in Chapter 1.

In this chapter, we want to understand better blood flow in the neighborhood of an A-V crossing by quantifying how the blood flow dynamics and cross-sectional area of a single blood vessel change in response to a prescribed impingement. The impingement is modeled by an external pressure with a localized spatial profile applied over a prescribed timescale on the vessel wall. Note that this external pressure distribution is a relatively crude analogue for mimicking both mechanical obstruction on the vein coming from arterial expansion at the site of A-V crossing, and also the compression occurring because of thrombus formation.

In this chapter, we model blood flow in a long single blood vessel that is being externally compressed and derive a mathematical model in the subsection 4.2. In the following subsection 4.3, we discuss the different numerical methods employed to solve this mathematical model. We then discuss the results of the steady state of the model in subsection 4.4, examining how the timescale of the compressive, time-independent pressure perturbation influences the outcome. Additionally, we analyze the resulting flow upstream and downstream of the constriction in subsection 4.5. Specifically, we investigate the role of inertial wave propagation from the site of occlusion, the impact of fluid accumulation upstream and downstream of the constriction, and the effect of upstream boundary conditions by analyzing blood flow driven by either a fixed inlet flux or a fixed inlet pressure. In the subsection 4.6, we apply a time-dependent external pressure perturbation to observe the effect of the external pressure perturbation on the blood flow in a single vessel model. In subsection 4.7, we conclude the chapter by outlining the key outcomes obtained from this chapter.

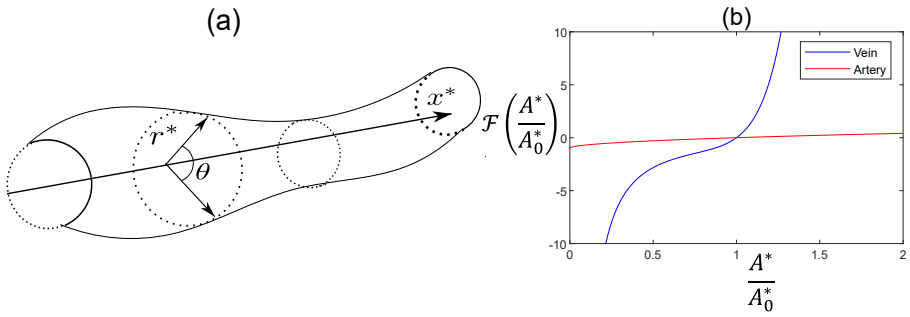

Figure 4.1: Schematic diagram showing (a) the single vessel structure characterized by the cylindrical polar coordinates (r^*, θ, x^*) and (b) different constitutive models for the vessel response to changes in blood pressure, showing our choice of 'tube law' $\mathcal{F} = ((A^*/A_0^*)^{10} - (A^*/A_0^*)^{-3/2})$ (blue solid line), the revised tube law for arteries considered here $\mathcal{F} = ((A^*/A_0^*)^{1/2} - 1)$ (red solid line).

4.2 Derivation of the model

The flow of blood is considered to be Newtonian, homogeneous, and incompressible, as appropriate for blood vessels of diameter greater than 100μm [14]. We begin with a single, long, straight blood vessel of length L^*. The vessel is characterized by cylindrical polar coordinates (r^*, θ, x^*) oriented along the axes of the tube, where r^* and θ represent the typical radial and azimuthal coordinates, respectively, and x^* is measured along the axis of the tube with corresponding unit vectors $\mathbf{e}_r$, $\mathbf{e}_\theta$ and $\mathbf{e}_x$. Figure 4.1(a) shows a schematic diagram of a single blood vessel structure characterized by the cylindrical polar coordinate (r^*, θ, x^*).

Time is denoted by t^*. In general, we consider that the vessel wall is located at a radius $r^* = R^*(\theta, x^*, t^*)$, and the vessel cross-sectional area is given by $A^*(x^*, t^*)$. The baseline radius is R_0^* with baseline cross-sectional area A_0^*. The typical baseline velocity of blood is U^*, and the blood viscosity (assumed to be constant) is μ^*. In practice, the viscosity will depend on the size of the blood vessel [61]. In this simple model, we use two possible upstream boundary conditions, either a prescribed inlet flux Q_0^* or a prescribed inlet pressure P_0^*. The outlet pressure is denoted by p_0^*, and the pressure external to the blood vessel is denoted by $p_e^*(x^*, t^*)$ with maximum amplitude Δp_e^*. The baseline elastic stiffness of the vessel wall is given by k^*. We denote the density of the blood as ρ^*, which is assumed to be constant. The baseline values are adopted directly from the literature, as presented in table 1.1 and table 4.1. However, in Chapter 6 for the three-generation arterio-venous network, the baseline values for radius R_0^*, length L^* and area A_0^* are directly measured from clinical images as described in Chapter 3 to provide a patient-specific measurement of retinal blood flow during retinal vein occlusion.

In the next subsection 4.2.1, we describe the 'tube law', which relates the wall deformation to the transmural pressure. The form of the applied localized constriction is given in subsection 4.2.2. Then, in the following subsections 4.2.3, 4.2.4, and 4.2.5, we derive the dimensionless governing equations, the dimensionless boundary conditions, and the dimensionless 'tube law'. In the following section 4.2.6, we simplify the model by assuming that each cross-section is

axis-symmetric, and so the resulting system of equations does not depend on θ. Then the long-wavelength version of the model is derived in subsection 4.2.7. In the next two subsections, we derive two different types of models, namely the inertial model (see subsection 4.2.8) and the viscous model (see subsection 4.2.9). The final forms of the two models are given in subsection 4.2.10. All the model parameters are listed in subsection 4.2.11. The time-independent static solutions of the two models are provided in subsection 4.2.12.

4.2.1 The 'tube law'

We do not solve the full problem for the deformation of the $3D$ vessel wall. Studies have indicated that the pressure–area relationships of uniform elastic tubes of different sizes and wall thickness can be approximately characterised by a 'tube law' [30]. In particular, we consider a simple elastic response modelled in the form of a 'tube law' when the transmural pressure is written as

$$p^* - p_e^*(x^*,t^*) = k^* \mathcal{F}\left(\frac{A^*}{A_0^*}\right), \qquad (r^* = R^*), \tag{4.1}$$

defined in terms of the local cross-sectional area $A^*(x,t)$ and vessel wall stiffness k^*. The form of the external pressure $p_e^*(x^*,t^*)$ is discussed below in subsection 4.2.2. In this case, $\mathcal{F}$ is a nonlinear function of the tube cross-sectional area representing the local resistance to expansion or compression, and it is given by

$$\mathcal{F}\left(\frac{A^*}{A_0^*}\right) = \left(\left(\frac{A^*}{A_0^*}\right)^m - \left(\frac{A^*}{A_0^*}\right)^{-n}\right),$$

where $m,n \geq 0$ and most data for m,n are obtained *ex vivo* [136]. The parameters m and n discussed above are used to distinguish between arteries and veins. In this work, we choose the exponents $m = 10$ and $n = 3/2$ for the veins, which are values proposed for the giraffe jugular vein [30]. Later these values are also used to characterise human veins [95, 111] and also for retinal veins [136, 165]. From figure 4.1(b), we see that the large values of m in the expansion mean that the tube stiffens rapidly as it expands, and n opposes the vessel collapse. We know arteries are much stiffer (i.e, k^* values are larger) than veins, so to mimic a vein properly, we use a revised choice of exponents and consider $m = 1/2, n = 0$ [111]. The functional form of an artery is plotted as a red line in figure 4.1(b). From figure 4.1, it is clear that to see even a small change in the cross-sectional area of the tube, the system must exert a large amount of pressure on the tube.

In particular, we estimate the dimensional vessel stiffness parameter k^* in terms of the Young's modulus of the tissue, denoted by E^*, its Poisson ratio ν, the vessel wall thickness h^*, and inner

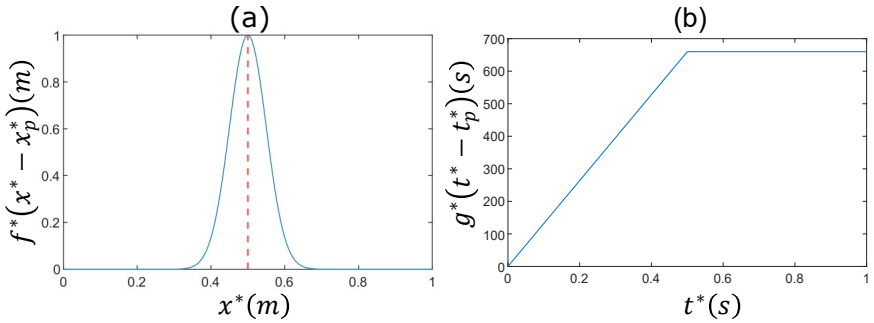

Figure 4.2: Structures of the functions:(a) $f^*(x^*-x_p^*)$ and (b) $g^*(t^*-t_p^*)$. The spatial extent $k_p^*=200$ and the pressure perturbation applied over the time interval $t_p^*=0.5sec$ on the middle of the vessel $x_p^*=0.5m$ along the length of the vessel $L^*=1m$.

lumen radius r_0^* [136, 83]. For arteries, we consider [111]

$$k^*=\frac{E^*}{(1-\nu^2)}\left(\frac{h^*}{r_0^*}\right) \tag{4.2a}$$

while for veins we consider [111]

$$k^*=\frac{E^*}{12(1-\nu^2)}\left(\frac{h^*}{r_0^*}\right)^3. \tag{4.2b}$$

The parameter values specific to arteries and veins are given in table 1.1 and table 4.1.

4.2.2 Applied localised constriction of the vein

To mimic impingement by the corresponding artery and occlusion due to thrombus accumulation in the vein, we apply a localised compression centred at some location $x^*=x_p^*$ over the timescale t_p^* through a prescribed external pressure, choosing p_e^* of the form

$$p_e^*=\Delta p_e^* g^*(t^*-t_0^*)f^*(x^*-x_p^*), \tag{4.3}$$

where Δp_e^* is the maximal amplitude and f^*, g^* are prescribed functions chosen in the form

$$f^*(s^*)=e^{-k_p^* s^{*2}}, \tag{4.4}$$

and

$$g^*(t^*)=\begin{cases}\frac{(t^*-t_0^*)}{t_p^*}, & t_0^*\le t^*\le t_p^*+t_0^*,\\ 1, & t^*\ge t_p^*+t_0^*.\end{cases} \tag{4.5}$$

We choose $g^*(t^*)$ as a function of time t^* which rises linearly over timescale t_p^* until it attains its unit amplitude and then remains constant, while $f^*(x^*)$ is spatial function which takes the value 1 around $x^* = x_p^*$ and decays exponentially in either direction to ensure the effect is localized. This assumption introduces five parameters namely x_p^*, k_p^*, t_0^*, t_p^* and Δp_e^*, where x_p^* is the location of the occlusion, k_p^* describes the spatial extent of the occlusion, t_p^* is the time interval over which the external pressure is applied, t_0^* is the starting time and Δp_e^* is the maximal pressure amplitude.

Figure 4.2 plots these functions, including the spatial profile of f^* (see figure 4.2a) and the temporal profile of g^* (see figure 4.2b).

4.2.3 Dimensionless governing equations

We non-dimensionalise all lengths on the square root of the baseline cross-sectional area $(A_0^*)^{1/2}$, velocities on a general scale U^* (determined later), time on $(A_0^*)^{1/2}/U^*$, and pressure on a general pressure scale P^* (specified later). All dimensionless variables are denoted without the asterisk, while their dimensional counterparts are given with the asterisk. This choice of non-dimensional scales yields the following dimensionless groups

$$Q_0 = \frac{Q_0^*}{U^* A_0^*}, \quad P_0 = \frac{P_0^*}{P^*}, \quad k = \frac{k^*}{P^*}, \quad \Delta p_e = \frac{\Delta p_e^*}{P^*}, \quad x_p = \frac{x_p^*}{(A_0^*)^{1/2}}, \quad t_p = \frac{U^* t_p^*}{(A_0^*)^{1/2}}, \quad t_0 = \frac{U^* t_0^*}{(A_0^*)^{1/2}},$$

where Q_0 is the non-dimensional inlet flux, P_0 is the non-dimensional inlet pressure, Δp_e is the non-dimensional maximum amplitude of the external pressure, k is the non-dimensional vessel wall stiffness, x_p is the non-dimensional location of the occlusion, t_p is the non-dimensional time interval over which the external pressure is applied and t_0 is the non-dimensional starting time $t_0 = 0$. We also introduce $\mathcal{I} = (\rho^*(U^*)^2/P^*)$ as the ratio of the inertial pressure based on U^* to the general pressure scale P^*, while $\mathcal{V} = \mu^* U^*/((A_0^*)^{1/2} P^*)$ is the ratio of the viscous pressure scale based on U^* to the general pressure scale P^*.

For simplicity, we assume that the flow is axis-symmetric throughout, so all variables are independent of the polar coordinate θ, and the azimuthal component of the fluid velocity is zero ($u_\theta = 0$). In this case, the cross-section of the tube is always circular, and so $A(x,t) = \pi R^2(x,t)$. The dimensionless (axis-symmetric) flow velocity $\mathbf{u} = u_r \mathbf{e}_r + u_x \mathbf{e}_x$ and dimensionless blood pressure p follow the non-dimensional Navier-Stokes equations

$$\mathcal{I}\left(\frac{\partial \mathbf{u}}{\partial t} + \mathbf{u} \cdot \nabla \mathbf{u}\right) = -\nabla p + \mathcal{V} \nabla^2 \mathbf{u}, \tag{4.6}$$

$$\nabla \cdot \mathbf{u} = 0, \tag{4.7}$$

where the gradient operator is defined in (dimensionless) cylindrical polar coordinates.

4.2.4 Boundary conditions

Assuming axis-symmetry, we apply a dimensionless kinematic boundary condition on the tube wall in the form

$$u_r = \frac{\partial R}{\partial t} + u_r \frac{\partial R}{\partial r} + u_x \frac{\partial R}{\partial x}, \quad (r = R). \tag{4.8}$$

We also apply the no-slip boundary condition on the tube wall in the form

$$\mathbf{u} \cdot \hat{\mathbf{t}} = 0, \quad (r = R), \tag{4.9}$$

where $\hat{\mathbf{t}}$ is a unit tangent to the wall in the $\mathbf{e}_x - \mathbf{e}_r$ plane.

4.2.5 Dimensionless tube law

The dimensional 'tube law' (4.1) reduces to

$$p = p_e + k(A^m - A^{-n}), \tag{4.10}$$

in dimensionless variables, where $A(x,t)$ is the dimensionless cross-sectional area of the tube.

4.2.6 Model reduction

The corresponding axial flux along the vessel is given as

$$q = 2\pi \int_0^R u_x r \, dr. \tag{4.11}$$

The non-dimensional Navier-Stokes equations (4.6-4.7) along with the boundary conditions (4.8-4.9) and the tube law (4.10) are (in principle) solvable for $\mathbf{u}$, p and $A(x,t)$. However, to close the system, we must impose boundary conditions at the ends of the vessel to drive the flow. As discussed above, at the upstream end of the vessel, we prescribe either fixed flux Q_0 or fixed pressure P_0, in the form

$$q = Q_0 \ \text{ or } \ p = P_0, \ \text{ at } \ x = 0. \tag{4.12}$$

If we prescribe one of these (either flux or pressure at $x = 0$), then the other can be calculated as part of the solution. At the outlet, we prescribe free return of the fluid to the heart so that the pressure is effectively zero, so that $p = 0$. In cases where $p_e(L,t) = 0$, we obtain the reduced condition $A(L,t) = 1$.

It emerges that there are now several pertinent limits that can be considered. In the first instance, we retain flow inertia (see subsection 4.2.7) and derive the 'inertial model' (see subsection 4.2.8), and then reduce to a 'very viscous model' (see subsection 4.2.9).

4.2.7 Derivation of the long-wavelength model

Retaining flow inertia, we set $P^* = k^*$ and $\mathcal{I} = 1$ which implies $U^* = (k^*/\rho^*)^{1/2}$. This choice of scaling yields the following dimensionless groups

The non-dimensional Navier-Stokes equations reduce to

$$\frac{\partial \mathbf{u}}{\partial t} + \mathbf{u} \cdot \nabla \mathbf{u} = -\nabla p + \frac{1}{\mathcal{R}} \nabla^2 \mathbf{u} \tag{4.13}$$

$$\nabla \cdot \mathbf{u} = 0. \tag{4.14}$$

Since the blood vessels of retinal circulation are typically long compared to their radius, we reduce the complexity of the model using a long-wavelength approximation. We construct a small parameter $\beta = 1/L \ll 1$ and re-scale the independent variables according to

$$x = \beta^{-1}\tilde{x}, \qquad t = \beta^{-1}\tilde{t}, \qquad r = \tilde{r},$$

the dependent variables according to

$$u_x = \tilde{u}_{\tilde{x}}, \qquad u_r = \beta \tilde{u}_{\tilde{r}}, \qquad p = \tilde{p}, \qquad R = \tilde{R}, \qquad A = \tilde{A},$$

and the model parameters according to

$$\mathcal{R} = \beta^{-1}\tilde{\mathcal{R}}, \quad P_0 = \tilde{P}_0, \quad k_p = \beta^{-1}\tilde{k}_p, \quad x_p = \beta^{-1}\tilde{x}_p, \quad k = 1, \quad Q_0 = \tilde{Q}_0, \quad \Delta p_e = \widetilde{\Delta p_e}.$$

All long-wavelength variables and parameters are denoted using the same symbol as before, but with a tilde. The final system of governing equations, neglecting terms involving $O(\beta^2)$, reduces to

$$\frac{\partial \tilde{u}_{\tilde{x}}}{\partial \tilde{t}} + \tilde{u}_{\tilde{r}} \frac{\partial \tilde{u}_{\tilde{x}}}{\partial \tilde{r}} + \tilde{u}_{\tilde{x}} \frac{\partial \tilde{u}_{\tilde{x}}}{\partial \tilde{x}} = -\frac{\partial \tilde{p}}{\partial \tilde{x}} + \frac{1}{\tilde{\mathcal{R}}} \frac{1}{\tilde{r}} \frac{\partial}{\partial \tilde{r}} \left(\tilde{r} \frac{\partial \tilde{u}_{\tilde{x}}}{\partial \tilde{r}} \right), \tag{4.15a}$$

$$\frac{\partial \tilde{p}}{\partial \tilde{r}} = 0, \tag{4.15b}$$

$$\frac{1}{\tilde{r}} \frac{\partial}{\partial \tilde{r}} (\tilde{r} \tilde{u}_{\tilde{r}}) + \frac{\partial \tilde{u}_{\tilde{x}}}{\partial \tilde{x}} = 0, \tag{4.15c}$$

subject to a dimensionless, long-wavelength, kinematic condition

$$\tilde{u}_{\tilde{r}} = \frac{\partial \tilde{R}}{\partial \tilde{t}} + \tilde{u}_{\tilde{x}} \frac{\partial \tilde{R}}{\partial \tilde{x}}, \quad (\tilde{r} = \tilde{R}), \tag{4.16}$$

and long wavelength no-slip condition $\tilde{u}_{\tilde{x}}(\tilde{R}, \tilde{t}) = 0$.

Integrating over the vessel cross-section, the conservation of mass equation (4.15c) becomes

$$2\pi[\tilde{r}\tilde{u}_{\tilde{r}}]_0^{\tilde{R}} + 2\pi\int_0^{\tilde{R}} \frac{\partial \tilde{u}_{\tilde{x}}}{\partial \tilde{x}}\tilde{r}d\tilde{r} = 0. \tag{4.17}$$

Now the first term can be obtained directly using the boundary conditions at $\tilde{r} = \tilde{R}$ and $\tilde{r} = 0$, and the second term can be written using the Leibniz integral rule, in the form

$$2\pi\tilde{R}\tilde{u}_{\tilde{r}}\Big|_{\tilde{r}=\tilde{R}} + 2\pi\frac{\partial}{\partial \tilde{x}}\int_0^{\tilde{R}} \tilde{u}_{\tilde{x}}\tilde{r}d\tilde{r} - 2\pi\tilde{R}\frac{\partial \tilde{R}}{\partial \tilde{x}}\tilde{u}_{\tilde{x}}\Big|_{\tilde{r}=\tilde{R}} = 0. \tag{4.18}$$

Substituting the kinematic condition (4.16) we obtain

$$2\pi\tilde{R}\frac{\partial \tilde{R}}{\partial \tilde{t}} + 2\pi\frac{\partial}{\partial \tilde{x}}\int_0^{\tilde{R}} \tilde{u}_{\tilde{x}}\tilde{r}d\tilde{r} = 0. \tag{4.19}$$

Since the tube is assumed to be axis-symmetric, we express equation (4.19) entirely in terms of cross-sectional area $\tilde{A} = \pi\tilde{R}^2$ in the form

$$\frac{\partial \tilde{A}}{\partial \tilde{t}} + 2\pi\frac{\partial}{\partial \tilde{x}}\int_0^{\tilde{R}} \tilde{u}_{\tilde{x}}\tilde{r}d\tilde{r} = 0. \tag{4.20}$$

Writing in terms of the dimensionless axial flux $q = \tilde{q}$ (see equation (4.11)), then equation (4.20) reduces to

$$\frac{\partial \tilde{A}}{\partial \tilde{t}} + \frac{\partial \tilde{q}}{\partial \tilde{x}} = 0. \tag{4.21}$$

The corresponding conservation of momentum equation (4.15a) becomes

$$2\pi\int_0^{\tilde{R}} \frac{\partial \tilde{u}_{\tilde{x}}}{\partial \tilde{t}}\tilde{r}d\tilde{r} + \int_0^{\tilde{R}} \left(\tilde{u}_{\tilde{r}}\frac{\partial \tilde{u}_{\tilde{x}}}{\partial \tilde{r}} + \tilde{u}_{\tilde{x}}\frac{\partial \tilde{u}_{\tilde{x}}}{\partial \tilde{x}}\right)\tilde{r}d\tilde{r} = -2\pi\int_0^{\tilde{R}} \frac{\partial \tilde{p}}{\partial \tilde{x}}\tilde{r}d\tilde{r} + \frac{2\pi}{\tilde{\mathcal{R}}}\left[\tilde{r}\frac{\partial \tilde{u}_{\tilde{x}}}{\partial \tilde{r}}\right]_0^{\tilde{R}}. \tag{4.22}$$

Manipulating the convective inertia term in equation (4.22) and using the conservation of mass equation (4.15c) and the kinematic condition (4.16) we obtain

$$2\pi\frac{\partial}{\partial \tilde{t}}\int_0^{\tilde{R}} \tilde{u}_{\tilde{x}}\tilde{r}d\tilde{r} + 2\pi\frac{\partial}{\partial \tilde{x}}\left(\int_0^{\tilde{R}} \tilde{u}_{\tilde{x}}^2\tilde{r}d\tilde{r}\right) = -2\pi\int_0^{\tilde{R}} \frac{\partial \tilde{p}}{\partial \tilde{x}}\tilde{r}d\tilde{r} + \frac{2\pi}{\tilde{\mathcal{R}}}\tilde{R}\frac{\partial \tilde{u}_{\tilde{x}}}{\partial \tilde{r}}\Big|_{\tilde{r}=\tilde{R}}. \tag{4.23}$$

Rewriting the first term of the equation (4.23) (the unsteady inertia term) in terms of axial flux, while from equation (4.15b) it is clear that $\tilde{p}$ is independent of $\tilde{r}$, so we have

$$\frac{\partial \tilde{q}}{\partial \tilde{t}} + 2\pi\frac{\partial}{\partial \tilde{x}}\left(\int_0^{\tilde{R}} \tilde{u}_{\tilde{x}}^2\tilde{r}d\tilde{r}\right) = -\tilde{A}\frac{\partial \tilde{p}}{\partial \tilde{x}} + \frac{2\pi}{\tilde{\mathcal{R}}}\tilde{R}\frac{\partial \tilde{u}_{\tilde{x}}}{\partial \tilde{r}}\Big|_{\tilde{r}=\tilde{R}}. \tag{4.24}$$

4.2.8 Derivation of the inertial model

The long-wavelength system of equations (4.21) and (4.24) is not closed. There are a handful of approaches available in the literature on flow in collapsible tubes to close the system based on specific assumptions or empirical measurements [15]. Here, we impose a modified Hagen-Poiseuille flow profile of the form

$$\tilde{u}_{\tilde{x}} = \frac{2\tilde{q}}{\pi \tilde{R}^4}(\tilde{R}^2 - \tilde{r}^2), \qquad (0 \leq \tilde{r} \leq \tilde{R}). \tag{4.25}$$

This empirical flow profile automatically applies the no-slip condition on the vessel wall, and the governing equations can be written in closed form as

$$\frac{\partial \tilde{A}}{\partial \tilde{t}} + \frac{\partial \tilde{q}}{\partial \tilde{x}} = 0, \tag{4.26a}$$

$$\frac{\partial \tilde{q}}{\partial \tilde{t}} + \frac{4}{3}\frac{\partial}{\partial \tilde{x}}\left(\frac{\tilde{q}^2}{\tilde{A}}\right) = -\tilde{A}\frac{\partial \tilde{p}}{\partial \tilde{x}} - \frac{8\pi \tilde{q}}{\tilde{\mathcal{R}}\tilde{A}}. \tag{4.26b}$$

The model includes both viscous and inertial contributions and will henceforth be referred to as the 'inertial model'.

4.2.9 Derivation of the viscous model

However, we also wish to consider the limit where the flow is dominated by viscous effects. In this case, it is easier to use a different non-dimensionalisation where we set $\mathcal{V} = 1$ and define P_0^* or Q_0^* based on the upstream boundary condition. For instance, for a prescribed upstream flux, we set $U^* = (Q_0^*/A_0^*)$ and as $\mathcal{V} = 1$ which implies $P^* = (\mu^* Q_0^*/(A_0^*)^{3/2})$. Conversely, for a prescribed upstream pressure we set $P^* = P_0^*$ and $U^* = (P_0^*(A_0^*)^{1/2}/\mu^*)$. In both cases, the model can be written in terms of the non-dimensional parameters

$$\mathcal{I} = \mathcal{R} = \frac{\rho^* U^* (A_0^*)^{\frac{1}{2}}}{\mu^*}, \quad k = \frac{k^*}{P^*}, \quad \Delta p_e = \frac{\Delta p_e^*}{P^*},$$

where $\mathcal{R}$ is again a Reynolds number (see subsection 4.2.7 above).

The non-dimensional Navier-Stokes equations for this viscous model reduce to

$$\mathcal{R}\left(\frac{\partial \mathbf{u}}{\partial t} + \mathbf{u}\cdot\nabla\mathbf{u}\right) = -\nabla p + \nabla^2 \mathbf{u}, \tag{4.27}$$

$$\nabla \cdot \mathbf{u} = 0, \tag{4.28}$$

We again assume long-wavelength deformations ($\beta = 1/L \ll 1$) and re-scale the independent variables according to

$$x = \beta^{-1}\tilde{x}, \quad t = \beta^{-1}\tilde{t}, \quad r = \tilde{r},$$

dependent variables according to

$$u_x = \tilde{u}_{\tilde{x}}, \;\; u_r = \beta \tilde{u}_{\tilde{r}}, \;\; p = \beta^{-1}\tilde{p}, \;\; R = \tilde{R}, \;\; A = \tilde{A}$$

and the model parameters according to

$$\beta\mathcal{R} = \tilde{\mathcal{R}}, \;\; P_0 = \tilde{P}_0, \;\; k_p = \beta^{-1}\tilde{k}_p \;\; , k = \beta^{-1}\tilde{k}, \;\; Q_0 = \tilde{Q}_0, \;\; \Delta p_e = \beta^{-1}\widetilde{\Delta p_e}.$$

In a simplified version of the viscous model, we assume the flow is very viscous and so set $\mathcal{R} = 0$. The final long-wavelength version of the governing equations becomes

$$\frac{\partial \tilde{p}}{\partial \tilde{x}} = \frac{1}{\tilde{r}}\frac{\partial}{\partial \tilde{r}}\left(\tilde{r}\frac{\partial \tilde{u}_{\tilde{x}}}{\partial \tilde{r}}\right), \tag{4.29}$$

along with the boundary conditions (4.12). In this case, we do not need to use a flow profile assumption, and instead, (4.29) can be integrated directly to obtain

$$\tilde{u}_{\tilde{x}} = \frac{2\tilde{q}}{\pi \tilde{R}^4}(\tilde{R}^2 - \tilde{r}^2), \; (0 \le \tilde{r} \le \tilde{R}), \; \tilde{q} = -\frac{\tilde{A}^2}{8\pi}\frac{\partial \tilde{p}}{\partial \tilde{x}}. \tag{4.30}$$

Note that this profile is entirely consistent with the Hagen-Poiseuille profile assumed in subsection 4.2.7. Substituting into (4.21), we finally obtain the governing equation for viscous flow in the closed form as

$$\frac{\partial \tilde{A}}{\partial \tilde{t}} = \frac{\partial}{\partial \tilde{x}}\left(\frac{\tilde{A}^2}{8\pi}\frac{\partial \tilde{p}}{\partial \tilde{x}}\right). \tag{4.31}$$

We henceforth refer to this system as the 'viscous model'.

4.2.10 Final model

We now consider these two models in the subsequent discussion; as already stated, we refer to (4.26) as the inertial model and the model (4.31) as the viscous model. In both cases, the non-dimensional, long-wavelength version of the 'tube law' is given by

$$\tilde{p}(\tilde{x},\tilde{t}) = \tilde{p}_e(\tilde{x},\tilde{t}) + \tilde{k}(\tilde{A}^m - \tilde{A}^{-n}), \tag{4.32}$$

where the external pressure $\tilde{p}_e(\tilde{x},\tilde{t})$ is assumed of the form

$$\tilde{p}_e = \widetilde{\Delta p_e}\tilde{g}(\tilde{t} - \tilde{t}_0)\tilde{f}(\tilde{x} - \tilde{x}_p).$$

In the derivation of the inertial model, we set $P^* = k^*$, which gives $k = 1$, so the 'tube law' reduces to

$$\tilde{p}(\tilde{x},\tilde{t}) = \tilde{p}_e(\tilde{x},\tilde{t}) + (\tilde{A}^m - \tilde{A}^{-n}). \tag{4.33}$$

Using this in the system of equations (4.26) for the inertial model, we obtain a closed system that can be written as

$$\frac{\partial \tilde{A}}{\partial \tilde{t}} + \frac{\partial \tilde{q}}{\partial \tilde{x}} = 0, \tag{4.34a}$$

$$\frac{\partial \tilde{q}}{\partial \tilde{t}} + \frac{4}{3}\frac{\partial}{\partial \tilde{x}}\left(\frac{\tilde{q}^2}{\tilde{A}}\right) = -\tilde{A}\left(\frac{\partial \tilde{p}_e}{\partial \tilde{x}} + \left(m\tilde{A}^{m-1} + n\tilde{A}^{-n-1}\right)\frac{\partial \tilde{A}}{\partial \tilde{x}}\right) - \frac{8\pi\tilde{q}}{\tilde{\mathcal{R}}\tilde{A}}, \tag{4.34b}$$

subject to the boundary conditions (assuming $\tilde{p}_e(0,\tilde{t}) = \tilde{p}_e(1,\tilde{t}) = 0$)

$$\tilde{q} = \tilde{Q}_0 \text{ or } \tilde{p} = (\tilde{A}^m - \tilde{A}^{-n}) = \tilde{P}_0 \qquad (\tilde{x} = 0), \tag{4.34c}$$

$$\tilde{p} = 0 \qquad (\tilde{x} = 1). \tag{4.34d}$$

Conversely, in the case of the viscous model, we define the dimensionless stiffness of the vessel in terms of the upstream driving conditions, so the 'tube law' reduces to

$$\tilde{p}(\tilde{x},\tilde{t}) = \tilde{p}_e(\tilde{x},\tilde{t}) + (\tilde{A}^m - \tilde{A}^{-n}). \tag{4.35}$$

Substituting the viscous model equation (4.31) facilitates a closed system that can be written in terms of the cross-sectional area $\tilde{A}$ only in the form

$$\frac{\partial \tilde{A}}{\partial \tilde{t}} = \frac{\partial}{\partial \tilde{x}}\left(\frac{\tilde{A}^2}{8\pi}\left(\frac{\partial \tilde{p}_e}{\partial \tilde{x}} + \tilde{k}\left(m\tilde{A}^{m-1} + n\tilde{A}^{-n-1}\right)\frac{\partial \tilde{A}}{\partial \tilde{x}}\right)\right), \tag{4.36a}$$

subject to boundary conditions (assuming $\tilde{p}_e(0,\tilde{t}) = \tilde{p}_e(1,\tilde{t}) = 0$)

$$\frac{\partial \tilde{A}}{\partial \tilde{x}} = -\frac{8\pi\tilde{Q}_0}{\tilde{k}\left(m\tilde{A}^{m+1} + n\tilde{A}^{-n+1}\right)} \text{ or } \tilde{p} = \tilde{k}(\tilde{A}^m - \tilde{A}^{-n}) = \tilde{P}_0, \ (\tilde{x} = 0), \tag{4.36b}$$

$$\tilde{A} = 1, \text{only if } \widetilde{\Delta p_e} = 0 \qquad (\tilde{x} = 1). \tag{4.36c}$$

[12].

4.2.11 Model Parameters

Recall that in Chapter 2, we measured the ratio of length, radius, and cross-sectional area of arteries and veins in the superior temporal quadrant (generations 3 and 5) of the human retinal circulation from clinical fundus images, and then compared the values extracted from the images with an idealised retinal circulation [61]. In this chapter, we use the morphological and geometric parameters of the idealised retinal arteries and veins given in Table 1.1 in Chapter 1.

As discussed previously, the central retinal artery and vein (CRA, CRV) enter the eye through the optic nerve. These are denoted as generation 1. Upon entering the retina, the CRA and CRV divide into four primary branches: the superior temporal branch, inferior temporal branch,

Table 4.1: Reference parameter values applicable to both the vein generation 3.

parameter	symbols	unit	arterial value	venous value	source
tube law parameter	m	-	$\frac{1}{2}$	10	[111]
tube law parameter	n	-	0	$\frac{3}{2}$	[111]
maximum amplitude	Δp_e^*	$mmHg$	$1-20$	$1-20$	-
timescale of perturbation	t_p^*	sec	$0.0001-0.1$	$0.0001-0.1$	-
location of occlusion	x_p^*	μm	$\frac{1}{2}L^*$	$\frac{1}{2}L^*$	-
starting time	t_0^*	sec	0	0	-
spatial extent	k_p^*	-	200	200	-

Table 4.2: Non-dimensional parameter values for generation 3 used in simulations

	parameter	symbol	arterial value	venous value
Inertial Model	length	L	7.59461	7.953921
	Reynolds number	$\tilde{\mathcal{R}}$	58.0286	1.7570
	inlet flux	$\tilde{Q}_0$	0.0012	0.0246
	inlet pressure	$\tilde{P}_0$	-	-
	maximum amplitude	$\widetilde{\Delta p_e}$	$0.00046-0.0092$	$0.6567-13.135$
	timescale of perturbation	$\tilde{t}_p$	$2.3437-2343.7$	$0.0435-43.4818$
Viscous Model	**parameter**	**symbol**	**arterial value**	**venous value**
	length	L	7.59461	7.95392
	inlet flux	$\tilde{Q}_0$	1	1
	inlet pressure	$\tilde{P}_0$	-	
	vessel wall stiffness	$\tilde{k}$	41993.306	62.29877
	maximum amplitude	$\widetilde{\Delta p_e}$	46.9353-442.56	$46.935-938.70$
	timescale of perturbation	$\tilde{t}_p$	$0.002823-2.823$	$0.001069-1.069$

superior nasal branch, and inferior nasal branch. In this chapter, we consider a single blood vessel in each of generations 3 and 5 in the superior temporal quadrant of the retinal circulation using an idealised description [61]. Unless stated otherwise, the parameter values used for simulation in this chapter are given in table 1.1 and table 4.1. The parameter values listed in the table 4.2 are non-dimensional parameter values derived using the non-dimensionalisation described in subsection 4.2.3 and in table 4.1.

4.2.12 Static solutions

We begin by isolating the time-independent (static) solution of the inertial model (4.34), both with and without external pressure perturbation $\tilde{p}_e$. Throughout the chapter, static solutions are denoted with the superscript $^{(s)}$.

Static solutions of the perturbed inertial model (4.34) must have constant flux ($\tilde{q} = \overline{q}$) while the corresponding cross-sectional area profile $\tilde{A} = \tilde{A}^{(s)}(\tilde{x})$ must satisfy the first order nonlinear

ordinary differential equation (ODE)

$$(\tilde{A}^{(s)})_{\tilde{x}} = -\left((m(\tilde{A}^{(s)})^m + n(\tilde{A}^{(s)})^{-n} - \frac{4}{3}\left(\frac{\overline{q}}{\tilde{A}^{(s)}}\right)^2 \right)^{-1} \left(\frac{8\pi\overline{q}}{\tilde{\mathcal{R}}\tilde{A}^{(s)}} + \tilde{A}^{(s)}\frac{\partial \tilde{p}_e}{\partial \tilde{x}} \right), \qquad (0 \le \tilde{x} \le 1). \tag{4.37}$$

Conversely, for static solutions of the unperturbed inertial model (4.34), we consider $\widetilde{p_e} = 0$ in (4.37).

For the flux-driven boundary condition, we impose $\overline{q} = \tilde{Q}_0$ at the inlet $\tilde{x} = 0$ (see table 4.3 for baseline inlet blood flow value $\tilde{Q}_0$). Conversely, for the pressure-driven boundary condition the inlet flux $\tilde{Q}_0$ must be solved for as part of the solution, where we impose the additional constraint $(\tilde{A}^{(s)}(0))^m - (\tilde{A}^{(s)}(0))^{-n} = \tilde{P}_0$ where $\tilde{P}_0$ (see table 4.3 for value of $\tilde{P}_0$) is the prescribed inlet pressure at the boundary $\tilde{x} = 0$.

Similarly, the static solution of perturbed steady state viscous model (4.36) must also have constant flux ($\tilde{q} = \overline{q}$) while the corresponding cross-sectional area profile $\tilde{A} = \tilde{A}^{(s)}(\tilde{x})$ must satisfy

$$(\tilde{A}^{(s)})_{\tilde{x}} = -\tilde{k}^{-1}\left(m(\tilde{A}^{(s)})^{m+1} + n(\tilde{A}^{(s)})^{-n+1}\right)^{-1}\left(8\pi\overline{q} + \left(\tilde{A}^{(s)}\right)^2\frac{\partial \tilde{p}_e}{\partial \tilde{x}}\right), \qquad (0 \le \tilde{x} \le 1). \tag{4.38}$$

Conversely, to find the static solution of the unperturbed system, we consider $\tilde{p}_e = 0$ in (4.38).

As for the inertial model, for a flux boundary condition at $\tilde{x} = 0$ we have $\overline{q} = \tilde{Q}_0$ whereas for the pressure boundary condition at $\tilde{x} = 0$ the inlet flux $\tilde{Q}_0$ must be solved for as part of the solution for $\tilde{A}$ by setting the additional constraint $\tilde{k}((\tilde{A}^{(s)}(0))^m - (\tilde{A}^{(s)}(0))^{-n}) = \tilde{P}_0$ where $\tilde{P}_0$ is the given constant inlet pressure.

In all cases discussed above, at the outlet, we prescribe free return of the fluid to the heart so that the pressure is effectively zero, so that $\tilde{p} = 0$. In cases where $\tilde{p}_e(1) = 0$, we obtain the reduced condition $\tilde{A}^{(s)} = 1$.

4.3 Numerical Methods

This section describes the numerical schemes used to solve both the steady and the unsteady versions of both the inertial and viscous models. Numerical simulations for both models were carried out using MATLAB version 2023a.

In each case, we discretise the spatial domain onto a uniformly spaced grid $\tilde{x}_j = j(d\tilde{x})$ for $j = 0, 1, 2, ...N$ grid points in the computational domain with the step size $d\tilde{x} = 1/N$. The temporal grids $\tilde{t}_l = l(d\tilde{t}), l = 0, 1/d\tilde{t}, 2/d\tilde{t}, .., \tilde{t}_p/d\tilde{t}$ are discretized using step size $d\tilde{t}$. The relationship between $d\tilde{x}$ and $d\tilde{t}$ is model-specific and is addressed separately for each model in section 4.3.2. The geometrical representation of the spatial discretisation is given in figure 4.3. We discretise all spatial derivatives using second-order finite difference stencils and temporal derivatives using a

first-order finite difference stencil, respectively. In all instances, we denote $\tilde{A}(x_j, t_l)$ and $\tilde{q}(x_j, t_l)$ as $\tilde{A}_j^l$ and $\tilde{q}_j^l$, respectively. Our unsteady semi-implicit scheme used here is inspired by the work of Stewart et. al. [60], where they found that an implicit representation of the highest order spatial derivative in each governing equation and an explicit representation of all the remaining terms is sufficient to ensure the numerical stability [60]. Moreover, the semi-implicit scheme remains stable and convergent within the time steps that are practically attainable in our simulations.

In subsection 4.3.1, the numerical methods employed to solve the steady-state solutions of both the viscous and inertial models are discussed. Subsection 4.3.2 provides a detailed description of the implicit and semi-implicit schemes used to solve the full unsteady versions of both models.

4.3.1 Numerical methods for static models

To solve the non-linear static inertial (4.37) and viscous (4.38) models, we discretize the spatial derivatives using the method listed above and employ Newton's method to compute the profiles $\tilde{A}^{(s)}(\tilde{x})$ using the 'fsolve' solver in MATLAB to solve these nonlinear algebraic equations. At internal grid points, the corresponding discretisations follow in the expected manner from the finite difference approximations. However, the boundary conditions require careful consideration.

In all cases, at the outlet we assume the effect of the external perturbation is negligible and use the Dirichlet boundary condition $\tilde{A}^{(s)}(\tilde{x} = 1) = 1$ which sets $\tilde{A}_N^{(s)} = 1$. At the inlet at $\tilde{x} = 0$, application of the boundary condition depends on the case being considered.

In case of the pressure driven viscous model (4.38) model, where the inlet pressure is specified as $\tilde{p}(0) = \tilde{P}_0$, the value of $\tilde{A}$ can be solved directly by setting an additional constraint $\tilde{k}((\tilde{A}_0^{(s)}(\tilde{x} = 0))^m - (\tilde{A}_0^{(s)}(\tilde{x} = 0))^{-n}) = \tilde{P}_0$ where $\tilde{P}_0$ is the given constant inlet pressure (for more detailed discussion see subsection 4.2.12). The chosen value of $\tilde{P}_0$ is given in Table 4.3.

For the pressure-driven inertial model (4.37), we follow the same process as discussed in the case of the viscous model above. However, the constraint for solving $\tilde{A}_0^{(s)}(\tilde{x} = 0)$ is slightly different and is given by $(\tilde{A}_0^{(s)}(\tilde{x} = 0))^m - (\tilde{A}_0^{(s)}(\tilde{x} = 0))^{-n} = \tilde{P}_0$.

For a flux-driven viscous model, where the inlet flux is prescribed as $\tilde{q} = \tilde{Q}_0 = 1$ (flux is constant everywhere), we discretise the first-order derivative in (4.38) using a second-order off-centred finite difference stencil. The chosen value of $\tilde{Q}_0$ is given in table 4.3.

For a prescribed flux-driven inertial model (4.37) where inlet flux is given as $\tilde{q}(0) = \tilde{Q}_0$, the spatial derivative at the inlet $\tilde{x} = 0$ is again discretised using an off-centred finite difference approximation, as in the viscous case.

4.3.2 Numerical methods for unsteady models

Full unsteady, non-linear simulations of both the inertial model (4.34) and the viscous model (4.36) can be constructed using a semi-implicit finite difference method. We start with a semi-

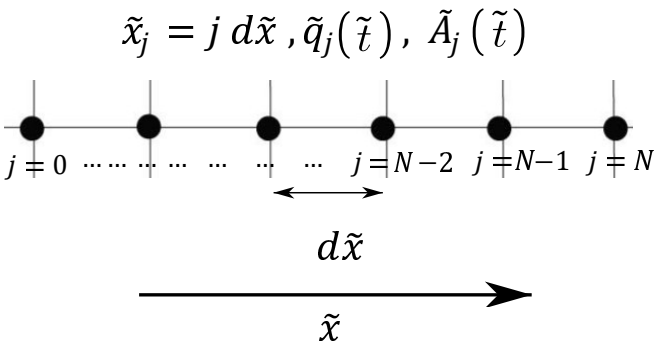

Figure 4.3: Finite difference scheme for approximation of spatial derivatives.

implicit approach where the highest-order spatial derivative involving $\tilde{q}$, $\tilde{A}$ is treated implicitly while all other terms are handled explicitly. To analyse the stability of our numerical scheme, we explore different combinations of explicit and implicit discretisation techniques. For instance, a second strategy involves implicitly treating the terms associated with the highest-order spatial derivative, external pressure, and its derivative while keeping the remaining terms explicit. We use this strategy later in subsection 4.5 to check if the implicit vs explicit discretisation makes any difference to the convergence of the unsteady numerical scheme.

At all internal grid points $j = 1, 2, ..., N-1$ in the computational domain, we obtain a system of linear equations in the $2N-2$ unknowns on $\tilde{A}_j^l$, $\tilde{q}_j^l$ for the inertial model (4.34) while for the viscous model (4.36) we formulate a system of linear equations for the $N-1$ unknowns on $\tilde{A}_j^l$.

In all cases, at the outlet we impose the Dirichlet boundary condition $\tilde{A} = 1$ (assuming $\tilde{p}_e = 0$ at $\tilde{x} = 1$) which gives $\tilde{A}_N^l = 1$.

In case of the flux-driven boundary condition, for the inertial model (4.34) at the inlet $j = 0$, we impose $\tilde{q}_0^l = \tilde{Q}_0$ directly and use an off-centered stencil to compute the corresponding spatial derivatives of $\tilde{A}$ and $\tilde{q}$ (for details see subsection 4.2.12).

In the case of pressure boundary condition for the inertial model (4.34), at the inlet $j = 0$ where the inlet pressure $\tilde{P}_0$ is prescribed, we determine $\tilde{A}_j^l(0,\tilde{t})$ by setting $(\tilde{A}_j^l(0,\tilde{t})^m - (\tilde{A}_j^l(0,\tilde{t}))^{-n} = \tilde{P}_0$ and we obtain this constraint directly from 'tube law' given in (4.35) where the external pressure $\tilde{p}_e = 0$, as explained in subsection 4.2.12.

In case of the flux-driven viscous model at the inlet $j = 0$, we introduce a fictitious node at the inlet $\tilde{x} = -d\tilde{x}$ and compute the corresponding cross-sectional area $\tilde{A}_j^l$ at the fictitious node by solving the boundary condition (4.36b). We then use the ghost point value to evaluate the second-order stencil for the given equation (4.36).

In case of pressure driven viscous model (4.36), at the inlet $j = 0$ the pressure $\tilde{P}_0$ is prescribed. We find $\tilde{A}$ by setting $\tilde{k}(((\tilde{A}_j^l(0,\tilde{t}))^m - (\tilde{A}_j^l(0,\tilde{t}))^{-n}) = \tilde{P}_0$.

We observe that how we discretise (i.e., implicitly or explicitly) the spatial terms present in the final model makes no difference to the outcome. The other factor, for example, the spatial grid size, plays a crucial role (see the detailed discussion in subsection 4.5).

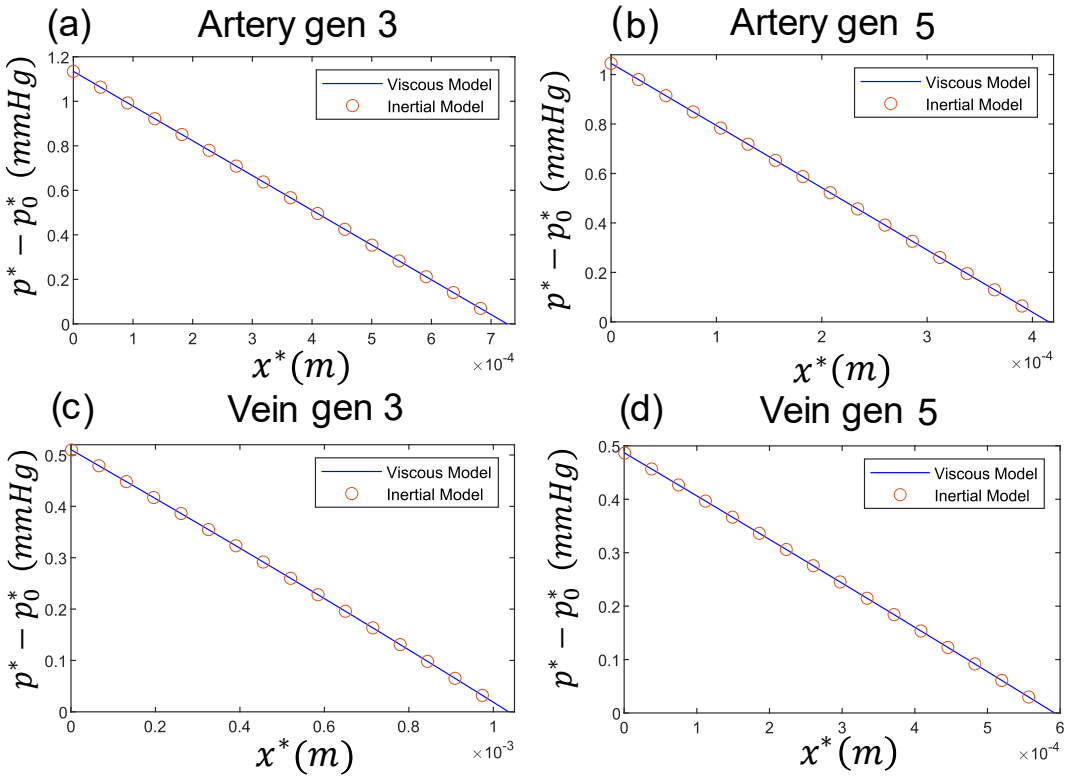

Figure 4.4: Behavior of the single vessel viscous and inertial models of vein and artery of two generations 3 & 5 using flux boundary condition at a steady state when maximum pressure amplitude $\Delta p_e^* = 0$: spatial profiles of the blood pressure along the vein of (a) generation 3 & (b) generation 5 and spatial profiles of the blood pressure along the artery of (c) generation 3 & (d) generation 5. $p_0^* = 0$ is the prescribed pressure at the outlet of the vessel. The solid blue line represents the viscous response, and the red circle represents the inertial response.

4.4 Steady Model Results

To understand the steady state behaviour of the viscous and inertial models in response to a fixed external pressure perturbation p_e^*, we begin by isolating the time-independent steady state solutions. Throughout this work, we consider the baseline blood flow direction from left to right.

In subsection 4.4.1, we examine normal blood flow conditions in the absence of external pressure p_e^* applied to the blood vessel. The key differences in the responses of different generations (3 and 5) of arteries and veins are outlined. Next, to assess the impact of a fixed (localised) external pressure perturbation on the shape of the retinal artery and vein, we perturb the steady-state models by applying a fixed external pressure of the form (4.3), which is spatially localised but uniform in time. The responses of these perturbed models are presented in the subsection 4.4.2.

4.4.1 Steady baseline case with no external pressure

We start by analysing the baseline case first, where we study the steady unperturbed solutions by considering $\tilde{p}_e = 0$ for both the inertial model (4.37) and for the viscous model (4.38) for a single

Table 4.3: Comparison of steady pressure drop between viscous model (4.38) and [61]

		Artery$(mmHg)$			**Vein**$(mmHg)$		
Gen No.	$Q_0^*(ml\,s^{-1})$	Δp_v^*	Δp_i^*	Δp_T^*	Δp_v^*	Δp_i^*	Δp_T^*
3	1.88×10^{-4}	1.1418	1.1297	1.1	0.5190	0.5190	0.5
4	9.41×10^{-5}	1.1082	1.1027	1.1	0.5021	0.5021	0.5
5	4.71×10^{-5}	1.0472	1.0448	0.9	0.4942	0.4942	0.5
6	2.35×10^{-5}	0.9801	0.9791	0.9	0.4692	0.4692	0.5
7	1.18×10^{-5}	0.8965	0.8961	0.9	0.4463	0.4463	0.4
8	5.88×10^{-6}	0.8303	0.8303	0.7	0.4069	0.4069	0.4
9	2.94×10^{-6}	0.7371	0.7371	0.6	0.3811	0.3811	0.4
10	1.47×10^{-6}	0.6426	0.6426	0.6	0.3439	0.3439	0.4
11	7.35×10^{-7}	0.5578	0.5578	0.4	0.2937	0.2937	0.3
12	3.68×10^{-7}	0.4619	0.4619	0.4	0.2536	0.2536	0.2
13	1.84×10^{-7}	0.3669	0.3669	0.3	0.2182	0.2182	0.2

vessel under a prescribed inlet flux boundary condition. Additionally, in subsection 4.4.1.1, we compare the influence of prescribed inlet flux and prescribed inlet pressure on the steady-state responses. In the next subsection 4.4.1.2, we compute the total pressure drop across different generations of arteries and veins calculated from the unperturbed inertial and viscous models and compare the results with values reported in the literature [61].

Figure 4.4 plots the arterial (see figure 4.4a,b) and venous (see figure 4.4c,d) responses for generations 3 and 5 for both viscous and inertial responses solved using flux-driven boundary conditions. The pressure profiles for both arteries and veins (see figure 4.4) for both generations decrease almost perfectly linearly with the slope set by the prescribed flow rate. The negative pressure gradient is due to the work done against viscous effects in the baseline flow. For this choice of parameters, the prediction of the inertial model agrees almost perfectly with that of the viscous model in all cases. However, the pressure gradients are much smaller in the vein as the vein is less stiff than the artery. In both types of vessel (artery and vein), we observe that the pressure drop is much larger in generation 3 than in generation 5 because the corresponding flow rate in generation 3 is four times larger compared to that in generation 5.

In the next subsection 4.4.1.1, we compare the steady responses obtained by using the pressure boundary condition and flux-driven boundary condition.

4.4.1.1 Comparison of flux and pressure-driven steady flow

Figure 4.5 compares the steady flow along a vein of generation 3 computed using both the inertial model (4.37) and the viscous model (4.38). In each case, we prescribe one of the upstream pressure or upstream flow rate and compute the corresponding quantity using the numerical solution of the steady model (see subsection 4.2.12). In figure 4.5, we plot these two quantities against one another and find that in the absence of external pressurisation, the inertial and viscous models

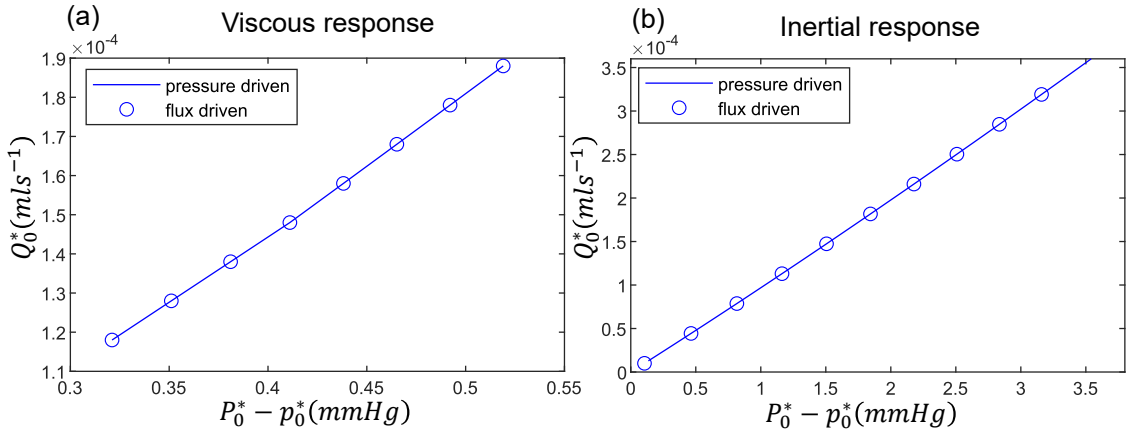

Figure 4.5: Comparison of boundary conditions for venous response of generation 3 for steady models showing inlet flux Q_0^* vs inlet blood pressure P_0^* showing (a) viscous model and (b) inertial model. $p_0^* = 0$ is the prescribed pressure at the outlet of the vessel. The solid line is for a pressure-driven boundary condition, and the circle is for a flux-driven boundary condition.

show almost identical qualitative and quantitative behaviour. This is because the inertial model (4.37) differs from the viscous model (4.38) only by one additional term, the convective inertia term, which, for these parameters, has a minimal impact on the response since the inlet flux is relatively small.

In summary, for the steady-state unperturbed model, the inlet pressure P_0^* and inlet flux Q_0^* are interchangeable, allowing Q_0^* to be determined explicitly when P_0^* is given, and vice versa.

4.4.1.2 Comparison of steady flow for upstream boundary conditions

We now calibrate these steady predictions to a small network which mimics the superior temporal quadrant of the human eye [61]. We denote the pressure difference between the inlet and outlet of the vessel by Δp^*, where Δp_i^* is obtained from the inertial model, p_v^* from the viscous model, and p_T^* from the model retina given in [61]. Figure 4.6 and table 4.3 compute the pressure difference $\Delta p_i^*, \Delta p_v^*$ across different generations from 3 to 13 for both arteries (see figure 4.6a) and veins (see figure 4.6b) from the unperturbed steady state (i.e., $\tilde{p}_e = 0$) for inertial (4.37) and viscous (4.38) models using the prescribed flux boundary condition and then compare these values with the baseline values (Δp_T^*) available in the literature, assuming a retinal vessel as a rigid tube [61]. Similarly in figure 4.6(c,d), we compare the inlet flow rate Q_v^*, Q_i^* obtained from the steady unperturbed viscous (4.38) and inertial model (4.37) solved using pressure-driven boundary condition for different generations of vessels and then compare these inlet flow rates with the baseline flow rate Q_0^* given for rigid tube in the literature [61]. Note that the flow at each generation is assigned by equally splitting the total retinal blood flow across all bifurcations.

For both arteries and veins, the pressure drop decreases with each successive generation along the vascular tree (see table 4.3, figure 4.6). From figure 4.6(a,b), we see that the responses from the inertial and the viscous models become increasingly similar with each successive generation along the vascular tree. As previously discussed, the only distinction between the two steady

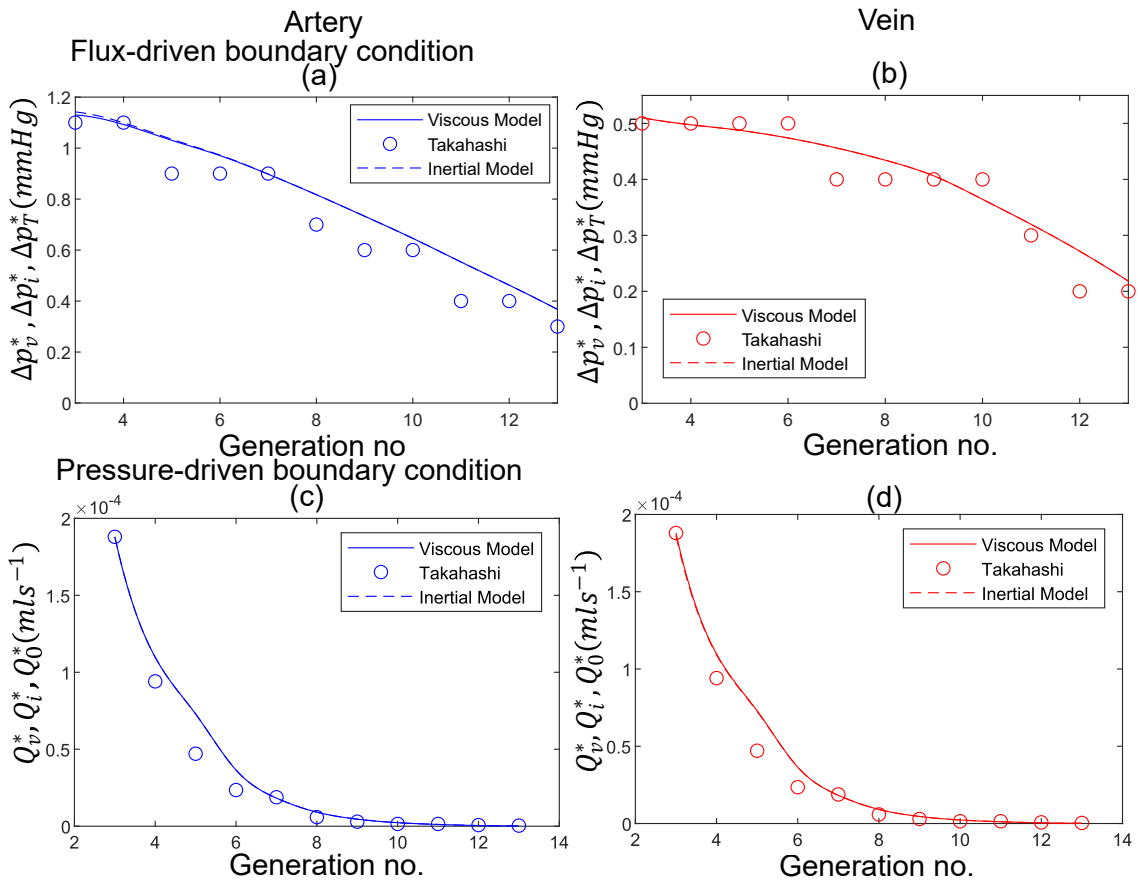

Figure 4.6: Comparison of steady flow for upstream flux-driven boundary condition: comparisons of $\Delta p_v^*, \Delta p_i^*, \Delta p_T^*$ vs generation number for steady (i.e., $\tilde{p}_e = 0$) in viscous (4.38) model and steady inertial model (4.37) with the model retina values given in [61] (a) for artery, (b) for the vein and comparison of Q_v^*, Q_i^*, Q_0^* between different generation shown for (c) for the artery and (d) for the vein. Here Δp^* and Q_0^* are the inlet and outlet pressure difference across each generation calculated and inlet flow condition from our model, $\Delta p_v^*, Q_v^*$ for the viscous model, $\Delta p_i^*, Q_i^*$ for the inertial model, and $\Delta p_T^*, Q_0^*$ denote the pressure difference calculated from [61]. The blue line represents the arterial response, and the red line for the viscous response. The solid line represents the viscous model, the dashed line represents the inertial response, and the circle represents the baseline parameter values.

models is the convective inertia term in the inertial model. However, for the given parameters, this term has minimal influence on the system's response, as the inlet flux decreases with each successive generation, and viscous effects are getting stronger compared to inertial effects.

Looking at figure 4.6(a,b), we observe that our model is slightly over-predicting the pressure drops compared to the Takahashi et. al., listed in table 4.3; they developed a theoretical model describing hemodynamics in the retinal microvascular network under the assumption of vessels with fixed cross-sectional area. For a detailed discussion on this model, see the subsection 1.3 of Chapter 1. Conversely, in our models (4.37,4.38), retinal vessels have flexible walls, allowing for interaction with the blood flow. Moreover, since the outlet pressure condition we choose is $\tilde{p} = 0$, the vessel can not inflate at the outlet. As a result, the vessel has to inflate at every other point along the vessel to account for the work done against the viscous effects. This inflation

causes the overall increase in pressure as we move backwards along the vessel. Also, the values quoted by Takahashi et al. in [61] are rounded up to one significant digit, which is also a potential source of discrepancies between our predictions.

Similarly, for the pressure-driven case, our predicted inlet flux is initially slightly higher than their values (see figure 4.6(c,d)) reported in the literature [61], but as we move towards smaller values, our predictions show increasing agreement. This is because larger vessels are more compliant than smaller vessels. As a result, the vessel has to inflate at all other points in the vessel except at boundaries where values are already prescribed. This inflation causes an increase in flow rate compared to the rigid-tube case. However, as vessel size decreases, our predictions align with theirs. Also, as discussed before, the values obtained from [61] are rounded up to two significant digits, which might be another source for discrepancies.

Overall, the predictions obtained from our steady unperturbed models (for both viscous and inertial models under the flux-driven and the pressure-driven boundary conditions) are not significantly different from those of the rigid-tube model reported in [61]. This indicates that if we want to model the blood flow in a healthy retina, we can consider blood vessels as rigid tubes. This approach reduces the computational complexity of the numerical scheme developed to solve the model. Having established the behaviour in the healthy case, in subsection 4.4.2, we concentrate on pathological scenarios, specifically retinal vein occlusion (RVO).

4.4.2 Steady baseline case with fixed external pressure

We start with the same steady unperturbed model (sup) as described in subsection 4.4.1, where for the artery in the case of the flux-driven boundary condition, we prescribe the baseline inlet flux $Q_0^* = 1.88 \times 10^{-4} ml\,s^{-1}$ [61] and for the pressure-driven case, we prescribe the baseline inlet pressure $P_0^* = 1.1344 mmHg$. In this section, we consider the vein of generation 3. For instance, in the flux-driven case, we consider the baseline inlet flux $Q_0^* = 1.88 \times 10^{-4} ml\,s^{-1}$ [61], and in the pressure-driven case, we prescribe the baseline inlet pressure $P_0^* = 0.5209 mmHg$. At the inlet $p_e^* = 0$ and as discussed in subsection 4.4.1.1, when $p_e^* = 0$, the inlet pressure P_0^* and inlet flux Q_0^* are interchangeable. The values of P_0^* for both artery and veins can be obtained directly from the flux-driven case. However, to mimic the effect of retinal vein occlusion on a single vessel and to see how the vessel cross-sectional area and blood pressure change, we perturb the sup inertial (4.37) and sup viscous (4.38) models by applying a time-independent localized external pressure perturbation p_e^* of the form (4.3) at the midpoint along the length of the vessel. While keeping everything else identical, we directly compare the responses of this steady perturbed model (sp) with the sup response. In the following two subsections 4.4.2.1 and 4.4.2.2, we discuss the effect of spatial extent k_p^* and maximum pressure amplitude Δp_e^* on the responses of steady perturbed model.

Figure 4.7 compares the sup and sp flow along a vein (or artery, see figure 4.8) of generation 3 obtained from the inertial model (4.37) and the viscous model (4.38) solved using either a

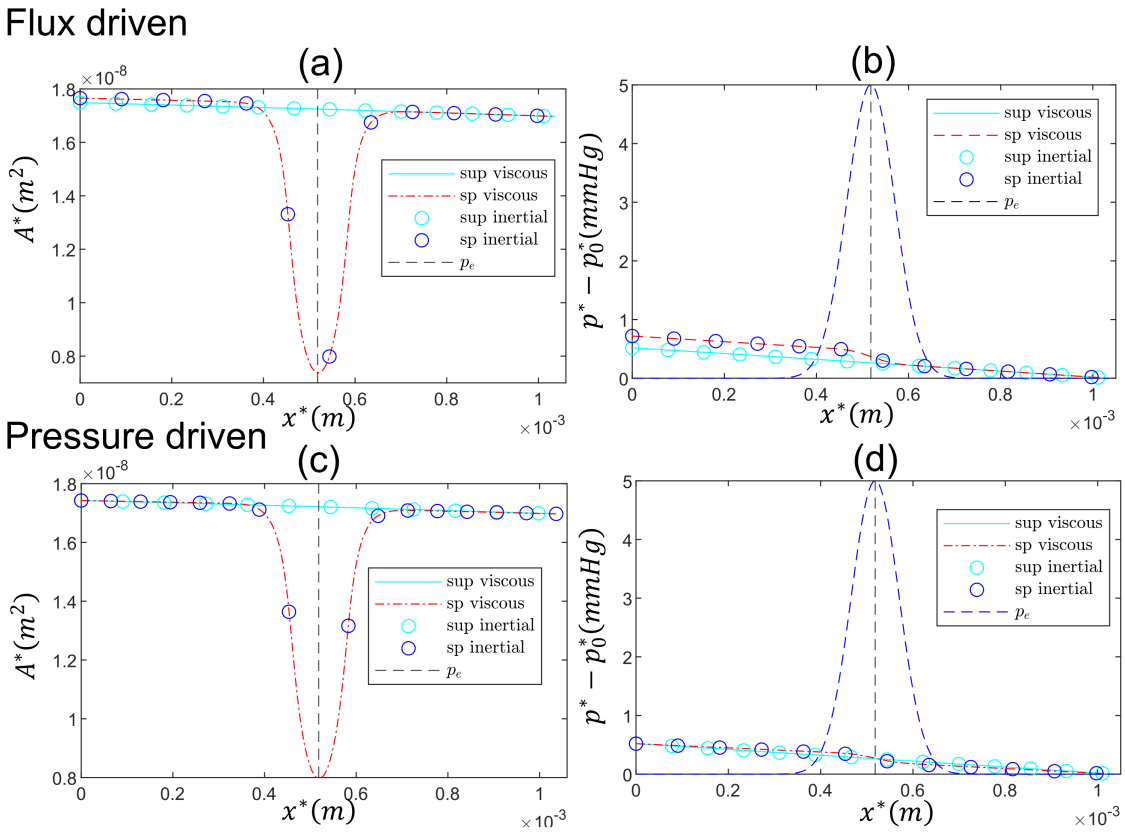

Figure 4.7: Steady-state responses of vein of generation 3 for the inertial and the viscous models, obtained using flux boundary conditions under an externally applied pressure perturbation with a maximum amplitude of $\Delta p_e^* = 5mmHg$, showing: (a) cross-sectional area A^*, (b) blood pressure p^*, and external pressure perturbation p_e^* for flux-driven boundary condition, (c) cross-sectional area A^* and (d) blood pressure p^*, and external pressure perturbation p_e^* for pressure-driven boundary condition. The black dashed line represents the spatial location of the point of occlusion. The red-dashed lines are for the steady perturbed (SP) viscous response, the blue circles for the steady perturbed (SP) inertial response, the solid cyan line for the steady viscous response, and the cyan dashed line for the steady inertial response. 'sup' stands for steady unperturbed state.

prescribed upstream flux (see figure 4.7(a,b) for vein and figure4.8 (a,b) for artery) or a prescribed upstream pressure boundary condition (see figure 4.7(c,d) for vein and figure 4.8(c,d) for artery).

Looking at flux-driven flow for vein of generation 3 given in figure 4.7(a,b), the constriction restricts the local blood flow, and so the blood is displaced and redistributed upstream (i.e., the left side of the point of constriction, the black dashed line in figure 4.7) and downstream (i.e., the right side of the point of constriction, the black dashed line in figure 4.7). As expected, the cross-sectional area A^* (the red dashed line and blue circles in figure 4.7a) expands upstream of the point of constriction compared to the sup profile (cyan solid line and cyan circle in figure 4.7a) to accommodate the displaced fluid. Similarly, pressure p^* (red dashed line and blue circles in figure 4.7b) increases upstream of the point of construction relative to the sup state (cyan solid line and cyan circle in figure 4.7b). However, we note that downstream of the constriction, the pressure remains almost unchanged and the area profile is similar to the sup case. This lack of

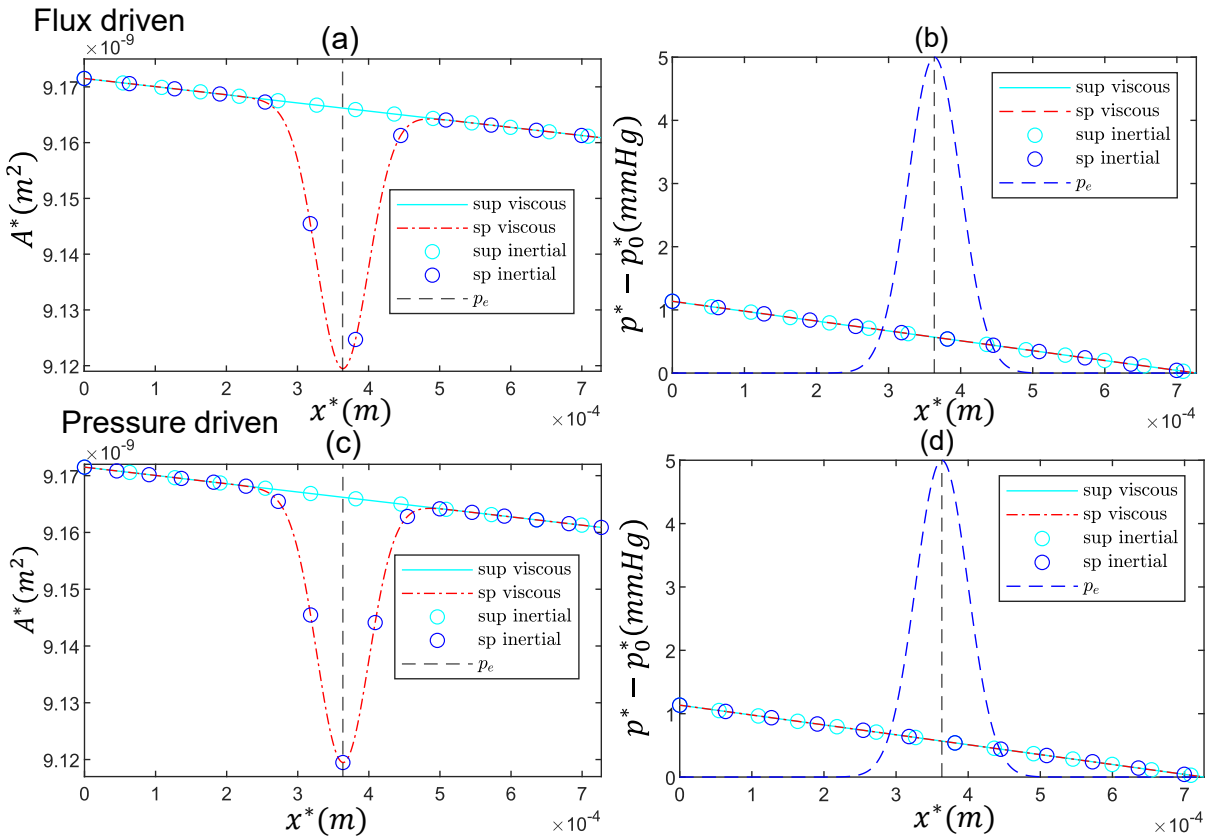

Figure 4.8: Steady-state responses of artery of generation 3 for the inertial and the viscous models, obtained using flux boundary conditions under an externally applied pressure perturbation with a maximum amplitude of $\Delta p_e^* = 5mmHg$, showing: (a) cross-sectional area A^*, (b) blood pressure p^*, and external pressure perturbation p_e^* for flux-driven boundary condition, (c) cross-sectional area A^* and (d) blood pressure p^*, and external pressure perturbation p_e^* for pressure-driven boundary condition. The black dashed line represents the spatial location of the point of occlusion. The red-dashed lines are for the steady perturbed (SP) viscous response, the blue circles for the steady perturbed (SP) inertial response, the solid cyan line for the steady viscous response, and the cyan dashed line for the steady inertial response.

expansion can be attributed to the downstream boundary condition assuming the outlet pressure to remain fixed. As the vessel is inflated, pressure p^* is higher than the external pressure p_e^* (i.e., $p^* > p_e^*$) both in the upstream and downstream regions whereas the external pressure p_e^* is much higher than the blood pressure p^* in the middle of the vessel as we apply the constriction externally in the middle of the vessel along the length.

Now looking at the pressure-driven case for vein given in figure 4.7(c,d), the slope of the pressure profile at the inlet (the cyan line in figure 4.7d) in the sp state is set by the pressure drop between the inlet (i.e.,$\tilde{p} = \tilde{P}_0$) and the outlet (i.e.,$\tilde{p} = 0$) of the vessel. Unlike the flux-driven case, we observe that the area and pressure profiles are inflated both upstream and downstream of the constriction (see figure 4.7c,d). However, the amount of expansion for the pressure-driven case is much smaller than the flux-driven case, and the overall pressure gradient is reduced both up and downstream as the global value must be maintained (the gradient of the profile is reduced). As a result, the inlet flow rate for the viscous model reduces by 75.3% to $1.416 \times 10^{-4} mls^{-1}$

compared to the baseline value for the sup state given above. For the inertial model, the inlet flow rate reduces by 75.47% to $1.419 \times 10^{-4} ml s^{-1}$. Following our discussion for the sup state given in subsection 4.4.1, we can conclude that the effect of upstream boundary conditions is only negligible before the flow is perturbed. However, in pathological situations when the constriction is applied to the vein, the boundary condition now has a significant impact on the behaviour of the model. This will be particularly interesting in the context of upstream propagation of pressure through a larger network, where boundary conditions are set by matching to neighbouring vessels.

The artery of generation 3 is much stiffer (i.e., by three orders of magnitude) than the corresponding vein of generation 3, resulting in smaller expansions in the artery (see figure 4.8a,b,c,d) compared to the vein (see figure 4.7a,b,c,d) in response to the same external pressure applied and similar boundary conditions. Now comparing the responses obtained from prescribed pressure-driven boundary condition (see figure 4.8c,d) and prescribed flux-driven boundary condition (see figure 4.8a,b), we observe that for a pressure-driven system, the inlet flow through the viscous model decreases to $Q_0^* = 1.877 \times 10^{-4} ml s^{-1}$ ($Q_0^* = 1.879 \times 10^{-4} ml s^{-1}$ for inertial model) compared to the baseline flow rate given for the flux-driven boundary condition of sup model. Thus, for the pressure-driven case, we observe only limited upstream effect for both cross-sectional area A^* (see figure 4.8c) and pressure p^* (see figure 4.8d) responses compared to the flux-driven flow. To this end, it is safe to conclude that to see a noticeable deformation in an artery, we need to apply a substantial amount of external pressure perturbation, which is much smaller for the vein of the same generation. However, it is important to note that we are primarily interested in studying the mechanism of retinal vein occlusion. Henceforth, we disregard the arteriole network and continue to work with the vein in the rest of this chapter. We return to the arterioles in Chapter 5 as it is important to build a complete arterio-venous network in Chapter 6.

4.4.2.1 Effect of the spatial extent of occlusion k_p^*

To examine how the control parameter k_p^*, which dictates the spatial extent of the occlusion, influences the responses of the sp model, we start with the sp inertial model (4.38) and the sp viscous model (4.37) discussed in subsection 4.4.2. For the vein of generation 3, in flux-driven case, we consider the baseline inlet flux $Q_0^* = 1.88 \times 10^{-4} ml s^{-1}$ and for the pressure-driven case, we prescribe the baseline inlet pressure $P_0^* = 0.5209 mmHg$ and systematically we vary the value of k_p^*, allowing us to observe how the cross-sectional area A^* changes in each case (figure 4.9a,b). Also, we discuss how the inlet pressure P_0^* changes under a flux-driven boundary condition (see figure 4.9c) and the inlet flow rate Q_0^* varies under a pressure-driven boundary condition for different values of k_p^* (see figure 4.9d).

As we increase k_p^*, the spatial effect of the external pressure p_e^* becomes confined around the immediate vicinity of the point of occlusion x_p^*. As expected, we observe a corresponding confinement in the profile of the cross-sectional area A^* for both flux-driven and pressure-driven cases (see the dot-dashed line corresponding to $k_p^* = 800$ in figure 4.9a,b). Furthermore, for the

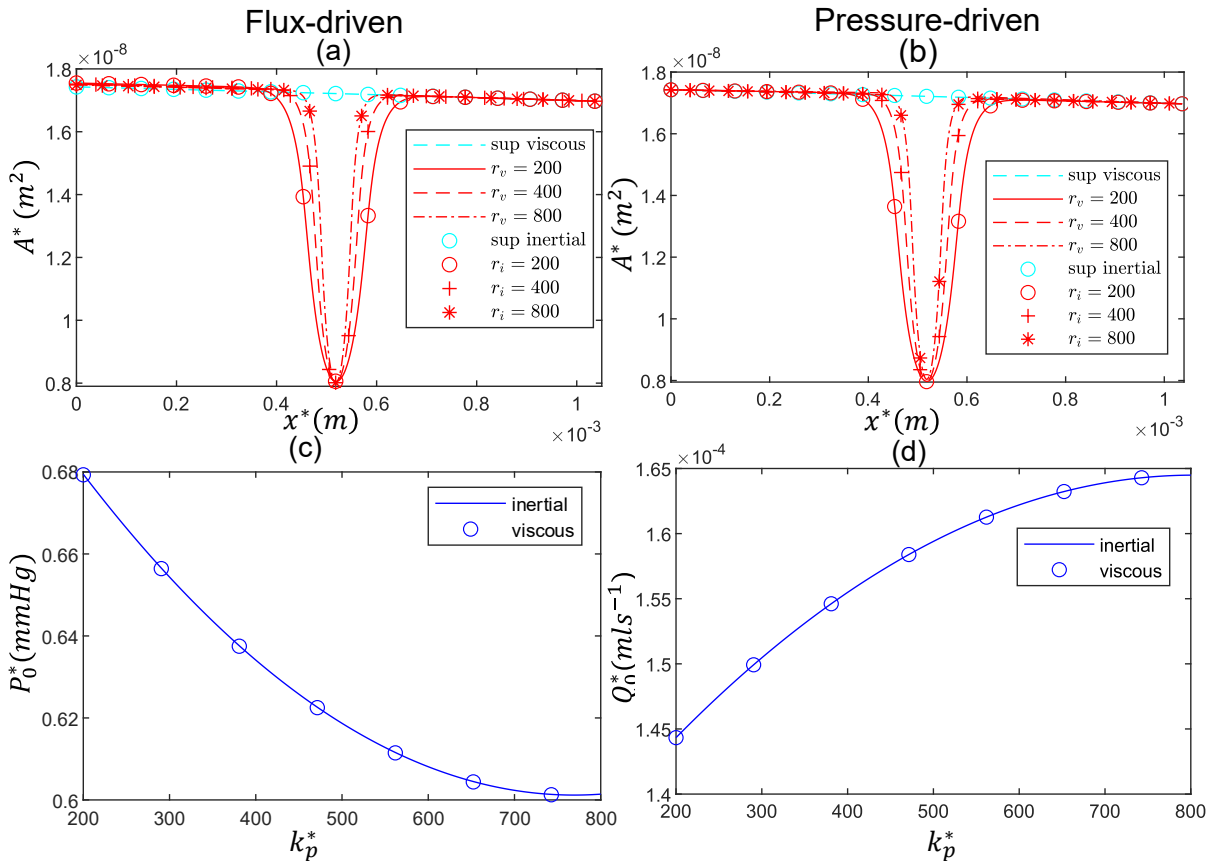

Figure 4.9: Effect of the three different spatial extents of occlusion k_p^* on the vein of generation 3 in the steady-perturbed inertial and viscous models, subjected to an externally applied pressure perturbation with a maximum amplitude of $\Delta p_e^* = 1 mmHg$, showing: (a) spatial profiles of the cross-sectional area A^* obtained for flux-driven case, (b) spatial profiles of the cross-sectional area A^* obtained for pressure-driven case, (c) inlet pressure P_0^*, and (d) inlet flux Q_0^* for three different k_p^*. r_v is for the viscous response, and r_i is for the inertial response. 'sup' denotes the steady unperturbed state.

flux-driven case, while the inlet flux Q_0^* is constant, the pressure drop along the vessel P_0^* for both viscous and inertial models decreases steadily as we increase the value of k_p^* (see figure 4.9c). This is because as we increase k_p^*, the effect of p_e^* becomes more confined to the point of occlusion x_p^* so the expansion of cross-sectional area from the sup state (see the cyan dashed line for viscous model and cyan circle for inertial model in figure 4.9a) becomes less evident in the upstream and downstream of the constriction (see figure 4.9a). As the blood pressure is connected to the area by 'tube law', so as the area expansion in the upstream end decreases with increasing k_p^*, the driving pressure P_0^* also decreases (see figure 4.9c). Now, looking at figure 4.9(d) for the pressure-driven case, we observe that the inlet flux Q_0^* increases as we increase k_p^*. Increasing k_p^* reduces the change in pressure gradient through the constriction, and therefore, the inlet flow Q_0^* must increase to maintain the overall pressure gradient. As the flow rate increases, we now observe minor discrepancies between inertial and viscous models.

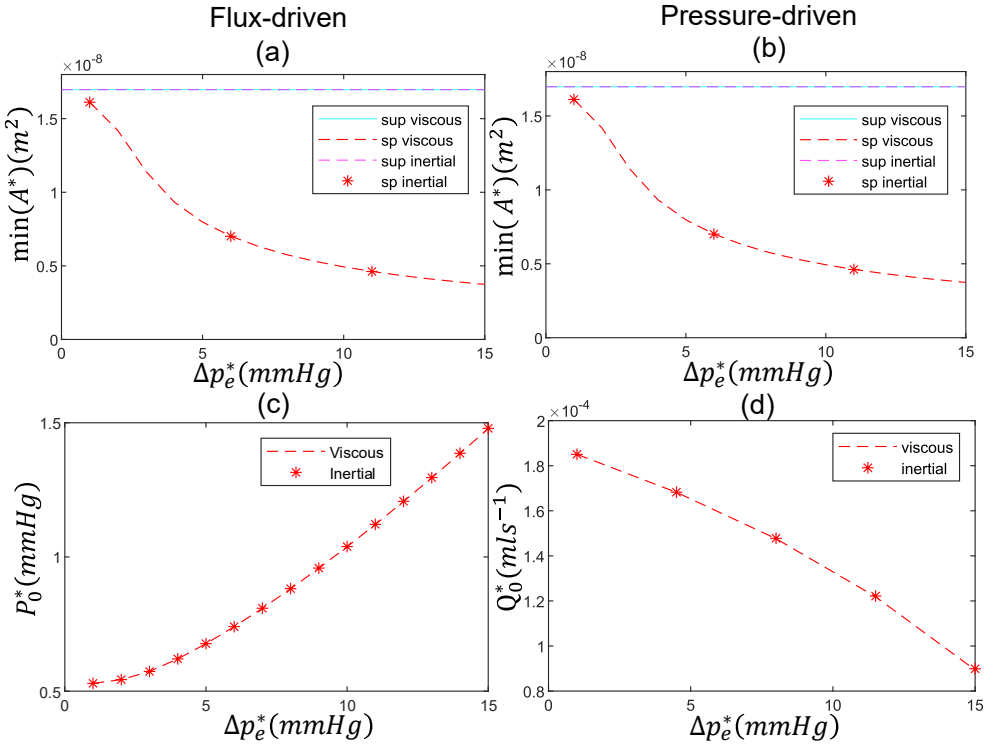

Figure 4.10: Effect of the different maximum amplitude of pressure Δp_e^* applied externally on the steady-state inertial and viscous models showing: (a) minimum cross-sectional area obtained using flux boundary condition, (b) minimum cross-sectional area obtained using pressure boundary conditions, (c) the inlet pressure P_0^* for flux-driven case, and (d) the inlet flux Q_0^* for pressure-driven case. 'sup' stands for steady unperturbed state and 'sp' stands steady perturbed state.

4.4.2.2 Effect of maximum pressure amplitude Δp_e^*

To examine the impact of the second control parameter, the maximum pressure amplitude Δp_e^* on the vein of generation 3, we start from the sp inertial (4.37) and sp viscous (4.38) discussed in subsection 4.4.2 and vary Δp_e^* between $1 mmHg$ and $15 mmHg$ and examine its influence on the degree of vessel constriction in the sp state. Figure 4.10 illustrates how the minimum area A^* changes for both flux-driven (see figure 4.10a) and pressure-driven (see figure 4.10b) boundary conditions and also the changes in driving pressure P_0^*(see figure 4.10c) and inlet flux Q_0^*(see figure 4.10d) as the maximum pressure amplitude Δp_e^* increases.

As we increase the amount of pressure perturbation Δp_e^*, the minimum value of the cross-sectional area for the constricted vessel reduces steadily and goes below the baseline value obtained from the sup state (see sup state in figure 4.10a,b). This is because as Δp_e^* increases, the vessel experiences greater constriction, leading to a reduction in the cross-sectional area A^* and, as a result, the minimum value of A^* reduces significantly.

Looking at the flux-driven case given in figure 4.10(c), when the inlet flux $Q_0^* = 1.88 \times 10^{-4} mls^{-1}$ is fixed, as we increase the maximum pressure amplitude Δp_e^*, P_0^* increases. In contrast, for the pressure-driven case when the driving pressure $P_0^* = 0.5209 mmHg$ is fixed, the inlet flux Q_0^* decreases with increasing Δp_e^* (see figure 4.10d) to maintain the overall pressure

gradient.

4.5 Unsteady Model Validation

Before exploring the full non-linear dynamical behaviour of both models, we first aim to understand the convergence of the numerical schemes developed to solve both the unsteady inertial system (4.34) and the viscous system (4.36); in this case, we consider prescribed upstream flux boundary conditions. In this section, we consider a vein in generation 3 with prescribed inlet flux $Q_0 = 1.88 \times 10^{-4} ml\,s^{-1}$, the steady baseline value computed earlier in the absence of any perturbation. To study the convergence of the numerical scheme, we investigate the role of two key numerical parameters: the time step $d\tilde{t}$ and the number of spatial grid points N, where the spatial step size is given by $d\tilde{x} = 1/(N-1)$. We consider four different values of N, i.e., $N = 801, 1201, 1601, 2501$, to understand the influence of the number of spatial grid points on the convergence of the numerical schemes. In the viscous model, the time step $d\tilde{t}$ is calculated using the balance $d\tilde{t} = \alpha_1 (d\tilde{x})^2$ while in the case of the inertial model, the time step $d\tilde{t}$ is calculated using the balance $d\tilde{t} = \alpha_2 (d\tilde{x})$, where in this case α_2 is called the Courant number. To investigate the impact of the choice of time-step $d\tilde{t}$, we choose different α_1 and α_2 values, and analyse the solution at three different spatial locations along the vessel namely $x^* = \frac{2}{5}L^*, \frac{1}{2}L^*, \frac{7}{10}L^*$, where L^* is the length of vein generation 3. We start with the unperturbed unsteady model in subsection 4.5.1. In the following subsection 4.5.2, we perturb the model by applying a non-zero time-independent fixed external pressure perturbation.

4.5.1 Zero external pressure perturbation

As no external pressure perturbation is applied ($\Delta p_e^* = 0, f^* = 0$ in equation 4.3), in this case, we consider unsteady simulations starting from the sup state (see subsection 4.2.12).

To understand the convergence of the numerical scheme, we quantify the relative errors by comparing the area and flux values $\upsilon = (\tilde{A}, \tilde{q})$ obtained from the unsteady unperturbed model (uup) at time $\tilde{t}$ with those responses obtained from the sup model for a given spatial location $\tilde{x}$. Mathematically, we define the error $e_\upsilon^{(1)}$ as a function of $\tilde{x}$ for each N as:

$$e_\upsilon^{(1)}(\tilde{x}) = \lim_{\tilde{t}\to\infty} \left| \frac{\upsilon(\tilde{x},\tilde{t}) - \upsilon_{sup}(\tilde{x})}{\upsilon_{sup}(\tilde{x})} \right|, \tag{4.39}$$

where $\upsilon_{sup}(\tilde{x})$ indicates the corresponding sup response of the corresponding system. In this calculation, it is not possible to actually consider the limit as $\tilde{t} \to \infty$, and so we approximate the infinite limit by a large value of $\tilde{t}$, which we denote as t_∞^*. We endeavour to choose $\tilde{t}_\infty$ such that the behaviour has settled down into the steady state.

We observe that when we start the unsteady simulation from the sup state with no perturbation

applied, the error $e_{\upsilon}^{(1)}$ does not accumulate substantially for any of the spatial grid resolution we tested, and remains essentially fixed for all time. Conversely, we also observe that as we change the values of α_1, α_2 while keeping all other parameters, including N fixed, no appreciable differences are observed in the convergence of the scheme.

We conclude that the choice of N and $d\tilde{t}$ has no significant impact on the convergence of the numerical scheme when no external pressure is applied.

4.5.2 Non-zero fixed external pressure perturbation

To understand the convergence of the perturbed unsteady viscous and inertial models (solved using flux-driven boundary condition), we introduce a non-zero but time-independent external pressure perturbation (i.e., $f^* = 1$ in equation 4.3) with a maximum amplitude $\Delta p_e^* = 1 mmHg$, while keeping all the other parameters the same as before. However, we consider a wider range of Δp_e^* in figure 4.13 below. In this section, we initiate all unsteady simulations from the sp state described in subsection 4.2.12, unless stated otherwise.

To quantify the errors in the numerical scheme, for a given spatial location $\tilde{x}$ we define the error as

$$e_{\upsilon}^{(2)}(\tilde{x}) = \lim_{\tilde{t}\to\infty} \left| \frac{\upsilon(\tilde{x},\tilde{t}) - \upsilon_{sp}(\tilde{x})}{\upsilon_{sp}(\tilde{x})} \right|, \quad \upsilon = (\tilde{A}, \tilde{q}), \tag{4.40}$$

where υ_{sp} indicates the sp state of the inertial and viscous models.

In the following two subsections 4.5.2.1 and 4.5.2.2, we consider the role of the spatial grid resolution N and time steps $d\tilde{t}$ in the convergence of the numerical scheme developed to solve the unsteady inertial and viscous models. The discrepancies observed in the convergence of the unsteady viscous model to the sp state motivate the introduction of a fixed point map to examine the unsteady viscous model in more detail, as discussed in subsection 4.5.2.3.

4.5.2.1 Convergence of the inertial model

To understand the dependence of the convergence of the numerical scheme developed for the inertial model on the spatial grid resolution, for a given factor $\alpha_2 = 0.01$, we consider four different numbers of spatial grid points, namely $N = 801, 1201, 1601, 2501$.

At time $t_\infty^* = 0.2s$, keeping $\alpha_2 = 0.01$, figure 4.11(a) plots the amplitude of $e_{\tilde{q}}^{(2)}$ at the spatial location $x^* = \frac{2}{5}L^*$, as we change N, while figure 4.11(b) keeps the value of $N = 801$ fixed and changes the value of α_2 plotted at spatial location $x^* = \frac{1}{2}L^*$. Figure 4.11(c) plots the value of $e_{\tilde{q}}^{(2)}$ at the spatial location $x^* = \frac{1}{2}L^*$ for different Δp_e^* while keeping $N = 801$ fixed. From figure 4.11(a), as we increase the spatial grid resolution, the amplitude of $e_{\tilde{q}}^{(2)}$ decreases, indicating that the unsteady perturbed inertial profiles are approaching the sp inertial state. As expected the error $e^{(2)}$ of the scheme is proportional to $\frac{1}{N^2}$ (see the solid blue line in figure 4.11a). It is important to note that the amplitude of $e_{\tilde{q}}^{(2)}$ is almost identical at all three spatial locations

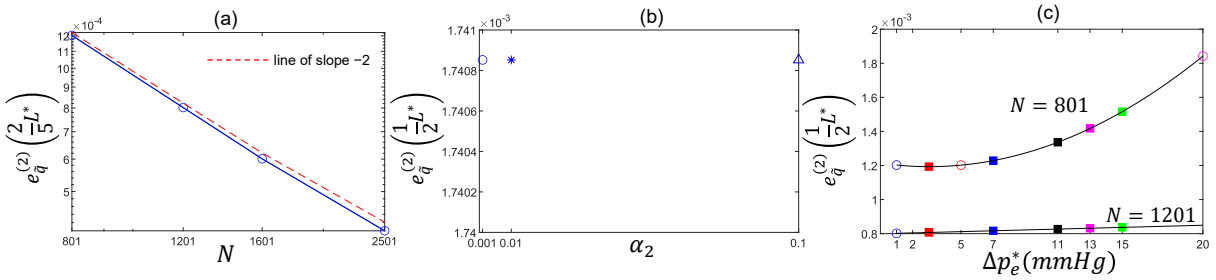

Figure 4.11: Effect of spatial grid-points and time-steps $N, d\tilde{t}$, respectively on inertial model (solved using flux-driven boundary condition) showing: measure of the error quantity $e^{(2)}_{\tilde{q}}$ obtained for (a) various spatial grid points N at the spatial locations $x^* = \frac{2}{5}L^*$, (b) for different values of $\alpha_2 = 0.001, 0.01, 0.1$ and (c) for different values of maximum pressure amplitude Δp^*_e at the spatial locations $x^* = \frac{1}{2}L^*$ where L^* is the baseline length of the vein generation 3. The red-dashed line in (a) is the reference line of slope -2. The final time of simulation in each spatial response is $t^*_\infty = 0.2s$.

$x^* = \frac{1}{4}L^*, \frac{1}{2}L^*, \frac{2}{5}L^*$ in the long-time limit (i.e, $t^*_\infty = 0.2s$) for large N. From this observation, we conclude that for arbitrarily large N, the predicted state from the unsteady perturbed inertial model will approach the sp model. Considering computational resources and time, we choose a large enough N such that the amplitude of $e^{(2)}_{\tilde{q}}$ remains sufficiently small over a simulation. To understand the role of $d\tilde{t}$, in figure 4.11(b) we change the α_2 value and plot $e^{(2)}_{\tilde{q}}$ as a function of α_2 at the spatial location $x^* = \frac{1}{2}L^*$. For fixed grid resolution $N = 801$, the values of $e^{(2)}_{\tilde{q}}$ obtained for three different α_2 are nearly identical (differences are of order 10^{-7}), indicating that α_2 has no significant influence on $e^{(2)}_{\tilde{q}}$ and, consequently, on the convergence behaviour of the numerical scheme. It is safe to conclude that when the number of grid points is fixed, the convergence of the numerical scheme developed for the inertial model does not depend explicitly on the choice of time step $d\tilde{t}$ when α_2 lies between 0.001 and 0.1. In figure 4.11(c), we observe that as we increase the maximum pressure amplitude Δp^*_e, the value of $e^{(2)}_{\tilde{q}}$ increases and reaches 1.8×10^{-3} for $\Delta p^*_e = 20mmHg$. However, if we increase spatial grid resolution to $N = 1201$, the value of $e^{(2)}_{\tilde{q}}$ decreases significantly and becomes 0.81×10^{-3} for $\Delta p^*_e = 15mmHg$. In this case, for $N = 801$ and $\Delta p^*_e = 20mmHg$, the error is 0.18% for the spatial location $x^* = \frac{1}{2}L^*$, which we deem to be acceptable.

In the following subsection 4.5.2.2, we discuss the convergence of the numerical scheme developed for the unsteady viscous model.

4.5.2.2 Convergence of the viscous model

Figure 4.12 plots the response of the viscous model including the temporal response of the cross-sectional area A^* (see figure 4.12a), and the axial flux q^* (see figure 4.12c) at three spatial locations $x^* = \frac{2}{5}L^*, \frac{1}{2}L^*, \frac{4}{5}L^*$, where L^* is the length of vein generation 3 and figure 4.12(b,d) plots the spatial responses of the cross-sectional area A^* (see figure 4.12b), axial flux q^* (see figure 4.12d).

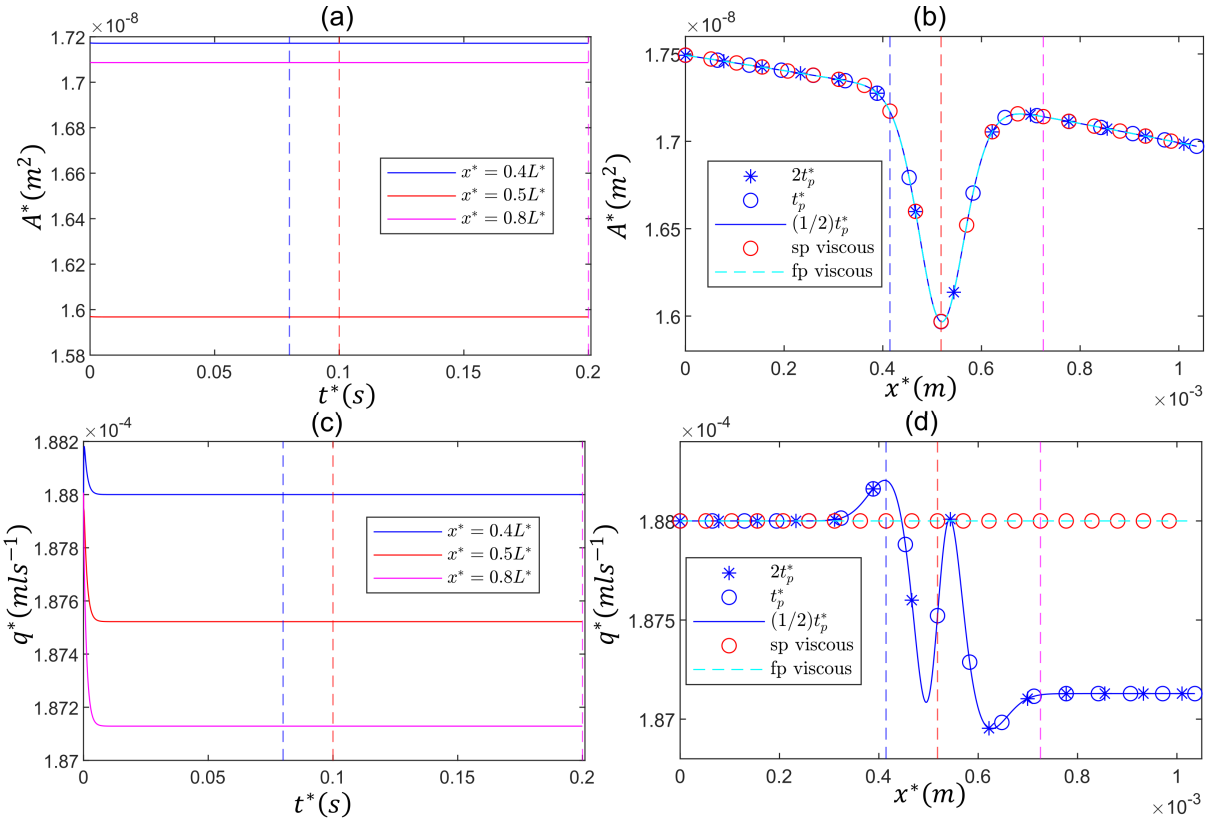

Figure 4.12: Responses of the viscous model (solved using flux boundary condition) response to a time-independent fixed pressure perturbation of maximum amplitude $\Delta p_e^* = 1 mmHg$ externally applied showing: (a) temporal profiles of the cross-sectional area A^* at three different spatial locations $x^* = \frac{2}{5}L^*, \frac{1}{2}L^*, \frac{4}{5}L^*$, (b) spatial profiles of the cross-sectional area A^* at three time steps $\frac{1}{2}t_p^*, t_p^*, 2t_p^*$, (c) time traces of the axial flux q^* at three different spatial locations $x^* = \frac{2}{5}L^*, \frac{1}{2}L^*, \frac{4}{5}L^*$, where L^* is the length of vein generation 3 and (d) spatial profiles of the cross-sectional area A^* at three time steps $\frac{1}{2}t_p^*, t_p^*, 2t_p^*$. The final time of the simulation is $t_\infty^* = 2t_p^* = 0.2s$.

We observe that the unsteady predictions of the viscous model for the cross-sectional area A^* and the axial flux q^* reach a steady configuration in the long-time limit at all three spatial locations (see figure 4.12a,c). Ideally, this state should be approaching the sp state from where the unsteady simulation begins. However, $e_{\tilde{q}}^{(2)}$ (see equation 4.40) is not precisely zero for all three spatial locations (e.g., for spatial location $x^* = \frac{1}{2}L^*$, $e_{\tilde{q}}^{(2)} = 2.5 \times 10^{-3}$) at the final time $t_\infty^* = 0.2s$ (where the system is already saturated), indicating that the unsteady response of the viscous model does not perfectly converge to the sp state.

Looking at spatial profiles given in figure 4.12(b,d), for the axial flux q^* in a long time limit, the discrepancies between unsteady profiles and sp viscous state (the cyan dashed line in figure 4.12d) at three different times $\frac{1}{2}t_p^*, t_p^*, 2t_p^*$ are now much greater than those observed for the cross-sectional area A^* (the cyan dashed line in figure 4.12b). From the temporal plot in figure 4.12(c), we see that all three different temporal profiles of q^* converge to a steady state which is significantly different from the sp viscous state (see figure 4.12d). The flux profile exhibits spa-

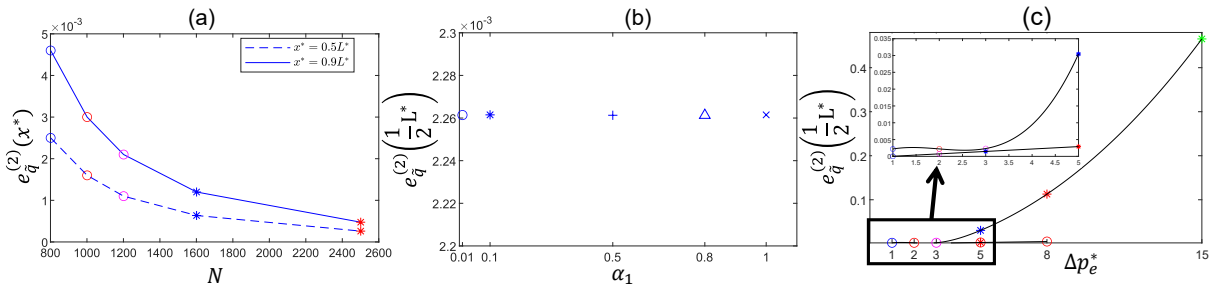

Figure 4.13: Effect of spatial grid-points and time-steps $N, d\tilde{t}$, respectively on viscous model (solved using flux-driven boundary condition) showing: measure of the error quantity $e_{\tilde{q}}^{(2)}$ obtained for (a) various spatial grid points N at the spatial location $x^* = \frac{1}{2}L^*, \frac{9}{10}L^*$, (b) for different values of $\alpha_1 = 0.01, 0.1, 0.5, 0.8, 1$ at the spatial location $x^* = \frac{1}{2}L^*$ and (c) for different maximum amplitude Δp_e^* plotted at the spatial location $x^* = \frac{1}{2}L^*$ for $N = 801$, and where L^* is the baseline length of the vein generation 3. The final time of simulation in each spatial response is $t_\infty^* = 0.2s$

tial oscillations across the externally perturbed region, and approaches a constant value different to the sp state near the downstream outlet.

We previously observed that when no external pressure is applied, the numerical scheme developed for the viscous model converges well (see the discussion in subsection 4.5.1). However, unlike the inertial model, the unsteady viscous model does not cunningly converge to the sp state of the model. It is important to note that keeping the numerical parameter values $N, d\tilde{t}$ fixed, we use different combinations by treating each term of the viscous model either implicitly or explicitly, but the outcome remains qualitatively unchanged, although results do improve as N becomes large. The discrepancies in the scheme appear because of the presence of the second-order spatial derivative in the external pressure p_e^* in the model (4.36).

Figure 4.13 plots the error quantities $e_{\tilde{q}}^{(2)}$ for the axial flux q^* obtained at different spatial locations from the different methods for different number of spatial grid points N (figure 4.13a), different time steps $d\tilde{t}$ (figure 4.13b) and different maximum pressure amplitude Δp_e^* (figure 4.13c). From figure 4.13(a), we observe that the error quantities $e_{\tilde{q}}^{(2)}$ related to the axial flux q^* obtained by comparing unsteady profiles q_∞^* obtained at the spatial location $x^* = \frac{1}{2}L^*, \frac{9}{10}L^*$ at time $t_\infty^* = 0.2s$ and the profiles obtained from the corresponding steady perturbed model at the same spatial locations, are getting smaller as we increase N. As mentioned for the inertial case (see 4.5.2.1), as the error of the spatial finite difference approximations is proportional to $1/N^2$, so $e_{\tilde{q}}^{(2)}$ decreases as we increase N. Figure 4.13(b) plots the error quantity $e_{\tilde{q}}^{(2)}\left(\frac{1}{2}L^*\right)$ as a function of five different values of $\alpha_1 = 0.01, 0.1, 0.5, 0.8, 1$, while keeping $N = 801$, and the maximum pressure amplitude $\Delta p_e^* = 1mmHg$ fixed. We observe that when N is fixed, $e_{\tilde{q}}^{(2)}$ does not change significantly as we vary α_1, meaning the flux profiles corresponding to different α_1 values converge to the same steady state as $t^* \to \infty$. A similar observation has been made while keeping the maximum pressure amplitude $\Delta p_e^* = 5mmHg$ fixed. This behaviour indicates that, for a fixed N, $0.01 \leq \alpha_1 \leq 1$ have no significant influence on the convergence behaviour of the numerical scheme, so the discrepancies between unsteady and sp profiles cannot be reduced

by using different α_1 values. As a result, the convergence of our numerical schemes does not depend significantly on the time step $d\tilde{t}$. Instead, the convergence of the numerical scheme depends crucially on the spatial grid resolution N.

To examine the influence of the maximum pressure amplitude Δp_e^* on $e_{\tilde{q}}^{(2)}$, figure 4.13(c) presents how the value of $e_{\tilde{q}}^{(2)}$ obtained at spatial location $x^* = \frac{1}{2}L^*$ changes by varying Δp_e^* between 1 and $15mmHg$, while keeping $\alpha_1 = 0.01$ and the spatial grid resolution N fixed. As we increase the maximum pressure amplitude Δp_e^*, the value of $e_{\tilde{q}}^{(2)}$ increases for a fixed grid resolution N, becoming approximately 0.03 for $\Delta p_e^* = 5mmHg$ (see figure 4.13c). For $\Delta p_e^* = 15mmHg$, $e_{\tilde{q}}^{(2)}$ is even larger (≈ 0.5). However, as we increase N to 2501, the value of $e_{\tilde{q}}^{(2)}$ significantly decreases for all cases ($e_{\tilde{q}}^{(2)}$ is 0.002 for $\Delta p_e^* = 5mmHg$).

Ideally, the acceptable error margin should be around 1% which would mean restricting Δp_e^* to $3mmHg$. However, to extend the range of analysis, for the viscous model, with the choice of the grid points $N = 801$, we restrict the maximum pressure amplitude Δp_e^* to a maximum of $5mmHg$ as seen in figure 4.13(c) where the error is $e_{\tilde{q}}^{(2)} = 0.03$ i.e., 3% for spatial location $x^* = \frac{1}{2}L^*$, which we deem to be acceptable. Identifying that in this regime, the error for running the unsteady viscous model is approximately 3%, and we consider $\Delta p_e^* \leq 5mmHg$ and $N = 801$ as our baseline case for the viscous model, which will be used in later chapters. Moreover, the pressure drop in the steady state along the retinal vein of this type is around $1mmHg$, and our consideration of Δp_e^* is still larger than the pressure drop along the retinal vein.

Following our discussions for the inertial model in subsection 4.5.2.1 and above, it is evident that the convergence of the numerical scheme depends on the choice of N. Now, we want to compare the value of $e_{\tilde{q}}^{(2)}$ with another error quantity obtained from the fixed point map.

4.5.2.3 Fixed point map of the unsteady viscous model

Recall that a point $\overline{x}^*$ is called a fixed point of a function F if $\overline{x}^* = F(\overline{x}^*)$. To quantify the error evident in the viscous numerical scheme (see subsection 4.5.2.2), we view the numerical method as a non-linear map from one timestep to the next and look for the fixed point of this map.

To construct such a map, we use similar numerical techniques as discussed in subsection 4.3.2. The highest-order spatial derivative is discretised implicitly, while all other terms are treated explicitly. This choice of discretisation results in a nonlinear algebraic system, linking each timestep to the next. However, if we impose that the dependent variables do not change over time, then we obtain a nonlinear algebraic system of equations, which can be solved using a Newton solver. We use the 'fsolve' solver in MATLAB to numerically solve the system and extract the fixed point of the map, denoted as v_{fp}. It is essential to note that fixed-point mapping is well-defined, and a detailed discussion on the existence of a fixed-point map for the model is beyond the scope of our work.

To quantify the error in the convergence of the numerical methods for the viscous model, we

introduce the error quantity $e^{(3)}$ defined as

$$e_{\upsilon}^{(3)}(\tilde{x}) = \lim_{\tilde{t}\to\infty}\left|\frac{\upsilon(\tilde{x},\tilde{t}) - \upsilon_{fp}(\tilde{x})}{\upsilon_{fp}(\tilde{x})}\right|, \tag{4.41}$$

where υ_{fp} denotes the profiles obtained from the fixed point map method. We aim to understand how the error quantity $e^{(3)}$ changes as we vary the spatial grid resolution N and the time step $d\tilde{t}$.

We find that for the baseline grid resolution $N = 801$ and $\Delta p_e^* = 5mmHg$, value of $e_{\tilde{q}}^{(3)}\left(\frac{1}{2}L^*\right)$ (see equation (4.41)) is $\approx 10^{-6}$ and is much smaller than $e_{\tilde{q}}^{(2)}\left(\frac{1}{2}L^*\right)$ (see figure 4.13c), stating that as $t^* \to \infty$ the unsteady response of the viscous model is indeed approaching the fixed point (fp) of the numerical map rather than the steady perturbed state (sp) of the viscous model (see red circles in figure 4.12b,d).

Based on the findings reported so far, we conclude that for large Δp_e^*, sufficiently large values of N are needed to ensure the numerical convergence of the scheme developed to solve the viscous model. However, this improvement comes at the cost of increased computational time and resources, requiring a trade-off. To conclude, we consider $\Delta p_e^* \leq 5mmHg$ and $N = 801$ as our baseline case for the viscous model.

4.6 Time-dependent external pressure perturbation

In section 4.5, we observed that when a time-independent external pressure perturbation of maximum amplitude Δp_e^* is applied, for large enough N values, both the inertial and viscous responses eventually converge to the steady states. However, the inertial model is strongly influenced by inertial effects during the initial period of the simulation. This raises an interesting question: What happens if we add a new timescale t_p^* over which we perturb the system? We aim to investigate how the time scale of perturbation and the inherent time scales of the model interact and how the responses of the inertial model differ from the viscous model across both short and long timescales. In this section, we start the unsteady simulation from the unperturbed steady state given in subsection 4.2.12 and apply a time-dependent external pressure perturbation of the form (4.5).

In the following two subsections 4.6.1 and 4.6.2, we discuss the key features obtained from the viscous and inertial models using both the flux-driven and the pressure-driven boundary conditions. In the following subsection and 4.6.3, we outline the thresholding approach needed to ensure we only extract realistic solutions from the inertial model. Then, in the last subsection 4.6.4, we outline the key differences between the viscous and inertial responses.

4.6.1 Unsteady Baseline Case: Viscous Model

To further understand the effect of the time-dependent external pressure, we analyse the time-dependent solution of the viscous model (4.36) solved using either the prescribed upstream flux condition (setting $Q_0^* = 1.88 \times 10^{-4}\ ml s^{-1}$) or the prescribed upstream pressure condition (setting $P_0^* = 0.5209\ mmHg$). An external pressure perturbation p_e^* of maximum amplitude $\Delta p_e^* = 2mmHg$ is applied midway along the vessel over the time interval $t_p^* = 0.01s$, and the solution is analysed within the time scale $t_f^* = 2t_p^*$. Figure 4.14 is obtained using an upstream prescribed flux-driven boundary condition, and figure 4.15 is obtained using an upstream prescribed pressure-driven boundary condition, each plotting the temporal (figure 4.14a,c,e and figure 4.15a,c,e) and spatial (figure 4.14b,d,f and figure 4.15b,d,f) profiles of the cross-sectional area A^*, axial flux q^*, and blood pressure p^* at three different spatial locations $x^* = \frac{2}{5}L^*, \frac{1}{2}L^*, \frac{7}{10}L^*$ and at times $t^* = \frac{1}{2}t_p^*, t_p^*, 2t_p^*$, where L^* is the length of vein generation 3.

Looking at spatial location $x^* = \frac{1}{2}L^*$ of the temporal profiles given in figure 4.14(a,c,e), as the constriction is applied, the cross-sectional area A^* decreases rapidly while the blood pressure p^* increases (through the 'tube law') as a combined effect of external pressure p_e^* and decreasing cross-sectional A^*. However, over time, the flow rate also increases, drawing fluid away from the part of the constriction. Note that this motion in the constriction is presumably due to the difference in response upstream and downstream of the constriction (see figure 4.14c). Once the external pressure p_e^* is fully applied, the flux profile reduces to the steady value over time, and the time-traces of A^* and p^* reach a plateau where the pressure is 18% of the applied pressure value around $t_\infty^* = 0.002s$.

Looking at the temporal profiles downstream of the constriction $x^* = \frac{7}{10}L^*$, in figure 4.14(a,c,e), as the constriction is applied, the time traces of area A^* increase to accommodate the displaced fluid, as does the time trace of flux q^*. The corresponding time trace of pressure p^* also increases. Once the external pressure p_e^* is fully applied, the temporal profile of the area almost stays constant, while the temporal profile of p^* slightly decreases over time towards the steady state.

Looking upstream of constriction, $x^* = \frac{2}{5}L^*$ in figure 4.14(a,c,e), as the vessel is constricted at the middle of the vessel, flux is driven backwards, i.e., upstream of the constriction (figure 4.14c) as a result initially flux seems to be decreasing. The corresponding time-traces of area and pressure increase initially (figure 4.14a,e). Once the external pressure p_e^* is fully applied, the temporal profile of flux gradually increases towards the steady value while the temporal profile of the cross-sectional area A^* and pressure p^* approach a plateau.

The corresponding spatial profiles given in figure 4.14(b,d,f) validate our observations from the temporal plots. Looking at profiles at early time $t^* = \frac{1}{2}t_p^*$, as the constriction is applied, the cross-sectional area decreases around the point of constriction. As the constriction is applied, the flow upstream moves upstream and the flow downstream moves downstream. However, incoming flow keeps coming in, and we observe a slight increase in flow crossing the constriction

(becomes asymmetric) and flow accumulates upstream (as flow can not leave across the upstream boundary)(figure 4.14d). To accommodate the displaced fluid, the cross-sectional area inflates upstream and downstream from the sup state (the cyan line in figure 4.14b). As expected, the pressure profile expands from the sup state; but the expansion is greater upstream of the constriction compared to downstream due to the global boundary condition imposed at the outlet. Looking at the profiles when the perturbation is fully applied ($t^* = t_p^*$), we observe that the area profile is now even more inflated from the sup state at the upstream end, but now slightly reduced at the downstream end due to the global boundary condition as flow leaves across the downstream boundary. The corresponding flux is again redistributed, but greater in the downstream than upstream (figure 4.14d). As time progresses, the corresponding pressure profile also expands from the sup state, where the expansion is more prominent at the upstream end compared to the downstream, again due to the global outlet boundary condition. For a long time, all the spatial profiles approach the sp steady state (figure 4.16b,d,f).

The corresponding plots for the pressure-driven system are shown in figure 4.15. The spatial responses remain almost unchanged at the downstream end for both flux and pressure-driven boundary conditions, as the global boundary condition is the same in both cases. However, the effect of the upstream boundary condition is evident upstream of the constriction. Comparing the flux-driven and pressure-driven viscous responses given in figure 4.14(b,d,f) and in figure 4.15(b,d,f), we observe that many features are similar. However, we only highlight the unique characteristics of the pressure-driven system responses. The temporal profile of flux is almost perfectly symmetric about the centre of the vessel $x^* = \frac{1}{2}L^*$ (see figure 4.15c). Flux now leaves from both ends of the vessel due to the prescribed pressure boundary condition (see figure 4.15c). As a result, we observe much less accumulation of fluid and a small increase in area up and downstream of part of maximal constriction (see figure 4.15b). Also, the increase in pressure is much more localised around the part of maximal constriction (see figure 4.15f).

It is important to note that the viscous model does not allow any wave formation. Over time, in the viscous model, the profiles for both flux-driven and pressure-driven boundary conditions spread out smoothly from the sup state, and the only way to transfer information is through blood flow. As a result, the viscous model responds instantaneously (but very slowly) at all parts along the vessel. We note that the significant differences between flow-driven and pressure-driven responses may have implications for flow in networks where the boundary conditions are more complicated.

4.6.2 Unsteady Baseline Case: Inertial Model

As discussed earlier, the pressure drop along the retinal vein is around $1 mmHg$. However, when the external pressure becomes large enough, the inertial model has the potential to exhibit other interesting behaviours such as wave propagation within the system. To study the influence of an unsteady perturbation on the inertial model, we isolate the solutions of the unsteady inertial

model (4.34) solved using a prescribed upstream flux (setting $Q_0^* = 1.88 \times 10^{-4}\ ml s^{-1}$) or a prescribed upstream pressure condition (setting $P_0^* = 0.5209\ mmHg$). It is important to note that the inlet flux Q_0^* and inlet pressure P_0^* result in the same steady state flow, and they are interchangeable as discussed in subsection 4.4.1.1. Now we are going to first focus on an extreme case, where the pressure amplitude is larger than section 4.5 and the pressure perturbation is applied more quickly. However, we also explore the responses of the unsteady inertial model with an external pressure perturbation $p_e^* = 5mmHg$ (as discussed in subsection 4.5) and compare with the viscous responses in section 4.6.4 below.

An external pressure perturbation p_e^* of maximum amplitude $\Delta p_e^* = 10mmHg$ is applied midway along the length of the vessel over the time interval $t_p^* = 0.002s$, and the solution is analysed within the time scale $t_f^* = 2t_p^*$. It is important to note that in this inertial case, for $N = 801$ and $\Delta p_e^* = 10mmHg$, the error is 0.12%, which we consider to be acceptable. Figure 4.16 is obtained using an upstream prescribed flux-driven boundary condition, and figure 4.17 is obtained using an upstream prescribed pressure-driven boundary condition, each plotting the temporal (figure 4.16a,c,e and figure 4.17a,c,e) and spatial (figure 4.16b,d,f and figure 4.17b,d,f) profiles of the cross-sectional area A^*, axial flux q^*, and blood pressure p^* at three different spatial locations $x^* = \frac{2}{5}L^*, \frac{1}{2}L^*, \frac{7}{10}L^*$ and at times $t^* = \frac{1}{2}t_p^*, t_p^*, 2t_p^*$, where L^* is the length of vein generation 3.

Looking at the spatial profiles in figure 4.16(b,d,e) obtained for flux-driven case, we observe that applying a constriction at the midpoint of the vessel along its length leads to a decrease in cross-sectional area in the neighbourhood of constriction (figure 4.16b). As the constriction is applied, it reduces the venous outflow across the constriction (see red line corresponding to the spatial location $x^* = \frac{1}{2}L^*$ in figure 4.16c), so the fluid is displaced, and over time the displaced fluid accumulates in the upstream and downstream of the constriction (figure 4.16c,d). As a result, the pressure profiles expand away from the constriction as time progresses (figure 4.16f). Looking at a profile while the perturbation is being applied, the perturbations are localised near the constriction, forming a wave front away from the constriction. As a result, we do not see an instantaneous response at the ends, and so the early time behaviour of the model is more symmetric between the upstream and downstream ends. Pressure increases up and downstream of the constriction. However, at later times, at $t^* = t_p^*$, the pressure profiles gradually start steepening in the far field from the constriction and develop large propagating fronts with very steep gradients. Over time, the maximum gradients of the front of the profile become even larger, forming sharp spikes. Looking at profiles corresponding to the later time $t^* = 0.00026s$, we observe that these oscillatory spikes become even steeper and reach both the upstream and downstream boundaries (figure 4.16b,d,f). In this case, the system is steepening toward a shock wave (or elastic jump) [136]. These waves eventually reflect at the boundaries. Then, interestingly, we observe that the effect of boundary conditions becomes more visible, which is discussed later in the section and observe that the response now becomes asymmetric (see figure 4.16d and figure 4.17d). Af-

ter reflecting from boundaries, propagating waves are moving back toward the constriction but with reduced amplitude. However, it is important to note that at later times, the profile gradients become so steep that our numerical scheme for solving the simulation is no longer reliable. Consequently, we can no longer guarantee that the profile steepening observed in figure 4.16(b,d,f) and figure 4.17(b,d,f) represent purely physical phenomena (such as shocks) rather than numerical instabilities. To guarantee that, we would have to solve the shock-capturing model [30], or include a membrane tension term in the model to stabilise the oscillation and disperse the shock [136]. Alternatively, upon detecting irregularities in the spatial and time traces of the inertial responses, we could devise a method to halt the simulation once the maximal gradient surpasses a pre-defined threshold value. The detailed discussion on the thresholding approach is given in subsection 4.6.3.

The effect of the upstream boundary condition is evident in the inertial model responses. Comparing with the spatial responses obtained from the flux-driven case (figure 4.16b,d,f) and from the pressure-driven case (figure 4.17b,d,f), we observe that, due to the same global boundary conditions at the downstream end, the spatial responses at the downstream end remain almost unchanged. However, the effect of the boundary condition is evident upstream of the constriction. For early times $t^* = (1/2)t_p^*$ and $t^* = t_p^*$, the responses of the inertial model for the flux-driven case and the pressure-driven case are almost identical, as the propagating pressure profiles are far from boundaries. However, the effect of boundary conditions is not realised until the wave hits the boundary as mentioned earlier. Looking at the spatial plot corresponding to time $t^* = 2t_p^*$, we observe that the pressure-driven and flux-driven responses are now very different for two boundary conditions (figure 4.16d,f and figure 4.17d,f). In the case of flux-driven condition, the flow continues to accumulate (blue profile in figure 4.16d), and so the pressure continues to rise (blue profile in figure 4.16f). Conversely, for the pressure-driven condition, the flow moves across the boundary, and so there is a much less pronounced increase in pressure upstream of the constriction (comparing blue profiles in figure 4.16f and figure 4.17f).

In the following subsection 4.6.3, we discuss the thresholding approach implemented in the inertial numerical scheme to make the prediction reliable.

4.6.3 Thresholding approach for the unsteady inertial model simulation

As discussed in Section 4.6.2, our numerical scheme cannot handle shocks, rendering the simulation unrealistic beyond a certain threshold. To achieve a realistic solution for the inertial model, we implement a threshold detection approach based on the gradient of the cross-sectional area $\left|\frac{\partial \tilde{A}}{\partial \tilde{x}}\right|$. The idea is to identify a global threshold value for the gradient that can be generally used for all similar parameter values, beyond which the profile front steepens, indicating that the simulation can no longer be trusted. Figure 4.18 plots how the cross-sectional area $\tilde{A}$ (figure 4.18a) and the gradient of the cross-sectional area change over space and time when an external pressure of maximum amplitude $\Delta p_e^* = 10 mmHg$ is applied over a timescale of $t_p^* = 0.0002s$ (figure

4.18b).

Upon closer inspection of figure 4.18(a), we observe that profile irregularities first appears at time $\tilde{t} \approx 0.08$ (the black line in figure 4.18a). As time progresses, indicated by the direction of the arrowheads, the profile becomes progressively more irregular and oscillatory.

To determine a threshold value, we calculate the maximum gradient of the cross-sectional area, $(\frac{\partial \tilde{A}}{\partial \tilde{x}})$ at each time point $\tilde{t}$. Looking at the temporal plots in figure 4.18(b) and comparing with corresponding spatial profiles given in figure 4.18(a), we observe that the maximum value of $\left(\frac{\partial \tilde{A}}{\partial \tilde{x}}\right)$ corresponding to the time $\tilde{t} = 0.08$ is 15.02 where we first observe the profile begins to steepen significantly. We therefore find and select 15.02 as our threshold value. The blue point in figure 4.18(b) corresponds to $\tilde{t} = 0.08$, and it indicates our chosen global threshold value for simulation. Beyond this point, the gradient at the front of the spatial profiles continues to steepen, and the solution becomes increasingly unreliable, prompting us to halt the simulation at this stage.

Building on the detailed discussion on the viscous (see subsection 4.6.1) and the inertial (see subsection 4.6.2) responses, we observe significant differences between their time-dependent behaviour. In the following subsection 4.6.4, we summarise our observations and key differences.

4.6.4 Differences between viscous and inertial responses

Figure 4.19 plots time-dependent spatial responses of both inertial and viscous models solved using the fixed upstream flux boundary condition. In this simulation, we consider the inlet flux $Q_0^* = 1.88 \times 10^{-4} ml\,s^{-1}$. We vary both the maximum pressure amplitude, Δp_e^*, and the time of perturbation, t_p^*, one at a time and observe how these two control parameters affect the overall responses of both the viscous and inertial models. Figure 4.19(a,c,e) describes the response of the inertial model, plotting the spatial profiles of the vessel cross-sectional area, and figure 4.19(b,d,f) shows the corresponding time-dependent spatial responses of the viscous model at three selected time points $\frac{1}{2}t_p^*, t_p^*, 2t_p^*$. We noted above in the subsection 4.5 that in the viscous model for the maximum pressure amplitude $\Delta p_e^* = 10 mmHg$, the error was too large to be acceptable with $N = 801$ so in this simulation we use a grid size of $N = 2501$ and the error amplitude $e_{\tilde{q}}^{(2)}$ at the spatial location $x^* = \frac{1}{2}L^*$ is 0.021 i.e., 2.1%, where L^* is the length of the generation 3.

Comparing figure 4.19(a,b) for $t_p^* = 0.0001 s$, the viscous model initially responds more quickly compared to the inertial model. Inertial model responses are limited by wave speed, so it takes time to get mass out of the way. In the inertial model, a propagating front is evident, whereas in the case of the viscous model, the boundary responds instantly, resulting in mass being more uniformly distributed upstream of the constriction (figure 4.19a,b). However, in both responses, we observe a localised peak close to constriction in the spatial responses of the cross-sectional area A^*, eventually overwhelmed by mass redistribution (figure 4.19a,b).

Now looking into figure 4.19(c,d), the observation is very similar to figure 4.19a,b), but now propagating wave fronts in the inertial model become very steep and tend toward a shock. In con-

trast, the viscous model responds instantaneously, and there are no steep wave fronts observed.

Now moving to figure 4.19(e,f), we observe that in this case, inertial and viscous model responses are almost indistinguishable at all times. However, in the case of inertial response, the profile of cross-sectional area A^* corresponding to the time step $t^* = \frac{1}{2}t_p^*$ has some evidence of wave propagation in the upstream region and also it takes slightly longer time to adjust at the downstream end (figure 4.19e) compared to corresponding viscous response given in figure 4.19(f).

In summary, for rapid perturbation times and large enough maximum pressure amplitude, the inertial model responds by sending a rapidly propagating wave both up and downstream of the constriction, followed by a slower adjustment in flow. Conversely, the viscous model only allows flow adjustment. However, as the perturbation time t_p^* increases, profile steepening at the front is not visible in the inertial response any more, and profiles are expanded almost linearly from the sup state. For long enough t_p^*, the wave reaches the boundaries at very early times and so the effect is quickly washed out of the system while the perturbation is being applied (see blue line corresponds to the time $2t_p^*$ in Figure 4.19e). Moreover, for large enough t_p^*, the qualitative behaviour of the viscous and inertial models becomes nearly identical.

4.6.5 Finding a threshold for wave-dominated and flow-dominated responses

Following our discussion from the subsection 4.6.2, we observe that the responses of the inertial model can be divided broadly into two categories, namely steepening and no-steepening. Steepening of profiles is largely dominated by the wave and its reflection from the boundary and interaction with other waves present in the system. However, no-steepening is prevalent in flow-dominated response where an external pressurisation is applied for a long enough t_p^* as discussed in subsection 4.6.4. To quantify the threshold between wave-dominated and flow-dominated responses, we ran simulations for the inertial model with different t_p^* and Δp_e^* values. Based on the threshold identified above in subsection 4.6.3, figure 4.20 plots the corresponding parameter space of the inertial response (figure 4.20a) and the spatial responses for the cross-sectional area A^* for viscous and inertial models solved using flux-driven boundary conditions for different t_p^* and Δp_e^* values (figure 4.20 b-g). The system exhibits clearly two different states: steepening (a filled circle in figure 4.20a) and no-steepening (open circle in figure 4.20a), respectively. Following our discussion from subsection 4.6.4, the steepening is observed in two scenarios: either t_p^* is very small or Δp_e^* is very large. However, even at the large value of $\Delta p_e^* = 25 mmHg$, no steepening is observed for sufficiently large $t_p^* = 0.0005s - 0.0007s$. In contrast, when Δp_e^* is small enough, i.e., $5 mmHg$, even for smaller $t_p^* = 0.0001s$, the steepening of spatial profiles is not evident. We have seen that for large values of t_p^*, the inertial responses are largely dominated by the flow adjustment in the system, resembling the viscous responses, whereas for rapid perturbation time, i.e., small values of t_p^*, we observe steepening of the profile.

In summary, when an external pressure perturbation Δp_e^* is applied over a sufficiently short

timescale t_p^*, typically in milliseconds, the inertial model behaves distinctly from the viscous model, and steepening of the profiles is evident upstream and downstream of the constriction, leading to shock wave formation over time. Conversely, when Δp_e^* is applied over a longer duration, the viscous and inertial responses become comparable, and the response is predominantly viscous, with profiles spreading smoothly (with no steepening).

4.7 Conclusion

Clinical literature indicates that venous thrombus production caused by RVO is a slow process, often taking anywhere from several minutes to days to fully occlude the vein, which leads to haemorrhage [69]. As seen in figure 4.19(e,f), for the long-timescales the inertial and viscous responses are nearly identical. To observe the wave steepening in the inertial model, we need the maximum pressure amplitude Δp_e^* to be very large and an extremely short timescale of perturbation t_p^*. Note that, in cases of accidental or non-accidental head injury, the estimated timescale during a free-fall impact is typically measured in milliseconds [5]. Therefore, in such scenarios where retinal haemorrhage occurs due to trauma or an accident, a fast timescale is more appropriate to consider [136].

In this chapter, we constructed a model by considering the whole network of blood vessels as a long single blood vessel in section 4.2, developed numerical methods specific to viscous and inertial models along with the relevant boundary conditions in section 4.3. In section 4.4, we discussed the behaviour of the steady models (viscous and inertial) and the effects of all control parameters on the steady state results and then validated our results with available literature. In section 4.5, we studied the convergence of these numerical schemes by calculating different errors and discussing the dependence of the convergence of the numerical schemes on the spatial grid resolutions and time step. In the following section 4.6, we studied the behaviour of unsteady viscous and unsteady inertial models in response to a time-dependent perturbation applied to the middle of the vessel and discussed the main difference in the responses between the viscous and inertial models.

To conclude, we aim to study retinal haemorrhage followed by RVO and in line with insight obtained from clinical literature, we found that for thrombi production, the long-term scale is preferred, in which we are interested, the responses of the viscous and inertial model are nearly identical. Whereas shocks are only relevant for extremely fast perturbations. In principle, for our problem, it is safe to consider the viscous model only. In order to ensure numerically resolved perturbation in viscous model, we need the spatial grid points to be $N = 801$ when $\Delta p_e^* \leq 5mmHg$; otherwise, the error for the numerical scheme is unacceptable. This motivates our choices in later chapters.

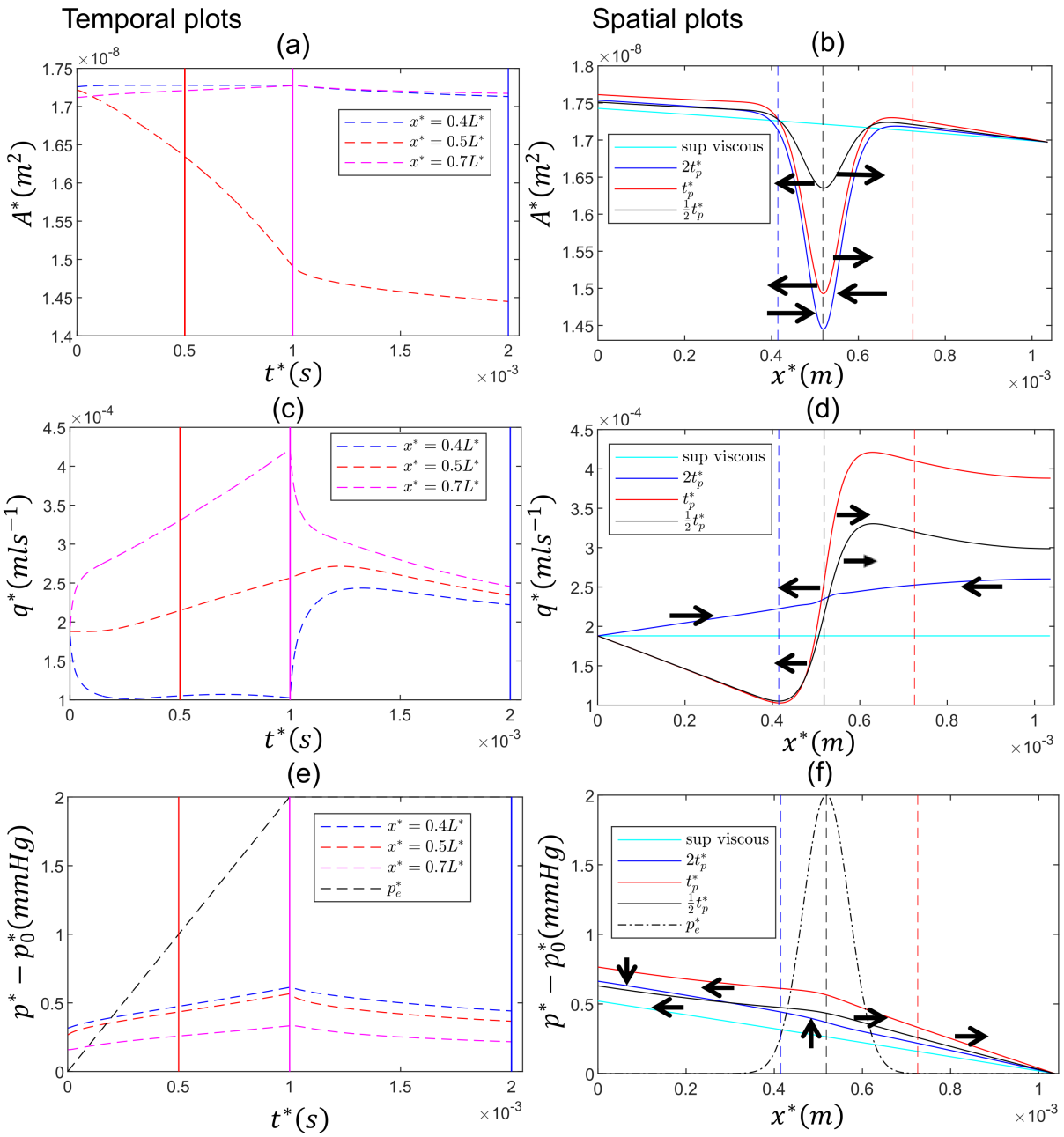

Figure 4.14: Temporal and spatial responses of viscous models solved using flux boundary condition and time-dependent pressure perturbation of maximum amplitude $\Delta p_e^* = 2mmHg$ externally applied over interval $t_p^* = 0.001s$ showing: temporal responses of (a) cross-sectional area A^*, (c) flux q^*, (e) blood pressure p^* and spatial responses of (b) cross-sectional area A^*, (d) flux q^* and (f) blood pressure p^*. The temporal profiles are plotted at three spatial locations $\frac{2}{5}L^*$, $\frac{1}{2}L^*$, and $\frac{7}{10}L^*$. The cyan line is for the unperturbed steady state (sup state). The red solid line is for $2t_p^*$, the magenta solid line is for t_p^*, and the blue solid line is for $\frac{1}{2}t_p^*$. The final time of simulation is $t_f^* = 2t_p^*$. The black dashed line in spatial plots represents the point of occlusion. The arrowhead in spatial plots indicates the direction of increasing t^*. 'sup' stands for steady unperturbed response.

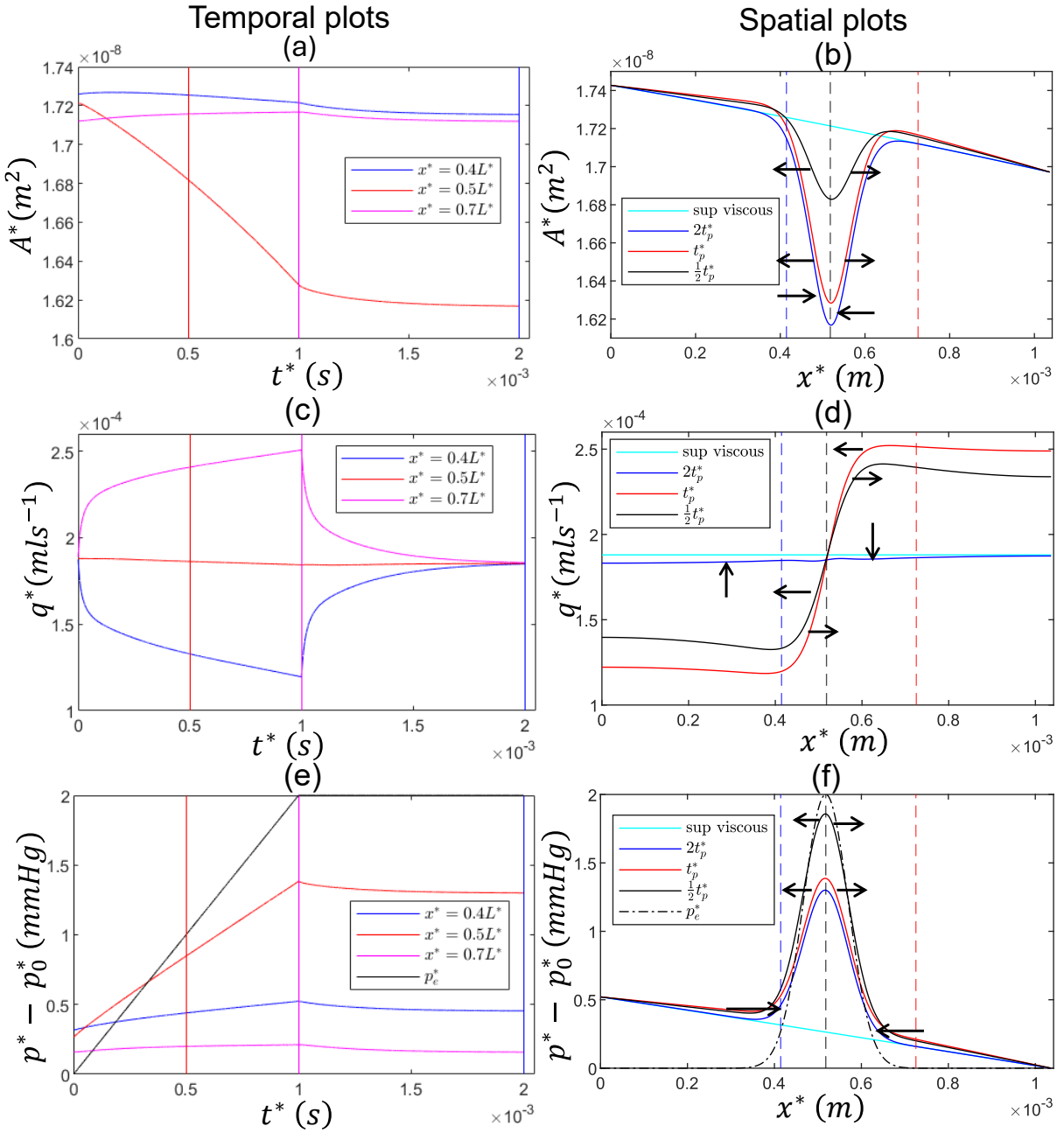

Figure 4.15: Temporal and spatial responses of viscous model solved using pressure boundary condition and time-dependent pressure perturbation of maximum amplitude $\Delta p_e^* = 2mmHg$ externally applied over interval $t_p^* = 0.001s$ showing: temporal responses of (a) cross-sectional area A^*, (c) flux q^*, (e) blood pressure p^* and spatial responses of (b) cross-sectional area A^*, (d) flux q^* and (f) blood pressure p^*. The final time of simulation is $2t_p^* = 0.002s$. The black dashed line and the arrow in spatial plots represent the point of occlusion and the increasing direction of time, respectively. The spatial profiles are plotted at three different temporal locations $2t_p^*$, t_p^*, and $\frac{1}{2}t_p^*$, and the temporal profiles are plotted at three spatial locations $\frac{2}{5}L^*$, $\frac{1}{2}L^*$, and $\frac{7}{10}L^*$, where L^* is the length of the vein of generation 3. The arrow in the spatial plots indicates the direction of increasing t^*. 'sup' stands for steady unperturbed response.

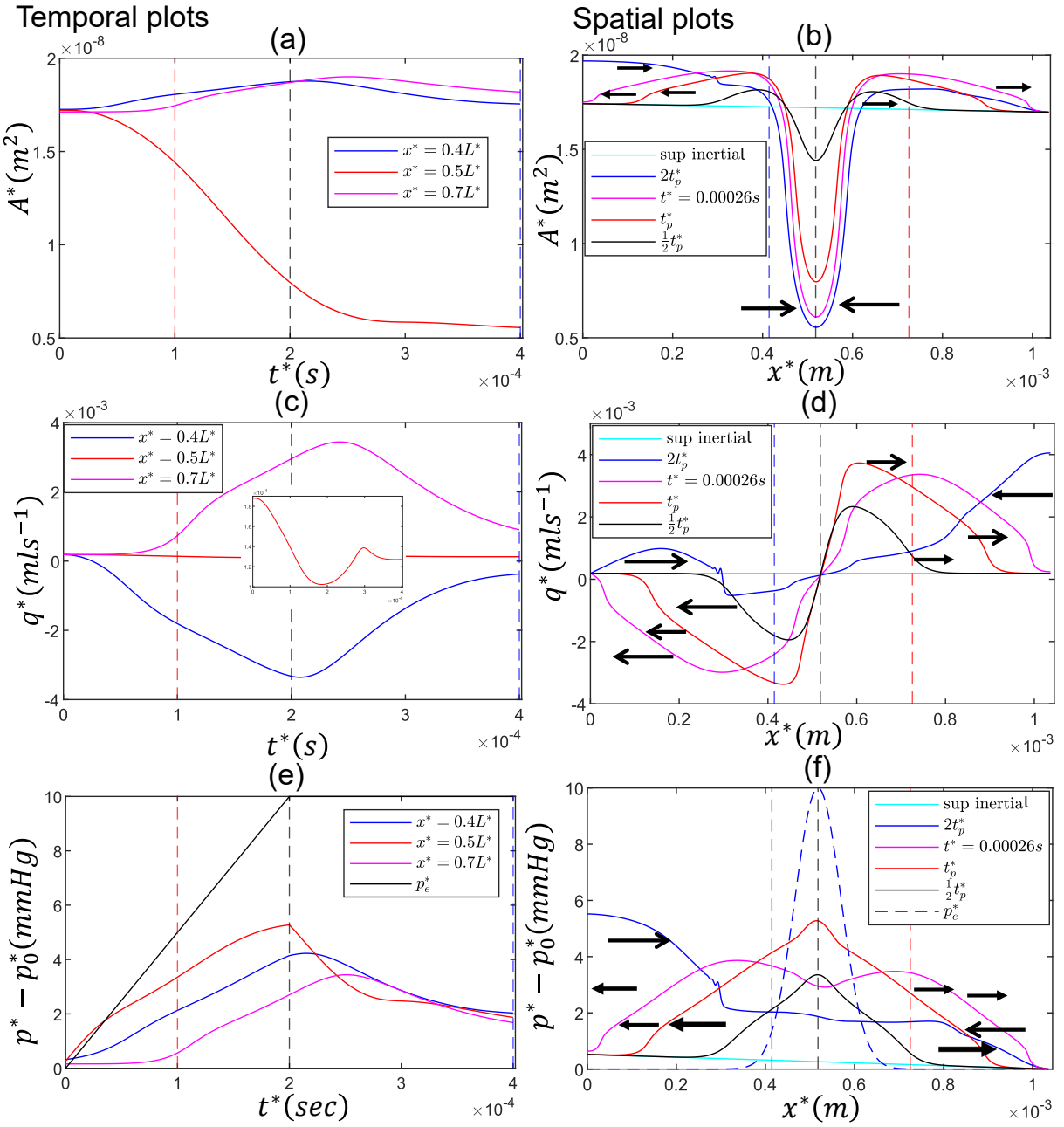

Figure 4.16: Temporal and spatial responses of inertial model solved using flux boundary condition and time-dependent pressure perturbation of maximum amplitude $\Delta p_e^* = 10mmHg$ externally applied over interval $t_p^* = 0.0002s$ showing: temporal responses of (a) cross-sectional area A^*, (c) flux q^* (inset figure: flux plotted at $x^* = \frac{1}{2}L^*$), (e) blood pressure p^* and spatial responses of (b) cross-sectional area A^*, (d) flux q^* and (f) blood pressure p^*. The final time of simulation is $2t_p^* = 0.0004s$. The black dashed line and the arrow in spatial plots represent the point of occlusion and the increasing direction of time, respectively. The spatial profiles are plotted at three different temporal locations $2t_p^*$, t_p^*, and $\frac{1}{2}t_p^*$, and the temporal profiles are plotted at three spatial locations $\frac{2}{5}L^*$, $\frac{1}{2}L^*$, and $\frac{7}{10}L^*$, where L^* is the length of the vein of generation 3. The arrow in the spatial plots indicates the direction of increasing t^*. 'sup' stands for steady unperturbed response.

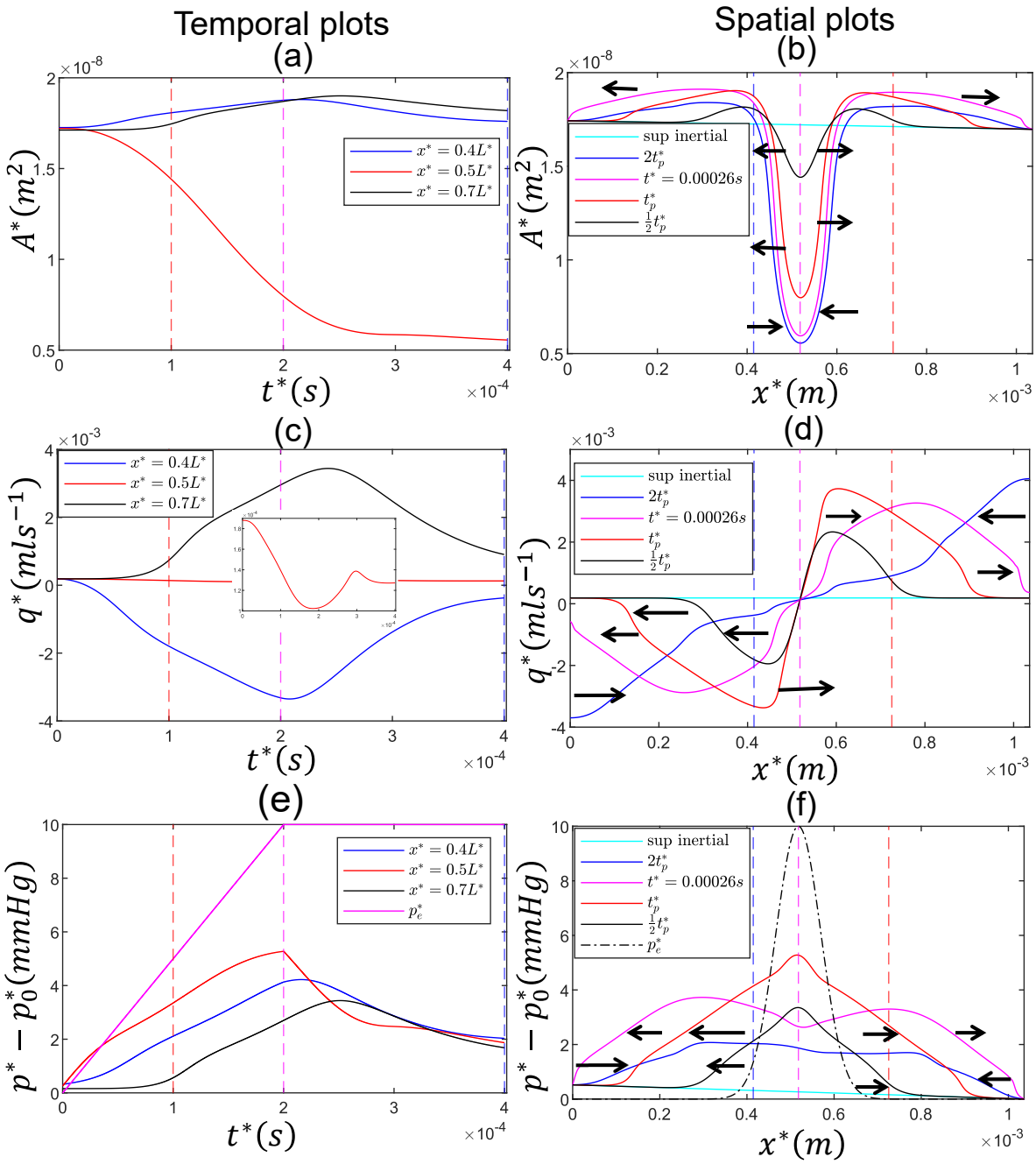

Figure 4.17: Temporal and spatial responses of inertial model solved using pressure boundary condition and time-dependent pressure perturbation of maximum amplitude $\Delta p_e^* = 10mmHg$ externally applied over interval $t_p^* = 0.0002s$ and inlet prescribed pressure $P_0^* = 0.5209mmHg$ showing: temporal responses of (a) cross-sectional area A^*, (c) flux q^* (inset figure: flux plotted at $x^* = \frac{1}{2}L^*$), (e) blood pressure p^* and spatial responses of (b) cross-sectional area A^*, (d) flux q^* and (f) blood pressure p^*. The final time of the simulation is $t_f^* = 2t_p^* = 0.0004s$. The black dashed line and the arrow in spatial plots represent the point of occlusion and the increasing direction of time, respectively. The spatial profiles are plotted at three different temporal locations $2t_p^*$, t_p^*, and $\frac{1}{2}t_p^*$, and the temporal profiles are plotted at three spatial locations $\frac{2}{5}L^*$, $\frac{1}{2}L^*$, and $\frac{7}{10}L^*$, where L^* is the length of the vein of generation 3. The arrow in the spatial plots indicates the direction of increasing t^*. 'sup' stands for steady unperturbed response

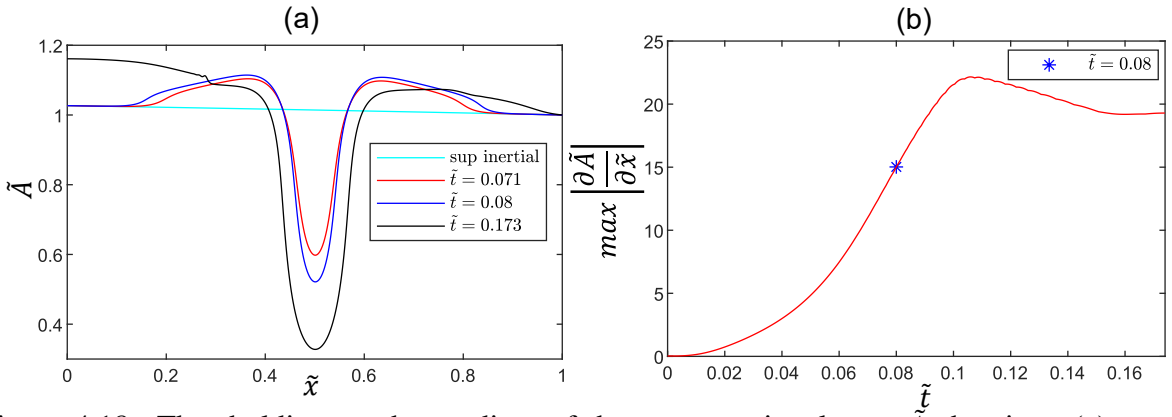

Figure 4.18: Thresholding on the gradient of the cross-sectional area $\tilde{A}$ showing: (a) cross-sectional area $\tilde{A}$ vs space $\tilde{x}$ and (b) $max\left(\left|\frac{\partial \tilde{A}}{\partial \tilde{x}}\right|\right)$ vs $\tilde{t}$ where $\Delta p_e^* = 10mmHg$ applied over the time-scale $t_p^* = 0.0002s$. The final time for the simulation is $t_f^* = 2t_p^*$. 'sup' stands for steady unperturbed response

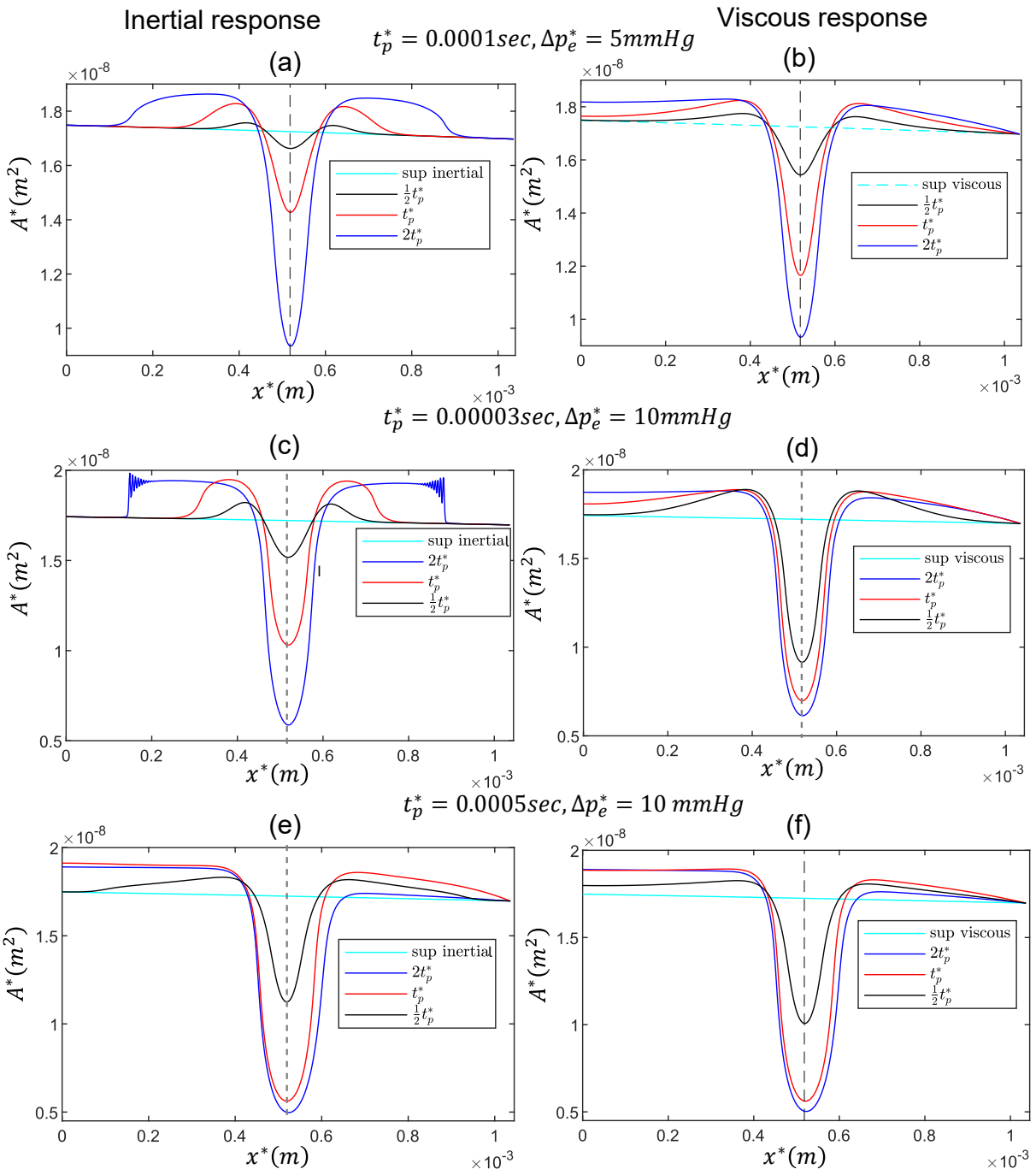

Figure 4.19: Responses of both models (inertia and viscous models solved using flux-driven boundary condition) to a pressure perturbation of maximum amplitude $\Delta p_e^* = 5mmHg, 10mmHg$ externally applied over the time interval $t_p^* = 0.0001s, 0.00003s, 0.0005s$ at three different time steps $2t_p^*, t_p^*, \frac{1}{2}t_p^*$ showing spatial profiles of the cross-sectional area: (a,b) $t_p^* = 0.0001s, \Delta p_e^* = 5mmHg$, (c,d) $t_p^* = 0.00003s, \Delta p_e^* = 10mmHg$, and (e,f) $t_p^* = 0.0005s, \Delta p_e^* = 10mmHg$. The left-hand panel is for the inertial responses (a,c,e), and the right-hand panel is for the viscous responses (b,d,f). The black dashed line in all figures represents the point of occlusion. 'sup' stands for steady unperturbed response.

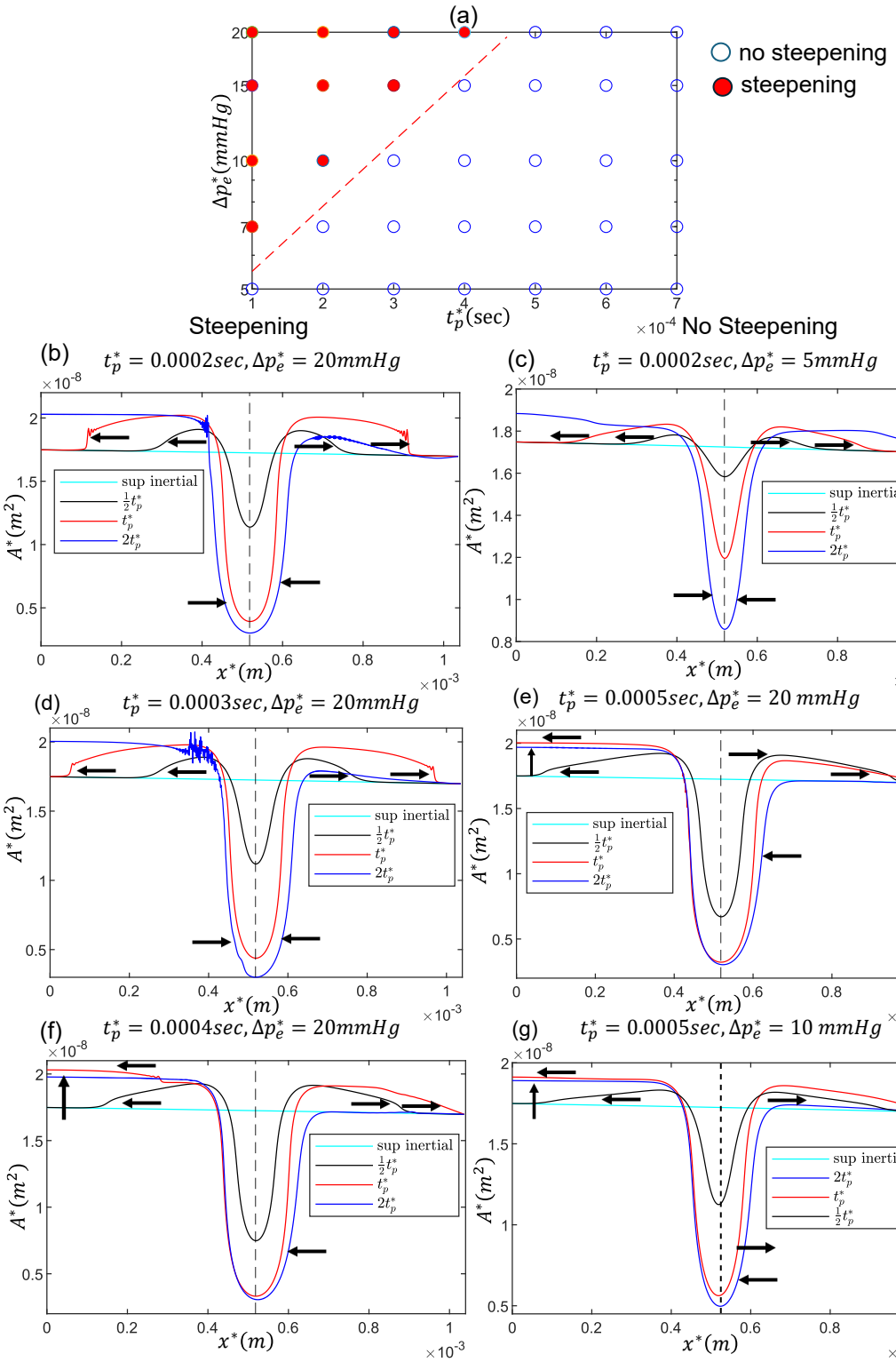

Figure 4.20: Time-dependent spatial responses of the inertial model obtained for different t_p^* and Δp_e^* solved using flux boundary conditions showing (a) Δp_e^* vs t_p^*,(b) $t_p^* = 0.0002s, \Delta p_e^* = 20mmHg$, (c) $t_p^* = 0.0002s, \Delta p_e^* = 5mmHg$, (d) $t_p^* = 0.0003s, \Delta p_e^* = 20mmHg$, (e) $t_p^* = 0.0005s, \Delta p_e^* = 20mmHg$, (f) $t_p^* = 0.0004s, \Delta p_e^* = 20mmHg$ and (g) $t_p^* = 0.0005s, \Delta p_e^* = 10mmHg$. The profiles are plotted at three temporal locations $\frac{1}{2}t_p^*, t_p^*$, and $2t_p^*$. The final time of each simulation is $t_f^* = 2t_p^*$. The cyan line represents the steady state of the inertial model. The black dashed line in all figures represents the point of occlusion, and the black arrow represents the direction in which time progresses.'sup' stands for steady unperturbed state.

Chapter 5

Flow through a venous bifurcation

5.1 Introduction

As discussed above, the retinal vasculature comprises a bifurcating network of arteries and veins connected by capillary beds, with several generations of blood vessels visible in the retinal fundus images (see Chapter 2). In this chapter, we aim to develop a mathematical model for a converging venous network to investigate the impact of retinal vein occlusion on venous blood flow. As explained in Chapter 4, considering the timescale of thrombus production and the timescales of disturbance propagation, it seems reasonable to consider only the viscous model for modelling the flow (see detailed discussion in subsection 4.6.4 of Chapter 4).

To model the flow in the single venous bifurcation, as shown in figure 5.1, we extend the existing mathematical model introduced in the Chapter 4 for the single-vessel by modelling each vessel of the network using the same framework. We label the parent vessel as generation 1, the daughter vessels are then in generation 2 and so on. As discussed in Chapter 4, to mimic an RVO, an external impingement is applied on the vein of generation 1 to stimulate an occlusion, modelled by an external pressure with a localised spatial profile applied over a prescribed timescale on the vessel wall (as given in subsection 4.2.2 of Chapter 4). In this chapter, we aim to gain a deeper understanding of the blood flow dynamics in a bifurcating network of blood vessels by analysing how blood flow, blood pressure, and the cross-sectional area of the daughter blood vessels (generation 2) change in response to the prescribed constriction on the vessel of generation 1.

In the following subsection 5.1.1, we discuss the structure and nomenclature used to describe the venous network in the rest of the thesis. The corresponding arterial counterpart follows the same protocol and is given in Appendix A.

5.1.1 Structure of the network

We consider a small converging network of veins shown in figure 5.1, consisting of two generations of blood vessels, where the two branch vessels from generation 2 converge to form the parent vessel in generation 1. In this work, the direction of blood flow is always from left to right in the network, so the daughter vessels on the left are draining into the parent vessel on the right.

We index each vessel of the network by an index i, where $i = 1$ represents the first-generation blood vessel, $i = 2$ represents the second-generation vessel, and so on, with increasing i indicating successive generations of branching blood vessels. It is important to note that for a venous system, two vessels in $(i+1)^{th}$ generation converge to form the one vessel in i^{th} generation (see figure 5.1). We introduce a second index, b, to denote the index of the vessel within each generation. For the venous system, we denote the b^{th} branch of the i^{th} generation as v_{bi}.

In this chapter, we restrict our discussion to a single venous bifurcation characterised by $b = 1, 2$ and $i = 1, 2$. It is important to note that a similar structure can be adopted for a larger venous network containing several generations of blood vessels. In order to model the whole arterio-venous network, we also need to understand the unsteady flow through an arterial bifurcation, but in this work, we are not considering an arterial constriction. The overall structure of the network for the arterial counterpart is analogous to that of this venous bifurcation and is given in Appendix A.

We start with deriving the long-wavelength model for the venous network as given in subsection 5.2. In subsection 5.3, we outline the numerical methods developed to solve the venous network model. The subsection 5.4 lists all the parameter values used for the venous network model simulation. In the following subsection 5.5, we explore the behaviour of the steady state venous network model, both with and without an applied external pressure. Subsection 5.6 discovers how an unsteady external perturbation is transmitted through a venous bifurcation, modelling the flow in the daughter vessels. Finally, in subsection 5.7, we discuss our observation from the venous network model to conclude the chapter.

5.2 Derivation of the venous network

Building upon the mathematical model derived for the single-vessel case in subsection 4.2 of Chapter 4, we now extend the formulation to describe the blood flow in a bifurcating venous network. While this chapter focuses on a bifurcating network of veins comprising three blood vessels, we present the derivation in a more general framework, allowing the same approach to be easily adopted in the Chapter 6 below for the arterio-venous network. This section specifically addresses the modified non-dimensionalisation relevant for the network formation; all other scalings and notation remain as those introduced in the single-vessel model, unless stated otherwise. The diverging arterial network construction is built using the same methodology as the converging venous network one and is discussed in detail in appendix A. To eliminate the notational

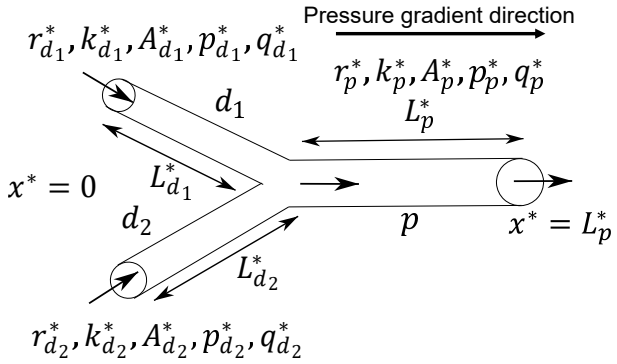

Figure 5.1: Schematic diagram of a converging venous network model showing two generations of vessels

ambiguity, all baseline parameter values are denoted with an overline in this chapter.

The length of the b^{th} branch of generation i is denoted by $\overline{L}^*_{bi}$. We use a local coordinate x^* along each vessel, which parameter from the inlet ($x^* = 0$) to the outlet ($x^* = \overline{L}^*_{bi}$). We also define a global coordinate X^*, which increases cumulatively with each generation. For the model derivation, we consider only the local coordinate. We then denote the cross-sectional area $A^*_{bi}(x^*, t^*)$. The baseline radius of the b^{th} branch in the i^{th} generation is $\overline{R}^*_{bi}$ with baseline cross-sectional area $\overline{A}^*_{bi}$.

For this kind of sophisticated vascular network in humans, flow in an individual vessel is always driven by a combination of both flux and pressure at the inlet, as both are continuous across each vessel junction. For simplicity, in this chapter, we use only a prescribed upstream flux boundary condition, where the prescribed inlet flux is denoted by $\overline{Q}^*_{bi}$, i.e., we prescribe the inlet fluxes into both daughter vessels. For steady flow, the flow rate along the parent vessel is $\overline{Q}^*_{11} = \overline{Q}^*_{12} + \overline{Q}^*_{22}$. The typical baseline velocity of the blood is selected based on the steady flow along the parent vessel in the venous network as $\overline{U}^*_{11} = \overline{Q}^*_{11}/\overline{A}^*_{11}$, and the blood viscosity in each vessel is denoted by μ^*_{bi}.

In subsection 5.2.1, we derive the dimensionless governing equation of the b^{th} branch of i^{th} generation of the network. In the following subsection 5.2.2, we state the 'tube law' for the b^{th} branch of the i^{th} generation of the network. Subsection 5.2.3 discusses the structure of the applied constriction on the parent vein. Boundary and continuity conditions used to solve the venous network are given in subsection 5.2.4. In the last subsection 5.2.5, we outline the final model along with all boundary and continuity conditions.

5.2.1 Dimensionless governing equation for the b^{th} branch of the i^{th} generation of the network

We non-dimensionalise all variables relative to the parent vessel where lengths are scaled on the square root of the baseline cross-sectional area of the parent vessel $(\overline{A}^*_{11})^{1/2}$, and time on $(\overline{A}^*_{11})^{1/2}/\overline{U}^*_{11}$. We choose a viscous pressure scale $P^* = \mu^*_{11}\overline{Q}^*_{11}/(\overline{A}^*_{11})^{3/2}$. The choice of non-

dimensional scales yields the following non-dimensional groups

$$\mathcal{R} = \frac{\rho^* \overline{U}^*_{11} (\overline{A}^*_{11})^{1/2}}{\mu^*_{11}}, \quad k_{bi} = \frac{k^*_{bi}}{P^*}, \quad \mu_{bi} = \frac{\mu^*_{bi}}{\mu^*_{11}}, \quad \overline{A}_{bi} = \frac{\overline{A}^*_{bi}}{\overline{A}^*_{11}}, \quad L_{bi} = \frac{L^*_{bi}}{(\overline{A}^*_{11})^{1/2}}, \; b,i = 1,2$$

where $\mathcal{R}$ is the Reynolds number, k_{bi} is the non-dimensional vessel wall stiffness of the i^{th} vein, μ_{bi} is the non-dimensional viscosity of the i^{th} vein, $\overline{A}_{bi}$ is the non-dimensional vessel cross-sectional area of the i^{th} vein, and L_{bi} is the non-dimensional vessel length of the b^{th} branch of the i^{th} vein.

We again assume long-wavelength deformations ($\beta = 1/L_{11} \ll 1$) and re-scale the independent variables according to

$$x = \beta^{-1}\tilde{x}, \;\; t = \beta^{-1}\tilde{t},$$

dependent variables according to

$$u_{xbi} = \tilde{u}_{\tilde{x},bi}, \;\; u_{rbi} = \beta\tilde{u}_{\tilde{r}bi}, \;\; p_{bi} = \beta^{-1}\tilde{p}_{bi}, \;\; A_{bi} = \tilde{A}_{bi}$$

and model parameters according to

$$\mathcal{R} = \beta^{-1}\tilde{\mathcal{R}}, \; k_{bi} = \beta^{-1}\tilde{k}_{bi}, \; \mu_{bi} = \tilde{\mu}_{bi}, \; \overline{A}_{bi} = \widetilde{\overline{A}}_{bi}, \; Q_{bj} = \tilde{Q}_{bj}, \; L_{bi} = \beta^{-1}\tilde{L}_{bi}.$$

For notational simplicity, we henceforth drop the tildes in all subsequent equations. Following the same derivation as described in subsection 4.2.9 in Chapter 4, we finally obtain the governing equation for the b^{th} branch vessel of i^{th} generation in the closed form as

$$\frac{\partial A_{bi}}{\partial t} = \frac{1}{\overline{A}_{bi}\mu_{bi}} \frac{\partial}{\partial x}\left(\frac{A^2_{bi}}{8\pi}\frac{\partial p_{bi}}{\partial x}\right). \tag{5.1}$$

The flux in the parent vessel v_{11} of the venous network is given by

$$q_{11} = -\frac{(A_{11})^2}{8\pi}\left(\frac{\partial p_e}{\partial x} + k_{11}\left(m(A_{11})^{m-1} + n(A_{11})^{-n-1}\right)\frac{\partial A_{11}}{\partial x}\right), \tag{5.2}$$

and the fluxes in the daughter vessels $v_{b2}, b = 1,2$ of generation 2 of the venous network are given by

$$q_{b2} = -\frac{k_{b2}}{8\pi\mu_{b2}}\left(\left(\frac{m}{(\overline{A}_{b2})^{m+2}}(A_{b2})^{m+1} + \frac{n}{(\overline{A}_{b2})^{-n+2}}(A_{b2})^{-n+2}\right)\frac{\partial A_{b2}}{\partial x}\right). \tag{5.3}$$

5.2.2 Dimensionless 'tube law' for bifurcating network

As discussed in subsection 4.2.5 of Chapter 4, the elastic response of the vessel wall is modelled using a 'tube law', and now it can be modified for a converging venous network. It is important

to note that, as mentioned in subsection 5.2.3, we apply the external pressurization only on the vein of generation 1. The modified 'tube law' for the generation 1 of the venous network is given by

$$p_{11}{}^{*} = p_e^* + k_{11}^* \mathcal{F}\left(\frac{A_{11}^*}{\overline{A}_{11}}\right), \tag{5.4}$$

and the'tube law' for the b^{th} branch of generation 2 of the venous network is given by

$$p_{b2}{}^{*} = k_{b2}^* \mathcal{F}\left(\frac{A_{b2}^*}{\overline{A}_{b2}}\right). \tag{5.5}$$

For all vessels the non-linear dimensionless function $\mathcal{F}$ is given by

$$\mathcal{F}(s) = s^m - s^{-n}. \tag{5.6}$$

A detailed discussion on 'tube law' is given in subsection 4.2.1 of chapter 4.

Assuming the long-wavelength approximation, the dimensionless 'tube law' for the parent vessel can be written as

$$p_{11}(x,t) - p_e(x,t) = k_{11}\left((A_{11})^m - (A_{11})^{-n}\right), \tag{5.7}$$

and the dimensionless 'tube law' for the other vessels in the network can be written as

$$p_{b2}(x,t) = k_{b2}\left(\left(\frac{A_{b2}}{\overline{A}_{b2}}\right)^m - \left(\frac{A_{b2}}{\overline{A}_{b2}}\right)^{-n}\right). \tag{5.8}$$

5.2.3 Applied localised constriction of the vein of generation 1

As discussed in subsection 4.2.2 of chapter 4, we apply a localized compression on the vein of generation 1 centred at some location $x^* = x_p^*$, over the timescale t_p^* through a prescribed external pressure p_e^* of the form

$$p_e^* = \Delta p_e^* g^*(t^* - t_0^*) f^*(x^* - x_p^*), \tag{5.9}$$

where Δp_e^* is the maximal amplitude and f^*, g^* are the prescribed functions of the form

$$f^*(s^*) = e^{-k_{11}^* s^{*2}}, \tag{5.10}$$

and

$$g^*(t^*) = \begin{cases} \frac{(t^* - t_0^*)}{t_p^*}, & t_0^* \le t^* \le t_p^* + t_0^*, \\ 1, & t^* \ge t_p^* + t_0^*. \end{cases} \tag{5.11}$$

The choice of external pressurisation yields the following non-dimensional groups

$$t_0 = \frac{\overline{U}^*_{11} t^*_0}{(\overline{A}^*_{11})^{1/2}},\ \Delta p_e = \frac{\Delta p^*_e}{P^*},\ \ x_p = \frac{x^*_p}{(\overline{A}^*_{11})^{1/2}},\ t_p = \frac{\overline{U}^*_{11} t^*_p}{(\overline{A}^*_{11})^{1/2}},$$

where t_0 is the non-dimensional starting time, Δp_e is the non-dimensional maximum amplitude of the external pressure, x_p is the non-dimensional location of the occlusion, t_p is the non-dimensional time interval over which the external pressure is applied on the vein of generation 1.

Again, assuming long-wavelength deformations, we re-scale the dependent variables according to $x_p = \beta^{-1}\tilde{x}_p$, $\Delta p_e = \beta^{-1}\widetilde{\Delta p_e}$, $t_0 = \beta^{-1}\tilde{t}_0$, $t_p = \beta^{-1}\tilde{t}_p$.

After dropping the tildes, the final long-wavelength version of external pressure $p_e(x,t)$ is assumed to be of the form

$$p_e = \Delta p_e g(t - t_0) f(x - x_p). \tag{5.12}$$

5.2.4 Boundary and continuity conditions of the network

Based on the structure of the network, we choose suitable boundary conditions at the inlet and outlet of the network, given in subsection 5.2.4.1. Also, to ensure the continuity of blood flow within the vessels of the network itself, we need to impose suitable continuity conditions on pressure and flow at each of the junction of the network, as discussed in the subsection 5.2.4.2.

5.2.4.1 Boundary conditions

As discussed above, in the case of the converging venous network consisting of two generations, we prescribed the fixed fluxes Q_{12} and Q_{22} at the two inlets of two vessels of generation 2 of the venous network. It is important to note that $Q_{12} + Q_{22} = 1$ to ensure the steady flow in the parent always has a unit flow rate. At the outlet of the venous network, the outlet of the vein in generation 1, we prescribe free return of fluid to the heart, so that the pressure is effectively zero, i.e., $p_{11} = 0$ at $x = 1$. In cases where the corresponding external pressure is zero $p_e(1,t) = 0$, we obtain the reduced condition $A(1,t) = 1$.

5.2.4.2 Continuity conditions at junction of the network

The continuity of flux condition is physically motivated by the requirement that mass is conserved through the junction (bifurcation) of the network.

The mass flux balance at the junction of generation 1 and generation 2 results in

$$q_{12}(L_{12},t) + q_{22}(L_{22},t) = q_{11}(0,t), \tag{5.13}$$

The continuity of pressure leads to the condition that the outlet pressure of generation 2 should exactly match the inlet pressure of generation 1 neighbouring generation, which is given by

$$p_{12}(L_{12},t) = p_{11}(0,t), \quad p_{22}(L_{22},t) = p_{11}(0,t), \tag{5.14}$$

5.2.5 Final model

The final system of equations for a vessel in the i^{th} generation of the venous network is obtained by substituting the 'tube law' (5.7-5.8) into (5.1) (see the discussion in subsection 5.2.2) and is given by

$$\frac{\partial A_{bi}}{\partial t} = \frac{1}{\overline{A}_{bi}\mu_{bi}} \frac{\partial}{\partial x}\left(\frac{(A_{bi})^2}{8\pi} \left(k_{bi}\left(m(A_{bi})^{m-1} + n(A_{bi})^{-n-1} \right) \frac{\partial A_{bi}}{\partial x} \right) \right). \tag{5.15a}$$

Hence, the final model for the parent vessel (i.e., $b = 1, j = 1$)

$$\frac{\partial A_{11}}{\partial t} = \frac{\partial}{\partial x}\left(\frac{(A_{11})^2}{8\pi} \left(\frac{\partial p_e}{\partial x} + k_{11}\left(m(A_{11})^{m-1} + n(A_{11})^{-n-1} \right) \frac{\partial A_{11}}{\partial x} \right) \right), \tag{5.15b}$$

subject to boundary conditions ($b = 1, 2$) at the inlet

$$\frac{\partial A_{b2}}{\partial x} = -\frac{8\pi Q_{b2}\mu_{b2}}{k_{b2}\left(m\frac{(A_{b2})^{m+1}}{(\overline{A}_{b2})^{m+2}} + n\frac{(A_{b2})^{-n+1}}{(\overline{A}_{b2})^{-n+2}} \right)}, \quad (x = 0), \tag{5.15c}$$

and at the outlet (assuming $p_e(0,t) = p_e(1,t) = 0$)

$$A_{11} = 1, \qquad (x = 1), \tag{5.15d}$$

and continuity of pressure and continuity of flux conditions at the junction between generation 1 and generation 2 in the venous network

$$p_{12}(L_{12},t) = p_{11}(0,t), p_{22}(L_{22},t) = p_{11}(0,t), \tag{5.15e}$$

$$q_{12}(L_{12},t) + q_{22}(L_{22},t) = q_{11}(0,t). \tag{5.15f}$$

5.2.6 Static solution

We begin by isolating the time-independent (static) solution of the venous network model (5.15), both with and without an external pressure perturbation p_e.

Static solutions of the perturbed model (or sp model) (5.15) must have constant flux ($q_{12} = Q_{12}, q_{22} = Q_{22}$, such that $Q_{12} + Q_{22} = Q_{11} = 1$) while the corresponding cross-sectional area

profile $A_{bi} = A_{bi}^{(s)}(x)$ must satisfy the first-order nonlinear ordinary differential equation (ODE) for the parent vessel

$$(A_{11}^{(s)})_x = -k_{11}^{-1}\left(m\left(A^{(s)}\right)^{m+1} + n\left(A^{(s)}\right)^{-n+1}\right)^{-1}\left(8\pi + \left(A_{11}^{(s)}\right)^2 \frac{\partial p_e}{\partial x}\right), \quad (0 \le x \le 1), \quad (5.16a)$$

and for daughters in generation 2

$$(A_{b2}^{(s)})_x = -k_{b2}^{-1}\left(\left(\frac{m}{(\overline{A}_{b2})^{m+2}}\right)(A_{b2}^{(s)})^{m+1} + \left(\frac{n}{(\overline{A}_{b2})^{-n+2}}\right)(A_{b2}^{(s)})^{-n+1}\right)^{-1}\left(8\pi\mu_{b2}Q_{b2}\right), \quad (0 \le x \le L_{b2}), b = 1,2. \quad (5.16b)$$

Conversely, to find the static solution of the unperturbed system (or sup), we consider $p_e = 0$ in (5.16).

5.3 Numerical methods

This section describes the numerical schemes used to solve both the steady and the unsteady versions of the network model. Numerical simulations for both models were carried out using MATLAB version 2023a. It is important to note that we follow a similar technique used for the single model described in subsection 4.3 of Chapter 4. In this section, we discuss only the assumptions and techniques that differ for the network model. For the convenience of numerical computation, we collapse each governing equation into one consistent formulation. To do that, we first rescale each local x coordinate into $\xi = (x-1)/L_{bi}$, where $0 \le \xi \le 1$. The spatial coordinate ξ is local to each vessel. To facilitate a numerical solution, we discretise the spatial domain of each vessel onto a uniformly spaced grid $\xi_j = j(d\xi)$ for $j = 0, 1, ..., N$ grid points in the computational domain with the step size $d\xi = 1/N$. The geometrical representation of the spatial discretisation for the venous bifurcating network is given in figure 5.2. In subsection 5.3.1, we discuss the numerical methods developed to solve the steady state version of the network model. Then, in the following subsection 5.3.2, we focus on the numerical method used to solve the unsteady network model.

5.3.1 Numerical methods for static models

As mentioned earlier, we discretise the spatial derivatives present in the equation (5.16) using the second order finite difference method described in subsection 4.3.1 of Chapter 4 and employ Newton's method to compute the profiles $A_{bi}^{(s)}$ using the 'fsolve' solver in MATLAB to solve these nonlinear algebraic equations. Following the similar fashion adopted for the single vessel

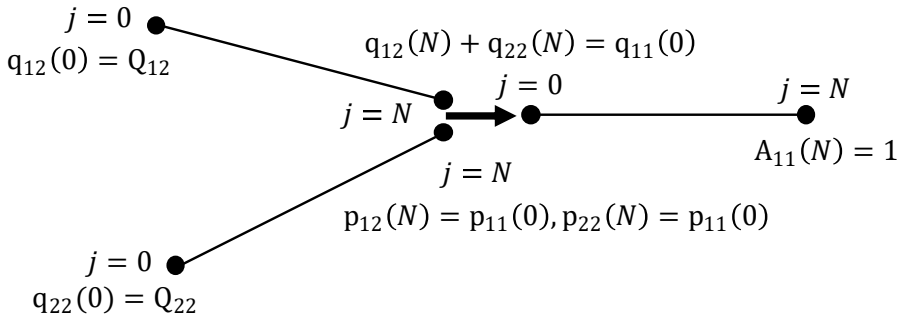

Figure 5.2: Finite difference scheme for venous bifurcating network for approximation of spatial derivatives

model, at the outlet of the parent vessel $\xi = 1$, we assume the effect of the external perturbation is negligible and use the Dirichlet boundary condition $A_{11}^{(s)}(\xi = 1) = 1$.

At the inlet $\xi = 0$ of the two daughter branches (i.e., the two inlets of the venous network), the inlet fluxes are prescribed as $q_{12}(0) = Q_{12} = 1/2,\ q_{22}(0) = Q_{22} = 1/2$ such that $Q_{12} + Q_{22} = Q_{11} = 1$. At the inlet ($\xi = 0$), the first-order spatial derivative in (5.16) is discretised using an off-centred finite difference approximation as described in subsection 4.3.1 of Chapter 4.

At the junction of the venous network, to employ the non-linear pressure conditions using the equation given in (5.15e), we use Newton's method to compute the value of $A_{bi}^{(s)}$. The value of $A_{bi}^{(s)}$ can be solved directly by setting

$$k_{12}\left(\left(\frac{A_{12}^{(s)}(\xi=1)}{\overline{A}_{12}}\right)^{m} - \left(\frac{A_{12}^{(s)}(\xi=1)}{\overline{A}_{12}}\right)^{-n}\right) = k_{11}(((A_{11}^{(s)})(\xi=0))^{m} - ((A_{11}^{(s)})(\xi=0))^{-n})$$

and

$$k_{22}\left(\left(\frac{A_{22}^{(s)}(\xi=1)}{\overline{A}_{22}}\right)^{m} - \left(\frac{A_{22}^{(s)}(\xi=1)}{\overline{A}_{22}}\right)^{-n}\right) = k_{11}(((A_{11}^{(s)})(\xi=0))^{m} - ((A_{11}^{(s)})(\xi=0))^{-n})$$

. We use 'fsolve' from MATLAB to solve the non-linear pressure formulae numerically without requiring any further simplification.

5.3.2 Numerical methods for unsteady models

For the unsteady simulation of a bifurcating network, we use a similar approach discussed for the single vessel model in subsection 4.3.2 of Chapter 4.

We again use second-order finite difference approaches to discretise spatial and temporal derivatives using a first-order finite difference stencil. The temporal grids $t_l = l(dt), l = 0, 1/dt, 2/dt, ..$ are discretised using step size dt. We use a semi-implicit approach where the highest-order spatial derivative involving A is treated implicitly while all other terms are handled explicitly as

explained in subsection 4.3.2 of Chapter 4.

At the outlet $\xi = 1$ of generation 1, we impose the Dirichlet boundary condition $A_{11} = 1$ (assuming $p_e = 0$ at $\xi = 1$).

At the two inlets to the two daughter vessels, where the fluxes are prescribed, we introduce a fictitious node at each inlet and compute the corresponding cross-sectional area at the fictitious nodes by solving the boundary conditions (5.15c). We then use the ghost point value to evaluate the second-order stencil for the given equation (5.15) in each vessel.

At the junction node, we impose the continuity of pressure condition by matching the pressure values at the inlet of the parent with the outlet pressure value of the two daughters. Mathematically, it can be written as

$$(p_{12})_N^{l+1} = (p_{11})_0^{l+1},\ (p_{22})_N^{l+1} = (p_{11})_0^{l+1},\ \ l = 0,1,2,... \tag{5.17}$$

where the superscripts indicate timesteps and the subscripts indicate grid locations. When written in terms of the tube cross-sectional area, this reduces to ($l = 0,1,2,...$)

$$k_{12}\left(\left(\frac{(A_{12})_N^{l+1}}{\overline{A}_{12}}\right)^m - \left(\frac{(A_{12})_N^{l+1}}{\overline{A}_{12}}\right)^{-n}\right) = k_{11}\left(\left(A_{11})_0^{l+1}\right)^m - \left((A_{11})_0^{l+1}\right)^{-n}\right), \tag{5.18}$$

$$k_{22}\left(\left(\frac{(A_{22})_N^{l+1}}{\overline{A}_{22}}\right)^m - \left(\frac{(A_{22})_N^{l+1}}{\overline{A}_{22}}\right)^{-n}\right) = k_{11}\left(\left(A_{11})_0^{l+1}\right)^m - \left((A_{11})_0^{l+1}\right)^{-n}\right). \tag{5.19}$$

To enforce the pressure continuity condition, we discretise (5.18) and (5.19) using a combination of explicit and implicit discretisation, following the same approach used for the governing equations. We write the non-linear terms involving A_{bi} at the new timestep $l+1$ in such a way that it is related to A_{bi} at the old time step l through a Taylor series. Mathematically, the Taylor expansion related to $\tilde{A}_{bi}$ is given by

$$((A_{bi})_j^{l+1})^m = ((A_{bi})_j^l)^m + m((A_{bi})_j^l)^{m-1}\left(\frac{\partial A}{\partial t}\right)\Big|_{bi} + \mathcal{O}(\Delta t^2) \tag{5.20}$$

$$= ((A_{bi})_j^l)^m + m((A_{bi})_j^l)^{m-1}((A_{bi})_j^{l+1} - (A_{bi})_j^l) + \mathcal{O}(\Delta t^2), \tag{5.21}$$

$$((A_{bi})_j^{l+1})^{-n} = ((A_{bi})_j^l)^{-n} - n((A_{bi})_j^l)^{-n-1}\left(\frac{\partial A}{\partial t}\right)\Big|_{bi} + \mathcal{O}(\Delta t^2) \tag{5.22}$$

$$= ((A_{bi})_j^l)^{-n} - n((A_{bi})_j^l)^{-n-1}((A_{bi})_j^{l+1} - (A_{bi})_j^l) + \mathcal{O}(\Delta t^2). \tag{5.23}$$

Using this Taylor series expansion, we linearise the non-linear terms present in the algebraic expressions (5.21) and (5.23) about the old time step l and end up with a non-linear correction term which involves only the old time step l. In this case, all the terms required at the new time step appear linearly. This formulation effectively linearises the nonlinear terms by expanding them around the known solution at the previous time step.

To impose the continuity of flux condition at the junction of the generation 1 and the gener-

ation 2, we consider

$$(q_{12})_N^{l+1} + (q_{22})_N^{l+1} = (q_{11})_0^{l+1}, \tag{5.24}$$

where q_{11}, q_{12}, q_{22} are given in (5.2) and (5.3). To discretise the continuity of flux-condition (5.24), we use a semi-implicit finite difference approach where the spatial derivative involving $\tilde{A}$ is computed implicitly (for details see subsection 4.2.12 of Chapter 4) and all other terms are handled explicitly. Following this approach, we again obtain an algebraic expression where non-linear terms appear only in terms of the old time-step l and all unknown terms in the new time-step $l+1$ are linear.

We finally have a system of linear equations for all grid points of the venous network when the (known) right-hand side involves nonlinear components of area evaluated at the old timestep. As the system of equations is linear, it is similar to the one used for the single vessel model. From the error control and convergence analysis of the numerical scheme presented in subsection 4.5 of Chapter 4, we restrict the maximum pressure amplitude Δp_e^* to $5mmHg$, use a spatial grid resolution of $N = 801$ and limit $\alpha_1 \leq 1$. Under these restrictions, the error in the unsteady viscous model remains (measured by $e^{(2)}$ as discussed in subsection 4.5.2.3 of Chapter 4) below 3%, and we consider these values as our baseline values for all network simulations used in this thesis, unless stated otherwise.

5.4 Parameter values of the bifurcating network

As discussed earlier in the subsection 1.3 of Chapter 1, in this work, we consider the parameter values of the superior-temporal quadrant of the retina, which initiates in the generation 3 of the retinal circulation. For generation 1 of our network model, we consider the parameter values for generation 1 of Takahashi's network given in the table 1.1 of Chapter 1. For the generation 2 of our network model, we consider the parameter values for generation 2 of Takahashi's network given in the table 5.1. It is important to note that, to the best of our knowledge, the Young's modulus and vessel thickness for different generations of arteries and veins of retinal microcirculations are not available in the literature. However, the Young's modulus and vessel thickness for the central retinal artery and central retinal vein are given in [136]. For these two parameters, we start with the values given in [136]. However, to maintain the biological rationale, we reduce the young's modulus and vessel wall thickness by 10% from one generation to the next [40]. In the case of homogeneous branching in generation 2, all the baseline values for the two branches υ_{12} and υ_{22} are assumed to be identical. Note that, in case of non-homogeneous branching, the lengths of vessels υ_{12} and υ_{22} in generation 2 are all sampled from a normal distribution $L_{b2}^* \sim \mathcal{N}(\overline{\overline{L}}_2^*, \sigma_1)$, $b = 1, 2$ centred with mean $\overline{\overline{L}}_2^*$ and a standard deviation $\sigma_1 = 0.2\overline{\overline{L}}_2^*$. It is important to note that the statistical baseline values are defined for the generation, not the individual vessel. All other parameters are held fixed.

	parameters	symbols	unit	value	source
v_{bi}	lumen radius	$\overline{\overline{R}}_2^*$	μm	57.65	[61]
	length	$\overline{\overline{L}}_2^*$	μm	783.4	[61]
	apparent viscosity	$\overline{\overline{\mu}}_2^*$	P	0.004	[61]
	blood flow	$\overline{\overline{Q}}_2^*$	mls^{-1}	9.41×10^{-5}	[61]
	wall thickness	$\overline{\overline{h}}_2^*$	μm	7.80	[136]
	wall stiffness	$\overline{\overline{k}}_2^*$	Pa	103.5757	derived from [136], [61]
	Young's modulus	$\overline{\overline{E}}_2^*$	Pa	437400	[136]
	Poisson ratio	ν	-	0.49	[91]
	density of blood	ρ^*	kgm^{-3}	10^3	[12]
v_{11}	lumen radius	$\overline{\overline{R}}_1^*$	μm	73.5	[12]
	length	$\overline{\overline{L}}_1^*$	μm	1036.2	[61]
	apparent viscosity	$\overline{\overline{\mu}}_1^*$	P	0.0042	[61]
	blood flow	$\overline{\overline{Q}}_1^*$	mls^{-1}	1.88×10^{-4}	[61]
	wall thickness	$\overline{\overline{h}}_1^*$	μm	8.667	[136]
	wall stiffness	$\overline{\overline{k}}_1^*$	Pa	76.1765	derived from [136], [61]
	Young's modulus	$\overline{\overline{E}}_1^*$	Pa	486000	[136]
	Poisson ratio	ν	-	0.49	[91]
	density of blood	ρ^*	kgm^{-3}	10^3	[12]

Table 5.1: Reference parameter values for the branches of the vein of generations 3 and 4 in the retinal network at the superior temporal quadrant.

5.5 Steady model results

To study the steady state behaviour of the venous network in response to a fixed external pressure perturbation p_e^*, we begin by isolating the time-independent steady state solutions. In this flux-driven flow, the flux $\overline{\overline{Q}}_2^* = 9.4\times10^{-5} mls^{-1}$ is prescribed at the inlet of each daughter of generation 2 of the venous network. From now on, we consider the global coordinate X^* to plot the behaviour of the network, which is clearly defined in figure 5.3; $X^* = 0$ is the bifurcation point. The two daughter veins run from $X^* = -L_{bi}^*$, $b,i = 1,2$ to $X^* = 0$ (figure 5.3) and parent vein is from $X^* = 0$ to $X^* = L_{11}^*$ where $X^* = L_{11}^*$ is the outlet of the network. In tandem, we use x^* to understand the local behaviour of each vessel of the network. Going forward, in all simulations v_{11} indicates the parent vein of generation 1 and v_{12}, v_{22} are the two daughter veins in generation 2. All the baseline parameter values for branches in generation 1 and generation 2 are listed in table 1.1 and table 5.1.

In subsection 5.5.1, we begin our discussion by examining the normal blood flow conditions

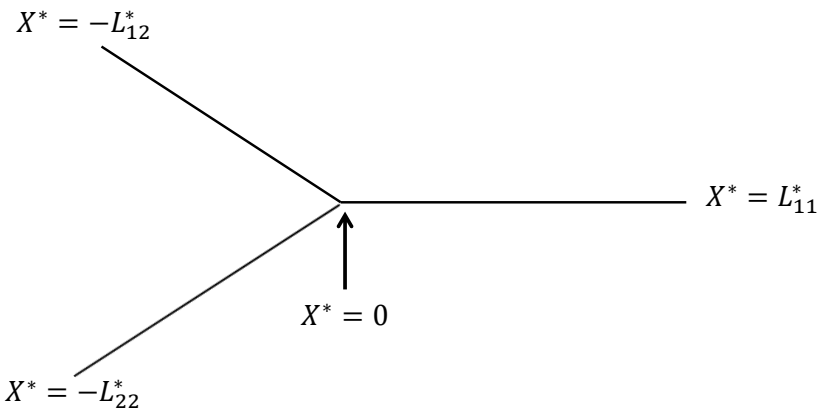

Figure 5.3: Global coordinate X^* showing the inlet $X^* = -L^*_{bi}$, $b, i = 1, 2$, junction $X^* = 0$ and the outlet $X^* = L^*_{11}$ of the bifurcating venous network.

in the absence of an external pressure perturbation p^*_e. To assess the impact of a fixed external pressure perturbation on the shape of the branch veins in generation 2, we perturb the steady-state models by applying a fixed external pressure of the form (5.9), which is spatially localised but uniform in time. The responses of these steady perturbed models are presented in subsection 5.5.2.

5.5.1 Steady baseline case with no external pressure

We consider a model network given in figure 5.1, which consists of one vessel of generation 1, denoted by υ_{11}, and two branch vessels of generation 2, denoted by υ_{12} and υ_{22}. We begin our discussion with the baseline case, where we study the sup response of the network by considering $\Delta p^*_e = 0$. Fluxes are prescribed at the two inlets of the network and assumed to be equal, where in dimensionless form $\tilde{Q}_{12} = 0.5$, $\tilde{Q}_{22} = 0.5$ and $\tilde{Q}_{11} = 1$. We consider two specific cases: one in which the two daughter branches, υ_{12} and υ_{22}, are identical (subsection 5.5.1.1), and another in which the branches are non-identical (subsection 5.5.1.2).

5.5.1.1 Identical branching (or ib)

In this subsection, two branches υ_{12} and υ_{22} of generation 2 of the venous networks are identical, meaning that all the parameter values are equal for these two branches. Figure 5.4 plots the steady state time-independent responses of the cross-sectional area (figure 5.4a) and blood pressure (figure 5.4b) of the vessels of generation 1 and generation 2 (see the insets of the figure 5.4) of the venous network when no external pressure is applied.

All the spatial profiles of the cross-sectional area decrease almost perfectly linearly with the slope set by the prescribed flow rate (see figure 5.4a). The pressure gradients are different across the two generations as flow is greater (in magnitude) across generation 1. As in Chapter 4, the negative pressure gradient is due to the work done against viscous effects in the baseline flow. From figure 5.4(b), we see that the outlet pressures of υ_{12} and υ_{22} are equal to the inlet pressure

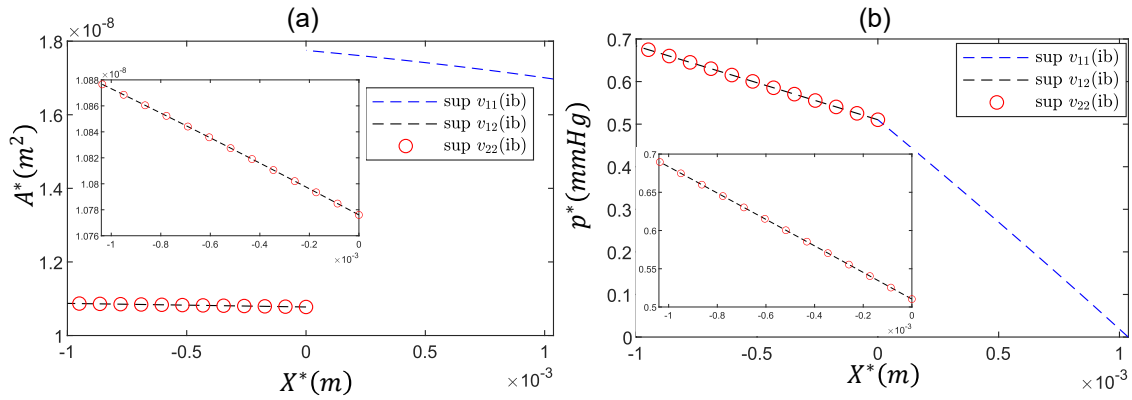

Figure 5.4: Behaviour of the venous network containing two generations of blood vessels (identical(ib)) at a steady state when maximum pressure amplitude $\Delta p_e^* = 0$ showing: spatial profiles of the (a) cross-sectional area A^* (inset: A^* profiles for daughters) and (b) blood pressure p^* (inset: p^* profiles for daughters). The blue-dashed line represents the response of the parent vessel v_{11}, the black-dashed line is for the daughter vessel v_{12}, and the red circle is for the daughter vessel v_{22}.

of v_{11} at the junction $X^* = 0$ between generation 2 and generation 1 of the network, as expected.

5.5.1.2 Non-identical branching (or nib)

Now, we consider that the two branches of generation 2 are non-identical, where they differ in their length. We systematically vary the baseline values of the lengths of v_{12} and v_{22}, to see how the inhomogeneity in the network structure changes the response of the two daughters while keeping all other parameter values fixed. Varying the baseline lengths of two daughters v_{12} and v_{22} of generation 2, figure 5.5 plots the cross-sectional area A^* (figure 5.5a) and pressure p^* (figure 5.5b) profiles for the generations 1 and 2 of the bifurcating venous network.

In particular, we set the baseline length of v_{22} to be $\frac{4}{5}\overline{\overline{L}}_2^*$, where $\overline{\overline{L}}_2^*$ is given in table 5.1. Although the two daughter vessels in generation 2 have the same prescribed inlet flow, their cross-sectional area profiles differ. In this case, we observe that the cross-sectional area of v_{22} decreases slightly steeply compared to the corresponding cross-sectional area observed in the identical branching case (black dashed line in figure 5.5a). Pressure profiles are almost identical between the two daughter vessels despite the difference in baseline cross-sectional area.

To understand the influence of the vessel length on the time-independent steady responses of the bifurcating venous network, in this section, the lengths of the two daughter veins v_{12} and v_{22} of the generation 2 are randomly sampled from a normal distribution $\mathcal{N}(\overline{\overline{L}}_2^*, 0.2\overline{\overline{L}}_2^*)$ while keeping all other parameters values fixed. Figure 5.6 plots a histogram of the maximal area (figure 5.6a) and maximal pressure (figure 5.6b) changes of the two branches of generation 2 due to the variation in their lengths. Looking at figure 5.6(a), the resulting histogram shows a pronounced peak around $1.0785 \times 10^{-8} m^2$, indicating that most samples exhibit similar maximum areas to these values. However, increasing the sample size and standard deviation would further smooth

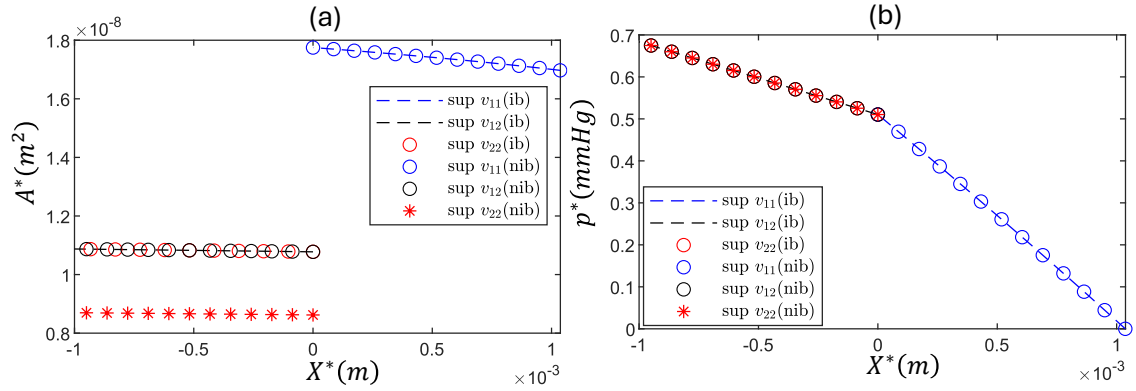

Figure 5.5: Behaviour of the venous network containing two non-identical branches (nib) of different baseline length in generation 2 at a steady state when maximum pressure amplitude $\Delta p_e^* = 0$ showing: spatial profiles of the (a) cross-sectional area A^* and (b) blood pressure p^*. For the 'nib' case, the blue circle is for the parent vessel v_{11}, the black circle is for the daughter vessel v_{12}, and the red star is for the daughter vessel v_{22}. For the 'ib' case, the blue dashed line is for parent vessel v_{11}, the black dashed line is for daughter vessel v_{12}, and the red circle is for daughter vessel v_{22}.

the histogram. The output variance ($\sigma_r = 0.14697$) of generation 2 for maximum area changes is much lower than the input variance ($\sigma_r = 1.18017$). A similar observation has been made for maximum pressure changes: for generation 2, the output variability in maximum pressure changes (where the coefficient of variance = 0.0358) is much lower than the input variance (where the coefficient of variance = 0.2). Hence, in the sup model, variations in baseline branch lengths have a relatively minor impact on the maximum area and maximum pressure change.

5.5.2 Steady baseline case with fixed external pressure

In this subsection, we start the simulation from the sup state as described in subsection 5.5.1. To mimic the effect of retinal vein occlusion on a venous network and to see how the vessel cross-sectional area and blood pressure of generation 2 of the network change as we perturb the sup network model, we apply a time-independent localised external pressure perturbation p_e^* of maximum amplitude $\Delta p_e^* = 5 mmHg$ at the midpoint along the length of the vessel of generation 1. We keep all the other baseline values fixed and vary the baseline area values of v_{12} and v_{22}, which are both sampled from a normal distribution $\mathcal{N}(\mu_2, \sigma_2)$ where the mean μ_2 is $\overline{\overline{A}}_2^*$ and the standard deviation σ_2 is given by the 20% of the sample mean $\overline{\overline{A}}_2^*$. Figure 5.7 plots the spatial responses of the cross-sectional area A^* (see figure 5.7a) and blood pressure p^* (see figure 5.7b) for a time-independent external pressure on the vein of generation 1.

As the constriction restricts the local blood flow along generation 1, and flow is redistributed upstream and downstream in the network (figure 5.7a). As expected, the cross-sectional area of v_{11} is decreased around the point of constriction, while it is expanded upstream and downstream of the constriction (compared to the sup profile, see the dashed line in figure 5.7a). However,

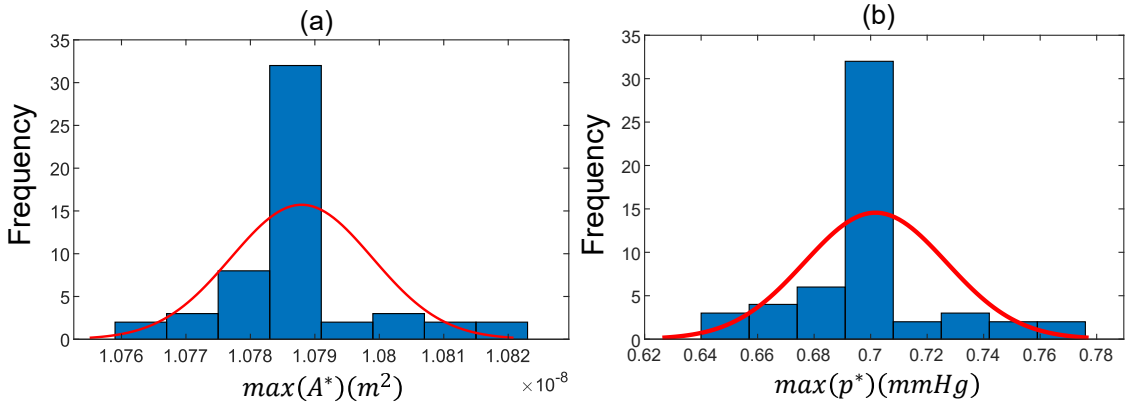

Figure 5.6: Histogram of maximum vessel area for steady unperturbed bifurcating network model showing: (a) maximum area changes and (b) maximum pressure changes in daughters, when the baseline lengths of two daughter branches υ_{12} and υ_{22} are chosen from a normal distribution with a mean of $\overline{\overline{L}}_2^*$ and the standard deviation of $0.2\overline{\overline{L}}_2^*$.

the expansion of the area is more evident at the upstream end of generation 1 compared to the downstream. As expected, the cross-sectional area of υ_{12} and υ_{22} (see the solid line in figure 5.7a) is increased compared to the sup profiles (see the dashed line in figure 5.7a) to accommodate the displaced fluid from generation 1. However, the daughter branches in generation 2 expand nearly uniformly from the corresponding sup state; the expansion of the two daughter branches is not equal, as they are non-identical, but with an almost identical pressure gradient (figure 5.7b). Looking at figure 5.7(b), the corresponding sp pressure profile of υ_{11} is inflated from the sup profile as we constrict the vessel. Again, the inflation is primarily observed in the upstream region. As a result, the pressure profiles of both branch vessels of generation 2 are also inflated uniformly from the corresponding sup state (figure 5.7b). However, the overall spatial structure of the sp profiles does not change qualitatively from the sup state, and as a result, the overall pressure gradient in vessels of generation 2 also remains essentially unchanged. At the downstream end of the constriction, there is almost no displacement in the area and pressure profiles relative to the corresponding sup state. This is an interesting feature of the steady perturbed flow with prescribed inlet flow rates, which is similar to our observation in the case of the single vessel model discussed in subsection 4.4.2 of Chapter 4.

We can conclude that due to a constriction applied on generation 1, we observe an increment of pressure throughout the network and as a result, branches of generation 2 are inflated, and a clear shift of the sp profiles from the sup state is observed in each case.

5.6 Unsteady model results for bifurcating venous network

In section 5.5, we observe that when a time-independent external pressure perturbation of maximum amplitude Δp_e^* is applied, both branches in generation 2 expand almost uniformly from the steady state. This raises an interesting question: how does the system reach a steady state when a

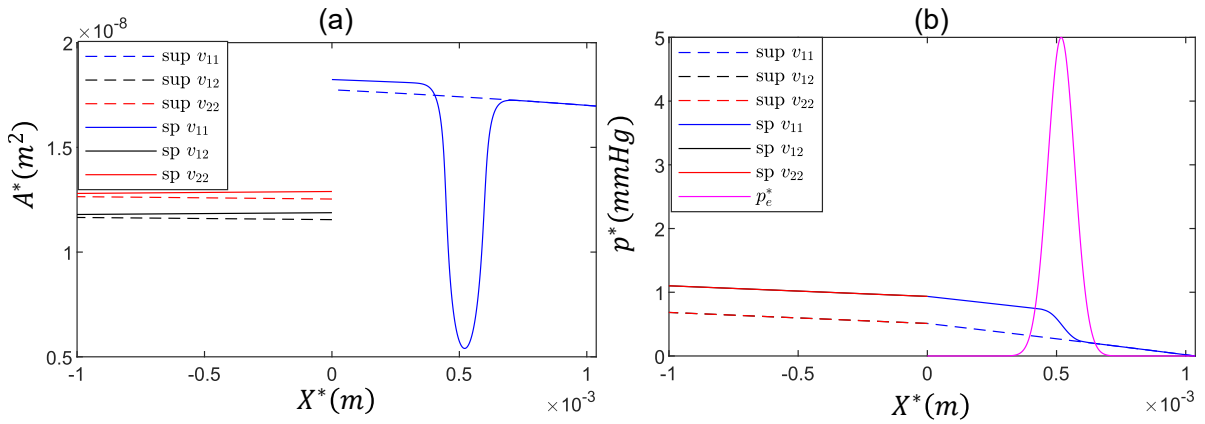

Figure 5.7: Steady-state responses of the venous network containing non-identical branches in generation 2 under an externally applied pressure perturbation with a maximum amplitude of $\Delta p_e^* = 5mmHg$, showing: (a) cross-sectional area profiles for v_{11}, v_{12} and v_{22} and (b) blood pressure profiles for v_{11}, v_{12} and v_{22}. The dashed line represents the sup state of the venous bifurcating network. The blue line represents the parent vein v_{11}, and the red and black lines represent the daughter veins v_{12} and v_{22}, respectively. The magenta line represents the external pressure p_e^*. The dashed line represents the sup profile and solid line represents the sp profile.

time-dependent external pressure is applied on the vein of generation 1? Moreover, we are interested in investigating the transient dynamics of the unsteady response of the bifurcating network and how it converges to the sp state of the system studied in subsection 5.5.2 in the long time limit. We aim to investigate how the time scale of perturbation and the inherent time scales of the model interact and what happens to the upstream of the network in response to the constriction on generation 1. In this section, we start the unsteady simulation from the sup state given in subsection 5.5.1 and apply a time-dependent external pressure perturbation of the form (5.12). All the baseline parameter values used for unsteady simulation for branches in generation 1 and generation 2 are listed in table 1.1 and table 5.1. It is important to note that the flow direction is from left to right of the network.

In the following subsection 5.6.1, we discuss the unsteady responses of the bifurcating network model when two daughter branches of generation 2 of the network are non-identical.

5.6.1 Unsteady Baseline Case: Non-identical Branching

To study the influence of an unsteady perturbation on the bifurcating venous network containing two non-identical branches in generation 2, we isolate the solutions of the unsteady venous network model (5.15) solved using the prescribed upstream flux $\overline{\overline{Q}}_2^* = 9.4\times10^{-5} ml\,s^{-1}$. We consider that the two branches of generation 2 are non-identical, where we reduce the length of the vessel v_{22} by 20% from its baseline value listed in table 5.1 and an external pressure perturbation p_e^* of maximum amplitude $\Delta p_e^* = 5mmHg$ is applied midway along the length of the vessel v_{11} over the time interval $t_p^* = 0.01s$, and the solution is analysed over $0 \le t \le t_f^* = 2t_p^*$. Figure 5.8 is obtained by plotting the temporal (figure 5.8 a,c,e) and spatial (figure 5.8 b,d,f) profiles of

the cross-sectional area, blood pressure and axial flux of parent v_{11} and two daughters v_{12}, v_{22} of the bifurcating venous network at three different spatial locations $x^* = 0, \frac{1}{2}L^*_{bj}, L^*_{bj}$ and at times $t^* = \frac{1}{2}t^*_p, t^*_p, 2t^*_p$ where $L^*_{bj}, b = 1,2, j = 1,2$ is the length of the b^{th} branch of the j^{th} vein generation.

As the constriction is applied at the middle of the parent vessel $x^* = \frac{1}{2}L^*_{11}$, fluid from the parent vessel is displaced and pushed upstream and downstream of the perturbed region. As a result, the flow rate and cross-sectional area of the parent vessel decrease over time (figure 5.8a,c). Now looking at the spatial location $X^* = 0$, i.e., the junction between daughters and parent of the network and the two inlets of the network at $X^* = -L^*_{12}, -L^*_{22}$, we observe that the displaced fluid leaves the parent vessel, moves across the bifurcation point $X^* = 0$, and travels upstream to the daughter branches in the network (figure 5.8c). At vessel inlets $X^* = -L^*_{12}, -L^*_{22}$, the overall flow rate across both daughter vessels increases over time due to the combined effect of the displaced fluid from the parent and inlet flow coming from the prescribed boundary (red and green solid lines for figure 5.8c). To accommodate the incoming fluid, the cross-sectional area of the two daughter vessels expands, which, through the 'tube law', causes a corresponding increase in the blood pressure (inset in figure 5.8a,e). In all three spatial locations plotted in figure 5.8, we observe an overshoot in the time traces of both pressure and cross-sectional area in both daughters, compared to the corresponding sp values. At each spatial location, there is a well-defined maximum pressure which overshoots the steady perturbed state, and this can be used as a basis for comparison as we vary the vessel properties of the daughters. This maximum pressure can be defined in two ways: either as a difference to the sup state (see figure 5.8f) or as a difference to the sp state. However, once the external pressure is fully applied, the flow rate of the parent and both the daughters at the junction decreases to reach the corresponding sp state (figure 5.8c). The corresponding time traces of area and pressure of the two daughters also decrease (inset in figure 5.8a,e).

The corresponding spatial responses validate our observation from the temporal plots. Looking at the spatial plots of the cross-sectional area given in figure 5.8(b), as constriction is applied on the parent vein, the cross-sectional area of the parent decreases from the sup state around the point of constriction. As an immediate consequence, fluid is displaced and driven upstream and downstream of the constriction (figure 5.8d). The cusp in the spatial flux profile upstream and downstream of the constriction across the parent (see figure 5.8d) is because the second-order derivative of the external pressure profile takes its maximum value around these two locations. It is important to note that this behaviour is a completely numerical issue which can be resolved using a finer grid resolution in the parent vessel.

5.6.2 Influences of the time of occlusion t^*_p on the response of the network

We compare this maximal pressure at different spatial locations across the venous network as we vary the ramping time t^*_p over which the external pressure perturbation of maximum amplitude

$\Delta p_e^* = 5mmHg$ is applied on the parent vein of generation 1.

Figure 5.9 plots the temporal responses of blood pressure p^* of the parent and two daughters at the midpoint of each vessel $x^* = \frac{1}{2}L_{bj}^*$ for different values of t_p^*. If the perturbation time t_p^* is really small, i.e., $t_p^* = 0.0001s$, we observe a significant difference between the responses of the parent and the two daughters (inset figure 5.9a). The maximum pressure values observed in the two daughter vessels are nearly $\approx 1.049mmHg$, which is $\approx 71.36\%$ higher than the corresponding steady value obtained from the sup state (figure 5.9a). Also, the maximum pressure value in the parent (i.e.,$\approx 2.5mmHg$) is much higher than the corresponding maximum pressure values obtained from two daughters (figure 5.9a). However, if we perturb the system for a longer duration, where the perturbation time t_p^* is $0.001s$, the maximal pressure for the parent decreases to $\approx 1.2mmHg$, while the daughters also exhibit a lower maximum value $\approx 0.98mmHg$. However, in this case, the maximum value of pressure for the daughter is only about 53% higher than the corresponding steady value obtained from the sup state (figure 5.9b). Furthermore, as we increase t_p^* to $0.01s$ (figure 5.9c) and $0.1s$ (figure 5.9d), the maximum values of pressures for the daughters are only increased by $\approx 29\%$ from the sup state.

The perturbation time t_p^* has a significant influence on the increase in maximal pressure for both the parent and daughters. As we increase t_p^*, the perturbation is ramped more slowly, allowing enough time to adjust the displaced flow across the network. However, for the larger perturbation times, the maximal pressure in the daughters now exceeds the maximal pressure in the parent. In this case, the perturbation induced in the pressure is now affected by the difference between the vessel pressure between generations in the sup state.

5.6.3 Influences of vessel length on the responses of the network

To understand the influence of the vessel length on the unsteady responses of the bifurcating venous network, in this section, the lengths of the two daughter veins v_{12} and v_{22} of generation 2 are randomly sampled from a normal distribution $\mathcal{N}(\overline{\overline{L}}_2^*, 0.2\overline{\overline{L}}_2^*)$ while keeping all other parameter values fixed. Figure 5.10 plots the histograms of the maximal net increase in pressure at three different spatial locations across the network, namely at the junction $X^* = 0$ (figure 5.10a,c) and at the inlets $X^* = -L_{12}^*, -L_{22}^*$ (figure 5.10b,d). We compare for two different perturbation timescales $t_p^* = 0.001s$, and $0.01s$ over which the time-independent external pressure of maximum amplitude $\Delta p_e^* = 5mmHg$ is applied on the parent vein v_{11} of generation 1.

Looking at two different timescales of perturbation $t_p^* = 0.001s$ and $t_p^* = 0.01s$, for small ramping time $t_p^* = 0.001s$, there is a wide spread in the net maximal pressure increase (figure 5.10 a,b). In contrast, for a longer ramping timescale $t_p^* = 0.01s$, the distribution of the net maximal pressure is significantly tighter compared to the $t_p^* = 0.001s$ case (figure 5.10c,d). The overall increase in the pressure at the inlets ($\approx 0.32mmHg$ for $t_p^* = 0.001s$, $\approx 0.241mmHg$ for $t_p^* = 0.01s$, see figure 5.10b,d) and at the junction or the bifurcation point $X^* = 0$ ($\approx 0.36mmHg$ for $t_p^* = 0.001s$, $\approx 0.2458mmHg$ for $t_p^* = 0.01s$, see figure 5.10a,c) is interesting: there is a much

greater difference between the maxima for the shorter ramping time ($t_p^* = 0.001s$), underlying a much stronger spatial decay along the vessel in that case. For $t_p^* = 0.01s$, the maximum values are almost perfectly comparable. Moreover, the output variation (the coefficient of variance= 0.0708 for $t_p^* = 0.001s$ and the coefficient of variance= 0.0237 for $t_p^* = 0.01s$) in all cases is much lower than the prescribed input variance (the coefficient of variance= 0.2). The variability in the branch length of daughters v_{12} and v_{22} in generation 2 has a relatively minor effect on the output.

5.7 Conclusion

The ultimate goal of this work is to develop an image-informed arterio-venous flow network to study the effect of retinal vein occlusion (RVO). To reduce the computational complexity, we first established a single-vessel model in Chapter 4 where we treated the entire arterial-venous network as a single vessel. From the single-vessel model response, we found that, to study thrombus production, the long-term time scale is preferred, which is of interest to us, and that the responses of the viscous and inertial models are nearly identical on this time scale. This observation from Chapter 4 greatly influences our choice of using a viscous model to study the blood flow dynamics in the venous network and then for the arterio-venous network in the next Chapter 6. In this chapter, we developed a converging venous network to study the effect of RVO in a bifurcating venous network. To mimic RVO, we applied an external pressurisation on the parent vein of generation 1. It is important to note that the venous network is converging as two daughters of generation 2 converge to form a parent in generation 1, which is opposite to the arterial network discussed in Appendix A.

Following our observation from the single vessel model in Chapter 4, in subsection 5.2, we considered only the viscous model (5.15) to construct the mathematical model to study the flow across the bifurcating venous network driven by a prescribed flux boundary condition at the two inlets of the network against a zero pressure outlet. This novel venous network modelling framework incorporates fluid-structure interaction to model the capacitance effect of the retinal veins. This is important for understanding how the blood vessels in the network accommodate a perturbation, which then causes the vessel to burst. To solve this venous network model numerically, we employ an efficient boundary condition at each junction of the network, as described in subsection 5.3.2. Implementing a pressure boundary condition (5.17) at the junction is particularly challenging as the pressure expression is connected to the area through the 'tube law' which is non-linear in A^*. To handle the non-linearity, we employ a novel technique by breaking the non-linear term both in new and old time steps in such a way that all non-linear terms are in old time steps, whereas linear terms are in new time steps.

Next, we solved the venous network model for the time-independent steady state in order to consider the behaviour of the two types of network, namely the bifurcating network having identical branches in generation 2 and non-identical branches in generation 2. In all cases, when

no external pressurisation was applied on the network, the cross-sectional area of all vessels decreased almost perfectly linearly with the slope set by the prescribed flow rate.

As our ultimate goal is to study the effect of RVO, a time-dependent external pressure perturbation was applied on the parent vein of the sup model, and we called it the steady perturbed model (sp) as before. We observed that the cross-sectional and pressure profiles of the daughter vessels expanded almost linearly from the corresponding sup state to accommodate the displaced fluid coming from the parent due to the constriction. However, it is also important to understand whether the unsteady model ever reaches the sp state.

To understand the transient dynamics of the venous network model, we considered the time-dependent response of the perturbed network model having non-identical daughter branches. Again, we chose the lengths of the daughter vessel independently by sampling from a normal distribution. Looking at the inlet, outlet and midpoints of each vessel, we observed that at each spatial location, there was a well-defined maximum pressure that overshot the sp state as the external pressure was applied to the parent. This overshoot of pressure was quite significantly influenced by the time of occlusion t_p^*. For very long t_p^*, we observed that the maximum pressure value in the daughter exceeded the maximum pressure value calculated from the parent, indicating possibly a high risk of vessel rupture in the daughter compared to the parent. Moreover, in the case of the unsteady response, the effect of variability in the branch length of daughters in generation 2 was significantly minor.

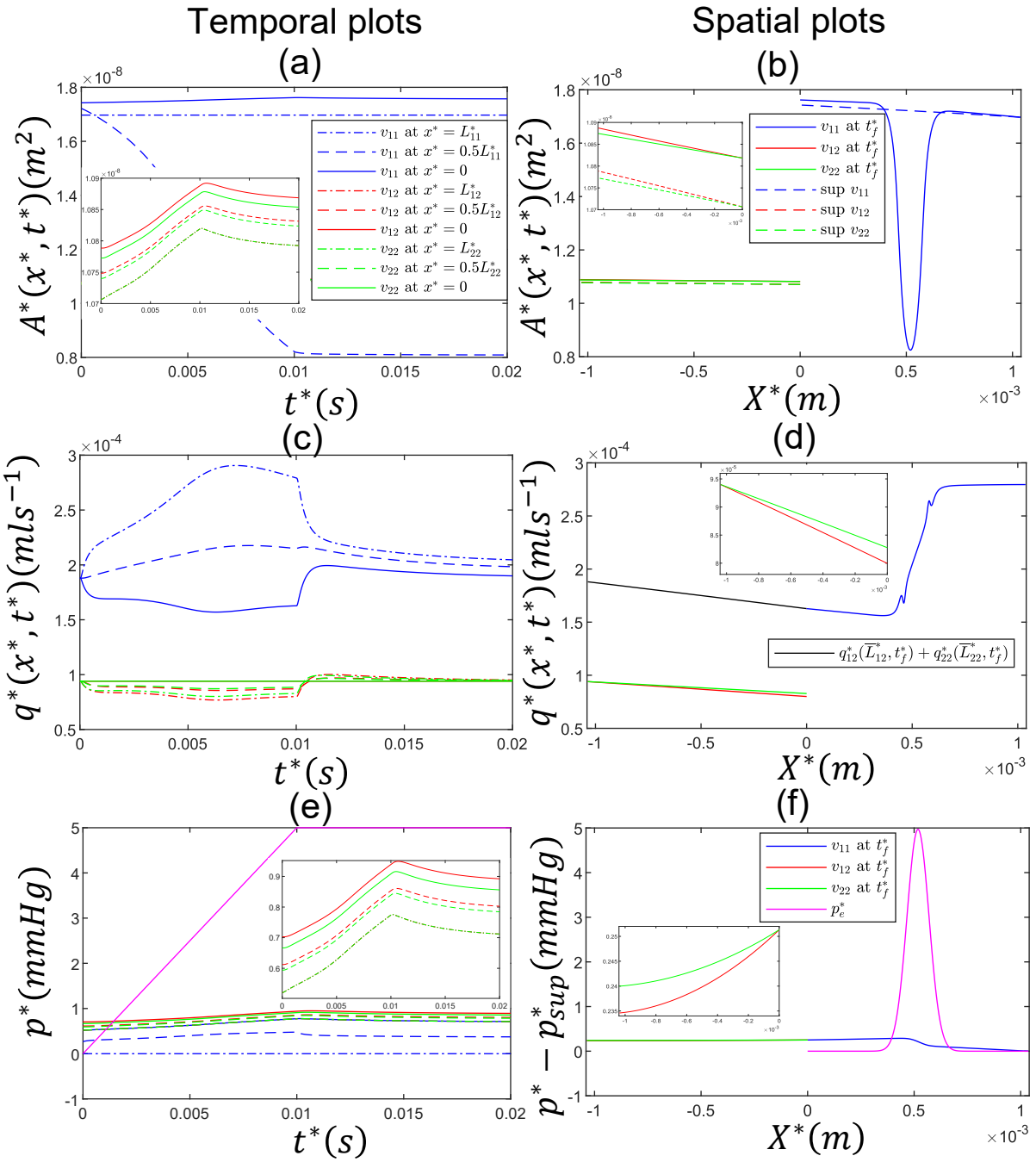

Figure 5.8: Time-dependent responses of the venous network containing non-identical branches in generation 2 where the length of υ_{22} is reduced by 20% from its baseline value under an externally applied pressure perturbation with a maximum amplitude of $\Delta p^*_e = 5mmHg$, showing: temporal responses of (a) cross-sectional area A^* (inset: υ_{12} and υ_{22}), (c) flux q^*, (e) blood pressure p^* (inset: υ_{12} and υ_{22}), and spatial responses of (b) cross-sectional area A^* (inset: υ_{12} and υ_{22}), (d) flux q^* (inset: υ_{12} and υ_{22}) and (f) blood pressure p^* (inset: υ_{12} and υ_{22}). The time of occlusion $t^*_p = 0.01s$ and the final time of the simulation is $t^*_f = 2t^*_p$. All Temporal profiles are plotted at three spatial locations $x^* = 0, 0.5L^*_{bi}, L^*_{bi}, b, i = 1,2$. The blue line is for the parent υ_{11}, the red line is for the daughter vessel υ_{12}, the green line is for the daughter vessel υ_{22} and the magenta line is for p^*_e.

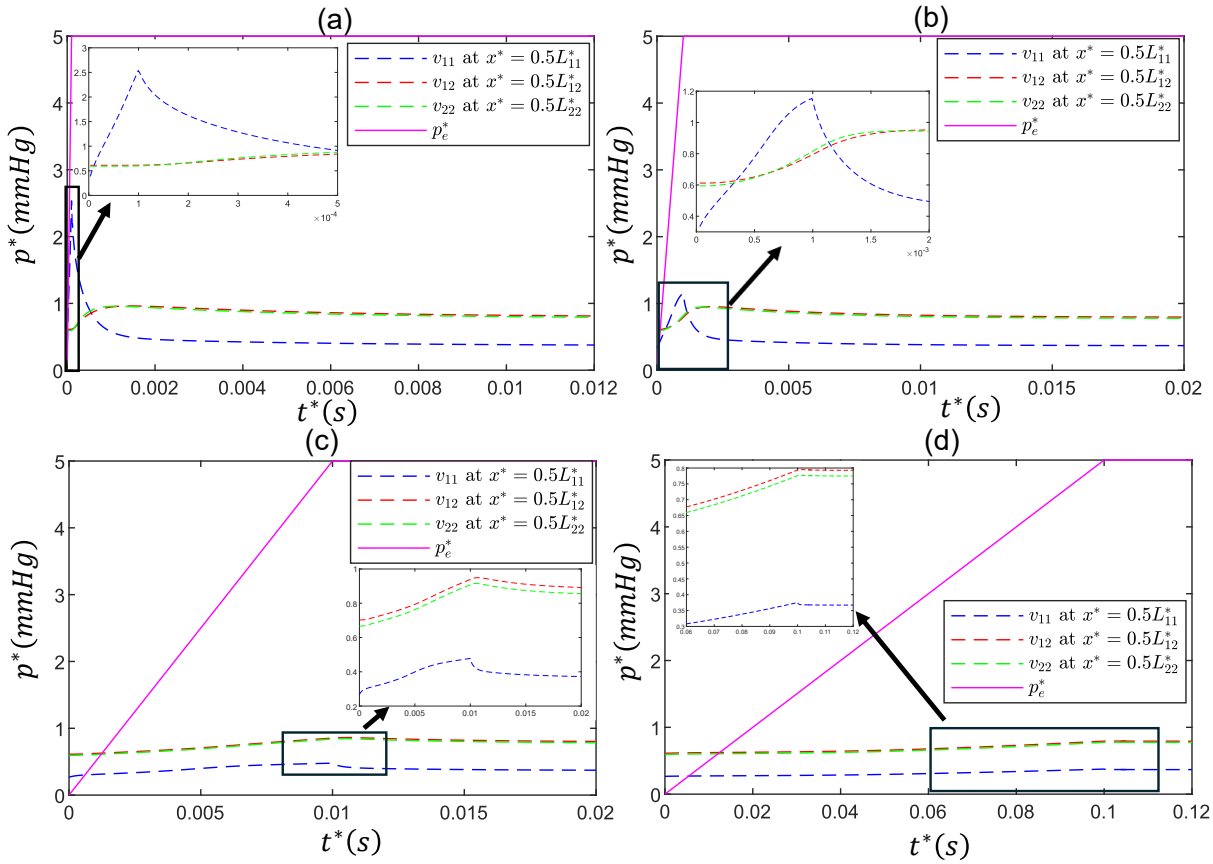

Figure 5.9: Effect of time of occlusion t^*_p when the time-dependent external pressure of maximum amplitude $\Delta p^*_e = 5mmHg$ applied on the vein of generation 1 of the bifurcating venous network showing: (a) $t^*_p = 0.0001s, t^*_f = 0.012s$, (b) $t^*_p = 0.001s, t^*_f = 0.02s$, (c) $t^*_p = 0.01s, t^*_f = 0.02s$ and (d) $t^*_p = 0.1s, t^*_f = 0.12s$, where t^*_f is the final time of the simulation. All temporal profiles are plotted at spatial location $x^* = 0.5L^*_{bi}, b, i = 1,2$. The blue dashed line is for the parent v_{11}, the red dashed line is for the daughter vessel v_{12}, the green dashed line is for the daughter vessel v_{22} and magenta line is for p^*_e.

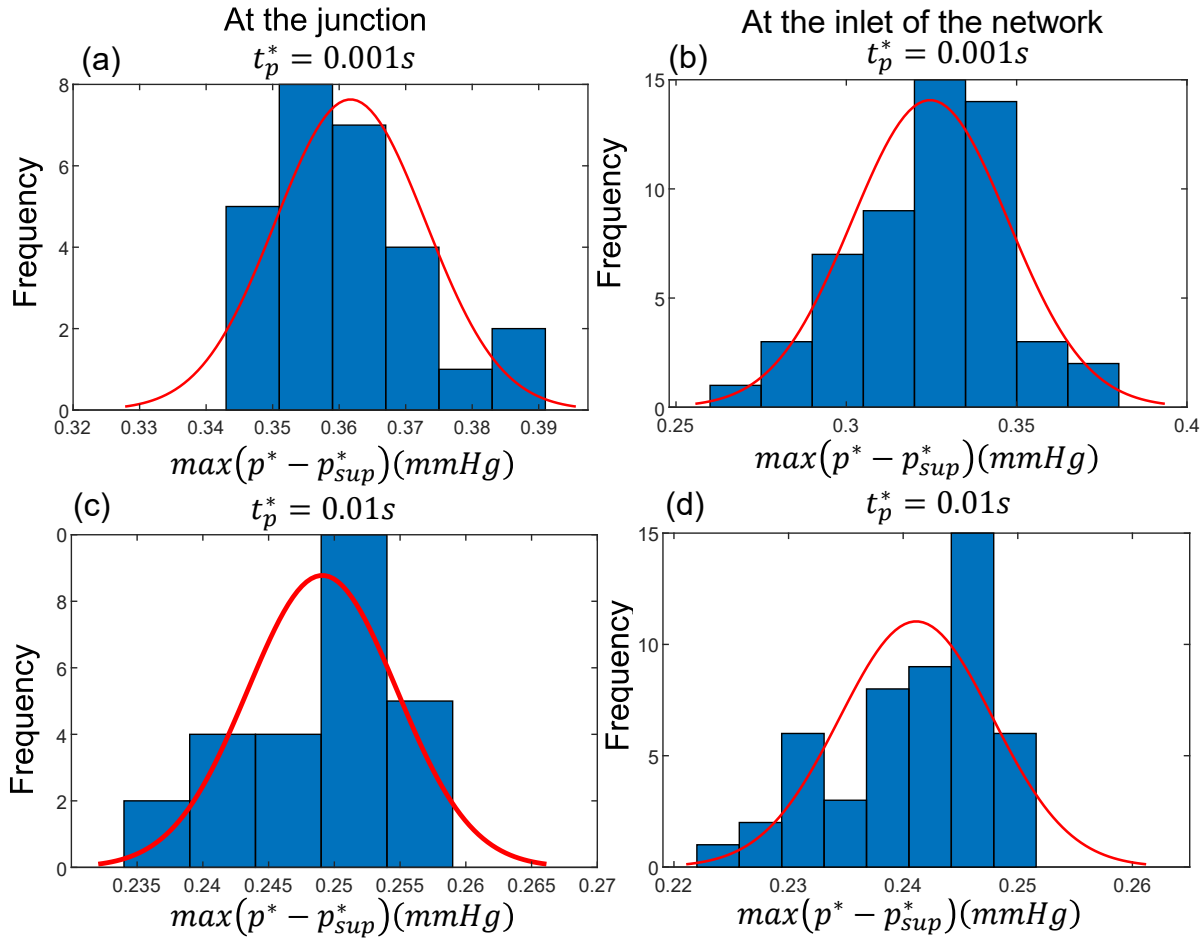

Figure 5.10: Histogram of maximum pressure value obtained from the time-dependent bifurcating network model as we apply the time-dependent external pressure of maximum amplitude $\Delta p_e^* = 5mmHg$ on the vein of generation 1 over two different timescales t_p^* showing: at the junction of the bifurcation network $X^* = 0$ for (a) $t_p^* = 0.001s$ and (c) $t_p^* = 0.01s$, and the inlets of the network $X^* = -L_{12}^*, -L_{22}^*$ for (b) $t_p^* = 0.001s$ and (d) $t_p^* = 0.01s$ when the baseline lengths of daughter veins v_{12} and v_{22} are chosen from a normal distribution with a mean of $\overline{\overline{L}}_2^*$ and a standard deviation of $\sigma_r = 0.2\overline{\overline{L}}_2^*$.

Chapter 6

Flow along the arterio-venous network

6.1 Introduction

The retinal microvascular network of humans comprises arteries, veins, arterioles, venules, small arteries and small veins. Together, they regulate blood pressure to ensure perfusion of the capillary vessels for nutrient exchange and the distribution of blood flow to meet the metabolic needs of the retinal tissue. In this chapter, we combine the divergent arterial network discussed in Appendix A and the convergent venous network developed in Chapter 5 to form a three-generation arterio-venous network, where the arterial network is connected to the venous network via capillary beds, and each arterial and venous network contains three generations of blood vessels.

To quantitatively assess the effect of retinal vein occlusion (RVO) on the arterio-venous network, we apply an external impingement on the parent vein of generation 1, but do not consider any arterial constriction. As discussed in Chapters 4 and 5, the impingement is modelled by an external pressure with a localised spatial profile applied over a prescribed timescale on the vessel wall. We want to understand the blood flow dynamics in an arterio-venous network of the blood vessels by analysing how blood flow, blood pressure, and the cross-sectional area of the blood vessels change in response to the prescribed constriction. In the following subsection 6.2, we introduce the three-generation arteriovenous network (the schematic diagram of the arterio-venous network is given in figure 6.1). As discussed for the arterial and venous networks, we label the parent vessel as generation 1, the daughter vessels are then in generation 2 and so on. In subsection 6.3, we outline the parameter values used to simulate the blood flow in the perturbed arterio-venous network. In the following subsection 6.4, we briefly outline the steady state responses of the arterio-venous network. In subsection 6.5, we discuss the time-dependent behaviour of the arterio-venous network in response to the external pressure perturbation applied to the parent vein. In subsection 6.6, we briefly discuss the image-informed network. Finally, in the subsection 6.7, we conclude the thesis by outlining the achievements of this work.

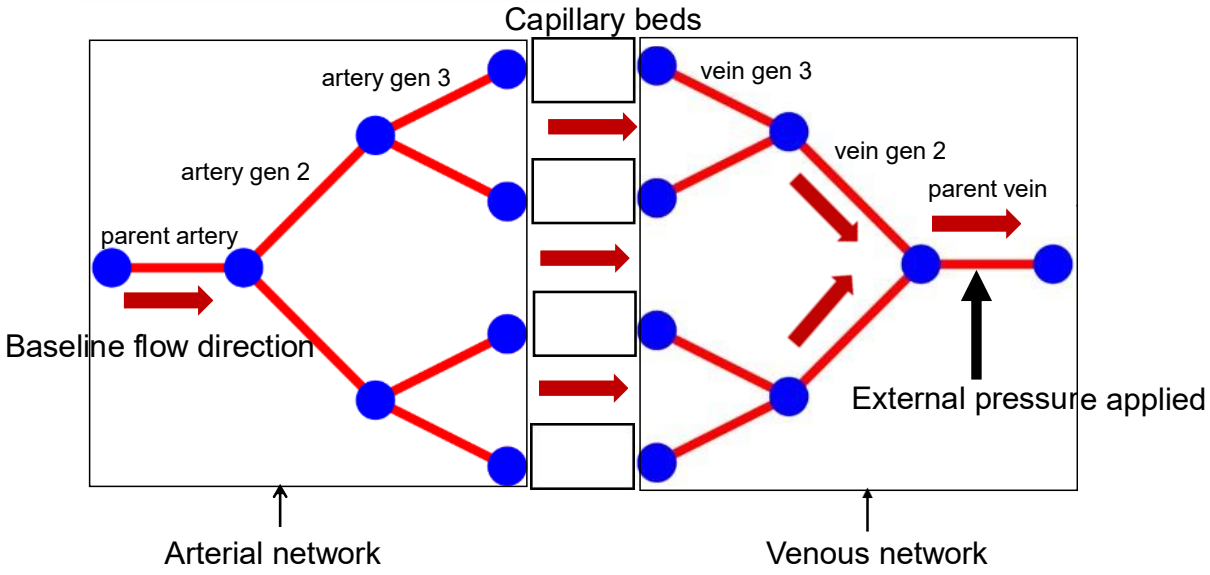

Figure 6.1: Schematic diagram of the arterio-venous network model consisting of the arterial network, the venous network and capillary beds used to study the blood flow in retinal microcirculation. The red arrow indicates the baseline flow direction of the arterio-venous network.

6.1.1 Structure of the arteriovenous network

We consider an arteriovenous network consisting of a divergent arterial network of three generations of arteries and a convergent venous network of three generations of veins, where the arterial and venous networks are connected by capillary beds, as shown in figure 6.1. As mentioned earlier in the case of the arterial network in Appendix A and for the venous network in Chapter 5, blood flow is always from left to right in the network as we plot the system. The parent artery on the left side of the arteriovenous network (figure 6.1) receives the blood flow at the inlet, while the parent vein on the right-hand side of the arteriovenous network (figure 6.1) drains the blood from the system across the outflow.

We are going to follow the same architecture for the arterio-venous network as for the arterial network, given in Appendix A and for the venous network model in Chapter 5. We use a superscript 'a' to denote all the parameters and variables related to the arterial network and the superscript 'v' to denote all the parameters and variables related to the venous network. In this chapter, we consider an arterio-venous network with three generations $i = 1, 2, 3$. The b^{th} branch artery of the i^{th} generation is denoted as a_{bi} and similarly the b^{th} branch vein of the i^{th} generation is given by v_{bi}.

6.2 Model description and boundary conditions

Building upon the mathematical model derived for the bifurcating venous network given in subsection 5.2 of Chapter 5 and the mathematical model for the divergent arterial network given in subsection A.1 of Appendix A, we follow the same protocol to describe the arteriovenous net-

work. This section only lists the non-dimensionalisation relevant for the arterio-venous network formation; all other scalings and notation remain the same as those introduced in the bifurcating venous network model from Chapter 5 and in appendix A, unless stated otherwise. For simplicity, again in this chapter, we use only an upstream flux-driven boundary condition, and we prescribe the inlet flux into the parent artery (see figure 6.1). The prescribed inlet flux is denoted by $\overline{Q}^{*a}_{11}$; in steady state, the steady flow across the parent vein is $\overline{Q}^{*a}_{11} = \overline{Q}^{*v}_{11}$. As mentioned in A.1 of Appendix A, all the non-dimensionalisation of variables and parameters are based on the baseline parameter values of the parent vein listed in Table 1.1. The typical baseline velocity of the blood is selected based on the properties of the steady flow in the parent vein in the venous network as $\overline{U}^{*v}_{11} = \overline{Q}^{*\ a}_{11} / \overline{A}^{*\ v}_{11}$.

6.2.1 Dimensionless governing equation for the b^{th} branch of the i^{th} generation of the arteriovenous network

We non-dimensionalise all variables relative to the parent vein where lengths are scaled on the square root of the baseline cross-sectional area of the parent vein, $\left(\overline{A}^{*v}_{11}\right)^{1/2}$, velocities on $\overline{U}^{*v}_{11}$ and time on $\left(\overline{A}^{*v}_{11}\right)^{1/2} / \overline{U}^{*v}_{11}$. We also choose a viscous pressure scale $P^* = \mu^{*v}_{11} \overline{Q}^{*a}_{11} / \left(\overline{A}^{*v}_{11}\right)^{3/2}$. The choice of non-dimensional scales yields the following non-dimensional groups obtained as

$$\mathcal{R} = \frac{\rho^* \overline{U}^{*v}_{11} \left(\overline{A}^{*v}_{11}\right)^{1/2}}{\mu^{*v}_{11}}, \quad k^v_{bi} = \frac{k^{*v}_{bi}}{P^*}, \quad k^a_{bi} = \frac{k^{*a}_{bi}}{P^*}, \quad \mu^v_{bi} = \frac{\mu^{*v}_{bi}}{\mu^{*v}_{11}}, \quad \mu^a_{bi} = \frac{\mu^{*a}_{bi}}{\mu^{*v}_{11}},$$
$$\overline{A}^v_{bi} = \frac{\overline{A}^{*v}_{bi}}{\overline{A}^{*v}_{11}}, \quad \overline{A}^a_{bi} = \frac{\overline{A}^{*a}_{bi}}{\overline{A}^{*v}_{11}}, \quad L^v_{bi} = \frac{L^{*v}_{bi}}{\left(\overline{A}^{*v}_{11}\right)^{1/2}}, \quad L^a_{bi} = \frac{L^{*a}_{bi}}{\left(\overline{A}^{*v}_{11}\right)^{1/2}}, \quad \overline{pc}_b = \frac{\overline{pc}^*_b}{P^*}$$

where $\mathcal{R}$ is the Reynolds number, $k^{a,v}_{bi}$ is the non-dimensional vessel wall stiffness of the b^{th} vessel in i^{th} generation, $\mu^{a,v}_{bi}$ is the non-dimensional viscosity of the b^{th} vessel in i^{th} generation, $\overline{A}^{a,v}_{bi}$ is the non-dimensional baseline vessel cross-sectional area of of the b^{th} vessel in i^{th} generation, $L^{a,v}_{bi}$ is the non-dimensional vessel length of the b^{th} branch of the i^{th} vessel and $\overline{pc}_b$ is the capillary pressure between the b^{th} branch artery of generation 3 and b^{th} branch vein of generation 3 of the arteriovenous network.

We again assume long-wavelength deformations ($\beta = 1/L^v_{11} \ll 1$) and re-scale the model parameters according to

$$\mathcal{R} = \beta^{-1}\tilde{\mathcal{R}}, \quad k^v_{bi} = \beta^{-1}\tilde{k}^v_{bi}, \quad k^a_{bi} = \beta^{-1}\tilde{k}^a_{bi}, \quad \mu^v_{bi} = \tilde{\mu}^v_{bi}, \quad \mu^a_{bi} = \tilde{\mu}^a_{bi}, \quad \overline{A}^v_{bi} = \widetilde{\overline{A}^v_{bi}},$$
$$\overline{A}^a_{bi} = \widetilde{\overline{A}^a_{bi}}, \quad Q^v_{bi} = \tilde{Q}^v_{bi}, \quad Q^a_{bi} = \tilde{Q}^a_{bi}, \quad L^v_{bi} = \beta^{-1}\tilde{L}^v_{bi}, \quad L^a_{bi} = \beta^{-1}\tilde{L}^a_{bi}.$$

All the independent variables and dependent variables remain the same and are already listed in

subsection 5.2.1 of Chapter 5 and in subsection A.1.1 of Chapter A. For notational simplicity, we drop all tildes and finally obtain the governing equation for the b^{th} branch vessel (for both artery and vein) of i^{th} generation in the closed form as

$$\frac{\partial A_{bi}^{a,v}}{\partial t} = \frac{1}{\overline{A}_{bi}^{a,v}\,\mu_{bi}^{a,v}} \frac{\partial}{\partial x}\left(\frac{\left(A_{bi}^{a,v}\right)^2}{8\pi}\frac{\partial p_{bi}^{a,v}}{\partial x}\right). \tag{6.1}$$

The flux along the parent vein v_{11} is given by (5.2) and the modified fluxes of vessels $v_{bi}, a_{bi}, b = 1,2,3,4, i = 2,3$ of the arteriovenous network are given by

$$q_{bi}^{a,v} = -\frac{k_{bi}^{a,v}}{8\pi\mu_{bi}^{a,v}}\left(\left(\frac{m}{\left(\overline{A}_{bi}^{a,v}\right)^{m+2}}(A_{bi}^{a,v})^{m+1} + \frac{n}{\left(\overline{A}_{bi}^{a,v}\right)^{-n+1}}(A_{bi}^{a,v})^{-n+2}\right)\frac{\partial A_{bi}^{a,v}}{\partial x}\right). \tag{6.2}$$

6.2.2 Dimensionless 'tube law' for the arteriovenous network

The dimensionless 'tube law' for the parent vein of generation 1 of the venous network is given by (5.4), and for all the other vessels in the arteriovenous network, it can be written as

$$p_{bi}^{a,v}(x,t) = k_{bi}^{a,v}\left(\left(\frac{A_{bi}^{a,v}}{\overline{A}_{bi}^{a,v}}\right)^{m} - \left(\frac{A_{bi}^{a,v}}{\overline{A}_{bi}^{a,v}}\right)^{-n}\right), \quad b = 1,2,3,4, \ i = 2,3. \tag{6.3}$$

For the arterial network, we choose the 'tube law' parameter values $m = 0.5$ and $n = 0$, and for the venous network, we consider $m = 10$ and $n = 1.5$. The detailed discussion on the 'tube law' parameters is given in table 1.1 in subsection 1.3 of Chapter 1.

6.2.3 Applied localised constriction of the vein of generation 1 of arteriovenous network

As discussed in subsection 5.2.3 of Chapter 5, we apply a localised compression on the parent vein at some location $x^* = x_p^*$, over a timescale t_p^*, through a prescribed external pressure p_e^* given in (5.9) and the final long-wavelength version of external pressure $p_e(x,t)$ is given by (5.12).

6.2.4 Boundary and continuity conditions of the arteriovenous network

To determine the boundary and continuity conditions, we follow the same protocol as already discussed for the arterial network and venous network. We only discuss each of these conditions very briefly in this chapter.

Again, for the continuity of pressure condition, we follow the same derivation described in subsection 5.2.1 of Chapter 5 and A.1.3 of Appendix A at except the junctions where the

arterial network is joined with the venous network. At all four junctions where the branches of generation 3 of the arterial networks connect to their counterparts in the venous network, we employ the four capillary beds shown in figure 6.1. To incorporate the capillary beds between arterial and venous networks, we simply use a prescribed pressure drop $\overline{pc}_d$, $d = 1,2,3,4$. This is a simpler representation of the smaller vessels and capillary plexii. We lump them together and model them as a pressure drop between the arterial network and venous network. As a result, the modified pressure continuity condition at these four junctions connecting the arterial and venous networks becomes

$$p^a_{b3}(N) = p^v_{b3}(0) + \overline{pc}_d, \; b,d = 1,2,3,4, \tag{6.4}$$

where p_{b3} is corresponding the blood pressure for b^{th} branch vessel in generation 3. For all other junctions on the arterial side, we employ (A.7), and for all junctions on the venous side, we use (5.14).

6.2.5 Final model for the arteriovenous network

We obtain the final system of equations for b^{th} branch (for both artery and vein) of the i^{th} generation of the arterio-venous network and is given by

$$\frac{\partial A^{a,v}_{bi}}{\partial t} = \frac{1}{\overline{A}^{a,v}_{bi}\,\mu^{a,v}_{bi}} \frac{\partial}{\partial x}\left(\frac{(A^{a,v}_{bi})^2}{8\pi} \left(k^{a,v}_{bi} \left(m(A^{a,v}_{bi})^{m-1} + n(A^{a,v}_{bi})^{-n-1} \right) \frac{\partial A^{a,v}_{bi}}{\partial x} \right) \right). \tag{6.5a}$$

The final model for the parent vein (i.e., $b = 1, j = 1$) where we apply the external pressure perturbation p_e is given by

$$\frac{\partial A^v_{11}}{\partial t} = \frac{\partial}{\partial x}\left(\frac{\left(A^v_{11}\right)^2}{8\pi} \left(\frac{\partial p_e}{\partial x} + k^v_{11} \left(m(A^v_{11})^{m-1} + n(A^v_{11})^{-n-1} \right) \frac{\partial A^v_{11}}{\partial x} \right) \right), \tag{6.5b}$$

subject to boundary conditions at the inlet of the network

$$\frac{\partial A^a_{11}}{\partial x} = -\frac{8\pi Q^a_{11}\mu^a_{11}}{k^a_{11}\left(m\frac{\left(A^a_{11}\right)^{m+1}}{\left(\overline{A}^a_{11}\right)^{m+2}} + n\frac{\left(A^a_{11}\right)^{-n+1}}{\left(\overline{A}^a_{11}\right)^{-n+2}} \right)}, \quad (x = 0), \tag{6.5c}$$

and at the outlet of the network (assuming $p_e(0,t) = p_e(1,t) = 0$)

$$A^v_{11} = 1, \qquad (x = 1), \tag{6.5d}$$

parameters	symbol	unit	value	source
capillary pressure	$\overline{pc}^*$	$mmHg$	22.9	[61]

Table 6.1: Prescribed capillary value at the four junctions of the arteriovenous network where the arterial network connects to the corresponding venous counterpart.

continuity of pressure conditions at the four junctions between generation 3 of the arterial network and generation 3 in the venous network

$$p^a_{b3}(L_{b3}) = p^v_{b3}(0) + \overline{pc}_b,\ b = 1,2,3,4, \tag{6.5e}$$

and continuity of pressure and continuity of flux conditions at all other junctions (these follow from our discussion given in subsection 6.2.4).

6.3 Parameter values

As mentioned in subsection 5.4 of Chapter 5 and subsection A.3 of Appendix A, in our arteriovenous network model, we consider the superior temporal quadrant, which originates from the first generation of our network, as shown in figure 6.1. For generation 1 of our network model, we consider the parameter values for generation 1 of Takahashi's network; for the generation 2 of our network model, we consider the parameter values for generation 2 of Takahashi's network and so on (see summary in tables 1.1, 5.1, A.1). The corresponding four capillary pressure drop values are adopted from [61], listed in table 6.1. For simplicity, we consider all four capillary values to be equal. In future, a systematic review will be done in order to understand how the capillary values can be changed for each of these four junctions.

6.4 Steady model results

To study the steady state behaviour of the arteriovenous network when no external pressure is applied, we begin by isolating the time-independent steady state solutions. In this subsection, we consider the arteriovenous network consisting of non-identical branches in generations 2 and 3. In this flux-driven flow, the flux $\overline{\overline{Q}}^{*a}_{11} = 1.88 \times 10^{-4} ml s^{-1}$ is prescribed at the inlet of the parent artery of generation 1 of the arteriovenous network.

We motivate our discussion by considering the baseline case, where we study the steady unperturbed arterio-venous network response (sup) by considering $\Delta p^*_e = 0$. The model arteriovenous network is sketched in figure 6.1. While keeping all other parameter values fixed, the length of the branches of generation 2 and generation 3 of arteries and veins are all randomly sampled from the normal distribution $L^{*a}_{bi} \sim \mathcal{N}\left(\overline{\overline{L}}^{*a}_i, 0.2\overline{\overline{L}}^{*a}_i\right)$, $b = 1,2,3,4$, $i = 2,3$ and $L^{*v}_{bi} \sim$

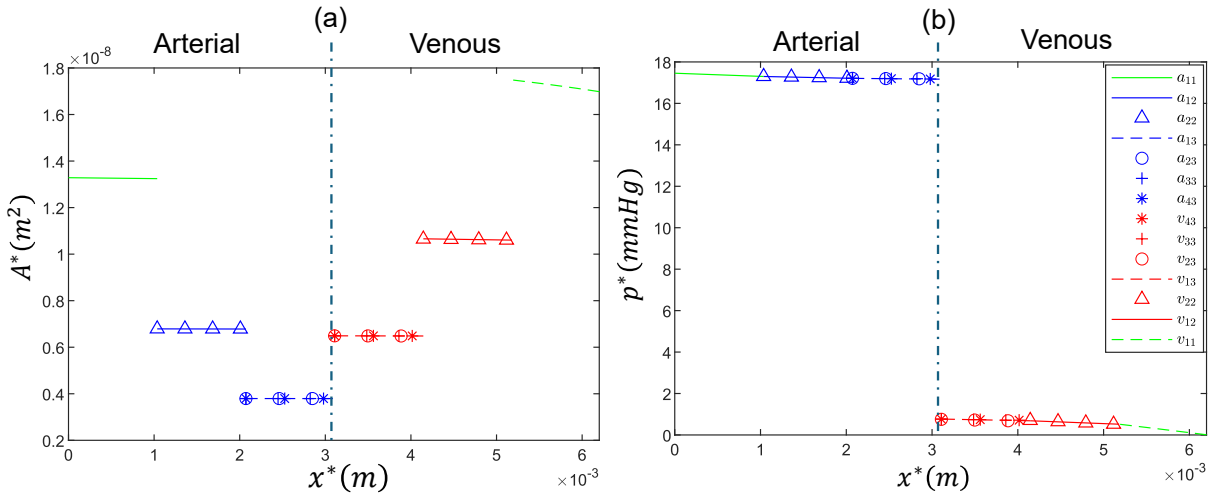

Figure 6.2: Behaviour of the arterio-venous network containing non-identical branches of different baseline cross-sectional area in generation 2 and 3 at a steady state, when maximum pressure amplitude $\Delta p_e^* = 0$: spatial profiles of the (a) cross-sectional area A^* and (b) blood pressure p^*. The blue dashed vertical line represents the junction between the arterial network and the venous network

.

$\mathcal{N}\left(\overline{\overline{L}}_i^{*v}, 0.2\overline{\overline{L}}_i^{*v}\right)$, $b = 1,2,3,4$, $i = 2,3$ respectively where mean is the baseline length $\overline{\overline{L}}_i^{*a}$ or $\overline{\overline{L}}_i^{*v}$ where $i = 2,3$, depending on whether the branch is arterial or venous and the standard deviation is chosen to be 20% of the mean value. Figure 6.2 plots the cross-sectional area A^* (figure 6.2a) and pressure p^* (figure 6.2b) profiles for the three-generation arterio-venous network.

All the spatial profiles of the cross-sectional area and pressure decrease almost perfectly linearly with the slope set by the prescribed flow rate (see figure 6.2a,b). As expected, the pressure gradients are different across each generation in line with the flow rate prescribed. Overall pressure differences across two networks are small in comparison to the prescribed capillary pressure drop. As mentioned earlier, this is not only the prescribed capillary pressure drop, but it reflects the combined contribution of the capillaries and the upstream microvascular network of small blood vessels.

6.5 Unsteady model results

Now, we aim to investigate the time-dependent behaviour of the arterio-venous network when applying a time-dependent external pressurisation given by (5.12) to the parent vein of the network (see figure 6.1). In this section, while keeping all other parameter values fixed, the length of all the branches of generation 2 and generation 3 are again randomly sampled from a normal distribution as mentioned in subsection 6.4. It is important to note that, in principle, other parameters could also be sampled randomly, leading to more stochastic variability in the outcome. In the following subsection 6.5.1, we begin our discussion with the baseline unsteady

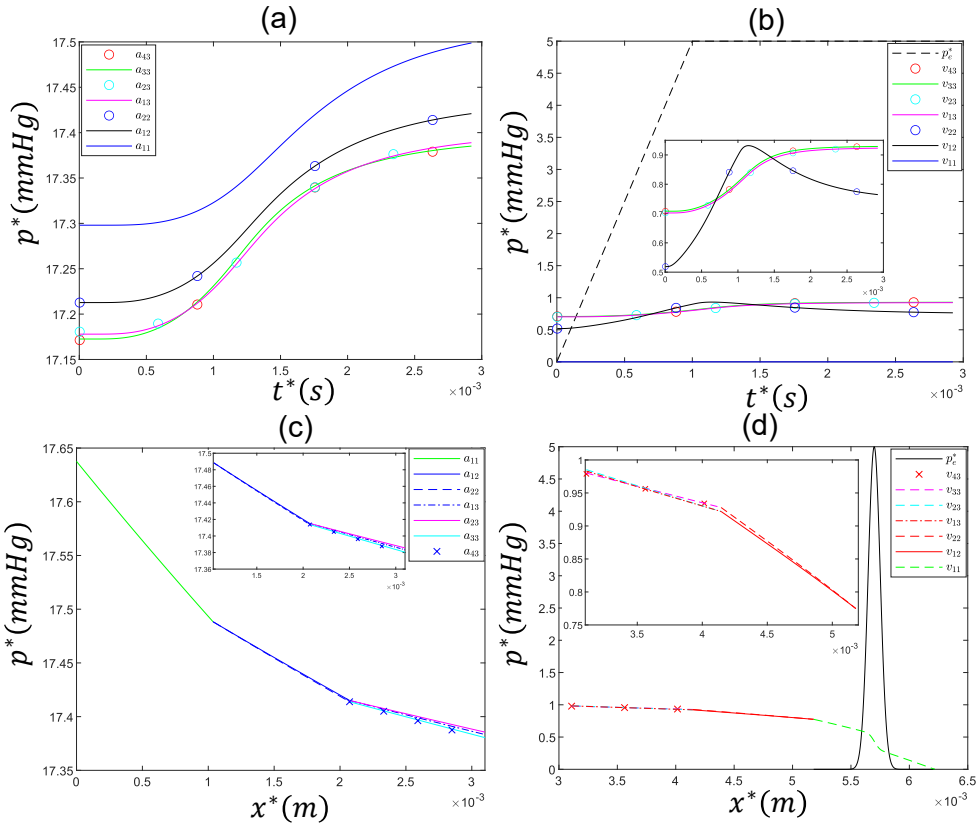

Figure 6.3: Time-dependent responses of the arteriovenous network containing non-identical branches in generation 2 and generation 3 where the length of all the branches of generation 2 and 3 are randomly sampled from a normal distribution $\mathcal{N}(\mu_r, \sigma_r)$ where mean μ_r is the baseline length $\overline{L}^{*a}_{12}$ or $\overline{L}^{*v}_{12}$, depending on whether the branch is arterial or venous and the standard deviation σ_r is chosen to be 20% of σ_r. Pressure perturbation with a maximum pressure amplitude of $\Delta p^*_e = 5mmHg$ has been applied externally showing: temporal responses of pressure p^* for (a) arterial network, (b) venous network (inset: branches in generations 2 and 3) and spatial responses of (c) arterial network (inset: branches in generations 2 and 3), (d) venous network (inset: branches in generations 2 and 3). The time of occlusion $t^*_p = 0.001s$, and the final time of the simulation is $t^*_f = 3t^*_p$.

case. Subsection 6.5.2 discusses the effect of the perturbation time t^*_p on the unsteady response of the arterio-venous network.

6.5.1 Unsteady baseline case

Figure 6.3 is obtained by plotting the temporal (figure 6.3a,b) and spatial (figure 6.3c,d) profiles of the blood pressure at the outlet of each branch of generation 2 and generation 3 of the arterio-venous network.

Looking at the venous side of the arteriovenous network, initially at time $t^* = 0$, the pressure in veins of generation 2 (black line for υ_{12} and blue circle for υ_{22} in figure 6.3b) is lower than the pressure in veins of generation 3 (magenta line for υ_{13}, cyan circle for υ_{23}, green line for υ_{33} and red circle for υ_{43} in figure 6.3b) as the pressure drop between generations drives the

flow. Once the parent vein becomes occluded, blood is displaced and redistributed upstream and downstream of the constriction in the network. Over time, all the branches in the generations 2 and 3 receive the displaced fluid, and in all cases, blood pressure starts to rise (figure 6.3b). It is important to note that the pressure of generation 2 overshoots in a significant manner, starting from nearly $0.54 mmHg$, then reaching up to $0.95 mmHg$, and once the effect of external pressure is fully established, the pressure value drops below $0.77 mmHg$ to reach the steady perturbed value (figure 6.3b). This indicates that once the system approaches the steady state, the overall pressure (steady) gain for generation 2 is $\approx 0.23 mmHg$, whereas during the transient overshoot, the pressure gain is much greater ($\approx 0.41 mmHg$). Although there is no evidence of overshooting for generation 3, we do observe quite a significant gain in overall pressure in this generation ($\approx 0.26 mmHg$). Once the effect of external pressure p_e^* is fully applied, the blood pressure in generation 2 decreases and temporal profiles in generation 2 and 3 switch dominance and eventually, the temporal profiles of pressure of all branches of generation 3 overtake the corresponding temporal responses of generation 2; this pressure difference between generations 2 and 3 is necessary to ensure the system can adapt a steady configuration.

Looking at the temporal responses of the arterial side of the network given in figure 6.3(a), as expected, the largest pressure is within the parent artery with pressure drops in subsequent generations (figure 6.3a). In all generations, blood pressure rises slowly over time as the system feels the effect of the incoming fluid forced from the parent vein as a result of constriction (see figure 6.3a). However, these pressure differences are much less pronounced than on the venous side of the network. The corresponding spatial plots validate our observation given in figure 6.3(c,d). As the constriction is applied to the parent vein, fluid is displaced upstream of the constriction and gradually into the arterial side. However, given the relatively large stiffness of the arteries, they are only expanded by a relatively small amount.

6.5.2 Influence of the time of occlusion t_p^* on the response of the arteriovenous network

As seen earlier for the venous network in subsection 5.6.2 of Chapter 5, the occlusion time t_p^* can have a significant influence on the increase in maximal pressure in subsequent generations. In this subsection, we compare this maximal pressure at the outlet of each vessel of the venous side of the arteriovenous network, where we vary the ramping time t_p^* over which the external pressure perturbation of maximum amplitude $\Delta p_e^* = 5 mmHg$ is applied on the parent vein of generation 1. Figure 6.4 plots the relative changes in blood pressure p^* of the parent vein and branches in generations 2 and 3 at the corresponding outlet of each generation for four different t_p^*. In each case, we sample the length of vessels in generations 2 and 3 from a normal distribution, as described above in subsection 6.4. In all cases, we compare to the steady state pressure profile obtained from the steady unperturbed model (sup model), denoting the pressure p_{sup}^*. In all

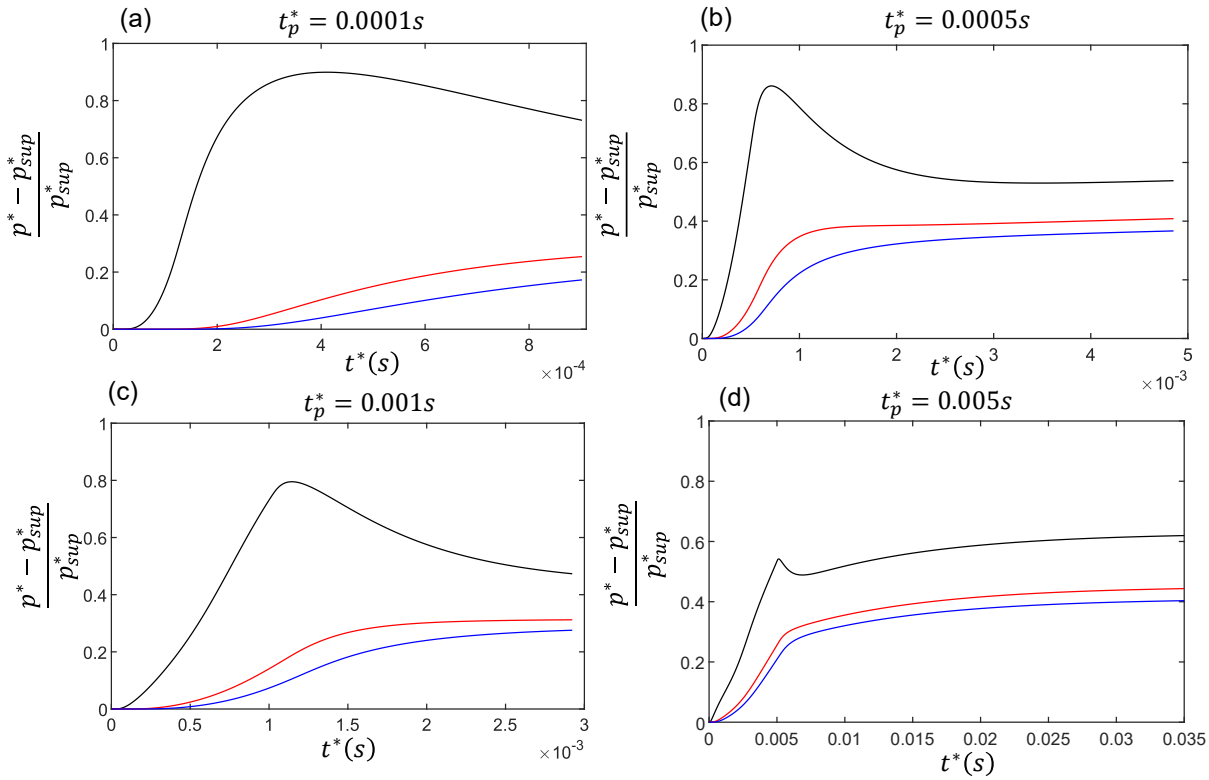

Figure 6.4: Effect of time of occlusion t_p^* when the time-dependent external pressure of maximum amplitude $\Delta p_e^* = 5mmHg$ is applied on the vein of generation 1 of the arteriovenous network, showing: the relative pressure increase for (a) $t_p^* = 0.0001s$, (b) $t_p^* = 0.0005s$, (c) $t_p^* = 0.001s$ and (d) $t_p^* = 0.005s$. p_{sup}^* is the steady state pressure profiles obtained from the sup model.

four cases, as expected, the change in pressure (the black line in figure 6.4a,b,c,d) is greater in generation 2 compared to generation 3, and we observe a significant overshoot in generation 2 (figure 6.4). As we vary the ramping time t_p^*, the final steady state must become the same in all cases. The overshoot value is greater for short ramping times and gradually diminishes toward zero as the ramping time t_p^* increases. It might be expected that the overshoot is eventually suppressed as ramping time increases further, but we have not yet been able to run the model to very long times.

6.6 Image-informed arteriovenous network

We have developed a theoretical model for an arterio-venous network consisting of three generations of arteries and three generations of veins. In Chapter 3, we have already extracted diameters of retinal blood vessels from the one segmented clinical image for three generations of arteries and veins from fundus images provided by our clinical collaborator. In this section, we want to use those diameter values extracted from images to parameterise the arteriovenous network developed in this chapter. We follow the clinical convention that the thicker vessel in the clinical image is considered a vein, and the thinner vessels are considered to be arteries. All the lengths

Vessel generation	Symbol	Vein(pixels)	Vein(μm)	Artery(pixels)	Artery(μm)
1	$\overline{\overline{R}}^*_1$	3.3744	148.1	2.46	108
2	$\overline{\overline{R}}^*_2$	3.1598	138.7	1.91	84
3	$\overline{\overline{R}}^*_3$	2.2120	97.1	1.5	66

Table 6.2: Vessel diameter of artery and vein calculated directly from fundus images.

of the corresponding branches of different generations are listed in table 3.1 of Chapter 3. It is important to note that, as the extracted diameters from the images are in pixels, it is important to convert the diameter to a physical unit, possibly in μm and then use that in the mathematical model. To convert retinal vessel diameter measurements (obtained from the fundus image) from pixels to physical units, we use the optic disc as an internal reference. There are relatively consistent measurements of the mean vertical diameter of the optic disc for healthy adults available in the literature, which is typically around $1.80\mu m$ [20]. Considering this, we have performed a pixel to μm conversion using the following scaling factor

$$s = \frac{D_{phy}}{D_{image}}(\mu m/pixel) = \frac{1800}{41} = 43.9$$

where $D_{phy} = 1800\mu m$ is the reference value obtained from [20], and $D_{image} = 41 pixels$ is the vertical diameter measured in pixels from the original fundus image given in 2.22(a). To change all the vessel diameter measurements obtained in pixels from the fundus images (figure 2.22a) listed in table 3.1 of Chapter 3 to a physical unit (μm), we multiply the vessel lengths (in pixels) by the scalling factor s. The table 6.2 represents the diameter obtained from the image in Chapter 3.

Figure 6.5 shows the prediction of our arteriovenous network model, which is parameterised based on the diameters extracted from real patient images. The diameter of the branches of generations 1,2 and 3 of arteries and veins are all randomly sampled from the normal distribution $L^{*a}_{bi} \sim \mathcal{N}\left(\overline{\overline{L}}^{*a}_i, 0.2\overline{\overline{L}}^{*a}_i\right)$, $b = 1,2,3,4$, $i = 2,3$ and $L^{*v}_{bi} \sim \mathcal{N}\left(\overline{\overline{L}}^{*v}_i, 0.2\overline{\overline{L}}^{*v}_i\right)$, $b = 1,2,3,4$, $i = 1,2,3$ respectively where mean is the baseline diameter $\overline{\overline{R}}^{*a}_i$ or $\overline{\overline{R}}^{*v}_i$ where $i = 2,3$, depending on whether the branch is arterial or venous and the standard deviation is chosen to be 20% of the mean value. The mean values of the diameter used in the simulation are listed in table 6.2. We note that in this image-informed case, the outcome is broadly very similar to the randomised case presented above, with the same key features evident.

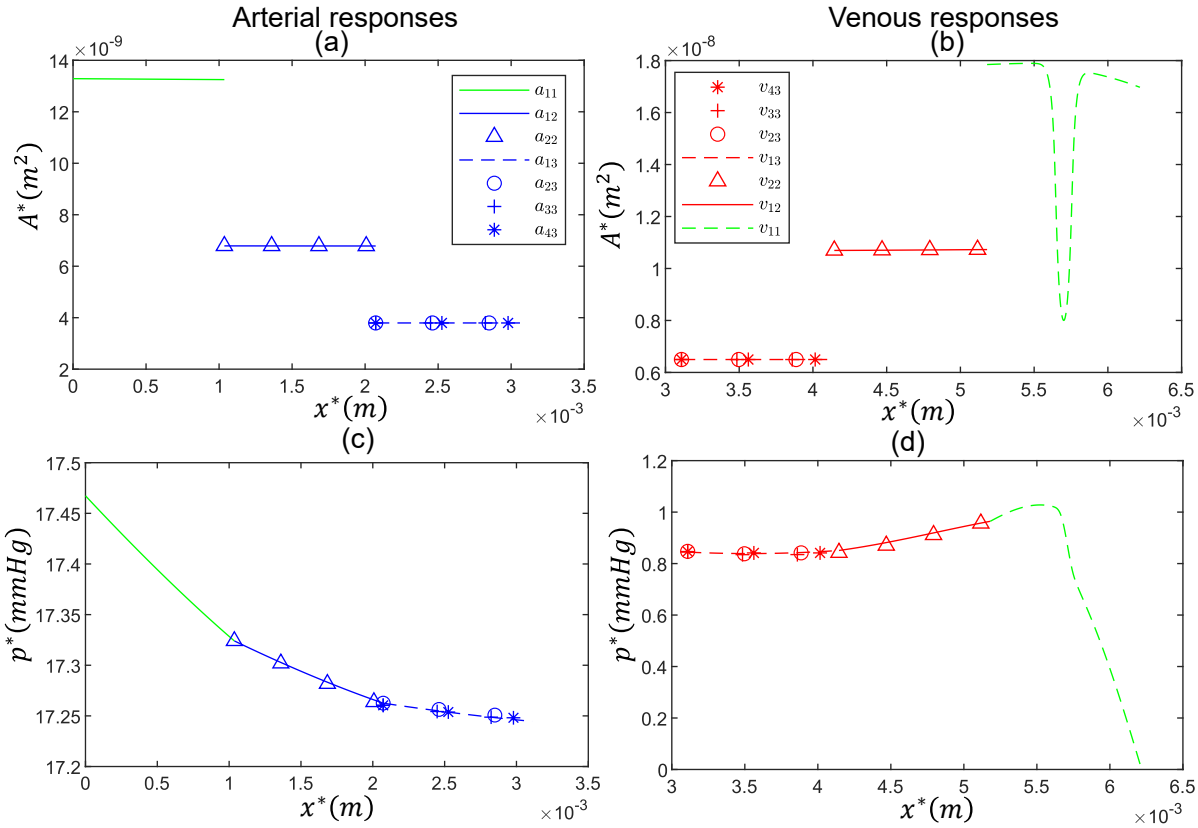

Figure 6.5: Image informed three generation arterio-venous network where pressure maximum pressure amplitude $\Delta p_e^* = 5mmHg$ is applied over a timescale $t_p^* = 0.0001s$, showing: spatial responses of (a) cross-sectional area, (c) pressure for arterial network and (b) cross-sectional area, (d) pressure for venous network. The final time of simulation is $t_f^* = 10t_p^*$.

6.7 Conclusion

To build a mathematical model for the three-generation arteriovenous network, we started with a single-vessel model, where, for simplicity, the whole network was treated as a single long vessel in Chapter 4. In Chapter 5, we extended the single-vessel mathematical model to the two-generation converging venous network. To study the effect of RVO on the parent vein, we apply a time-dependent external pressure perturbation. As the external pressure is applied to the parent vessel, we observe a well-defined maximum pressure in the daughter vessels that overshoots the eventual steady state. It is therefore interesting to study, within the arteriovenous network model, how these pressure peaks propagate through the network across the further generations.

Based on our observations from the venous network, we extend the existing venous network model to a three-generation arteriovenous network in Chapter 6. In this arteriovenous network, we consider a novel mathematical framework containing three generations of arteries and three generations of veins connected by capillary beds. We prescribe the baseline flow at the inlet of the parent artery, while everything else follows from the model of the venous network. To understand the impact of the variability in parameters on the arterio-venous network model, we choose the vessel lengths from a normal distribution. As an external pressure is applied to the parent vein,

this increases the maximum pressure in the next generation upstream, which exceeds the eventual steady value. However, this overshoot diminishes as the ramping time increases. Furthermore, the blood pressure in subsequent generations increases monotonically toward the steady state, and there is no overshoot. It is therefore not clear if this pressure propagation can eventually lead to a retinal haemorrhage, as there is no localised increase in pressure in the peripheral generations of the network.

At the end of this work, we have successfully built an image-informed three-generation arterio-ovenous network for the first time, considering the fluid-structure interaction for real prediction to study the effect of RVO on retinal microcirculation, and in principle, we can use all the information about the lengths and radius extracted from the images to parameterise this arterio-venous network. The simulation exhibits all the features identified in the randomised case discussed above.

Chapter 7

Overview, conclusion and future direction

In this chapter, we summarise the outcome of this thesis and discuss how it all fits together to predict pressure propagation across the retinal circulation, which may possibly lead to vessel bursting (potentially leading to retinal haemorrhage) in response to a retinal vein occlusion (RVO). The following subsection 7.1 provides the overview of the thesis. In subsection 7.2, we outline the clinical relevance of the proposed mechanism to understand RVO. In the following two subsections 7.3 and 7.4, we compare our approach with existing state-of-the-art studies to clarify its necessity, novelty and to discuss how it addresses gaps in the current literature. The last subsection 7.5 discusses the limitations and scope of this work.

7.1 Overview of the thesis

We analysed the clinical images of the retinal fundus, which have a visible retinal haemorrhage, obtained from our clinical collaborator, example given in figure 1.2(b) of Chapter 1. Using cutting-edge vessel segmentation algorithms (both classical machine learning-based approach and deep learning-based approach), we successfully extracted several generations of blood vessels in Chapter 2. The next step was to measure different geometrical attributes of the vessel in the network, e.g., their length and radius, from the extracted segmented vessel map to parameterise the arteriovenous network so that we could build a realistic mathematical model which closely resembles this structure. To do that, the first step was to extract a skeletonised tree, containing the centrelines of the blood vessels appearing in the segmented image. In Chapter 3, we used the graph-based reconstruction method to construct the vessel tree to compute the length and radius of each vessel of the network.

To build the corresponding mathematical model, we first considered the whole arterio-venous network as a long single blood vessel in Chapter 4. To mimic the RVO, we applied an external pressurisation at the centre of a single vessel to study the role of fluid accumulation on the other side of the occlusion and wave propagation away from the site of disturbance. To account for fluid accumulation, we employed a viscous model, whereas the effect of wave propagation was

analysed using an inertial model. As expected, for a purely viscous model with no inertia, we observed that upon applying constriction on the vessel, the vessel expanded almost uniformly from the corresponding steady state upstream to the point of constriction, depending on the boundary condition. In contrast, including the effect of fluid inertia, we also observed the wave propagation along the system due to the time-dependent constriction. Profile steepening was evident in some cases, and the wave approached as a shock. The numerical method employed was not shock-wave capturing, and so it was not possible to solve accurately once the profiles became sufficiently steep. An in-depth analysis of the viscous and inertial models indicates that for short perturbation times, the behaviour of the two models is very different. However, for long enough perturbation time, the qualitative behaviour of the viscous and inertial models resembled each other. In line with biological observation, the venous thrombus production caused by RVO was a slow process relative to the wave propagation timescale, and so we felt that the viscous model captured the essential physics. As a result, for further analysis, we proceeded with a viscous model to build the arterio-venous network.

In Chapter 5, we build an efficient mathematical model for a two-generation converging venous network, where the flow was prescribed at the two inlets of the daughter veins. To study the effect of RVO, we applied a time-dependent external pressure perturbation at the middle of the parent vein and in order to understand the effect of inhomogeneity, we chose the lengths of the daughter vessels independently from a normal distribution. As the external pressure was applied to the parent vein, we observed a well-defined maximum fluid pressure in the daughter vessels that overshot the eventual steady state value. It is important to understand how these pressure peaks propagate through the network across the further generations within the arteriovenous network model. This overshoot of pressure was quite significantly influenced by the perturbation ramping time, contributing its largest value when the ramping time is short. We observed that the maximum pressure value in the daughter exceeded the maximum pressure value calculated from the parent, indicating a possible high risk of vessel rupture in the daughter compared to the parent.

In Chapter 6, where we extended the existing venous network model to a three-generation arteriovenous network. In this arteriovenous network, three generations of arteries and three generations of veins were connected by capillary beds. As an external pressure applied to the parent vein, this increased the maximum pressure in the next generation upstream, which exceeded the eventual steady solution shown in Chapter 5. However, this overshoot diminished as the ramping time increased. The overshoot might eventually have been suppressed as the ramping time increased further, but we were not able to run the model to sufficiently long times. No overshoot was observed in any of the further generations, so this effect was very localised, not going to lead to pressure spikes in higher generations. Hence, it was not clear if this pressure propagation could eventually lead to a retinal haemorrhage.

We successfully constructed an image-informed three-generation arteriovenous network for

the prediction of the effect of localised constriction on the retinal microcirculation, where we could use information about the lengths and radius of vessels directly extracted from the real patient images to parameterise the geometry.

7.2 Clinical relevance of the hypothesis

From our extensive literature review in Chapter 1, we know that at a point of arterio-venous crossing, the artery and vein are fixed within a vascular sheath of fixed cross-sectional area. Due to diseases like arteriosclerosis, where the arterial wall becomes thickened, the corresponding vein can become compressed at the site of arterio-venous crossing. This compression of the venous wall damages the endothelial membrane of the vein, which then fails to regulate blood pressure and maintain the anticoagulant surface of the vascular bed. The damaged endothelium expresses procoagulant behaviour and loses its ability to repel blood cells. Consequently, platelets and red blood cells begin to adhere to the injured venous wall. As a result, blood flow through the vein slows, a condition known as stasis. The resulting stasis and cellular adhesion promote spontaneous development of an intravenous thrombus. This thrombus progresses to occlude the vein over time scales of minutes. The sudden obstruction of venous outflow prevents the retinal venous network from draining blood properly, leading to a rapid increase in intravascular pressure within the retinal circulation proximal to the site of the venous thrombus [22]. To understand the role of RVO in vessel bursting, in this project, we use a combination of mathematical modelling (based on continuum mechanics) and fundus image analysis to build a three-generation arteriovenous network.

Our model predictions have the potential to offer a shift in clinical understanding by providing early warnings of potential retinal haemorrhage, given the sign of occlusion already present in the patients. The work presented in this thesis can be considered as a first working tool towards this objective. Furthermore, the model highlights the importance of patient-specific vascular geometry in determining susceptibility to retinal vein occlusion and subsequent haemorrhage. There is the potential to make this model really robust and data-driven by using more clinical images so that we can build a solid understanding from the clinical data that can tell us how predisposed a patient is to have a retinal vein occlusion. In particular, investigating how morphological characteristics of the vascular network influence flow dynamics may help identify key triggers for retinal haemorrhage and improve risk assessment in clinical practice.

7.3 Comparison with previous works

There are existing studies on RVO which are primarily clinical in nature and focus on describing observed features such as venous dilation, haemorrhage, and macular edema [79]. Experimental animal models of RVO are widely used to study the pathogenesis of this disease, to understand

the disease mechanism and to develop new therapeutics [118]. However, these approaches do not provide a mechanistic and quantitative framework for understanding the underlying mechanism of RVO and its impact on flow dynamics.

Previous computational studies have attempted to address this gap. Image-based simulations have been used to study the blood flow in a healthy retinal vascular tree, typically treating the blood vessels as rigid tubes [102]. Other approaches focus on probabilistic description of occlusion formation, considering the cell-scale adhesion processes [123]. While these approaches offer valuable insights, they are often computationally expensive or primarily limited to modelling retinal blood circulation under healthy conditions.

Three-dimensional fluid–structure interaction (FSI) models offer a detailed description of blood flow in the cardiovascular system [165], and have been applied to individual vessel segments and junctions of the vascular network [112]. However, expanding these to model large sections of the cardiovascular system becomes computationally challenging, especially for networks spanning multiple vessel generations [150].

A more computationally efficient and tractable approach is to derive a reduced order model by averaging the three-dimensional governing equations across the vessel cross-section with an appropriate closure condition, yielding a spatially one-dimensional ($1D$) reduced order model of the flow [165]. This one-dimensional ($1D$) modelling framework shows great promise for accurately predicting blood flow and pressure across the vascular network at a significantly reduced computational cost [151].

Cardiovascular flows are considered as quasi $1D$ flow [7]. The existing $1D$ model, such as those for pulmonary networks, includes arterial and venous flows and pressures, and connects the arterial and venous sides using boundary conditions [68], with some models focusing specifically on the venous side of the circulatory system [95]. However, these models often consider simplified network structures by limiting to two generations of vessels and excluding capillary beds, instead directly coupling arterial and venous trees [68]. However, we develop a larger, three-generation arteriovenous retinal network where the arterial network is joined to the venous network through capillary beds, enabling a more physiologically realistic representation of retinal microcirculation. While more comprehensive pulmonary models exist that integrate structured-tree approaches for small vessels with patient-specific data [96], they employ a simplified version for constitutive relations for vessel wall mechanics. However, we introduce a fully nonlinear realistic 'tube law' relating blood pressure p^* to the cross-sectional area A^*, vessel stiffness k^* and external applied pressure p_e^*. This non-linear formulation captures nonlinear vessel deformation but presents significant numerical challenges, particularly at network junctions due to the nonlinear dependence on A^*.

7.4 Contribution and novelty of this thesis

In the clinical image (see figure 1.2b in Chapter 1), we observed the spatial separation between the site of haemorrhage and the site of occlusion. The localisation of haemorrhage was observed upstream of the point of occlusion. The possible mechanism of progression of venous occlusion at the A-V crossing was given in figure 1.3 in Chapter 1. These observations motivate the development of a quantitative framework to understand how a localised occlusion influences blood flow across the retinal microvascular network.

In this thesis, for the first time, the fundus image analysis was combined with patient-specific mathematical modelling (based on continuum mechanics), to investigate the mechanism of retinal haemorrhage following retinal vein occlusion. We presented a novel three-generation arterio-venous model incorporating the fluid-structure interaction to study $1D$ blood flow and blood pressure in a retinal microcirculation. A key contribution of this work was the incorporation of fluid–structure interaction in the three genera, which enabled the model to capture the reservoir effect of the vein. Under time-dependent external pressurisation on the parent vein, the displaced blood from the occluded vein led to a transient increase in blood flow in the vessels upstream of the point of constriction. This excess volume was accommodated through expansion of the vessel.

Another major contribution was the development of a novel numerical strategy to efficiently implement the nonlinear 'tube law'. The nonlinear 'tube law' introduced significant numerical challenges in enforcing the pressure continuity condition at all network junctions. To introduce this, we devised a novel, efficient approach by breaking the nonlinear term involving A^* into linear and non-linear parts, where linear components were treated implicitly at the new time step, while nonlinear contributions were evaluated explicitly using previous time-step values as discussed in Chapter 5. This semi-implicit approach ensured computational efficiency while retaining the essential nonlinear behaviour. In Chapter 6, we extracted the lengths and radii of all arteries and veins from a real patient image using a cutting-edge fundus image analysis technique, enabling realistic parametrisation of the network.

7.5 Limitations and future work

In this work, we considered a simple representation of the smaller vessels and capillary plexii. We lumped them together and modelled them as a pressure drop p_c between the arterial network and venous network. This is one of the limitations of the current arterio-venous network model. However, to form a realistic network for the retinal microcirculation, it is important to model each capillary plexus individually rather than lumping it together with smaller vessels of the network. There are different approaches available to model the capillary beds. For example, we could use the alveolar sac model, which is commonly used to study pulmonary gas exchange

and the microcirculation within the lungs [41]. This framework represents the capillary network as a highly interconnected, deformable surface surrounding the alveoli, allowing for detailed analysis of fluid exchange across the capillary walls. Alternative approaches include representing the capillary bed as a lumped hydraulic resistance, which introduces flow–pressure coupling but still neglects nonlinear rheological effects and network heterogeneity [120]. More sophisticated approaches, such as Windkessel-type representation, incorporate vascular compliance and thus capture transient storage effects [62]. Another approach to modelling the branching network is using Murray's law [104]. It states that the cube of the radius of a parent vessel equals the sum of the cubes of the radii of the daughters [104]. It provides constraints on vascular geometry but does not directly impose a boundary condition relating flow and pressure.

As a direction for future work, the arterio-venous network model could be extended further by incorporating alveolar sac–based representations to achieve a more physiologically realistic description of capillary beds between arterial and venous networks. Furthermore, there is a need for developing a detailed model of retinal vein occlusion (RVO) formation, including models of thrombus formation and growth. Development of fully three-dimensional (3D) flow models at bifurcations of the network to capture complex local haemodynamics would be beneficial.

There is a need to improve the numerical methods so that the numerical method can resolve flow behaviour in the presence of occlusion in the parent vein robustly. This can be done either by developing an adaptive grid technique or by using locally refined meshes in the parent vein.

In this work, we extracted the vessel network from a single colour fundus image. Expanding this analysis to include multiple images would provide more robust estimates of vessel lengths and radii. Also, the current modelling framework needs to be extended to construct larger vascular networks by incorporating all geometric information extracted directly from fundus images.

Uncertainty quantification remains an important challenge. Future work will focus on quantifying errors arising from image-based reconstruction and analysing how these uncertainties propagate through the network model to influence blood flow predictions. In particular, we aim to develop a systematic framework for quantifying and analysing uncertainty in patient-specific measurements and their influence on model outputs.

Appendix A

Arterial Network

A.0.1 Introduction

The arterial network branches divergently, where a parent bifurcates to form two subsequent daughter vessels, opposite to the divergent venous network. We consider a small diverging arterial network shown in figure A.1, consisting of two generations of blood vessels, where the parent vessel in generation 1 bifurcates to the two daughter branch vessels of generation 2 to form the arterial network. As mentioned earlier in this work for the venous network in Chapter 5, the direction of blood flow is always from left to right in the network, so the parent vessel on the left side of the network sends blood flow into the daughter vessels on the right and daughter vessels drain the blood flow from the system.

We index each vessel of the network by an index i, where $i = 1$ represents the first-generation blood vessel, i.e., parent, $i = 2$ represents the second-generation vessel, and so on, with increasing i indicating successive generations of branching blood vessels. It is important to note that for an arterial system, one vessel in i^{th} generation bifurcates into two vessels in $(i+1)^{th}$ generation (figure A.1). For the arterial system, we denote the b^{th} branch of the i^{th} generation as a_{bi}.

In this chapter, we restrict our discussion to a single arterial bifurcation characterised by $b = 1,2$ and $i = 1,2$. It is important to note that a similar structure can be adopted for a larger arterial network containing several generations of blood vessels. The overall structure of the network for the venous counterpart is analogous to that of this arterial bifurcation and is given in Chapter 5.

A.1 Derivation of the arterial network

Building upon the mathematical model derived for the single-vessel case in subsection 4.2 of Chapter 4, we now extend the formulation to describe the blood flow in a bifurcating arterial network. While this section focuses on a bifurcating network comprising three blood vessels, we present the derivation in a more general framework, allowing the same approach to be easily

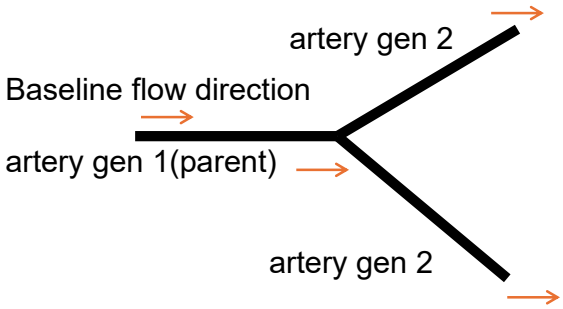

Figure A.1: Schematic diagram of a divergent arterial network model showing two generations of vessels

adopted for the arterial network in the Chapter 6 for the arterio-venous network. This section addresses the modified non-dimensionalisation relevant for the arterial network formation; all other scalings and notation remain as those introduced in the single-vessel model, unless stated otherwise. It is important to note that in the case of the arterial network, all non-dimensionalisations of variables are done based on the baseline parameter values of the parent vein listed in the table 5.1. We denote the parameter values of the parent vein by a superscript 'v' and parameter values of the parent artery by a subscript 'a'. To eliminate ambiguity in the notation used for constructing the network, all baseline parameter values are denoted with an overline.

For simplicity, in this chapter, we use only an upstream flux-driven boundary condition, where the prescribed inlet flux is denoted by $\overline{Q}^{*a}_{11}$, i.e., we prescribe the inlet flux into the parent artery and the blood viscosity of the arterial network is μ^{*a}_{bi}. The typical baseline velocity of the blood in arterial network is selected based on the properties of the parent vein as $\overline{U}^{*a}_{11} = \overline{Q}^{*a}_{11}/\overline{A}^{*v}_{11}$, where $\overline{A}^{*v}_{11}$ is the baseline cross-sectional area of the parent vein.

In subsection A.1.1, we derive the dimensionless governing equation of the b^{th} branch of i^{th} generation of the arterial network. In the following subsection A.1.2, we state the 'tube law' for the b^{th} branch of the i^{th} generation of the arterial network. Boundary and continuity conditions used to solve the arterial network are given in subsection A.1.3. In the last subsection 5.2.5, we outline the final model along with all boundary and continuity conditions.

A.1.1 Dimensionless governing equation for the b^{th} branch of the i^{th} generation of the arterial network

We non-dimensionalise all variables relative to the parent vein where lengths are scaled on the square root of the baseline cross-sectional area of the parent vein $\left(\overline{A}^{*v}_{11}\right)^{1/2}$, and time on $\left(\left(\overline{A}^{*v}_{11}\right)^{1/2}/\overline{U}^{*v}_{11}\right)$. We choose a viscous pressure scale $P^* = \mu^{*v}_{11}\overline{Q}^{*a}_{11}/\left(\overline{A}^{*v}_{11}\right)^{3/2}$. The choice

of non-dimensional scales yields the following non-dimensional groups

$$\mathcal{R} = \frac{\rho^* \overline{U}^{*v}_{11} \left(\overline{A}^{*v}_{11}\right)^{1/2}}{\mu^{*v}_{11}}, \qquad k^a_{bi} = \frac{k^{*a}_{bi}}{P^*}, \qquad \mu^a_{bi} = \frac{\mu^{*a}_{bi}}{\mu^{*v}_{11}}, \qquad \overline{A}^a_{bi} = \frac{\overline{A}^{*a}_{bi}}{\overline{A}^{*v}_{11}}, \qquad L^a_{bi} = \frac{L^{*a}_{bi}}{\left(\overline{A}^{*v}_{11}\right)^{1/2}},$$

where $\mathcal{R}$ is the Reynolds number, k^a_{bi} is the non-dimensional vessel wall stiffness of the b^{th} branch of the i^{th} artery, μ^a_{bi} is the non-dimensional viscosity of the b^{th} branch of the i^{th} artery, $\overline{A}^a_{bi}$ is the non-dimensional vessel cross-sectional area of the b^{th} branch of the i^{th} artery, and L^a_{bi} is the non-dimensional vessel length of the b^{th} branch of the i^{th} artery.

We again assume long-wavelength deformations ($\beta = 1/L^v_{11} \ll 1$), where L^v_{11} is the length of the parent vein and re-scale the independent variables according to

$$x = \beta^{-1}\tilde{x}, \;\; t = \beta^{-1}\tilde{t},$$

dependent variables according to

$$u_{xbi} = \tilde{u}_{\tilde{x},bi}, \;\; u_{rbi} = \beta\tilde{u}_{\tilde{r}bi}, \;\; p^a_{bi} = \beta^{-1}\tilde{p}^a_{bi}, \;\; A^a_{bi} = \tilde{A}^a_{bi}$$

and model parameters according to

$$\mathcal{R} = \beta^{-1}\tilde{\mathcal{R}}, \; k^a_{bi} = \beta^{-1}\tilde{k}^a_{bi}, \; \mu^a_{bi} = \tilde{\mu}^a_{bi}, \; \overline{A}^a_{bi} = \widetilde{\overline{A}^a}_{bi}, \; Q^a_{bi} = \tilde{Q}^a_{bi}, \; L^a_{bi} = \beta^{-1}\tilde{L}^a_{bi}.$$

For notational simplicity, we henceforth drop the tilde in all subsequent equations. Following the same derivation as described in subsection 4.2.9 in Chapter 4, we finally obtain the governing equation for the b^{th} branch vessel of i^{th} generation in the closed form as

$$\frac{\partial A^a_{bi}}{\partial t} = \frac{1}{\overline{A}^a_{bi}\mu^a_{bi}} \frac{\partial}{\partial x}\left(\frac{\left(A^a_{bi}\right)^2}{8\pi}\frac{\partial p^a_{bi}}{\partial x}\right). \tag{A.1}$$

The flux in the b^{th} branch vessels $a_{bi}, b, i = 1, 2$ of the i^{th} generation of the arterial network is given by

$$q^a_{bi} = -\frac{k^a_{bi}}{8\pi\mu^a_{bi}}\left(\left(\frac{m}{(\overline{A}^a_{bi})^{m+2}}(A^a_{bi})^{m+1} + \frac{n}{(\overline{A}^a_{bi})^{-n+2}}(A^a_{bi})^{-n+1}\right)\frac{\partial A^a_{bi}}{\partial x}\right). \tag{A.2}$$

A.1.2 Dimensionless 'tube law' for arterial network

As discussed in subsection 4.2.5 of Chapter 4, the elastic response of the vessel wall is modelled by using the 'tube law', and now it can be modified for a diverging arterial network.

The'tube law' for the b^{th} branch of i^{th} generation of the arterial network is given by

$$p_{bi}^{*a} = k_{bi}^{*a} \mathcal{F}\left(\frac{A_{bi}^{*a}}{\overline{A}_{bi}^{a}}\right). \tag{A.3}$$

For all vessels the non-linear function $\mathcal{F}$ is given by

$$\mathcal{F}(s) = s^m - s^{-n}. \tag{A.4}$$

A detailed discussion on 'tube law' is given in subsection 4.2.1 of chapter 4.

Assuming the long-wavelength approximation, the dimensionless 'tube law' for the b^{th} branch of the i^{th} generation of the arterial network can be written as

$$p_{bi}^{a}(x,t) = k_{bi}^{a}\left(\left(\frac{A_{bi}^{a}}{\overline{A}_{bi}^{a}}\right)^{m} - \left(\frac{A_{bi}^{a}}{\overline{A}_{bi}^{a}}\right)^{-n}\right). \tag{A.5}$$

A.1.3 Boundary and continuity conditions of the network

Based on the structure of the network, we choose suitable boundary conditions at the inlet and outlet of the network, given in subsection A.1.3.1. Also, to ensure the continuity of blood flow within the vessels of the network itself, we need to impose suitable continuity conditions on pressure and flow at each of the junctions of the network, as discussed in the subsection 5.2.4.2.

A.1.3.1 Boundary conditions

For the converging arterial network consisting of two generations, we prescribed the fixed flux $Q_{11}^{a} = 1$ at the inlet of the parent vessel of generation 1 of the arterial network. It is important to note that $Q_{12}^{a} + Q_{22}^{a} = 1$. At the outlet of the arterial network, the outlets of the daughters in generation 2, we prescribe free return of fluid to the heart, so that the pressure is effectively zero, i.e., $p_{12}^{a} = 0, p_{22}^{a} = 0$ at $x = 1$.

A.1.3.2 Continuity conditions at junction of the network

The continuity of flux condition is physically motivated by the requirement that mass is conserved through the junction (bifurcation) of the network.

The mass flux balance at the junction of generation 1 and generation 2 results in

$$q_{11}^{a}(L_{11},t) = q_{12}^{a}(0,t) + q_{22}^{a}(0,t), \tag{A.6}$$

The continuity of pressure leads to the condition that the outlet pressure of generation 1 should

exactly match the inlet pressure of generation 2 neighbouring generation, which is given by

$$p^a_{11}(L_{11},t) = p^a_{12}(0,t), \quad p^a_{11}(L_{11},t) = p^a_{22}(0,t). \tag{A.7}$$

A.1.4 Final model

The final system of equations for a vessel in the i^{th} generation of the arterial network is obtained by substituting the 'tube law' (A.5) into (A.1) (see the discussion in subsection A.1.2) and is given by

$$\frac{\partial A^a_{bi}}{\partial t} = \frac{1}{\overline{A}^a_{bi}\mu^a_{bi}} \frac{\partial}{\partial x}\left(\frac{(A^a_{bi})^2}{8\pi} \left(k^a_{bi}\left(m(A^a_{bi})^{m-1} + n(A^a_{bi})^{-n-1} \right) \frac{\partial A^a_{bi}}{\partial x} \right) \right), \tag{A.8a}$$

subject to boundary conditions ($b = 1,2$) at the inlet

$$\frac{\partial A^a_{11}}{\partial x} = -\frac{8\pi Q^a_{11}\mu^a_{11}}{k^a_{11}\left(m\frac{(A^a_{11})^{m+1}}{(\overline{A}^a_{11})^{m+2}} + n\frac{(A^a_{11})^{-n+1}}{(\overline{A}^a_{11})^{-n+2}} \right)}, \quad (x = 0), \tag{A.8b}$$

and at the two outlets

$$A^a_{12} = \overline{A}^a_{12}, \qquad (x = 1), \tag{A.8c}$$

$$A^a_{22} = \overline{A}^a_{22}, \qquad (x = 1), \tag{A.8d}$$

and continuity of pressure and continuity of flux conditions at the junction between generation 1 and generation 2 in the arterial network

$$p^a_{11}(L^a_{11},t) = p^a_{12}(0,t), \quad p^a_{11}(L^a_{22},t) = p^a_{22}(0,t), \tag{A.8e}$$

$$q^a_{11}(L^a_{11},t) = q^a_{12}(0,t) + q^a_{22}(0,t). \tag{A.8f}$$

A.1.5 Static solution

We begin by isolating the time-independent (static) solution of the arterial network model (A.8).

Static solutions of (A.8) must have constant flux ($q^a_{11} = Q^a_{11}$, such that $Q^a_{11} = Q^a_{12} + Q^a_{22} = 1$) while the corresponding cross-sectional area profile $A^a_{bi} = A^{a\,(s)}_{bi}(x)$ must satisfy the first-order

nonlinear ordinary differential equation (ODE) for the b^{th} branch vessel of the i^{th} generation

$$(A_{bi}^{a\,(s)})_x = -(k_{bi}^a)^{-1}\left(\left(\frac{m}{(\overline{A}_{bi}^a)^{m+2}}\right)(A_{bi}^{a\,(s)})^{m+1} + \left(\frac{n}{(\overline{A}_{bi}^a)^{-n+2}}\right)(A_{bi}^{a\,(s)})^{-n+1}\right)^{-1} 8\pi\mu_{bi}^a Q_{bi}^a, \quad (A.9)$$
$$(0 \le x \le L_{bi}^a), b, i = 1, 2.$$

A.2 Numerical methods

This section describes the numerical schemes used to solve both the steady and the unsteady versions of the network model. Numerical simulations for both models were carried out using MATLAB version 2023a. It is important to note that we follow the same technique used for the venous network in subsection 5.3 of Chapter 5. In this section, we discuss only the assumptions and techniques that differ from the venous network model discussed in subsection 5.3 of Chapter 5. In subsection A.2.1, we first discuss the numerical methods developed to solve the steady state version of the arterial network model. Then, in the following subsection A.2.2, we focus on the numerical method used to solve the unsteady arterial network model.

A.2.1 Numerical methods for static models

As mentioned earlier in subsection 5.3, we discretise the spatial derivatives present in the equation (A.9) using the second order finite difference method and employ Newton's method to compute the profiles $A_{bi}^{a\,(s)}$ using the 'fsolve' solver in MATLAB to solve these nonlinear algebraic equations. Following the similar fashion adopted for the venous network, at the outlet of the two daughter vessels $\xi = 1$, we use the Dirichlet boundary conditions $A_{12}^{a\,(s)}(\xi = 1) = \overline{A}_{12}^a$ and $A_{22}^{a\,(s)}(\xi = 1) = \overline{A}_{22}^a$.

At the inlet $\xi = 0$ of the parent vessel, the inlet flux is prescribed as $q_{11}^a(0) = Q_{11}^a = 1$ such that $Q_{11}^a = Q_{12}^a + Q_{22}^a = 1$. At the inlet ($\xi = 0$), the first-order spatial derivative in (A.9) is discretised using an off-centred finite difference approximation as described in subsection 5.3.1 of Chapter 5.

At the junction of the arterial network, to employ the non-linear pressure conditions using the equation given in (A.8f), we use Newton's method to compute the value of $A_{bi}^{a\,(s)}$. The value of $A_{bi}^{a\,(s)}$ can be solved directly by setting

$$k_{11}^a((((A_{11}^{a\,(s)})(\xi = 1))/\overline{A}_{11}^a)^m - (((A_{11}^{a\,(s)}(\xi = 1))/\overline{A}_{11}^a)^{-n}) = k_{12}^a(((A_{12}^{a\,(s)})(\xi = 0))^m - ((A_{12}^{a\,(s)})(\xi = 0))^{-n}) \quad (A.10)$$

and

$$k_{11}^{a}((((A_{11}^{a}{}^{(s)})(\xi=1)/\overline{A}_{11}^{a})^{m}-((A_{11}^{a}{}^{(s)})(\xi=1)/\overline{A}_{11}^{a})^{-n}) \\ = k_{22}^{a}(((A_{22}^{a}{}^{(s)})(\xi=0))^{m}-((A_{22}^{a}{}^{(s)})(\xi=0))^{-n}). \quad \text{(A.11)}$$

A.2.2 Numerical methods for unsteady models

For unsteady simulation of the arterial network, we use the same approach discussed for the venous in subsection 5.6 of Chapter 5. We only highlight the differences in the numerical scheme compared to the one presented for the bifurcating venous network; all remaining details follow 5.6 of Chapter 5.

At the two outlets $\xi = 1$ of the two daughters of generation 2, we impose the Dirichlet boundary condition $A_{12}^{a} = \overline{A}_{12}^{a}, A_{22}^{a} = \overline{A}_{22}^{a}$.

At the inlet of the parent in generation 1, where the flux is prescribed, we introduce one fictitious node at the inlet and compute the corresponding cross-sectional area at the fictitious nodes by solving the boundary condition (A.8b). We then use the ghost point value to evaluate the second-order stencil for the given equation (A.8).

At the junction node, we impose the continuity of pressure condition by matching the pressure values at the outlet of the parent with the two inlet pressure values of the two daughters. Mathematically, it can be written as

$$(p_{11}^{a})_{N}^{l+1} = (p_{12}^{a})_{0}^{l+1},\ (p_{11}^{a})_{N}^{l+1} = (p_{22}^{a})_{0}^{l+1},\ \ l = 1,2,... \quad \text{(A.12)}$$

where the superscripts indicate timesteps and the subscripts indicate grid locations. Then we follow the same approach discussed in 5.6 of Chapter 5.

To impose the continuity of flux condition at the junction of the generation 1 and the generation 2, we consider

$$(q_{11}^{a})_{N}^{l+1} = (q_{12}^{a})_{0}^{l+1} + (q_{22}^{a})_{0}^{l+1}, \quad \text{(A.13)}$$

where $q_{11}^{a}, q_{12}^{a}, q_{22}^{a}$ are given in (5.2) and (5.3). We then follow the same techniques given in 5.6 of Chapter 5.

A.3 Parameter values of the arterial network

Following the similar approach discussed in subsection 5.4 of Chapter 5, for our arterial network model, we begin with the superior temporal quadrant, which is the first generation of our arterial network, as shown in Figure A.1. For generation 1 of our arterial network model, we consider the parameter values for generation 1 of Takahashi's network given in the table 1.1 of Chapter 4. For the generation 2 of our network model, we consider the parameter values for generation 2 of

a_{bi}	parameters	symbols	unit	value	source
	lumen radius	$\overline{\overline{R}}_2^*$	μm	42.35	[61]
	length	$\overline{\overline{L}}_2^*$	μm	549.6	[61]
	apparent viscosity	$\overline{\overline{\mu}}_2^*$	$Pa-s$	0.0036	[61]
	blood flow	$\overline{\overline{Q}}_2^*$	mls^{-1}	9.41×10^{-5}	[61]
	wall thickness	$\overline{\overline{h}}_2^*$	μm	28.941	[136]
	wall stiffness	$\overline{\overline{k}}_2^*$	Pa	1895	[136]
	Young's modulus	$\overline{\overline{E}}_2^*$	Pa	218700	[136]
	Poisson ratio	ν	-	0.49	[91]
	density of blood	ρ^*	kgm^{-3}	10^3	[12]

Table A.1: Reference parameter values for the branches of the artery of generation 4 in the retinal network at the superior temporal quadrant.

Takahashi's network given in the table A.1. Everything else follows from our discussion in 5.4 Chapter 5

Bibliography

[1] Otto Frank. *Die grundform des arteriellen pulses: mathematische analyse. erste abhandlung*. 1899.

[2] Konrad Witzig. "Uber erzwungene Wellenbewegungen zaher, inkompressibler Flussigkeiten in elastischen Rohren". PhD thesis. Universitat Bern, 1914.

[3] JR Womersley. "Mathematical theory of oscillating flow in an elastic tube". In: *The Journal of physiology* 127.2 (1955), 37–8P.

[4] John R Womersley. *An elastic tube theory of pulse transmission and oscillatory flow in mammalian arteries*. 614. Wright Air Development Center, 1957.

[5] Richard G Snyder. *Human survivability of extreme impacts in free-fall*. Civil Aeromedical Research Institute, 1963.

[6] MG Taylor. "The input impedance of an assembly of randomly branching elastic tubes". In: *Biophysical journal* 6.1 (1966), pp. 29–51.

[7] Nicolaas Westerhof et al. "Analog studies of the human systemic arterial tree". In: *Journal of biomechanics* 2.2 (1969), pp. 121–143.

[8] Sir James Lighthill. *Mathematical biofluiddynamics*. SIAM, 1975.

[9] CG CARO and TJ PEDLEY. "RC SCHROTER, AND WA SEED". In: *Mechanics of the Circulation. Oxford, UK: Oxford Univ. Press* (1978).

[10] P Henkind, RI Hansen, J Szalay, et al. "Ocular circulation". In: *Physiology of the human eye and visual system* (1979), pp. 98–155.

[11] Alberto P Avolio. "Multi-branched model of the human arterial system". In: *Medical and Biological Engineering and Computing* 18.6 (1980), pp. 709–718.

[12] Timothy J Pedley and YC Fung. "The fluid mechanics of large blood vessels". In: (1980).

[13] Jean Serra. "Image analysis and mathematical morphology". In: *London: Academic Press* (1982).

[14] R Skalak. "The Fluid Mechanics of Large Blood Vessels. By TJ PEDLEY. Cambridge University Press, 1980. 446 pp.£ 35." In: *Journal of Fluid Mechanics* 115 (1982), pp. 535–536.

[15] Claudio Cancelli and TJ Pedley. “A separated-flow model for collapsible-tube oscillations”. In: *Journal of Fluid Mechanics* 157 (1985), pp. 375–404.

[16] P. Maragos and R. Schafer. “Morphological skeleton representation and coding of binary images”. In: *IEEE Transactions on Acoustics, Speech, and Signal Processing* 34.5 (1986), pp. 1228–1244. DOI: 10.1109/TASSP.1986.1164959.

[17] Stanley R Sternberg. “Grayscale morphology”. In: *Computer vision, graphics, and image processing* 35.3 (1986), pp. 333–355.

[18] Yann LeCun et al. “Handwritten digit recognition with a back-propagation network”. In: *Advances in neural information processing systems* 2 (1989).

[19] John B Zimmerman et al. “A psychophysical comparison of two methods for adaptive histogram equalization”. In: *Journal of Digital Imaging* 2 (1989), pp. 82–91.

[20] Harry A Quigley et al. “The size and shape of the optic disc in normal human eyes”. In: *Archives of ophthalmology* 108.1 (1990), pp. 51–57.

[21] VK Sud et al. “Mathematical modelling of flow distribution in the human cardiovascular system”. In: *Medical and Biological Engineering and Computing* 30 (1992), pp. 311–316.

[22] Sohan Singh Hayreh et al. “Retinal vein occlusion”. In: *Indian journal of ophthalmology* 42.3 (1994), p. 109.

[23] Mette Olufsen and Johnny Tom Ottesen. “A fluid-dynamical model of the aorta with bifurcations”. In: (1995).

[24] Bruno A Olshausen and David J Field. “Emergence of simple-cell receptive field properties by learning a sparse code for natural images”. In: *Nature* 381.6583 (1996), pp. 607–609.

[25] Laurent D Cohen and Ron Kimmel. “Global minimum for active contour models: A minimal path approach”. In: *International journal of computer vision* 24 (1997), pp. 57–78.

[26] David N Ku. “Blood flow in arteries”. In: *Annual review of fluid mechanics* 29.1 (1997), pp. 399–434.

[27] Yoshinobu Sato et al. “3D multi-scale line filter for segmentation and visualization of curvilinear structures in medical images”. In: *International Conference on Computer Vision, Virtual Reality, and Robotics in Medicine*. Springer. 1997, pp. 213–222.

[28] Alejandro F Frangi et al. “Multiscale vessel enhancement filtering”. In: *Medical Image Computing and Computer-Assisted Intervention—MICCAI’98: First International Conference Cambridge, MA, USA, October 11–13, 1998 Proceedings 1*. Springer. 1998, pp. 130–137.

[29] Annemette Sofie Olufsen. “Modeling the arterial system with reference to an anesthesia simulator”. In: (1998).

[30] BS Brook, SAEG Falle, and TJ Pedley. “Numerical solutions for unsteady gravity-driven flows in collapsible tubes: evolution and roll-wave instability of a steady state”. In: *Journal of Fluid Mechanics* 396 (1999), pp. 223–256.

[31] Mette S Olufsen. “Structured tree outflow condition for blood flow in larger systemic arteries”. In: *American journal of physiology-Heart and circulatory physiology* 276.1 (1999), H257–H268.

[32] Pierre Soille et al. *Morphological image analysis: principles and applications*. Vol. 2. 3. Springer, 1999.

[33] Richard B Chambers. “The role of mathematical modeling in medical research:“research without patients?””. In: *Ochsner Journal* 2.4 (2000), pp. 218–223.

[34] AD Hoover, Valentina Kouznetsova, and Michael Goldbaum. “Locating blood vessels in retinal images by piecewise threshold probing of a matched filter response”. In: *IEEE Transactions on Medical imaging* 19.3 (2000), pp. 203–210.

[35] Jane D Kivlin et al. “Shaken baby syndrome”. In: *Ophthalmology* 107.7 (2000), pp. 1246–1254.

[36] Andrew D Blann. “How a damaged blood vessel wall contibutes to thrombosis and hypertenasion”. In: *Pathophysiology of haemostasis and thrombosis* 33.5-6 (2003), pp. 445–448.

[37] MD Knudtson et al. “Variation associated with measurement of retinal vessel diameters at different points in the pulse cycle”. In: *British journal of ophthalmology* 88.1 (2004), pp. 57–61.

[38] Meindert Niemeijer et al. “Comparative study of retinal vessel segmentation methods on a new publicly available database”. In: *Medical imaging 2004: image processing*. Vol. 5370. SPIE. 2004, pp. 648–656.

[39] José Roberto Ortale, Luisa Carolina Borges Keiralla, and Luciana Sacilotto. “The posterior ventricular branches of the coronary arteries in the human heart”. In: *Arquivos brasileiros de cardiologia* 82 (2004), pp. 463–467.

[40] Axel R Pries, Bettina Reglin, and Timothy W Secomb. “Remodeling of blood vessels: responses of diameter and wall thickness to hemodynamic and metabolic stimuli”. In: *Hypertension* 46.4 (2005), pp. 725–731.

[41] Vinod Suresh et al. “A mathematical model of alveolar gas exchange in partial liquid ventilation”. In: *J. Biomech. Eng.* 127.1 (2005), pp. 46–59.

[42] Xiaoling Liu, Hui Li, and Zhiguo Guo. "Evaluation and implementation of dynamic production capacity in the workshop based on Dixtra algorithm [J]". In: *Microcomputer information* 12 (2006), pp. 96–98.

[43] João VB Soares et al. "Retinal vessel segmentation using the 2-D Gabor wavelet and supervised classification". In: *IEEE Transactions on medical Imaging* 25.9 (2006), pp. 1214–1222.

[44] Alauddin Bhuiyan et al. "Blood vessel segmentation from color retinal images using unsupervised texture classification". In: *2007 IEEE International Conference on Image Processing*. Vol. 5. IEEE. 2007, pp. V–521.

[45] Yunlong Huo and Ghassan S Kassab. "A hybrid one-dimensional/Womersley model of pulsatile blood flow in the entire coronary arterial tree". In: *American Journal of Physiology-Heart and Circulatory Physiology* 292.6 (2007), H2623–H2633.

[46] Elisa Ricci and Renzo Perfetti. "Retinal blood vessel segmentation using line operators and support vector classification". In: *IEEE transactions on medical imaging* 26.10 (2007), pp. 1357–1365.

[47] Leopold Schmetterer and Gerhard Garhofer. "How Can Blood Flow Be Measured?" In: *Survey of Ophthalmology* 52.6, Supplement (2007), S134–S138. ISSN: 0039-6257. DOI: https://doi.org/10.1016/j.survophthal.2007.08.008. URL: https://www.sciencedirect.com/science/article/pii/S0039625707001853.

[48] Leopold Schmetterer and Gerhard Garhöfer. "Retinal Blood Flow". In: *Retinal Vascular Disease*. Ed. by Antonia M. Joussen et al. Berlin, Heidelberg: Springer Berlin Heidelberg, 2007, pp. 167–174. ISBN: 978-3-540-29542-6. DOI: 10.1007/978-3-540-29542-6_9. URL: https://doi.org/10.1007/978-3-540-29542-6_9.

[49] Gérard Biau, Luc Devroye, and Gäbor Lugosi. "Consistency of random forests and other averaging classifiers." In: *Journal of Machine Learning Research* 9.9 (2008).

[50] Rachel B Clipp and Brooke N Steele. "Impedance boundary conditions for the pulmonary vasculature including the effects of geometry, compliance, and respiration". In: *IEEE transactions on biomedical engineering* 56.3 (2008), pp. 862–870.

[51] Herbert Gross, Fritz Blechinger, and Bertram Achtner. "Human eye". In: *Handbook of Optical Systems: Volume 4: Survey of Optical Instruments* 4 (2008), pp. 1–87.

[52] Jonathan P Mynard and P Nithiarasu. "A 1D arterial blood flow model incorporating ventricular pressure, aortic valve and regional coronary flow using the locally conservative Galerkin (LCG) method". In: *Communications in numerical methods in engineering* 24.5 (2008), pp. 367–417.

[53] Wilmer W Nichols and Michael F O'Rourke. "The life and times of Donald A. McDonald". In: *Artery Research* 2.1 (2008), pp. 1–8.

[54] Jordi Alastruey et al. "Analysing the pattern of pulse waves in arterial networks: a time-domain study". In: *Journal of engineering mathematics* 64.4 (2009), pp. 331–351.

[55] Delia Baleanu et al. "Wall-to-lumen ratio of retinal arterioles and arteriole-to-venule ratio of retinal vessels in patients with cerebrovascular damage". In: *Investigative ophthalmology & visual science* 50.9 (2009), pp. 4351–4359.

[56] Rafael C Gonzalez. *Digital image processing*. Pearson education india, 2009.

[57] J. Komala Lakshmi and M. Punithavalli. "A Survey on Skeletons in Digital Image Processing". In: *2009 International Conference on Digital Image Processing*. 2009, pp. 260–269. DOI: 10.1109/ICDIP.2009.21.

[58] Alireza Osareh and Bita Shadgar. "Retinal Vessel Extraction Using Gabor Filters and Support Vector Machines". In: *Advances in Computer Science and Engineering*. Ed. by Hamid Sarbazi-Azad et al. Berlin, Heidelberg: Springer Berlin Heidelberg, 2009, pp. 356–363. ISBN: 978-3-540-89985-3.

[59] Kim H Parker. "An introduction to wave intensity analysis". In: *Medical & biological engineering & computing* 47.2 (2009), pp. 175–188.

[60] Peter S Stewart, Sarah L Waters, and Oliver E Jensen. "Local and global instabilities of flow in a flexible-walled channel". In: *European Journal of Mechanics-B/Fluids* 28.4 (2009), pp. 541–557.

[61] Tatsuhisa Takahashi et al. "A mathematical model for the distribution of hemodynamic parameters in the human retinal microvascular network". In: *Journal of biorheology* 23.2 (2009), pp. 77–86.

[62] Nico Westerhof, Jan-Willem Lankhaar, and Berend E Westerhof. "The arterial windkessel". In: *Medical & biological engineering & computing* 47.2 (2009), pp. 131–141.

[63] Jinming Zou, Yi Han, and Sung-Sau So. "Overview of artificial neural networks". In: *Artificial neural networks: methods and applications* (2009), pp. 14–22.

[64] Michael D Abràmoff, Mona K Garvin, and Milan Sonka. "Retinal imaging and image analysis". In: *IEEE reviews in biomedical engineering* 3 (2010), pp. 169–208.

[65] Luca Formaggia, Alfio Quarteroni, and Allesandro Veneziani. *Cardiovascular Mathematics: Modeling and simulation of the circulatory system*. Vol. 1. Springer Science & Business Media, 2010.

[66] Anil K Jain. "Data clustering: 50 years beyond K-means". In: *Pattern recognition letters* 31.8 (2010), pp. 651–666.

[67] Vinod Nair and Geoffrey E Hinton. "Rectified linear units improve restricted boltzmann machines". In: *Proceedings of the 27th international conference on machine learning (ICML-10)*. 2010, pp. 807–814.

[68] Gareth DA Vaughan. "Pulse propagation in the pulmonary and systemic arteries". PhD thesis. University of Glasgow, 2010.

[69] Tien Y Wong and Ingrid U Scott. "Retinal-vein occlusion". In: *New England Journal of Medicine* 363.22 (2010), pp. 2135–2144.

[70] Justis P Ehlers and Sharon Fekrat. "Retinal vein occlusion: beyond the acute event". In: *Survey of ophthalmology* 56.4 (2011), pp. 281–299.

[71] Andrej Krenker, Janez Bešter, and Andrej Kos. "Introduction to the artificial neural networks". In: *Artificial Neural Networks: Methodological Advances and Biomedical Applications. InTech* (2011), pp. 1–18.

[72] Yubing Shi, Patricia Lawford, and Rodney Hose. "Review of zero-D and 1-D models of blood flow in the cardiovascular system". In: *Biomedical engineering online* 10.1 (2011), p. 33.

[73] Muhammad Moazam Fraz et al. "An approach to localize the retinal blood vessels using bit planes and centerline detection". In: *Computer methods and programs in biomedicine* 108.2 (2012), pp. 600–616.

[74] Muhammad Moazam Fraz et al. "An ensemble classification-based approach applied to retinal blood vessel segmentation". In: *IEEE Transactions on Biomedical Engineering* 59.9 (2012), pp. 2538–2548.

[75] Muhammad Moazam Fraz et al. "Blood vessel segmentation methodologies in retinal images–a survey". In: *Computer methods and programs in biomedicine* 108.1 (2012), pp. 407–433.

[76] Gerhard Garhofer et al. "Retinal blood flow in healthy young subjects". In: *Investigative ophthalmology & visual science* 53.2 (2012), pp. 698–703.

[77] Geoffrey E Hinton et al. "Improving neural networks by preventing co-adaptation of feature detectors". In: *arXiv preprint arXiv:1207.0580* (2012).

[78] Alex Krizhevsky, Ilya Sutskever, and Geoffrey E Hinton. "Imagenet classification with deep convolutional neural networks". In: *Advances in neural information processing systems* 25 (2012).

[79] Carlo La Spina et al. "Practical management of retinal vein occlusions". In: *Ophthalmology and Therapy* 1.1 (2012), p. 3.

[80] Mette S Olufsen et al. "Rarefaction and blood pressure in systemic and pulmonary arteries". In: *Journal of fluid mechanics* 705 (2012), pp. 280–305.

[81] Leopold Schmetterer and Jeffrey Kiel. *Ocular blood flow*. Springer Science & Business Media, 2012.

[82] Attila Budai and Jan Odstrcilik. *High Resolution Fundus (HRF) Image Database*. https://www5.cs.fau.de/research/data/fundus-images/. 2013.

[83] Augustus Edward Hough Love. *A treatise on the mathematical theory of elasticity*. Cambridge university press, 2013.

[84] Laurent Najman and Hugues Talbot. "Introduction to mathematical morphology". In: *Mathematical morphology: from theory to applications* (2013), pp. 1–33.

[85] Muhammad Umar Qureshi. "Simulating the pulse wave in the human pulmonary circulation". PhD thesis. University of Glasgow, 2013.

[86] Richard S Snell and Michael A Lemp. *Clinical anatomy of the eye*. John Wiley & Sons, 2013.

[87] Patrick Watts et al. "Newborn retinal hemorrhages: A systematic review". In: *Journal of American Association for Pediatric Ophthalmology and Strabismus* 17.1 (2013), pp. 70–78. ISSN: 1091-8531. DOI: https://doi.org/10.1016/j.jaapos.2012.07.012. URL: https://www.sciencedirect.com/science/article/pii/S1091853112004168.

[88] Jordi Alastruey, Anthony AE Hunt, and Peter D Weinberg. "Novel wave intensity analysis of arterial pulse wave propagation accounting for peripheral reflections". In: *International journal for numerical methods in biomedical engineering* 30.2 (2014), pp. 249–279.

[89] Pablo J Blanco et al. "An anatomically detailed arterial network model for one-dimensional computational hemodynamics". In: *IEEE Transactions on biomedical engineering* 62.2 (2014), pp. 736–753.

[90] A Das and J Byrd. "Retinal vasculature: structure and pathologies". In: (2014).

[91] Giovanna Guidoboni et al. "Intraocular pressure, blood pressure, and retinal blood flow autoregulation: a mathematical model to clarify their relationship and clinical relevance". In: *Investigative ophthalmology & visual science* 55.7 (2014), pp. 4105–4118.

[92] Gaurav Kumar and Pradeep Kumar Bhatia. "A Detailed Review of Feature Extraction in Image Processing Systems". In: *2014 Fourth International Conference on Advanced Computing Communication Technologies*. 2014, pp. 5–12. DOI: 10.1109/ACCT.2014.74.

[93] Rainer A Leitgeb et al. "Doppler optical coherence tomography". In: *Progress in retinal and eye research* 41 (2014), pp. 26–43.

[94] Lucas Omar Muller. “Mathematical modelling and simulation of the human circulation with emphasis on the venous system: application to the CCSVI condition”. In: (2014).

[95] Lucas O Müller and Eleuterio F Toro. “A global multiscale mathematical model for the human circulation with emphasis on the venous system”. In: *International journal for numerical methods in biomedical engineering* 30.7 (2014), pp. 681–725.

[96] M Umar Qureshi et al. “Numerical simulation of blood flow and pressure drop in the pulmonary arterial and venous circulation”. In: *Biomechanics and modeling in mechanobiology* 13.5 (2014), pp. 1137–1154.

[97] Karen Simonyan and Andrew Zisserman. “Very deep convolutional networks for large-scale image recognition”. In: *arXiv preprint arXiv:1409.1556* (2014).

[98] Hans E Grossniklaus, Eldon E Geisert, and John M Nickerson. “Introduction to the Retina”. In: *Progress in molecular biology and translational science* 134 (2015), pp. 383–396.

[99] Amit B Jain, Vadivelu Jaya Prakash, and Muna Bhende. “Techniques of fundus imaging”. In: *Med. Vis. Res. Found* 33 (2015), p. 100.

[100] Joonwhoan Lee, Suresh Raj Pant, and Hee-Sin Lee. “An adaptive histogram equalization based local technique for contrast preserving image enhancement”. In: *International Journal of Fuzzy Logic and Intelligent Systems* 15.1 (2015), pp. 35–44.

[101] Jonathan Long, Evan Shelhamer, and Trevor Darrell. “Fully convolutional networks for semantic segmentation”. In: *Proceedings of the IEEE conference on computer vision and pattern recognition*. 2015, pp. 3431–3440.

[102] Jihene Malek et al. “Computational analysis of blood flow in the retinal arteries and veins using fundus image”. In: *Computers Mathematics with Applications* 69.2 (2015), pp. 101–116. ISSN: 0898-1221. DOI: https://doi.org/10.1016/j.camwa.2014.11.017. URL: https://www.sciencedirect.com/science/article/pii/S0898122114005859.

[103] K Mohana, D Bhende, and D Muna. “Optical coherence tomography: newer techniques, newer machines”. In: *Sci J Med Vis Res Found* 2 (2015), pp. 75–78.

[104] Baptiste Moreau and Benjamin Mauroy. “Murray’s law revisited: Quémada’s fluid model and fractal trees”. In: *Journal of Rheology* 59.6 (2015), pp. 1419–1430.

[105] Olaf Ronneberger, Philipp Fischer, and Thomas Brox. “U-net: Convolutional networks for biomedical image segmentation”. In: *Medical image computing and computer-assisted intervention–MICCAI 2015: 18th international conference, Munich, Germany, October 5-9, 2015, proceedings, part III 18*. Springer. 2015, pp. 234–241.

[106] Ehsan Varnousfaderani Shahrian et al. "Vessels segmentation in color retinal images using ensemble of bagged decision trees and patched based principle component analysis and linear discriminant analysis". In: *Investigative Ophthalmology & Visual Science* 56.7 (2015), pp. 5262–5262.

[107] Christian Szegedy et al. "Going deeper with convolutions". In: *Proceedings of the IEEE conference on computer vision and pattern recognition*. 2015, pp. 1–9.

[108] Nico Westerhof, Patrick Segers, and Berend E Westerhof. "Wave separation, wave intensity, the reservoir-wave concept, and the instantaneous wave-free ratio: presumptions and principles". In: *Hypertension* 66.1 (2015), pp. 93–98.

[109] Shahab Aslani and Haldun Sarnel. "A new supervised retinal vessel segmentation method based on robust hybrid features". In: *Biomedical Signal Processing and Control* 30 (2016), pp. 1–12.

[110] Emily Dawn Cole et al. "Contemporary retinal imaging techniques in diabetic retinopathy: a review". In: *Clinical & experimental ophthalmology* 44.4 (2016), pp. 289–299.

[111] Christian Contarino et al. "Junction-generalized Riemann problem for stiff hyperbolic balance laws in networks: an implicit solver and ADER schemes". In: *Journal of Computational Physics* 315 (2016), pp. 409–433.

[112] David De Wilde et al. "Assessment of shear stress related parameters in the carotid bifurcation using mouse-specific FSI simulations". In: *Journal of biomechanics* 49.11 (2016), pp. 2135–2142.

[113] Kaiming He et al. "Deep residual learning for image recognition". In: *Proceedings of the IEEE conference on computer vision and pattern recognition*. 2016, pp. 770–778.

[114] Alireza Karimi et al. "Experimental verification of the healthy and atherosclerotic coronary arteries incompressibility via Digital Image Correlation". In: *Artery Research* 16 (2016), pp. 1–7. ISSN: 1872-9312. DOI: https://doi.org/10.1016/j.artres.2016.08.002. URL: https://www.sciencedirect.com/science/article/pii/S1872931216300369.

[115] Farnaz Farokhian et al. "Automatic parameters selection of Gabor filters with the imperialism competitive algorithm with application to retinal vessel segmentation". In: *Biocybernetics and Biomedical Engineering* 37.1 (2017), pp. 246–254. ISSN: 0208-5216. DOI: https://doi.org/10.1016/j.bbe.2016.12.007. URL: https://www.sciencedirect.com/science/article/pii/S0208521617300153.

[116] Hossein Nazari Khanamiri, Austin Nakatsuka, and Jaafar El-Annan. "Smartphone fundus photography". In: *Journal of Visualized Experiments: JoVE* 125 (2017), p. 55958.

[117] Ritesh Khatakalle and Rajesh Shekokar. "Artery and Vein Classification in Retinal Images using Graph Based Approach". In: *IJARCCE* 6 (Mar. 2017), pp. 170–173. DOI: 10.17148/IJARCCE.2017.6335.

[118] Meiaad Khayat et al. "Animal models of retinal vein occlusion". In: *Investigative ophthalmology & visual science* 58.14 (2017), pp. 6175–6192.

[119] Maliheh Miri et al. "A comprehensive study of retinal vessel classification methods in fundus images". In: *Journal of Medical Signals & Sensors* 7.2 (2017), pp. 59–70.

[120] Timothy W Secomb. "Blood flow in the microcirculation". In: *Annual Review of Fluid Mechanics* 49 (2017), pp. 443–461.

[121] Eva Tuba, Lazar Mrkela, and Milan Tuba. "Retinal blood vessel segmentation by support vector machine classification". In: *2017 27th International Conference Radioelektronika (RADIOELEKTRONIKA)*. IEEE. 2017, pp. 1–6.

[122] Muffy Calder et al. "Computational modelling for decision-making: where, why, what, who and how". In: *Royal Society open science* 5.6 (2018), p. 172096.

[123] Oliver Fleck and Thierry Savin. "A physical approach to model occlusions in the retinal microvasculature". In: *Eye* 32.2 (2018), pp. 189–194.

[124] Jiuxiang Gu et al. "Recent advances in convolutional neural networks". In: *Pattern recognition* 77 (2018), pp. 354–377.

[125] Yuki Hagiwara et al. "Computer-aided diagnosis of glaucoma using fundus images: A review". In: *Computer methods and programs in biomedicine* 165 (2018), pp. 1–12.

[126] Rikiya Yamashita et al. "Convolutional neural networks: an overview and application in radiology". In: *Insights into imaging* 9 (2018), pp. 611–629.

[127] Andrés Garcıa-Floriano et al. "A machine learning approach to medical image classification: Detecting age-related macular degeneration in fundus images". In: *Computers & Electrical Engineering* 75 (2019), pp. 218–229.

[128] Giovanna Guidoboni, Alon Harris, and Riccardo Sacco. *Ocular fluid dynamics*. Springer, 2019.

[129] Michelle Livne et al. "A U-Net deep learning framework for high performance vessel segmentation in patients with cerebrovascular disease". In: *Frontiers in neuroscience* 13 (2019), p. 97.

[130] Daniele Prada et al. "Vascular anatomy and physiology of the eye". In: *Ocular Fluid Dynamics: Anatomy, Physiology, Imaging Techniques, and Mathematical Modeling* (2019), pp. 23–45.

[131] Peter S Stewart and Alexander JE Foss. “Self-excited oscillations in a collapsible channel with applications to retinal venous pulsation”. In: *The ANZIAM Journal* 61.3 (2019), pp. 320–348.

[132] Fengjun Zhao et al. “Segmentation of blood vessels using rule-based and machine-learning-based methods: a review”. In: *Multimedia Systems* 25 (2019), pp. 109–118.

[133] Dingfu Zhou et al. “Iou loss for 2d/3d object detection”. In: *2019 international conference on 3D vision (3DV)*. IEEE. 2019, pp. 85–94.

[134] Mohiuddin Ahmed, Raihan Seraj, and Syed Mohammed Shamsul Islam. “The k-means algorithm: A comprehensive survey and performance evaluation”. In: *Electronics* 9.8 (2020), p. 1295.

[135] Humera Shaziya and K Shyamala. “Pulmonary CT images segmentation using CNN and UNet models of deep learning”. In: *2020 IEEE Pune section international conference (PuneCon)*. IEEE. 2020, pp. 195–201.

[136] TA Spelman and PS Stewart. “Shock wave propagation along the central retinal blood vessels”. In: *Proceedings of the Royal Society A* 476.2234 (2020), p. 20190269.

[137] Bharath Subramani and Magudeeswaran Veluchamy. “Fuzzy gray level difference histogram equalization for medical image enhancement”. In: *Journal of medical systems* 44.6 (2020), p. 103.

[138] Jonas Teuwen and Nikita Moriakov. “Convolutional neural networks”. In: *Handbook of medical image computing and computer assisted intervention*. Elsevier, 2020, pp. 481–501.

[139] Orhun Utku Aydin et al. “An evaluation of performance measures for arterial brain vessel segmentation”. In: *BMC medical imaging* 21.1 (2021), p. 113.

[140] Chunhui Chen et al. “Retinal vessel segmentation using deep learning: a review”. In: *IEEE Access* 9 (2021), pp. 111985–112004.

[141] Krishna Gopal Dhal et al. “Histogram equalization variants as optimization problems: a review”. In: *Archives of Computational Methods in Engineering* 28 (2021), pp. 1471–1496.

[142] Anuj Kumar, Harvendra Singh Bhadauria, and Annapurna Singh. “Descriptive analysis of dental X-ray images using various practical methods: A review”. In: *PeerJ Computer Science* 7 (2021), e620.

[143] Jay Aodh Mackenzie. “A 1D model for the pulmonary and coronary circulation accounting for time-varying external pressure”. PhD thesis. University of Glasgow, 2021.

[144] Zhang Chi et al. “Application of multiscale coupling models in the numerical study of circulation system”. In: *Medicine in novel technology and devices* 14 (2022), p. 100117.

[145] Edsger W Dijkstra. "A note on two problems in connexion with graphs". In: *Edsger Wybe Dijkstra: his life, work, and legacy*. 2022, pp. 287–290.

[146] doxygen 1.8.13. *Erosion on a Binary Image*. 2022. URL: https://docs.opencv.org/3.4/morph211.png.

[147] Julia García Cabello. "Mathematical Neural Networks". In: *Axioms* 11.2 (2022). ISSN: 2075-1680. DOI: 10.3390/axioms11020080. URL: https://www.mdpi.com/2075-1680/11/2/80.

[148] Kai Jin et al. "Fives: A fundus image dataset for artificial intelligence based vessel segmentation". In: *Scientific data* 9.1 (2022), p. 475.

[149] Robert Arnar Karlsson and Sveinn Hakon Hardarson. "Artery vein classification in fundus images using serially connected U-Nets". In: *Computer Methods and Programs in Biomedicine* 216 (2022), p. 106650. ISSN: 0169-2607. DOI: https://doi.org/10.1016/j.cmpb.2022.106650. URL: https://www.sciencedirect.com/science/article/pii/S0169260722000359.

[150] Kevin M Moerman et al. "Development of a patient-specific cerebral vasculature fluid–structure-interaction model". In: *Journal of biomechanics* 133 (2022), p. 110896.

[151] Martin R Pfaller et al. "Automated generation of 0D and 1D reduced-order models of patient-specific blood flow". In: *International journal for numerical methods in biomedical engineering* 38.10 (2022), e3639.

[152] Arkaniva Sarkar. *Retinal vessel segmentation using U-NET, Res-UNET, Attention U-NET, and Residual Attention U-NET (RA-UNET) [Computer software]*. GitHub. https://github.com/arkanivasarkar/Retinal-Vessel-Segmentation-using-variants-of-UNET. 2022.

[153] Inc. The MathWorks. *Morphological Dilation of a Binary Image*. 2022. URL: https://uk.mathworks.com/help/images/morph21.gif.

[154] Risheng Wang et al. "Medical image segmentation using deep learning: A survey". In: *IET image processing* 16.5 (2022), pp. 1243–1267.

[155] P Yugander et al. "Extraction of blood vessels from retinal fundus images using maximum principal curvatures and adaptive histogram equalization". In: *2022 First International Conference on Electrical, Electronics, Information and Communication Technologies (ICEEICT)*. IEEE. 2022, pp. 1–4.

[156] Christopher M Bishop and Hugh Bishop. "Convolutional Networks". In: *Deep Learning: Foundations and Concepts*. Springer, 2023, pp. 287–324.

[157] Elsa Wilma Böhm et al. "Methods to measure blood flow and vascular reactivity in the retina". In: *Frontiers in Medicine* 9 (2023), p. 1069449.

[158] Amod Gupta et al. *Ophthalmic Signs in Practice of Medicine*. Springer, 2023.

[159] Mojdeh Mehdizadeh, Kioumars Tavakoli Tafti, and Parisa Soltani. "Evaluation of histogram equalization and contrast limited adaptive histogram equalization effect on image quality and fractal dimensions of digital periapical radiographs". In: *Oral Radiology* 39.2 (2023), pp. 418–424.

[160] Abdelwahid Oubaalla, Hicham El Moubtahij, and Nabil El Akkad. "Medical image segmentation using deep learning: A survey". In: *International Conference on Digital Technologies and Applications*. Springer. 2023, pp. 974–983.

[161] Reza Azad et al. "Medical image segmentation review: The success of u-net". In: *IEEE Transactions on Pattern Analysis and Machine Intelligence* (2024).

[162] Leonard A Levin, Paul L Kaufman, and Mary Elizabeth Hartnett. *Adler's physiology of the eye e-book*. Elsevier Health Sciences, 2024.

[163] Rahul Manoj et al. "Quantification of reflected wave magnitude and transit time using a multi-rayleigh flow waveform model: a simplified approach to arterial wave separation analysis". In: *Biomedical Signal Processing and Control* 93 (2024), p. 106129.

[164] Qing Qin and Yuanyuan Chen. "A review of retinal vessel segmentation for fundus image analysis". In: *Engineering Applications of Artificial Intelligence* 128 (2024), p. 107454.

[165] Tamsin A Spelman et al. "Elastic jump propagation across a blood vessel junction". In: *Royal Society Open Science* 11.7 (2024), p. 232000.

[166] Giri Babu Kande et al. "Multi scale multi attention network for blood vessel segmentation in fundus images". In: *Scientific reports* 15.1 (2025), p. 3438.

[167] Jay A. Mackenzie et al. "Post-processing of coronary and myocardial spatial data". In: *Computers in Biology and Medicine* 196 (2025), p. 110868. ISSN: 0010-4825. DOI: https://doi.org/10.1016/j.compbiomed.2025.110868. URL: https://www.sciencedirect.com/science/article/pii/S0010482525012193.

[168] Al Khalili Y. Mahabadi N. *Neuroanatomy, Retina*. https://www.ncbi.nlm.nih.gov/books/NBK545310/.

[169] Tripathy K. Mishra C. *Fundus Camera.[Updated 2023 Aug 25]*. https://www.ncbi.nlm.nih.gov/books/NBK585111/.

[170] Webvision. http://webvision.med.utah.edu/.